University of Salford MANCHESTER

Study of the Properties of Hydrogen and Deuterium in Beta Phase Palladium Hydride and Deuteride

SIMON ANTHONY STEEL

18/04/2018

Materials and Physics Research Group

School of Computing Science & Engineering

This thesis is submitted in partial fulfilment of the requirements for the degree of Doctor of Philosophy

This work is dedicated to the memory of Professor Donald Keith Ross.

“I may not have gone where I intended to go,

but I think I have ended up where I needed to be.”

Douglas Adams

Contents

Figures

Acknowledgements

This research project would not have been possible without generous funding from AWE[1] and EPSRC[2] through the Industrial CASE (iCASE[3]) program, or the use of premises, equipment, services and financial support from the University of Salford. In particular, I owe thanks to Andrew Wallwark[1] for starting the project as well as the advice he gave me in my first year, and John Knowles[1] for the time and effort he has put in as my industrial supervisor thereafter.

I'd like to thank all the administrative staff that have helped take this project from an idea through to completion, including those in the Partnerships Team (Janet Morana, Marie Watts, Victoria Russell, Vicky Beckett, and Paul Cihlar), Catriona Nardone and her colleagues in Research Support, Sue Platt and her colleagues in Finance, and everyone else at the University of Salford that has helped me in any way. I would also like to thank the university itself for the support I've received I've received outside my academic work.

I owe an awful lot to my good friend and academic supervisor Dr Dan Bull (UoS) who stepped in to help me complete this work after the tragic passing of Professor Donald Keith Ross (UoS). It would be impossible to overstate how lucky I have been to work with him and how grateful I am for everything he has done.

I wish I could thank Keith Ross. Without him, I might have never started down this path. Working with him was occasionally terrifying but incredibly rewarding. I hope he'd be impressed with the outcome of this work if he'd have been able to see it.

I also extend my gratitude to Professor Alan Oates (UoS) for the time that he has spent discussing this work with me, Geoff Parr (UoS) for his time and expertise, and the numerous members of Physics, Chemistry and SoBE that have lent me equipment, given me advice, helped me solve problems, found a few extra hours of teaching / research work when I've needed it, been there to listen when I've been at my wits end, and just made my time at Salford memorable.

[1] Atomic Weapons Establishment: http://www.awe.co.uk
[2] Engineering and Physical Sciences Research Council: http://www.epsrc.ac.uk
[3] EPSRC - iCASE: http://www.epsrc.ac.uk/skills/students/coll/icase

I owe thanks to Dr Franz Demmel & Mark Kibble at ISIS[4] for all their help on the experimental work contained in this document that was performed on OSIRIS and Dr Jacques Ollivier at the ILL[5] for his help on the experimental work in this document that was conducted on IN5.

I owe thanks to Dr Spencer Howells & Eliott Oram at ISIS and Ian Bush & Antti Soininen at the ILL for their help getting data from IN5 and LAMP into MantidPlot, as well as Martyn Gigg at ISIS for all of his help with the software more generally. Without the efforts of everyone that has contributed to MantidPlot, this work would have been vastly more complicated.

I'd also like to thank the STFC. I have only been able to conduct this research thanks to the work of many people, past and present, at their facilities and those of their partners.

And finally, I owe enormous thanks to my friends and family for their help and support during, what can only be described as, "a difficult time in my life". They have kept me sane, smiling, fed, warm and dry.

Mum, Dad, Nick, Nina, Lou, Eddie, Kerrie, Jay, Chris, Sid, Binge, the whole 'Play Team', and Dan (again) – You've all done something special for me in this time. I really don't know if I'd have reached this point without you.

And to anyone else that's helped to see me though this – thanks to you too.

[4] ISIS Neutron & Muon Source: http://www.isis.stfc.ac.uk/
[5] Institut Laue Langevin (Grenoble): https://www.ill.eu/

Glossary

AGHS	Active Gas Handling System (@JET)	**JET**	Joint European Torus
CCR	Closed Cycle Refrigerator	**O-O**	Octahedral to Octahedral
FCC	Face Centred Cubic	**O-T**	Octahedral to Tetrahedral
FWHM	Full Width Half Maximum	**O-T-O**	Octahedral to Tetrahedral to Octahedral
HWHM	Half Width Half Maximum	**OSIRIS**	OSIRIS Spectrometer (@ISIS)
IN5	IN5 Spectrometer (@ILL)	**PID**	Proportional Integral Differential
INS	Inelastic Neutron Scattering	**QENS**	Quasi Elastic Neutron Scattering
ILL	Institut Laue Langevin	**SRO**	Short Range Ordering
ITER	International Thermonuclear Experimental Reactor	**T-T**	Tetrahedral to Tetrahedral
ISIS	ISIS Neutron & Muon Source	**UoS**	University of Salford

Units, Constants, and Standard Values

Symbol	Value	Description
STP	$273.15\ K$, $1\ bar$ $(10^5\ Pa)$	Standard Temperature and Pressure
NTP	$293.15\ K$, $1\ atm$ $(101.325\ kPa)$	Normal Temperature and Pressure (NIST standard)
barn	$10^{-28}\ m^2$	Unit of neutron cross section
Å	$10^{-10}\ m$	Angstrom
$\boldsymbol{h}$	$4.1357 \times 10^{-15}\ eV\ s$	Planck's Constant
$\hbar$	$6.5821 \times 10^{-16}\ eV\ s$	Reduced Planck's Constant $(h/2\pi)$
$\boldsymbol{k_B}$	$8.6173 \times 10^{-5}\ eV\ K^{-1}$	Boltzmann Constant

Conventions in this Document

Data type	Format	Example
Equation	Chapter – equation number	(2-1)
Figure	Chapter – figure letter (upper case)	(2-A)
Chemical Formula	Chapter – formula number in roman numerals	(2-i)
Table	Chapter – table letter (lower case)	(2-a)

The word “Hydrogen” is used in many different contexts within this document. Wherever there is potential for confusion it will be clarified as to whether it references: molecular hydrogen, atomic hydrogen, protium / ^{1}H, or a collective term for all hydrogen isotopes. The isotopes: protium, deuterium, and tritium are either referred to by name, as H, D and T, or ^{1}H, ^{2}H, ^{3}H. All of these conventions are common in existing literature. Mixed isotope molecules are referred to by a combination of the letters H, D, and T (e.g. HD).

Where mentioned, the spin isomers of hydrogen molecules will be labelled as ortho- (or ↑↑) or para- (or ↑↓) hydrogen with the conventions above used to denote the isotopic pairing if necessary.

Abstract

Work is underway in numerous countries around the world to design a viable nuclear fusion power station. It is hoped that this technology may one day provide a large amount of the world's baseline power requirements. There are still numerous problems to be overcome in this field. The processing and refinement of hydrogen isotopes from mixed isotope sources is one such issue. Palladium already plays a part in existing infrastructure for this purpose. Existing work about the exact nature of the isotopic differences in the palladium hydride (/deuteride / tritide) system contains much conflicting evidence.

This work is a study on the properties of the two lighter hydrogen isotopes (protium and deuterium) dissolved in palladium at high concentrations to form the well-established beta phase. Direct measurements of the tracer diffusion of these isotopes have been made for two sample geometries using quasielastic neutron scattering on Osiris at ISIS (Harwell, UK) and IN5 at The Institut Laue Langevin (Grenoble, France). Separate sorption measurements are also reported for each isotope to allow accurate determination of diffusion coefficients.

Diffusion coefficients are reported for octahedral - octahedral jump diffusion in the beta phase for both isotopes. These results are used to calculate a temperature for the 'crossover point' in the diffusion rate of these isotopes ($\sim 730\ K$).

This work also presents several unexpected results from these experiments:

- A second diffusive motion, that does not appear to match any previously described, is reported for all samples and instruments. While it has not been possible to fully characterise this motion, its properties are investigated and discussed.
- A high degree of ordering amongst the deuterium is inferred in the beta phase deuteride at temperatures between 433 and $500\ K$ with around 55% of the available palladium interstitials occupied. This phenomenon has not previously been reported above $150\ K$.
- Evidence for similar ordering and a possible transition in the ordered structure are reported for the beta phase hydride at similar temperatures and pressures.

1 Introduction

1.1 History

1.1.1 In the Beginning…

It is probably quite safe to say that when The Philosophical Transactions of the Royal Society first published Henry Cavendish's "Three Papers, Containing Experiments on Factitious Air" (1766) that neither the editors, nor the author himself fully understood the importance of the flammable gas that he had isolated. Today we know that hydrogen accounts for around 74% 'normal' (baryonic) matter in the universe (Suess & Urey, 1956) and, through fusion processes in the core of stars, is the initial building block from which all other elements are created. It is also now seen as one of the key components in energy production and storage.

In July 1802, William Hyde Wollaston made a note in his lab book about a new metal that he had separated from a mixture containing platinum ore. In August of that year that he gave this new metal the name palladium. Initially, the discovery was questioned by Richard Chenevix who claimed to believe the material to be an alloy of platinum and mercury. The following year Chenevix received the Copley Medal for his published work on palladium. It would be a further two years until Wollaston would publish the true history of its discovery (Wollaston, 1805)[6].

Almost exactly 100 years after Cavendish's paper on "inflammable air" Thomas Graham published a paper on his discovery that certain materials could absorb "many times their own volume" of the gas (Graham, 1866). One material particularly piqued his interest. This material could absorb over 900 times its own volume of hydrogen at 0°C and it could be expelled by heating, leaving the sample visibly unchanged. The material in question was Wollaston's palladium and three years after his initial paper on hydrogen sorption, Graham published the findings from his experiments with it (Graham, 1869).

In the late 19th and early 20th century understanding of the fundamental nature of matter was changing rapidly. In 1913 two people independently, but almost simultaneously,

[6] Further details of the history the discovery of palladium, and the circumstances around it, can be found in "The Wollaston/Chenevix controversy over the elemental nature of palladium: A curious episode in the history of chemistry" (Usselman, 1978) and "Rhodium and palladium – Events surrounding their discoveries" (Griffith, 2003)

published work on radioactive decay paths that led to materials that have the same chemical properties as known elements but a different atomic mass (Fajans, 1913), (Soddy, 1913). During a conversation with a family friend (Margret Todd), the name “isotope”[7] was suggested (Nagel, 1982) for these materials. Several years later, during his Nobel acceptance lecture, Soddy gave the following description of isotopes "[…] their atoms have identical outsides but different insides." (Soddy, 1922). During the same year JJ Thomson published his discovery that every sample of neon gas that he could obtain appeared to contain a mixture of radioactively stable atoms, some of mass 20 AMU and some of mass 22 AMU (Thomson, 1913).

Once the theory of isotopes had been established, numerous labs began to look into the phenomenon and discoveries of new nuclides (stable and radioactive) have been a regular feature of scientific literature ever since[8].

In 1932 Harold Urey published the discovery of an isotope of hydrogen with a mass of 2 AMU (Urey, Brickwedde, & Murphy). This prompted Adolf Sieverts to pick up the work of Thomas Graham and build on it by conducting sorption experiments with both known isotopes of hydrogen. In 1935 he and a colleague published a paper detailing their findings that there were observable differences in the interaction of palladium with protium (^{1}H or H) and deuterium (^{2}H or D) (A. Sieverts & Zapf, 1935). Around the time of Sieverts experiments news of a third isotope of hydrogen (tritium) was coming from Lord Rutherford’s group at the Cavendish Laboratory, Cambridge (Oliphant, Harteck, & Rutherford, 1934). This radioactive isotope of mass 3 AMU (tritium, ^{3}H or T) was later isolated and characterised by Alvarez and Cornog (1939).

A thorough review of the discovery and formation of the 38 known isotopes of palladium was conducted in 2011 by Kathawa, Fry, and Thoennessen (2013). As the palladium used in this work was of ‘natural’ isotopic composition (see section 2.1), these individual discoveries will not be discussed further here.

[7] From the Greek for “same place”

[8] A video timeline of these discoveries produced by staff at the National Superconducting Cyclotron Laboratory at Michigan State University can be found at: http://www.youtube.com/watch?v=ZvuMRwvJhHw

1.1.2 Significant Pd-H/D/T System Discoveries and Firsts

There have now been almost 150 years of active research into the palladium hydride system. To detail every finding in the literature would require an entire book. Numerous literature reviews have been published on the system including and extensive set by F.A. Lewis between 1960 and 1982[9] as well as his book: The Palladium Hydrogen System (1967) and comprehensive review articles by Wicke, Brodowsky, and Züchner (1978), Flanagan and Oates (1991) & Jewell and Davis (2006). This section aims to provide a brief overview of some of the more important discoveries and outline areas where research is currently active in the field. These, and other, discoveries will be discussed in more detail (where appropriate) in later sections of this text.

The dawn of nuclear reactors in the 1940s gave scientists an unprecedented opportunity to look inside materials and assess their internal structure. The first neutron diffractometer was built by W.H Zinn in 1947 at the Argonne National Laboratory (Willis & Carlile, 2013). Soon after, experiments were underway at Oak Ridge National Laboratory and in 1957 the first diffraction patterns of β-PdH and β-PdD were recorded (Worsham Jr, Wilkinson, & Shull, 1957). These showed that hydrogen and deuterium ions reside in the octahedral interstitial sites in the palladium lattice. Occupation of the palladium octahedral interstitial sites is now well established amongst the research community. There is still an ongoing debate about the possibility of occupation of the tetrahedral interstitial sites in the palladium lattice as well as how to define 'occupation' (McLennan, Gray, & Dobson, 2008; Pitt & Gray, 2003).

The detail of the of the superconducting phase is another topic that has been, and still is, hotly debated. There seems to be no argument with the initial discovery of a low temperature superconducting phase (Skoskiewicz, 1972) at a near 1:1 Pd to H ratio. Or that the critical temperature can be raised by a few degrees by doping the palladium with silver (Buckel & Stritzker, 1973). However, there have been various claims over the years of high temperature superconducting phases including a fairly recent public argument between two research groups (Baranowski & Dębowska, 2007; Tripodi, Di Gioacchino, Borelli, & Vinko, 2003; Tripodi, Di Gioacchino, & Vinko, 2004, 2009). Every claim about superconducting phases of Pd-H/D/T in existing literature involves situations outside of the ranges of interest

[9] A full list of these was compiled by for Platinum Metals Review in an article about his contributions to the journal by Ted B. Flanagan (2008)

in this work ($T \leq 17K$ or very high loading, i.e. $PdH(/D/T)_x$ where $x \geq 1$). The only subject in the topic that crosses into the territory of this work is the well documented "inverse isotope effect" (Hertel, 1974; Schirber, Mintz, & Wall, 1984; Yussouff, Rao, & Jena, 1995) whereby heavier hydrogen isotopes have a higher critical temperature at similar H/D/T loading. Similar "inverse isotope effects" can also been seen in the rate of diffusion of hydrgen isotopes through the palladium lattice.

The first direct measurements of the rate of tracer diffusion of hydrogen in Pd-H were made via quasielastic neutron scattering (QENS) using the R2 reactor at Studsvik, Sweden[10] by Sköld and Nelin (1966) who followed this up shortly afterward with measurements in the pure alpha phase (1967). The first similar measurements for β-Pd-H were taken on the HERALD research reactor at AWRE[11], Aldermaston, UK by Beg and Ross (1970). Since then, many QENS experiments have been conducted in both the alpha and beta phases at various temperatures (Anderson, Ross, & Carlile, 1978b; Carlile & Ross, 1974; Janßen et al., 1997; Nelin & Sköld, 1975).

In the 1980s attention moved toward acquiring other direct measurements of the Pd-H/D/T system including the isotope dependence of hydrogen gas solubility (Lasser & Klatt, 1983), isotope dependence of the system's phase boundaries (Lässer, 1985), and its thermodynamic properties (Oates, Lässer, Kuji, & Flanagan, 1986). These measurements, and others like them, gave insights into the limiting steps in ab / desorption cycles and the isotope dependence of these steps. Every new piece of information that is verified brings about the possibility of improved mathematical and, with the rapid increase in available computing power in recent years, computational models of the system. In recent years this led to computational predictions of the proton wave function in the octahedral site, built on ab initio calculations, that were later verified using inelastic neutron scattering (Kemali, Totolici, Ross, & Morrison, 2000; Ross et al., 2001). Through the use of density functional theory (DFT) a claim has also arisen that the classic model of hydrogen dissociation at the surface of palladium (requiring two empty octahedral sites at the surface) may need to be

[10] Details of the instrument can be found in Holmryd, Sköld, Pilcher, and Larsson (1964)
[11] Now AWE

re-thought (Lopez, Łodziana, Illas, & Salmeron, 2004), although this is still currently debated (Groß & Dianat, 2007).

Research into the Pd-H/D/T system (and related systems such as palladium alloys) is still highly active. With the rise in interest in the use of hydrogen as a fuel there is an ever increasing need for hydrogen purification systems on both small and industrial scales[12]. Palladium is also seen as a simple, well researched, system that can be used to investigate the fundamental properties of hydrogen (isotope) –metal interactions. And, as the world moves towards a viable nuclear fusion power station there has also been a surge in interest in systems that have the potential to be used in (or aid understanding of) hydrogen isotope separation. With almost 80 years of research into isotope effects in the Pd-H/D/T system it is a prime candidate.

[12] One of the most common systems involves filtration through PdAg membranes. Further information on methods of hydrogen production can be found in (Riis, Hagen, Vie, & Ulleberg, 2006)

1.2 Motivation

According to official UK government statistics (DECC, 2013) demand for electricity in the UK has been steadily increasing over the last 40 years. Figures from the International Energy Agency (IEA, 2012) show an even stronger rate of rise in demand globally.

In December 1997, due to the growing evidence that human activity may lead to a long term shift in the global climate, a paper was drafted in Kyoto that called on all UN member nations to commit to reducing overall greenhouse gas emissions. The terms were agreed by nearly all member states the protocol adopted the following year (United Nations, 1998). Since then many member states, including the UK, (HMSO, 2008) have introduced further national regulation of greenhouse gas emissions.

For many years both bulk (in power stations) and localised power production (petrol, diesel, and coal fired steam engines) have relied on the combustion of fossil fuels. As such, energy production has long been one of the primary man-made sources of greenhouse gas emissions. It follows then, that if you are attempting to reduce emissions, particularly in a climate of increasing power usage, that a shift to other primary sources of energy is required.

The mass production of energy without the associated production of greenhouse gases is now a global problem. Almost all developed nations are currently engaged in some sort of project to create 'clean' energy. An enormous amount of progress has been made in recent years in 'renewables' such as wind, solar, tidal and geothermal. Each of these methods suffers from inherent drawbacks which make them unsuitable as a global solution to providing baseline power: each is only suitable in a limited set of geographic locations and, a lack of control over the initial source of the energy creates periods of overproduction (or waste) and periods where demand cannot be met. The obvious solution to this is to store the energy in a way that allows it to be used when it is needed. However, a simple and financially viable solution has, so far, proved elusive[13].

Nuclear fission was once seen as the solution to the emissions problem. It is estimated that, since their adoption into national energy networks, energy generated by traditional nuclear power plants has prevented 64 gigatonnes of CO_2 equivalent greenhouse gas emissions that

[13] A detailed discussion of current research into energy storage falls outside the scope of this document.

would have resulted from the combustion of fossil fuels in thermal power stations (Kharecha & Hansen, 2013). However, following a series of major accidents (such as Chernobyl[14], Three Mile Island[15] and, most recently, Fukushima Daiichi[16]) as well as numerous smaller accidents and leaks[17], and concerns about safety / ongoing costs, it has suffered a decline in popularity with the public and politicians around the world.

[14] http://en.wikipedia.org/wiki/Chernobyl_disaster
[15] http://en.wikipedia.org/wiki/Three_Mile_Island_accident
[16] http://en.wikipedia.org/wiki/Fukushima_Daiichi_nuclear_disaster
[17] http://en.wikipedia.org/wiki/List_of_nuclear_power_accidents_by_country and http://en.wikipedia.org/wiki/Nuclear_reactor_accidents_in_the_United_States

1.2.1 Nuclear Fusion

Nuclear fusion is seen as one of the most promising long term solutions to creating a large energy base load with no greenhouse gas emission associated with the energy conversion process (Smith, 2005). The two most successful technologies in the race for controlled nuclear fusion to date are inertial confinement; where a pellet of fuel is made to undergo fusion by bombardment with lasers (or secondary radiation that is initiated by laser) and, tokomaks; where a plasma is magnetically confined in a toroidal reactor and heated to a temperature (and pressure) where fusion will occur. There are also several other possible technologies (magnetic pinch, stellarator, and combined laser / magnetic approaches) that

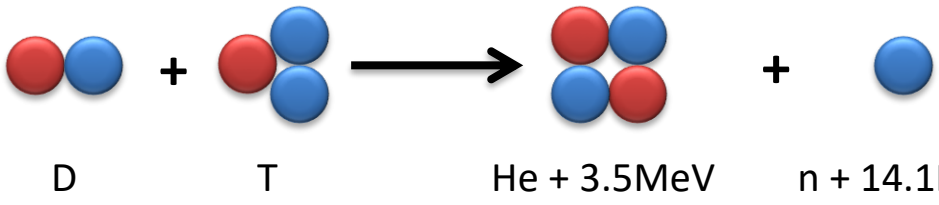

1-A The D-T Fusion Reaction

are, at the time of writing, under development. However, these are much further from viability as a commercial energy source. These technologies face a diverse array of challenges and the necessary equipment in each case can be extremely different but, they all share the same basic operating principle: fusion of deuterium and tritium to produce helium, a neutron and energy (figure 1-A).

Deuterium is naturally abundant and accounts for 0.0156% of all the hydrogen atoms in the Earth's oceans (around 10^{15} tons). It has been calculated that around 1000 tons of deuterium per year would be enough to cover global energy use at the current rate of consumption (McCracken & Stott, 2013). Deuterium can be recovered from water using electrolysis although it needs to be separated from any protium that is also produced before it can be used as fuel.

Tritium is radioactive and has a half-life of just over 12 years. Trace amounts of it can be found naturally. This is created in the upper atmosphere in reactions involving cosmic ray bombardment (i.e. ${}^{14}N + n \rightarrow {}^{12}C + {}^{3}H$). If it then bonds with oxygen in the atmosphere, it can precipitate to the planet's surface as water. The average tritium content of rainwater is around 1 in 10^{18} of the hydrogen atoms. Ocean surface waters contain around a fifth of

this amount (von Buttlar & Libby, 1955). Obviously, this is not a suitable source for even the most modest uses. So, for a power station to function, it needs a source of tritium.

The most convenient method of tritium production for a fusion reactor involves a 'blanket' of liquid lithium surrounding as much of the reactor vessel as possible. Natural lithium consists of two stable isotopes; one of mass 6 AMU (6.4%) and one of mass 7 AMU (92.6%). Bombardment of the lithium with the neutrons produced in the D-T (deuterium – tritium) reaction will lead to the following two reactions:

$$^{6}Li + n \rightarrow {}^{4}He + T + 4.8\ MeV \qquad \text{(1-i)}$$

$$^{7}Li + n \rightarrow {}^{4}He + T + n - 2.5\ MeV \qquad \text{(1-ii)}$$

Through careful balancing of the isotopic composition of the lithium 'blanket' around the reactor, the ^{7}Li reaction provides an ongoing 'chain' of neutrons to produce the tritium that fusion reaction needs, while the ^{6}Li reaction should help to reduce the need for external heating without creating too many dead ends in that chain.

It can be seen above that, even if the vast majority of neutrons produced by D-T reactions (or the subsequent neutron released from a ^{7}Li reaction) are captured by lithium nuclei in the blanket that 'break-even' of tritium annihilated in fusion reactions to that produced will be very hard to achieve. This means that for a fusion reactor to be viable as an energy source, all tritium that is produced needs to be recovered from the breeder blanket and any tritium that hasn't undergone fusion needs to be recovered from the exhaust of a reactor.

Accurately accounting for tritium stock is also a major safety concern for any potential facility. Tritiated water is readily absorbed by living organisms and gaseous tritium can be ab/adsorbed by numerous materials. As such, losses to the environment and leaks (or material contamination) within a facility must be accurately understood so that appropriate action can be taken.

1.2.2 Isotope Separation

Several techniques are commonly employed in the separation of hydrogen isotopes. A brief overview of the more common ones is provided below.

1.2.2.1 Cryogenic Distillation

There is a difference of around 5K in the boiling points of the isotopically pure hydrogen isotopes (H_2 = 20.3K, D_2 = 23.3K, T_2 ≈ 25K[18]). Isotopic mixtures (HD, HT & DT) have boiling points close to the mean of the species involved ("Deuterium," 2014). This can also be seen in deuterated and tritiated water (Jones, 1968) although the effect is much smaller.

Cryogenic cooling is an energy intensive process. It also requires stocks of refrigerants whose production can also be energy intensive. For fusion to be viable as an energy source, the amount of energy necessary to operate the facility must be minimised. Therefore, this, on its own, is not an ideal solution.

1.2.2.2 Chromatography

Isotopic mixtures can be purified using a chromatography column. This involves allowing a small amount of the gas to be absorbed at one end of a long column containing a sorbent material. The dissolved H/D/T allowed to diffuse through the material. Isotopes with a faster rate of diffusion will arrive at the other end of the column faster than those with a slower rate. Each cycle can result in a small amount of isotopically pure gas, thereby reducing the composition in the remaining mixed gas. This has the added benefit of producing isotopically pure diatomic gas at the time extremes of each pass through the column.

1.2.2.3 Other Techniques

Partial isotopic separation can be achieved by absorbing mixed isotope gas into a solid. One isotope may be preferentially absorbed over another due to the difference in their chemical potentials. At equilibrium, the balance of the chemical potentials in the gasses and the solid set up a separation factor (a difference in the composition of the gas to the solid). The remaining gas can then be rapidly evacuated leaving behind the mixture present in the solid.

1.2.2.4 Current Industrial Systems

Heavy water fission reactors (such as the CANDU[19] design) produce tritium through neutron capture by deuterium. The partially tritiated water from these reactors is passed through a catalyst in the presence of pure deuterium. The resulting DT / D_2 is then cryogenically distilled (in a multiple stage process) removing over 99% of the tritium. This process was

[18] (Jones, 1968)
[19] https://en.wikipedia.org/wiki/CANDU_reactor

originally conceived for detritiating water. As such, it was not optimised for producing isotopically pure tritium.

When the initial D-T experimental runs were conducted at the Joint European Torus (JET) at Culham in Oxfordshire, an isotope separation / tritium recovery plant was constructed on the site. This uses a complex combination of the methods mentioned above and requires the mixed isotope gas to pass through multiple purification stages. A comprehensive overview of this process falls outside the scope of this work but details can be found in existing literature (Lässer, Bell, & Bainbridge, 1999; Lässer, Bell, Bainbridge, et al., 1999).

1.2.3 Why Now?

In 1991 the "world's first controlled release of deuterium-tritium fusion power" (UKAEA, 2012) was achieved at the Joint European Torus (JET) in Oxford, UK. In 1997, Construction of the International Thermonuclear Experimental Reactor (ITER) is well underway in Cadarache, France[20] and plans for a full scale demonstration power plant based around the tokamak design (DEMO) are currently being drawn up (Maisonnier et al., 2006). ITER has been designed to answer many of the chemistry, physics, materials, and engineering questions that still stand in the way of a viable fusion power source. It will be required to operate with D-T fuel and have several experimental tritium breeder blanket 'windows' around the vessel. A permanently operational tritium recovery and isotope separation facility is being built on the site (M. Glugla et al., 2007; M. Glugla, Dörr, Lässer, Murdoch, & Yoshida, 2002; M. Glugla et al., 2006). This facility will provide an experimental site for the bulk separation of hydrogen isotopes on an unprecedented scale. It has already been reported that palladium is expected to have a part to play in this, and any future "industrial", facility (Manfred Glugla, Cristescu, Cristescu, & Demange, 2006).

Many of the macroscopic properties of the Pd-H/D/T system are well documented. This has facilitated its use in industrial hydrogen purification as well as the experimental facilities described above. However, the same cannot be said of the fundamental properties that underlie them. There is still even active debate in published articles about the sites that H/D/T ions occupy when dissolved in a palladium lattice (McLennan et al., 2008; Pitt & Gray, 2003).

[20] http://www.iter.org/

Isotope separation via metal – hydrogen interactions has the potential to be simpler to achieve in engineering terms and less energy intensive than cryogenic distillation. A better understanding of the underlying processes that cause the isotope dependent properties could greatly advance the field.

1.3 Aims and Objectives of this Work

The broad aim of this work is to improve knowledge of the palladium – hydrogen / deuterium system with particular attention paid to where this may be useful in hydrogen isotope separation.

The following specific objectives were determined during the early stages of this project:

- Determine the rate of diffusion of hydrogen and deuterium (independently) in beta phase palladium hydride (and deuteride) as a function of temperature.
- Determine the temperature at which these rates are equal (the “crossover point”).
- Determine whether existing models in the literature accurately describe the diffusive motion seen for both isotopes in the beta phase.

2 The Palladium Hydride System

2.1 Palladium

$_{46}Pd$
106.42

Palladium (Pd) is a platinum group transition metal with a face centred cubic (FCC, space group 225, $Fm\bar{3}m$) structure (figure 2-B). At STP (Standard Temperature and Pressure), it has a lattice constant of 3.889Å and a density of $12.023 gcm^{-3}$. Pure palladium is reported to have a melting point of around $1828\ K$ (RSC.Org, 2018).

Isotope	Mass (AMU)	Abundance (%)
^{102}Pd	101.906	1.02
^{104}Pd	103.904	11.14
^{105}Pd	104.905	22.33
^{106}Pd	105.903	27.33
^{108}Pd	107.904	26.46
^{110}Pd	109.905	11.72

2-A Palladium isotope abundance (NIST, 2014)

Natural samples of palladium contain six stable isotopes and trace amounts of one radio isotope ($^{107}_{46}Pd$) that has a half-life of 6.5×10^6 years. Given the relative abundances of these isotopes (figure 2-A), the atomic mass of natural palladium is commonly taken to be $106.42 AMU$.

Due to the FCC structure of the crystal, palladium has two potentially available interstitial sites that repeat throughout the lattice: octahedral (figure 2-C) and tetrahedral (figure 2-D). Every octahedral site has eight neighbouring tetrahedral sites, one per face (and, conversely, every tetrahedral site has 4 octahedral neighbours). These two sites tessellate to fill the three-dimensional structure with palladium atoms at the location of their vertices.

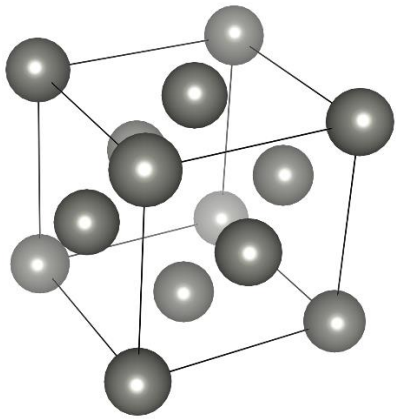

2-B Palladium FCC structure

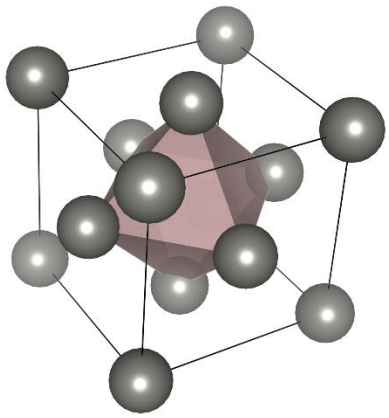

2-C FCC octahedral site

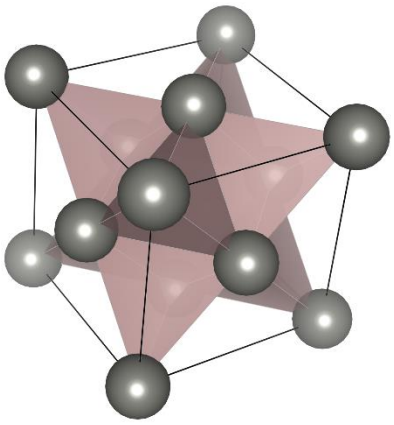

2-D FCC tetrahedral sites

2.2 Palladium Hydride

Hydrogen forms a binary interstitial (intermetallic) hydride with palladium. Unlike many of the other known metallic hydrides, very little macroscopic deformation of the palladium lattice occurs from the process[21] of repeated loading / unloading, and the mechanical properties of the hydride are very similar to the pure metal. Repeated cycling below the critical temperature creates microscopic lattice defects due to the uneven growth of the alpha and beta phases. This gives rise to trapping sites where hydrogen has been shown to preferentially diffuse along the dislocation core (Heuser et al., 2014; Schiavone & Trinkle, 2016; Trinkle, Ju, Heuser, & Udovic, 2011). However, these defects can commonly be 'repaired' via a simple annealing process. For these reasons, palladium (and alloys thereof, commonly PdAg) are of particular interest for industrial processes where repeatability of processes and longevity of materials are vital considerations.

Evidence from previous neutron scattering experiments shows that hydrogen resides in the octahedral sites in the palladium lattice[22]. At $1:1$ loading[23], this gives rise to an interlaced FCC hydrogen 'lattice' translated from the corresponding palladium lattice by $(\frac{1}{2},\frac{1}{2},\frac{1}{2})$. This is a classic 'NaCl' type arrangement with alternating palladium and hydrogen atoms (figure 2-E: Pd atoms grey, H atoms red). At high concentrations the structure bears a superficial resemblance to an alternating simple cubic structure. However, the underlying system is still FCC, but with a two atom basis (albeit, with vacancies at below 1:1 loading).

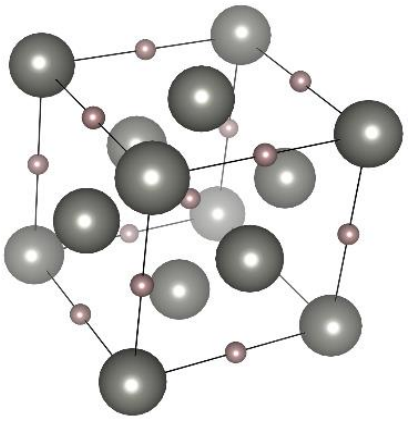

2-E Pd-H (1:1 concentration)

Considering the 150 years of study into palladium hydride, it is surprising to note that there is still much debate about its phases and their boundaries. There are some indisputable features. At high concentrations (near $1:1$) and below $9\ K$, there exists a phase that exhibits

[21] Many metallic hydrides become brittle as hydrogen concentration is increased. The distortion to the lattice caused by the introduction of interstitial hydrogen can even cause a host lattice to collapse into a powder.
[22] There have been several suggestions of tetrahedral occupancy including McLennan et al. (2008); Pitt and Gray (2003), although this remains controversial.
[23] Concentrations above $H/Pd = 1$ have been reported in some work that describes electrochemically loaded samples. None of these appear have been reproducible.

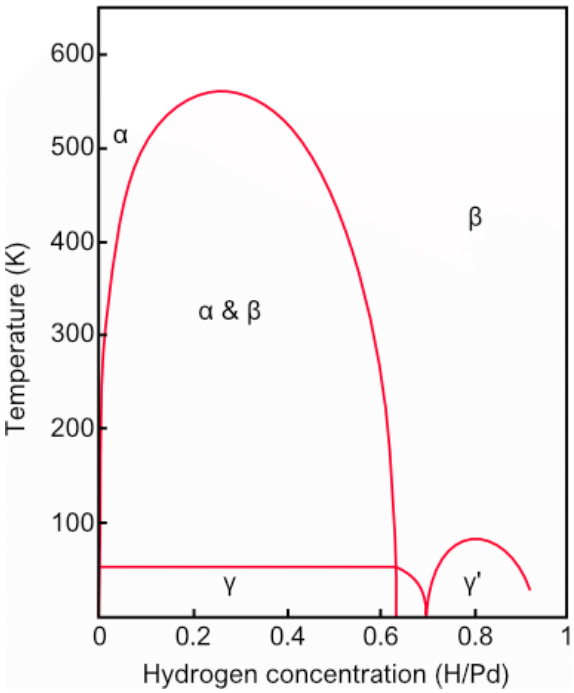

2-F Palladium hydride phase diagram
Reproduced from original in Fukai (1993)

superconductivity[24]. At around $50\ K$ across a wide range of concentrations, there are numerous reports of an anomaly in the thermodynamic properties of the material that appear to suggest an order / disorder transition. Above this temperature there are two distinct phases with associated distortions to the host palladium lattice. At low concentrations is an alpha phase with a nominal lattice parameter of $3.895\ \text{Å}$ (dependent on actual concentration and temperature). At high concentrations (above around $H/Pd = 0.5$ to 0.6) exists a pure beta phase with a nominal lattice parameter of $4.025\ \text{Å}$ (again, this is dependent on exact composition and temperature). Below the critical temperature of around $570\ K$ ($\sim 297\ °C$)[25] is a miscibility gap, where both alpha and beta phases exist simultaneously, across a wide concentration range. Above this temperature, only one of these two phases is present. Which one is dependent on concentration, but exactly where the border between them sits is poorly reported (and possibly poorly defined). An example of the generally reported phase diagram is shown in figure 2-F.

The transitions between the superconducting and sub $50\ K$ (denoted here as γ) phases, and the gamma / mixed alpha + beta phase have no reported associated lattice distortion. Traditionally, the $50\ K$ transition has been described as the transition between full ordering of the hydrogen in the palladium lattice and the subsequent gradual breakdown of this order as temperature increases. This picture was challenged by Blaschko (1984) who showed structure amongst the hydrogen atoms in the lattice at temperatures up to $150\ K$ across a range of compositions. In this temperature region, there also appears to be a change in the

[24] The superconducting phase is not discussed further here as it does not feature in any of the measurements described in later chapters.
[25] Examples of reported critical temperatures include: $568K$ (Jewell & Davis, 2006), and $571\ K$ (Johansson et al., 2010)

relationship between lattice parameter and temperature at high hydrogen concentration[26] (Abbenseth & Wipf, 1980).

The exact temperature of the "$50\ K$" transition, and how this changes for compositions beyond the mixed / beta phase boundary, has been questioned by Araki et al. (2004). Further to this, their work suggests that the superconducting phase may have a more complex temperature and concentration dependence than has previously been reported. Figure 2-G shows their proposed phase boundaries (with the superconducting region in the lower right hand corner).

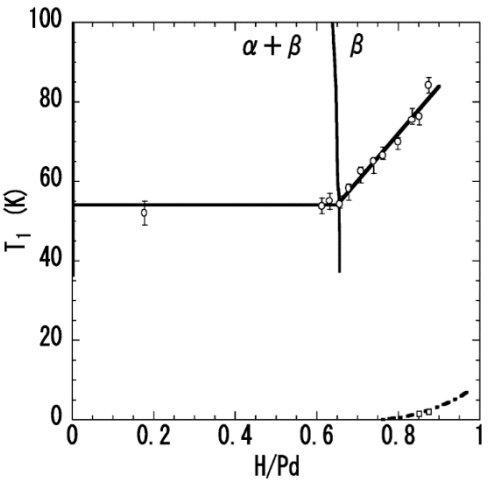

2-G High concentration 50K phase transition (Araki et al., 2004)

Molecular hydrogen (and isotopes thereof) readily dissociates at the surface of palladium. For this to occur, there must be a number of neighbouring available octahedral sites (unoccupied by hydrogen) at the surface of the material. Whether this requires two or three neighbouring sites is still debated. Scanning tunnelling electron microscopy work by Mitsui, Rose, Fomin, Ogletree, and Salmeron (2003) shows compelling experimental evidence for the need for three neighbouring available surface sites. This picture is questioned in ab initio molecular dynamics – density functional theory (AIMD-DFT) calculations by Groß and Dianat (2007), who suggest that the traditional Langmuirian picture (requiring only two available sites) is energetically valid. However, a similar DFT method employed by Lopez et al. (2004), appears to agree with the three site model.

There is general agreement between the two models that the mechanism is a hybridisation of d-orbitals amongst the palladium atoms in neighbouring available sites creating a 'potential well' that is deep enough to polarise a nearby H_2 (D_2, T_2, HD, etc.) molecule. This, in turn causes the bond between the two hydrogen atoms to stretch until the attractive force at the surface overcomes that of the, previously adjoined, hydrogen atom. It should be noted that the strength of the bond in the diatomic hydrogen molecule is dependent both

[26] A plot from the Abbenseth & Wipf paper that shows this can be found in Appendix E.

on its isotopic composition and whether the pair are in the *ortho* or *para* isomer state although this is does not directly affect the work described here.

The fact that this potential is disturbed by occupation by hydrogen for *individual* sites appears to suggest that, once absorbed, the electron associated with the hydrogen ion remains fairly localised when diffusive jumps occur.

Once separated from the diatomic molecule, the hydrogen atom occupies one of the available octahedral sites at the surface of the metal. It can then diffuse through the lattice by 'jumping' to any available neighbouring octahedral site (see section 2.3.1)

As discussed in section 2.2, diffusion in palladium hydride occurs via a series of jumps between octahedral interstitial sites in the palladium lattice. Measurements of these jumps (such as those from QENS) give direct information about single particle motions in the system. For an isotropic FCC lattice gas, the chemical diffusion coefficient D at any given temperature is related to the jump frequency (the inverse of the mean residence time τ) and the mean jump length l by:

$$D = \frac{l^2}{6\tau} \tag{2-1}$$

While hydrogen has a measurable residence time in only the octahedral sites in the palladium lattice, the tetrahedral sites provide the pathway for diffusion. Figure 2-H shows the energy potential of several straight paths from the central octahedral site to the edge of the unit cell. The $< 001 >$ path leads directly to the neighbouring palladium atom and, as such, shows an extremely steep rise at a very low radial distance. The $< 110 >$ path is a straight line to the nearest neighbouring octahedral site. This passes directly between two nearest neighbour palladium atoms and so has a steep rise in the potential in this region. The $< 111 >$ path is a direct path between octahedral (at the origin) and tetrahedral sites (labelled as T). This represents the lowest energy barrier in the system. In the diagram, it can be seen that this barrier (O-T) is roughly 200 to $250\ meV$ and that the T-O barrier is considerably lower (and is generally thought to be even lower than suggested here). Continuing to travel in this direction leads to a palladium atom, hence the steep rise in the potential (similar to that seen in the $< 001 >$ path). However, the tetrahedral site has four possible 'exits' to neighbouring octahedral sites.

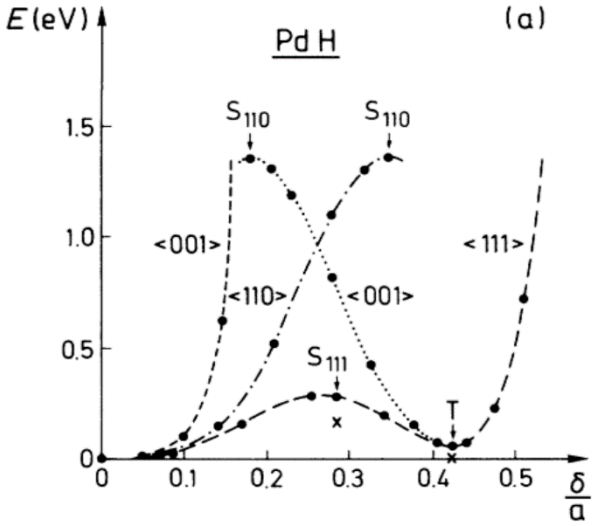

2-H Pd-H potentials from octahedral site (Krimmel, Schimmele, Elsasser, & Fahnle, 1994)

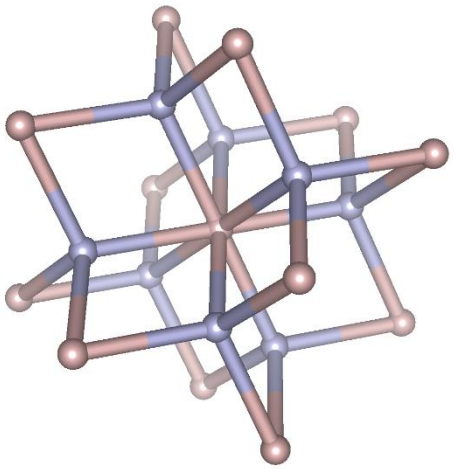

2-I Pd-H jump network

This leads to a 'network' of octahedral sites, linked via the tetrahedral sites. A map of of this jump site network is shown for a unit cell in figure 2-I (palladium atoms not shown for clarity). In this figure, octahedral sites are marked in red, and tetrahedral sites in blue. Quasielastic neutron scattering studies appear to support the 'approximately zero residence time in the tetrahedral site' model as no direct O-T or T-O jump diffusion has been shown. There are, however, numerous reports of O-O jumps with an activation energy in the region expected for O-T transitions.

Occupation of an octahedral site causes local deformation of the palladium lattice (figure 2-K) giving rise to the lattice expansion seen in the alpha and beta-phases. In the alpha-phase this results in a small average expansion of the bulk lattice. Above a certain concentration (dependent on temperature) it becomes energetically favourable for a sudden jump in the palladium lattice parameter to occur. This has been shown in numerous neutron diffraction studies where, in the miscibility gap, two lattice parameters relating to distinct alpha and beta phases are seen with relative intensities determined the proximity of the concentration to the pure phase boundaries. The shift in the lattice parameter with transition into the beta phase is considerably larger than would be expected from the lattice distortion effect seen in the alpha phase (figure 2-L).

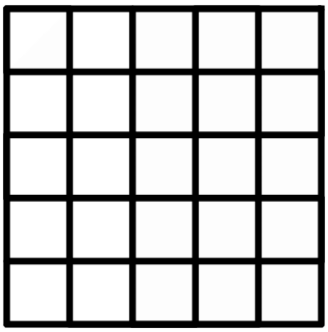

2-J Schematic of Pd lattice

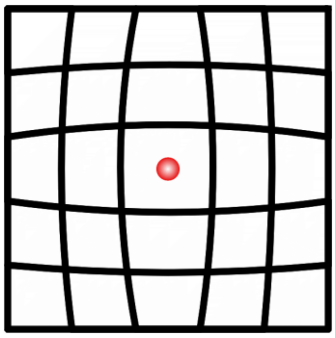

2-K Schematic of lattice deformed by interstitial hydrogen

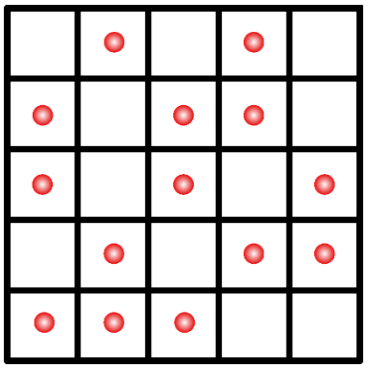

2-L Schematic of lattice expansion at H/Pd = 0.56

Further lattice expansion with increasing temperature and hydrogen concentration has been shown to occur at a different rate in the beta phase to the alpha phase (Abbenseth & Wipf, 1980).

2.2.1 Order / Disorder

The previous section discussed the reported order / disorder transition at low temperature. In palladium hydride, the palladium atoms are essentially in fixed positions whereas the hydrogen is free to jump between the octahedral sites. However, it has been shown that the interaction between the hydrogen atoms can cause certain octahedral sites to become favourably occupied over others. In the Pd-H system, this is thought to be caused by repulsion between the highly charged and poorly shielded hydrogen nuclei. This gives rise to 'short range ordering' (SRO) that creates larger superstructures in the lattice.

This phenomenon is physically similar to the ordering seen in binary alloys (though with a higher mobility). Clapp and Moss (1968) describe three superstructures that can arise from particle pair interactions in FCC solids. These are shown in figure 2-M.

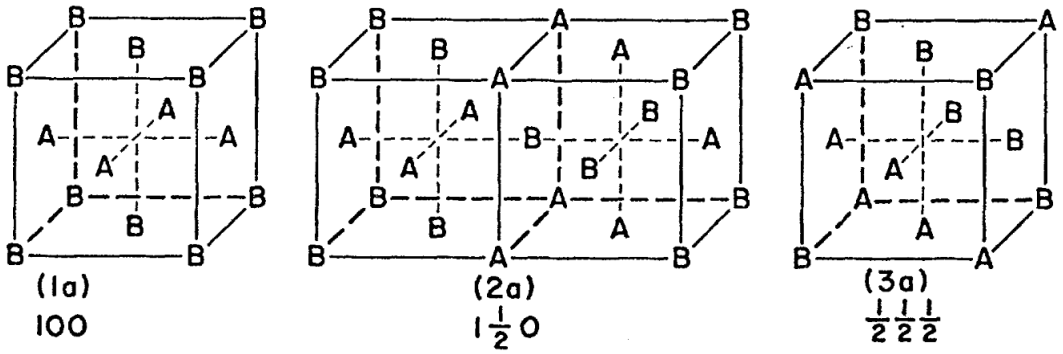

2-M Possible FCC binary alloy superstructures (Clapp & Moss, 1968)

In palladium hydride, the binary system is not given by two species of atoms but, rather, hydrogen atoms and vacancies in the octahedral sites in the host palladium lattice. These possible structures are shown in figure 2-N. Preferentially occupied octahedral sites can be seen in each case where the yellow planes bisect the red markers (and those nearest the marked plane in the $\left(1, \frac{1}{2}, 0\right)$ case).

Which of these structures will be formed, is dependent on the interaction potential between the hydrogen atoms in the lattice[27].

The host palladium lattice appears to be largely unaffected by the specific type of ordering exhibited by the hydrogen[28] (only the overall concentration). This is demonstrated by the lack of any associated change in lattice parameter at the previously described $50\ K$ transition.

It should be noted that ordered phases have been shown to occur when around half the available octahedral sites are occupied. However, the exact concentration region where they occur is poorly defined in existing literature.

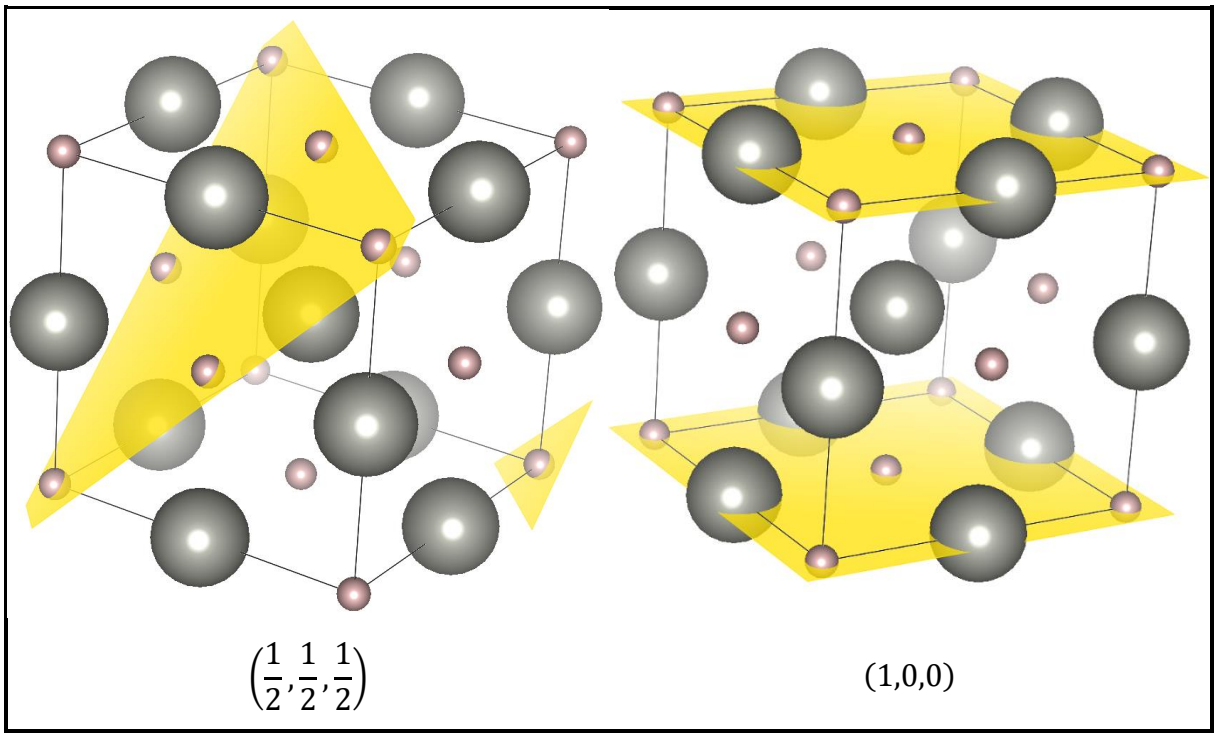

[27] Further discussion on this subject can be found in section 4.5.2

[28] Although there is a possibility that the rate lattice expansion with temperature may be affected.

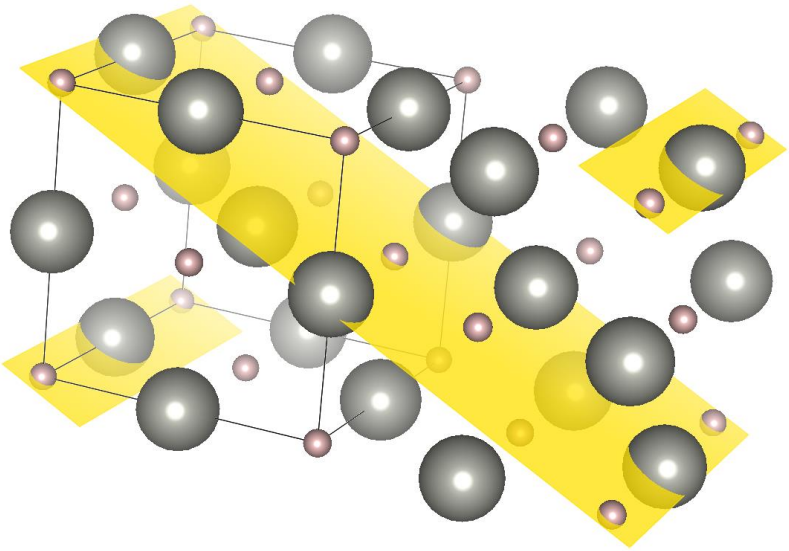

$\left(1, \frac{1}{2}, 0\right)$

2-N Possible Pd-H ordered structures

2.2.2 Isotope Dependence

Due to the relative difference in their masses, protium, deuterium, and tritium display the largest difference in chemical properties of any set of isotopes. This leads to some fairly substantial differences in the properties of palladium hydride, deuteride and tritide. These differences are widely documented[29]. Information that is specifically relevant to this work is summarised here.

The mass difference in the three isotopes of hydrogen gives rise to vastly different vibrational energies in their diatomic gas molecules. Similar trends are seen for the zero point and vibrational energies of the isotopes in the octahedral sites in palladium. These energies are summarised in Lasser and Klatt (1983). This summary is presented in figure 2-O where, for the two lattice gas phases, zero point energy is shown on the left, and vibrational energy on the right.

[29] (Lasser, 1984; Lässer, 1985; Lässer & Powell, 1987), (T B Flanagan & Oates, 1991), (Joubert & Thiébaut, 2009), etc.

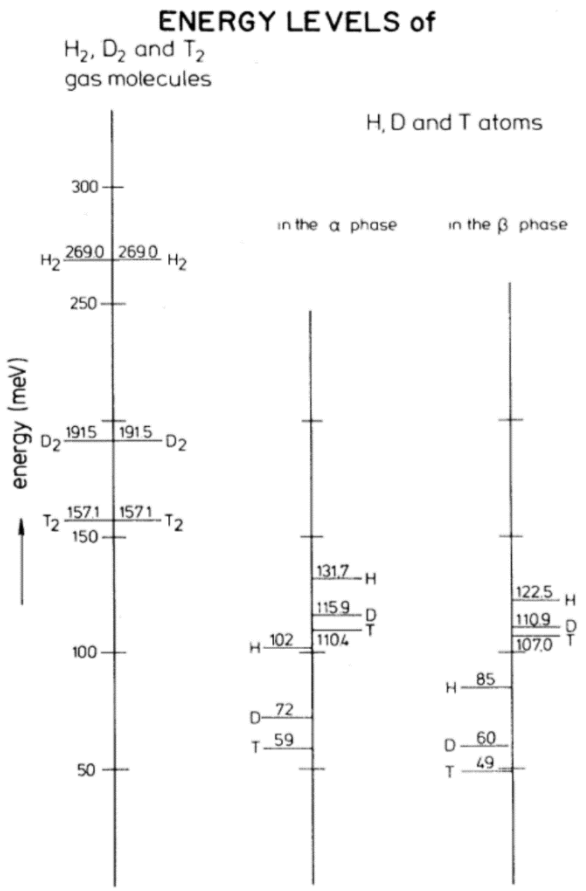

2-O Zero point and vibrational energies of hydrogen isotopes (Lasser & Klatt, 1983)

All three isotopes display the general Pd-H(/D/T) phase structure described in figure 2-F but the phase boundaries are shifted to different temperatures. The gas pressures required to achieve similar compositions (via gas sorption) at any given temperature, varies dramatically. In this work, achieving similar compositions in the beta phase at around $200\ °C$ requires pressures around an order of magnitude higher (in Bar) for deuterium than for hydrogen[30].

The lattice distortions associated with protium, deuterium and tritium in octahedral interstitial sites in palladium have a similar inverse mass relationship. The nominal lattice parameters of Pd-H and Pd-D are summarised in table 2-a. Comparing the alpha phase lattice parameters to the nominal lattice parameter of $3.889\ \text{Å}$ for pure palladium, gives some indication as to the scale of this phenomenon around a single occupied site.

[30] Measurements showing this are reported in chapter 4. Supporting data can be found in Appendices C and D.

	α (Å)	β (Å)
Pd-H	3.894	4.025
Pd-D	3.89	4.021

2-a Lattice parameters of Pd-H(/D)

Work by Abbenseth and Wipf (1980) shows that, counterintuitively, lattice expansion with increasing temperature (relative to an arbitrary starting point at $80\ K$) in the beta phase, rises faster for the deuteride than the hydride when a similar number lattice sites are occupied by the relevant isotope. Extrapolation from their data suggests that the lattice parameter of Pd-$H_{0.7}$ and Pd-$D_{0.7}$ may converge at around $735\ K$, with the lattice parameter of the deuteride eventually overtaking that of the hydride[31]. The picture of this subject in existing literature is patchy and there appears to be no comparable data available for the tritide.

The three isotopes show vastly different temperature dependence in their rates of diffusion. At low temperatures they display a well-documented 'inverse isotope effect' (where heavier isotopes diffuse faster than their lighter counterparts). At higher temperatures, this pattern is reversed. There are numerous reports in existing literature of this behaviour for the hydride and deuteride. There are far fewer for the tritide. These reports use a wide variety of techniques and cover a wide range of temperature, and compositions. However, many of them are not easily (or at all) comparable. Further to this, the temperatures given for the point at which the diffusion rates of beta Pd-H and beta Pd-D coincide, run from around $500\ K$ to over $1600\ K$.

2.3 Diffusion

Two definitions for the term "diffusion" are used in this work. The is first Fick (or 'chemical') diffusion. This describes the mass motions of particles starting from a situation where a concentration gradient exists, eventually leading to their uniform distribution throughout a volume at equilibrium.

[31] This value is only provided as a rough guide to the temperature region where this phenomenon may be seen. A brief overview of the method employed in its calculation can be found in Appendix E.

The second is commonly referred to as 'tracer' (or 'self') diffusion. This describes the specific motion of an individual particle and is the underlying motion that gives rise to chemical diffusion. While chemical diffusion tends to zero as equilibrium particle distribution is reached, tracer diffusion is continuous (for any system where motion is possible).

It should always be explicit throughout this work, which of these processes is being described.

As discussed in section 2.2, diffusion in palladium hydride occurs via a series of jumps between octahedral interstitial sites in the palladium lattice. Measurements of these jumps (such as those from QENS) give direct information about single particle motions in the system. For an isotropic FCC lattice gas, the chemical diffusion coefficient D at any given temperature is related to the jump frequency (the inverse of the mean residence time τ) and the mean jump length l by:

$$D = \frac{l^2}{6\tau} \tag{2-1}$$

2.3.1 Jump Diffusion

Jump diffusion can be described as particles moving between neighbouring sites that are bounded by some sort of barrier that can be overcome. If the barrier is too low, the particle never 'resides' in any site and moves freely around the volume. If the barrier is too high, the particle is trapped, and no further jumps occur. "Jump diffusion" spans the gap between these extremes where an individual particle resides in each site for longer than it takes to complete a jump.

2.3.2 Arrhenius Behaviour

The Arrhenius equation describes the relationship between the rate constant of a chemical reaction k, the energy needed to activate the underlying process E_a, and the absolute temperature of the system T (mediated by Boltzmann's constant k_B), and an experimentally determined pre-exponential factor A:

$$k = Ae^{-\frac{E_a}{k_B T}} \tag{2-2}$$

Taking logs of each element in the equation gives:

$$\ln(k) = \ln(A) - \frac{E_a}{k_B}\left(\frac{1}{T}\right) \tag{2-3}$$

Therefore, plotting $\ln(k)$ as a function of $1/T$, should give a straight line where the gradient of the line yields the activation energy and Y intercept yields the pre-exponential factor.

In the measurements described in this work, this is applied to jump diffusion measurements from QENS. In this case, it is reasonable to assume that any calculated activation energy is a measure of the barrier that must be overcome to make a single diffusive jump.

2.4 Sample Materials

In the brief for this work, the sponsor requested that all sample materials be commercially available. As palladium is used widely in both research and industry, many different forms, purities, and geometries can be purchased.

2.4.1 Spherical Palladium Powder

Most of the measurements reported in this work have been conducted on a 'spherical' palladium powder purchased from Alfa Aesar (Thermo Fischer Scientific, 2018b). This is sold as having a purity of 99.95% with the balance made up by trace amounts of transition group metals and oxygen.

This powder has a different geometry to most of those commonly available. The majority of commercially available palladium powders have particles with an almost fractal surface shape. These powders have an extremely large surface area per gram. The powder used in this work has roughly spherical particles. These vary in size from around $0.1\ \mu m$ to $1\ \mu m$. Figure 2-P shows SEM images of this powder and a standard palladium powder. Aside from the three particles visible toward the centre of the bottom left image, this powder can be seen to have roughly spherical particle shape and a narrow range of particle size.

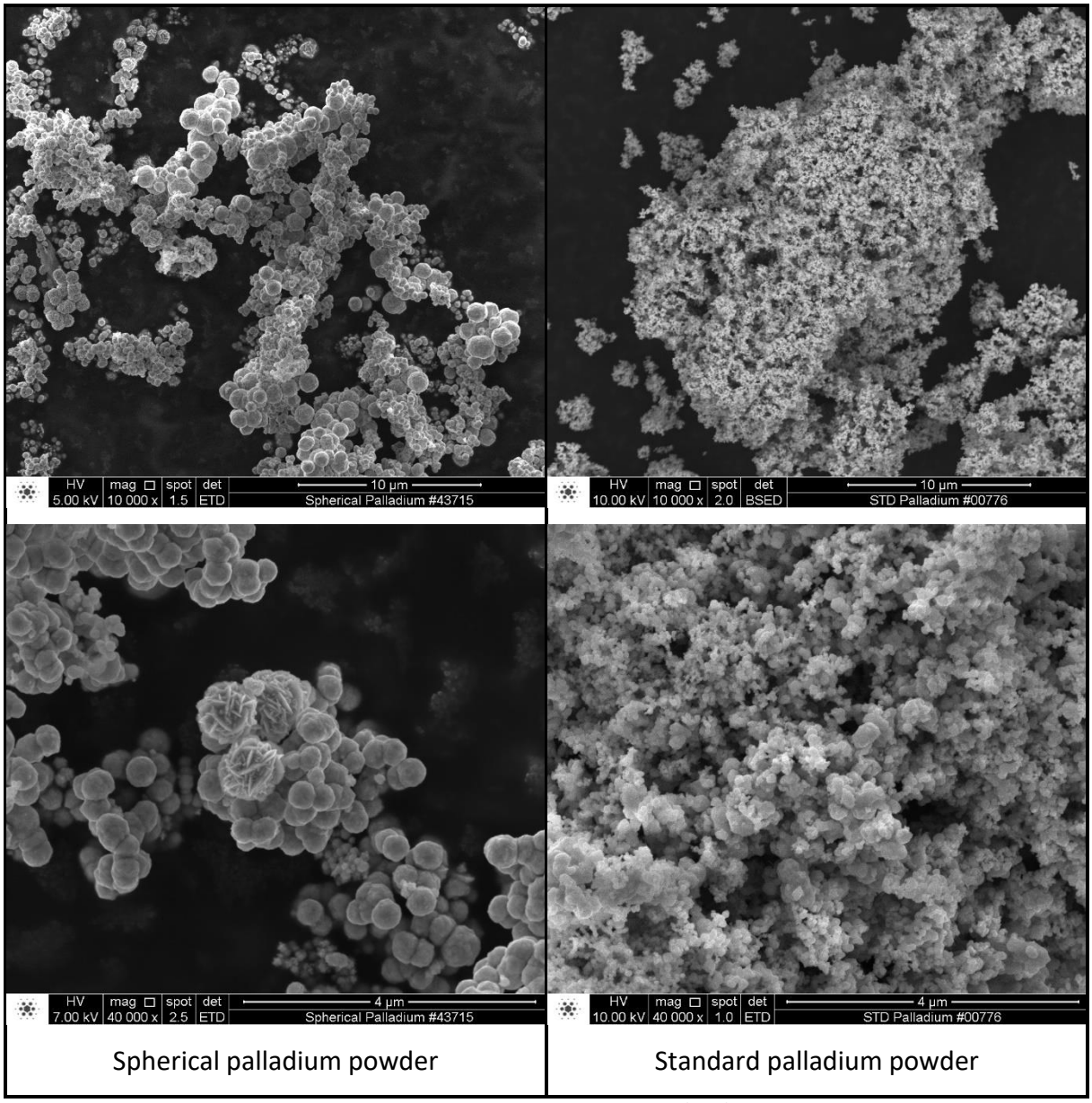

2-P Spherical Pd Vs standard Pd powder (SEM)

Preliminary measurements on this powder showed that its sorption properties[32] are almost identical to bulk palladium[33].

2.4.2 Palladium Foil

Some of the measurements described in chapter 5 were conducted on palladium foil (Thermo Fischer Scientific, 2018a) rather than the spherical powder. This foil was, again, purchased from Alfa Aesar. It is sold as having a purity of 99.9%, with the balance made up by trace amounts of transition group metals and oxygen. This foil measures $0.1 \times 50 \times$

[32] The relationship between pressure, composition, and temperature (PCT), as well as sorption kinetics.
[33] The source data for this observation are not available for publication.

$50\ mm$. Further details about this material can be found in the section describing the experiment where this material is used (see section 5.4.2)

2.5 Determining Concentration

Two different techniques have been used in this work to determine the hydrogen concentration of sample materials at a given pressure and temperature. Both methods measure gas sorption as a function of pressure, temperature, and time. These methods are discussed in the following two sections.

2.5.1 Gravimetric Sorption

Automated gravimetric sorption analysis was developed in mid to late 1980s as a method of measuring the magnitude and kinetics of ab/de sorption of gases and vapours in materials. Benham and Ross (1989) describes the principles and methods that would go on to be used in the design of the Hiden IGA (Intelligent Gravimetric Analyser) used in this work.

Gravimetric analysers attempt to 'weigh' the mass of an ab/adsorbed species. This is achieved by measuring the force on a suspended sample in a pressurised chamber. It is common to use a counterweight balance as this gives a direct measure of mass and therefore is not subject to contributions from local fluctuations in the magnitude of gravitational force at any given location around the globe. Figure 2-Q shows the basic layout of such a device. In principle, the force on the balance is simply the difference between the mass of the sample (m_s) and the mass of the counterweight (m_{cw}). This can either be measured by the deviation in the position of the balance arm (as in a manual pan balance) or implied by the force required to restore the balance to a horizontal position (as in the IGA). This simplified case is only true in the case of measurements in a complete vacuum. Where a gas is present in the chamber, both sides of the balance are subject to buoyancy. Buoyant force may either increase or reduce the apparent mass of an object suspended in a gas or fluid. The force for any object is described by the following relationship between the volume of the object (V), the density of the gas / fluid (ρ), and the force due to gravity (g):

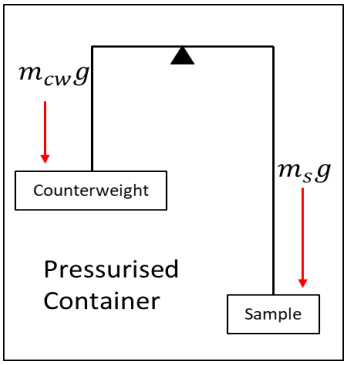

2-Q Basic Gravimetric Analyser Schematic

$$f_{buoyancy} = V_{object} \times \rho_{gas} \times g \qquad (2\text{-}4)$$

The density of the gas in the chamber can be calculated using the real gas law that relates measured pressure (P), the volume of the container (V), the number of moles of gas present (n), compressibility of the species (Z, where $Z = Z(P,T)$), and temperature (T) via the universal gas constant (R):

$$PV = nZRT \tag{2-5}$$

Substituting $n = m/m_M$ (number of moles is equal to the measured mass divided by the molar mass of the species) into equation (2-5) and rearranging in terms of m gives:

$$m = \frac{Vm_M P}{ZRT} \tag{2-6}$$

Dividing equation (2-6) by V to give density ($\rho = m\backslash V$), shows that this can be calculated from direct measurement of just pressure and temperature:

$$\rho = \frac{m}{V} = \frac{m_M P}{ZRT} \tag{2-7}$$

For a complete picture of the effect of buoyancy on the measurements in this work, it should be considered in the specific case of the equipment used. A schematic of the IGA is shown in figure 2-R.

The IGA is a microbalance system that operates on the same basic principle as shown in figure 2-Q. It has three chambers made of stainless steel that are connected by small apertures to allow each to be maintained at different temperatures. The top chamber houses a balance head with two horizontal arms. This chamber is regulated to the calibration temperature of the specific head unit used (T_b). In the case of the unit used, this is 55°C. At the end of each arm is a length of gold chain that passes through the apertures into the counterweight and sample chambers. Hanging from the end of each chain is a short section of tungsten wire that leads to either the counterweight (a piece of coiled stainless steel wire) or the sample container. In this work, a small bucket made from quartz glass was used to

hold the sample. The counterweight chamber is externally exposed to the room (in this case, maintained at 21°C). It is assumed that the temperature inside this chamber (T_{cw}) is equal to the external temperature. The sample chamber is surrounded by a furnace. Thermocouples monitor the temperature at the sample (T_s) inside the chamber and of the furnace (external to the chamber). For each measurement, a temperature and pressure are set, the system is allowed to reach equilibrium, and the force on the balance is recorded as a mass. Pressure is monitored near the balance chamber. Different buoyant forces are present on each side of the balance due to the difference in volume of the material in each chamber and the effect of temperature on gas pressure. The buoyant force on each side of the balance is equal to the sum of the components in the respective chamber. Where the weights and densities of the individual components are known, the overall force due to buoyancy on the balance head is given by:

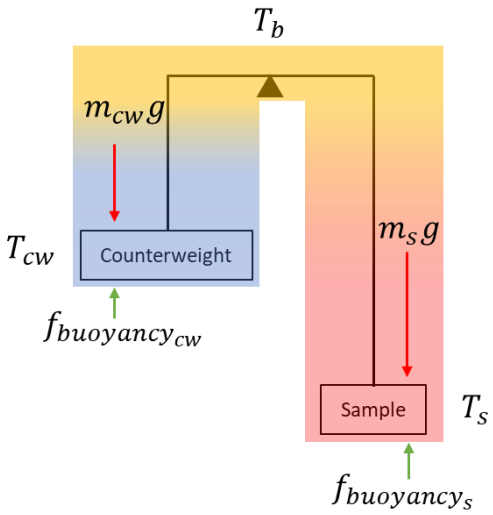

2-R IGA Schematic

$$f_{buoyancy} = \rho_{Hs}\left(\frac{m_{sh}g}{\rho_{sh}} + \frac{m_{sp}g}{\rho_{sp}} + \frac{m_s g}{\rho_s}\right) - \rho_{Hcw}\left(\frac{m_{ch}g}{\rho_{ch}} + \frac{m_{cw}g}{\rho_{cw}}\right) \quad (2\text{-}8)$$

Where the subscripts denote:

sh	Sample hangdown
sp	Sample pan
s	Sample (dry @0bar)
ch	Counterweight hangdown
cw	Counterweight
Hs	Hydrogen at sample
Hcw	Hydrogen at counterweight

The overall force on the balance is given by:

$$f_{measured} = f_{actual} - f_{buoyancy} \quad (2\text{-}9)$$

Substituting equation (2-8) into equation (2-9), cancelling g from all terms, and rearranging gives the actual mass as:

$$m_{actual} = m_{measured} + \left(\rho_{Hs} \left(\frac{m_{sh}}{\rho_{sh}} + \frac{m_{sp}}{\rho_{sp}} + \frac{m_s}{\rho_s} \right) - \rho_{Hcw} \left(\frac{m_{ch}}{\rho_{ch}} + \frac{m_{cw}}{\rho_{cw}} \right) \right) \quad (2\text{-}10)$$

Finally, the mass of the absorbed species is then simply given by the difference between the dry mass (pre-ab/adsorption) and the measured mass after correction for buoyancy:

$$m_{sorb} = m_{actual} - m_{dry} \quad (2\text{-}11)$$

It should be noted that, the buoyancy correction does not account for changes in the sample density due to increased mass (introduced by sorption) or sample volume from lattice expansion from temperature, concentration, and phase changes. In the case of the palladium hydride (/deuteride) system these changes are likely to fall within the combined measurement error of the correction as mass uptake is limited to less than 1% (in the hydride case, 2% in the deuteride case) and lattice expansion from pure palladium to the beta-phase hydride in the temperature range used is also slightly less that 1%.

Mass uptake is not an easy parameter to compare between samples. Therefore, it is useful to generalise this in terms of the ratio of H (/D) to Pd atoms in a given sample. Dividing the measured masses of each species by their atomic mass gives the number of moles present. The molar ratio “H/Pd” is then given by:

$$\frac{H}{Pd} = \frac{n_H}{n_{Pd}} = \frac{\left(\frac{m - m_{dry}}{1.00794} \right)}{\left(\frac{m_{dry}}{106.42} \right)} \quad (2\text{-}12)$$

And, the ratio D/Pd can be calculated by substituting the appropriate atomic mass (2.0141 AMU) into the numerator of equation (2-12).

This ratio also serves as a very accurate approximation to the number of filled octahedral sites in any sample where the ratio of surface to bulk atoms is not significant.

Gravimetric sorption measurements are independent of one another (the final state of a measurement is not dependent on any previous measurements – only the initial masses and the current pressure and temperature readings). This means that it is theoretically possible to measure the points of an isotherm in any order[34]. It also allows any number of points to be measured in a single pass along an isotherm. This technique is particularly useful in this work as it is also possible to make single measurements any pressure within the operating range.

The specific design of the IGA means that the sample, balance head, and counterweight are held at different temperatures (see figure 2-R). While gas is allowed to flow almost freely (aside from the relatively unobtrusive apertures) this creates small pressure gradients and convection currents around the internal volume of the instrument. This results in turbulence that disturbs the balance head that gets worse as the pressure and sample temperature are increased. It also further complicates the buoyancy correction and possibly adds a further error that results from the mean force of convection on the balance.

2.5.2 Manometric Sorption

Manometric sorption is the most common method for measuring gas uptake in solids. It is commonly referred to as “Sieverts’ Method”, a reference to Adolf Sieverts, one of the early pioneers of the technique (Adolf. Sieverts, 1929). Rather than making a direct measurement of the gas ab/adsorbed by a sample (as is the case in gravimetric sorption), uptake is inferred from a drop in pressure. It is possible to conduct this type of measurement to a relatively high degree of accuracy with basic ‘off the shelf’ components that have been put together by hand. However, many computer driven automated systems are available commercially. The manometric measurements in this work were conducted using a Hiden Isochema HTP1. This section discusses the general method employed, making reference to this specific device where necessary.

The most basic possible layout of a manometric sorption rig is shown in figure 2-S.

[34] This is not true in the region of phase boundaries where hysteresis may occur.

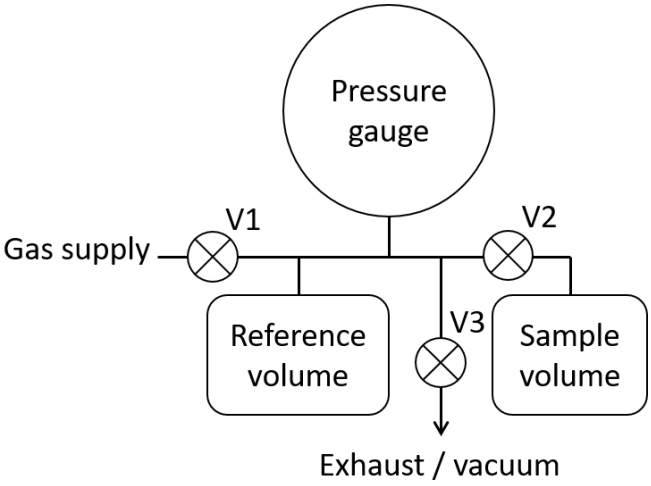

2-S Manometric sorption rig schematic

Prior to making any measurements, the desired gas must be connected to the inlet and the sample to be tested placed in the sample volume. Next, with valve one (V1) closed and valves two and three open, the rig (including both volumes) is fully evacuated. Then valves two and three are closed, and valve one is opened to fill the reference volume to the desired pressure. Once the pressure is reached and valve one has been closed, valve two can be opened allowing the gas to expand to fill the full volume (the reference volume, sample volume and the pipe network that links them). If no gas is absorbed by the sample, the change in the measured pressure should be proportional to the change in the volume that contains it. If not, a drop in pressure will be seen.

For any volume containing a gas, the pressure is given by:

$$P = \frac{nZRT}{V} \tag{2-13}$$

In the method described, an initial pressure (P_i) exists in the initial volume (V_i) between valves one and two. When valve two is opened, gas expands to fill both the initial volume and the sample volume (V_s). The total volume of the system is now V_f. Assuming that the system is held at constant temperature and no gas is absorbed, nRT is constant, so:

$$\frac{P_i V_i}{Z_i} = \frac{P_f V_f}{Z_f} \tag{2-14}$$

where $V_f = V_i + V_s$. It then follows that,

$$P_f = \frac{P_i V_i Z_f}{V_f Z_i} = \frac{P_i V_i Z_f}{(V_i + V_s) Z_i} \tag{2-15}$$

However, if gas is absorbed by the sample, the number of moles of gas present after valve two is opened is reduced (by the number of moles absorbed). It therefore follows that the condition before opening valve two is given by:

$$P_i V_i = n_i Z_i RT \tag{2-16}$$

And the final condition is given by:

$$P_f V_f = n_f Z_f RT \tag{2-17}$$

Since equations (2-16) and (2-17) describe the state of the gas in a sealed system, it stands to reason that the number of moles ab/adsorbed, is the difference between n_i and n_f.

$$\Delta n = n_i - n_f = \frac{P_i V_i}{Z_i RT} - \frac{P_f (V_i + V_s)}{Z_f RT} \tag{2-18}$$

Valve two is then closed, maintaining the pressure in the sample volume, and the reference volume is filled (to a pressure higher than the sample volume). Then the process of expanding the gas into the full volume can then be repeated. For each subsequent step, the calculation is complicated by the fact that the sample volume does not start under vacuum. The pressure contained in the sample volume V_s at the start of each measurement is the final measured pressure from the previous step[35]. As such, errors compound with each new measurement.

Further to this, the technique relies on having accurate values for the internal volumes. Since the 'dead' space in the sample volume is determined by the volume of the sample itself, changes in the lattice parameter of the sample material due to concentration changes will introduce a further error.

[35] A full treatment of this method is available in Broom (2011)

The difference in the lattice parameter between palladium and beta palladium hydride is around 3.5%. However, this change in volume is extremely small when compared to the volume that the pressure is measured over and, as such, is not thought to contribute much to the measurement errors present in the system. Concentration values quoted in this work have been rounded appropriately to account for these errors.

3 Neutron Scattering

Not long after the discovery of the neutron by James Chadwick (1932), researchers began to look into the possibility of its use as a probe for studying structure and dynamics in materials. By 1936 two groups had shown that diffraction of neutrons by solids was possible. With the rapid expansion of fission reactor programmes in the 1940s, many high flux neutron sources became available allowing the field of neutron scattering to develop rapidly. Within a few years, Brockhouse and Stewart (1955) had published the first neutron spectroscopy results[36]. Since then, numerous dedicated facilities have advanced neutron scattering techniques and allowed their reach to extend to an ever growing number of research fields.

3.1 Why Use Neutrons?

Neutrons generally interact with other particles via the strong nuclear force[37]. This makes them an ideal probe for measuring the positions and motions of nuclear particles. It also means that the potential for interaction within a solid is much lower than for particles that interact predominantly via electromagnetic force. This allows for much greater penetration depth than would be possible with the complimentary technique of x-ray scattering.

Due to the low potential for interaction with a sample, it is possible to design experiments where the majority of neutrons measured by a detector will only have made a single interaction. As such, interactions with different properties are theoretically separable. This makes it possible to use the technique to investigate individual components of systems where multiple forms of motion may be present. Other established techniques for measuring lattice gas diffusion in solids (permeation, sorption, etc.) yield diffusion information about the 'system as a whole' rather than any specific motions that are present.

[36] This, along with his continued work in the field, gained Bertram N. Brockhouse the 1994 Nobel Prize in Physics (shared with Clifford G. Shull) (Nobelprize.org, 2018)

[37] The magnetic moment of the Neutron is approximately three orders of magnitude smaller than that of the electron (Odom, Hanneke, D'Urso, & Gabrielse, 2006) (Particle Data Group et al., 2012). This property has been used widely to probe magnetic properties of materials using polarised neutron beams but forms no part of this work and, as such, will not be discussed further here.

The scattering lengths (the amplitude of interaction) and cross sections (the effective radius for potential interaction – measured in 'barns'[38]: $10^{-28}m^2$), that define the outcome of an interaction of a neutron with a specific nucleus, are not linearly dependent on Z (the atomic number of an element or isotope) or A (the total number of nucleons in an element / isotope). Instead, they 'appear' to vary randomly with changes in A and Z.

Hydrogen is an extremely strong scatterer of neutrons having both a large total cross section and a large scattering length. Conversely, as x-ray scattering relies on interaction with the electron cloud of a particle, low Z particles are virtually invisible to the technique. As such, neutron scattering is particularly well suited to measuring the motion of hydrogen (and hydrogen containing) particles.

3.2 Neutron Scattering Basics

The interaction of energetic neutrons with particles is essentially wave based in nature. It is, however, often useful to describe the process in a semi-classical sense as the transfer of momentum or energy between particles or waves. Both descriptions will be used in this section as appropriate.

3.2.1 Properties of Neutrons

The neutron is a baryon consisting of one up and two down quarks. It has no intrinsic electric charge and a mass slightly larger than that of the proton (1.0087 AMU as opposed to 1.0073 AMU). As a baryon, it is fermionic and, as such, has half integer spin. Free (unbound) neutrons have a half-life of around 15 minutes (decaying via beta-decay) but bound neutrons have been shown to be essentially stable[39]. Neutrons have a magnetic moment of a similar order of magnitude to the proton but roughly three orders of magnitude smaller than that of the electron[37].

Neutrons in motion with regard to another particle display both wave and particle properties. In a non-relativistic system (where the relative motion is not a 'significant

[38] The name 'barn' was originally a joke amongst scientists working on the Manhattan Project at Perdue University in reference to the idiom "couldn't hit the broad side of a barn" because of the incredibly low probability of any one Neutron in a particle beam interacting with any individual nucleus (Perricone, 2006).
[39] Bound neutrons may undergo beta-decay but this is due to the overall properties of the nucleus rather than an intrinsic half-life of the neutron.

fraction' of the speed of light in a vacuum), the wavelength of the neutron is given by the De Broglie relation:

$$\lambda = \frac{h}{p} = \frac{h}{m_N v} \tag{3-1}$$

where,

λ	=	Wavelength
h	=	Planck constant
p	=	Momentum
m_N	=	Neutron mass
v	=	Velocity

Energetic neutrons used for crystallographic structure determination and dynamics experiments often have wavelengths of a few angstroms (Å, $10^{-10}m$). These wavelengths are of a similar scale to the inter-atomic distances in a solid.

The kinetic energy of the neutron can be calculated by substituting the standard form of the equation for kinetic energy:

$$KE = E = \frac{1}{2}mv^2 = \frac{p^2}{2m} \tag{3-2}$$

and rearranging to give:

$$E = \frac{h^2}{2m_n\lambda^2} \tag{3-3}$$

Typically, neutrons with the wavelengths mentioned above will have energies of a few meV.

It is often more useful to consider equations (3-1) and (3-3) in the form that is more naturally suited to their wave (rather than particle) nature:

$$\vec{p} = \hbar\vec{k} \tag{3-4}$$

$$E = \hbar\omega \tag{3-5}$$

where,

$\vec{p}$ = Momentum vector

ω = Angular frequency

E = Energy

$\vec{k}$ = Wave vector

$\hbar$ = Reduced Planck constant ($h/2\pi$)

3.2.2 Neutron Interactions

This section discusses the properties and mechanisms that underlie the interaction between free neutrons and nuclei. The implications of these with regard to neutron scattering experiments are discussed in sections 3.4 and 3.5, while those for the specific experiments described later in this document, can be found in section 3.6.

When energetic neutrons interact with a nucleus there are two possible outcomes: absorption or scattering. Almost all interactions hold the possibility of either of these outcomes. The likelihood of either outcome is described by the relative magnitude of the absorption (see section 3.2.2.1) and total scattering cross sections (σ_{abs}, and σ_{tot}).

The total scattering cross section is the sum of two components: coherent (σ_{coh}) and incoherent (σ_{inc}). Properties leading to, and arising from, these two components are discussed in section 3.2.2.4.

3.2.2.1 Neutron Absorption

When a neutron encounters nucleus there is a finite probability that it may be absorbed[40]. The immediate result of such absorption is for the nucleus to maintain its atomic number and simply increase in mass ($Z' = Z$, $A' = A + 1$). There are a number of possible outcomes after this process has taken place depending on the properties of the newly formed nucleus:

- The new nucleus may be stable (no further process takes place with the possible exception of gamma emission)
- Fissionable nuclei that absorb a neutron will become unstable and undergo fission (with a half-life specific to the newly formed nucleus)

[40] This process is also commonly referred to as 'neutron capture'. The probability of such events is expressed by the magnitude of the neutron capture cross section for the specific nucleus.

- The new nucleus may undergo nuclear decay, forming a further new nucleus.

In most neutron scattering work, this phenomenon is deliberately minimised by careful selection of elements and isotopes with small absorption cross sections. Materials in the beam that absorb neutrons may transmute distorting results, or simply become too active for safe handling after neutron irradiation.

3.2.2.2 Geometry of Scattering

Before discussing the mechanics of neutron – nucleus interactions, it is necessary to define the geometry of the system and the terminology that will be used to describe it in the following sections.

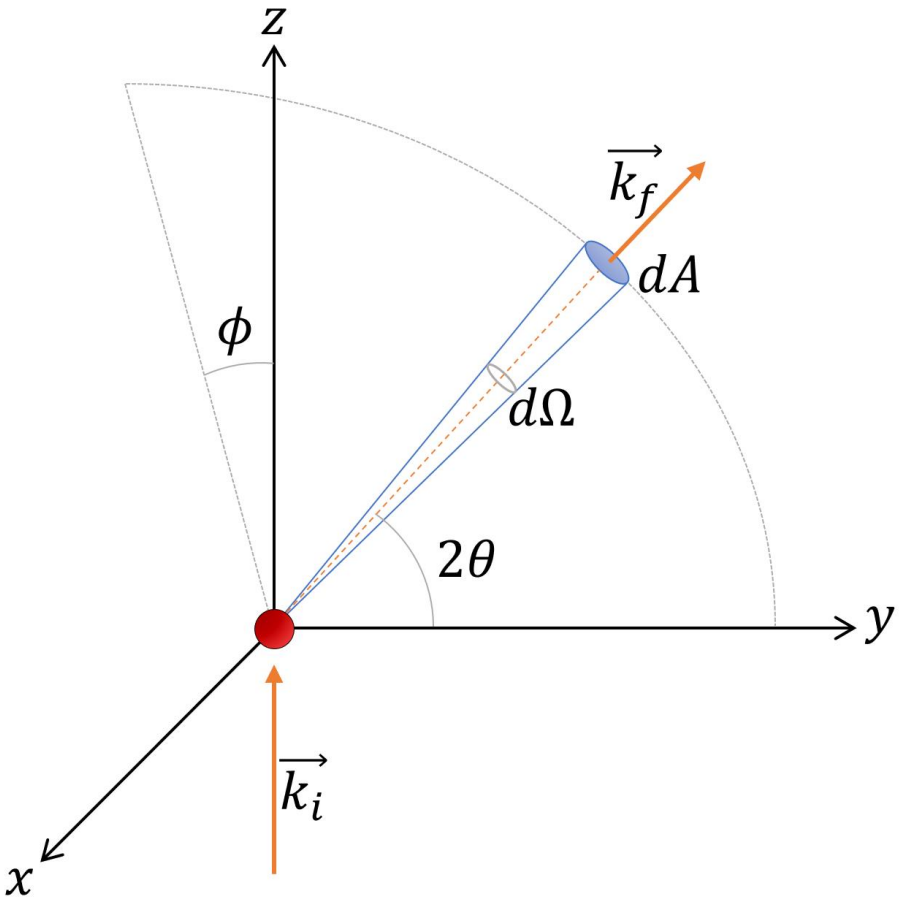

3-A Geometry of a scattering experiment

An incident neutron with wavevector $\overrightarrow{k_i}$ (where $\left|\vec{k}\right| = k = \frac{2\pi}{\lambda}$) is scattered into a new state with wavevector $\overrightarrow{k_f}$. The origin of the coordinate system is at the position of the nucleus. The scattering direction is described by the azimuthal angle ϕ and the angle between $\overrightarrow{k_i}$ and

$\overrightarrow{k_f}$, 2θ. If the magnitude of the incoming and outgoing wavevectors are equal (i.e. $\overrightarrow{k_i} = \overrightarrow{k_f}$), there is no transfer of energy between the neutron and nucleus. This is known as 'elastic' scattering (see section 3.4). The alternative case, where energy IS transferred between the neutron and nucleus ($\overrightarrow{k_i} \neq \overrightarrow{k_f}$), is known as 'inelastic' scattering (see section 3.5). Energy transfer in inelastic scattering events is taken with reference to the sample: energy transfer is regarded as positive where the neutron loses energy ($\overrightarrow{k_i} > \overrightarrow{k_f}$), and negative where the neutron gains energy ($\overrightarrow{k_i} < \overrightarrow{k_f}$).

The total scattering cross section σ_{tot} of any given nucleus is defined as:

$$\sigma_{tot} = \frac{number\ of\ neutrons\ scattered\ in\ all\ directions}{number\ of\ neutrons\ incident\ on\ sample} \tag{3-6}$$

The denominator is most often expressed through the incident neutron flux I_0. This is defined as the number of neutrons incident on a unit area per second and is commonly expressed in units of units of $n\ cm^{-2}\ s^{-1}$ for neutron instruments.

The total scattering in all directions from a sample is not easily measured. Instead, the number neutrons scattered in a given direction is required. For any solid angle Ω (measured in steradians), this is determined by the differential cross section:

$$\frac{d\sigma}{d\Omega} = \frac{neutrons\ per\ second\ scattered\ into\ sold\ angle\ d\Omega}{I_0 d\Omega} \tag{3-7}$$

(The solid angle Ω defines an area A at any radial distance from the origin.)

Where momentum transfer is expected, the parameter of interest is also dependent on the final energy of any scattered neutrons:

$$\frac{d^2\sigma}{d\Omega dE_f} = \frac{\begin{matrix} neutrons\ per\ second\ scattered\ into\ a\ solid\ angle\ d\Omega\ with \\ a\ final\ energy\ between\ E_f\ and\ E_f + dE_f \end{matrix}}{I_0 d\Omega dE_f} \tag{3-8}$$

This is commonly known as the double differential cross section.

3.2.2.3 Mechanics of Scattering

The magnitude of any given scattering interaction between a single neutron and a nucleus as a function of their radial distance is described by the Fermi-pseudopotential:

$$V(r) = \frac{2\pi\hbar^2}{m_n} b\delta(r) \tag{3-9}$$

where b is the bound scattering length of the nucleus in question, m_n is the mass of the neutron, and $\delta(r)$ is the Dirac delta function[41].

The wavelength of a neutron in most scattering experiments can be assumed to be much larger than the radius of interaction of any nucleus. As a result, the nucleus can be assumed to be a point source (hence the delta function describing the radius of interaction) making the potential, and the resulting scattered wave, spherically symmetric.

Equation (3-9) can be generalised to cover arrangements of N nuclei (labelled i, with scattering length b_i, at a radial distance r_i from the origin r_0) such as those in a crystal:

$$V(r) = \frac{2\pi\hbar^2}{m_n} \sum_{i=1}^{N} b_i \delta(r_0 - r_i) \tag{3-10}$$

Equations (3-9) and (3-10) show that the magnitude of the interaction of a neutron and any given nucleus (or assembly of nuclei) is determined by the scattering length of that nucleus.

3.2.2.4 Scattering Length and Cross Section

Neutron 'scattering length' is a measure of the amplitude of interaction between an incident neutron and a nucleus. It can be both positive and negative, giving rise to repulsive and attractive Fermi-pseudopotentials (equation (3-9)) respectively.

It is partly the result of the strong nuclear force and partly a quantum phenomenon that stems from the spin of the neutron ($s = 1/2$) and the spin of nucleus (I) that it interacts with. As these spins can be either parallel or anti-parallel, the combined spin (J) is given by:

$$J = I \pm \frac{1}{2} \tag{3-11}$$

[41] $\delta(r)$ describes the spatial density of a point source. It is zero for all r except $r = 0$. Its integral over all r is $\int_{-\infty}^{\infty} \delta(r) = 1$.

Different scattering lengths are associated with these parallel and anti-parallel states (b^+ and b^- respectively). The statistical probability of either state occurring (w^+ and w^-) is proportional to the number of spin orientations that could give rise to it ($2J+1$). Setting $w^+ + w^- = 1$ gives:

$$w^+ = \frac{I+1}{2I+1} \tag{3-12}$$

And,

$$w^- = \frac{I}{2I+1} \tag{3-13}$$

The coherent scattering length b_{coh} of a nucleus is given by:

$$b_{coh} = w^+ b^+ + w^- b^- \tag{3-14}$$

Where, for an elemental material containing multiple isotopes (labelled r, with relative abundance c_r), this becomes the average of the scattering lengths over all isotopes and spin states:

$$b_{coh} = \langle b \rangle = \sum_r c_r (w_r^+ b_r^+ + w_r^- b_r^-) \tag{3-15}$$

The incoherent scattering length b_{inc} is proportional to the difference between b^+ and b^- (Hammouda, 2016):

$$b_{inc} = \sqrt{w^+ w^-}(b^+ - b^-) \tag{3-16}$$

The coherent cross section σ_{coh} is then defined as:

$$\sigma_{coh} = 4\pi b_{coh}^2 = 4\pi \langle b \rangle^2 \tag{3-17}$$

The incoherent cross section σ_{inc} is defined as the difference between the total and coherent cross sections:

$$\sigma_{inc} = \sigma_{tot} - \sigma_{coh} \tag{3-18}$$

Where the total cross section is given by:

$$\sigma_{tot} = 4\pi\langle b^2\rangle = 4\pi \sum_r c_r(w_r^+(b_r^+)^2 + w_r^-(b_r^-)^2) \tag{3-19}$$

The experiments described in this work use palladium of natural isotopic composition. However, a specific hydrogen isotope is used for each measurement. The implications of this are discussed in section 3.6.

3.3 Coherent Vs. Incoherent Scattering

Section 3.2.2.4 discussed the calculation of coherent and incoherent scattering cross sections and scattering lengths. These two components provide different information about a single system.

Coherent scattering is best described as interference between the incoming neutron wave and a collection of 'spin-coherent' atoms in the sample. As such, this yields information about the relative positions of atoms and their collective dynamics.

Conversely, incoherently scattered neutrons can be interpreted as having scattered from a single nucleus. They carry information about the specific interaction with this nucleus (such as the motion of an individual particle).

These two components are both measured in any real scattering experiment with the resulting data being a composite of the two.

3.4 Elastic Scattering

Neutrons that have interacted with a nucleus resulting in a change to their momentum but no transfer of energy, are said to have been elastically scattered. The resulting momentum transfer in such a collision is given by the vector $\vec{Q}$, where:

$$\vec{Q} = \overrightarrow{k_i} - \overrightarrow{k_f} \tag{3-20}$$

This is shown pictorially in figures 3-B, 3-C and 3-D (where C & D show two common equivalent representations).

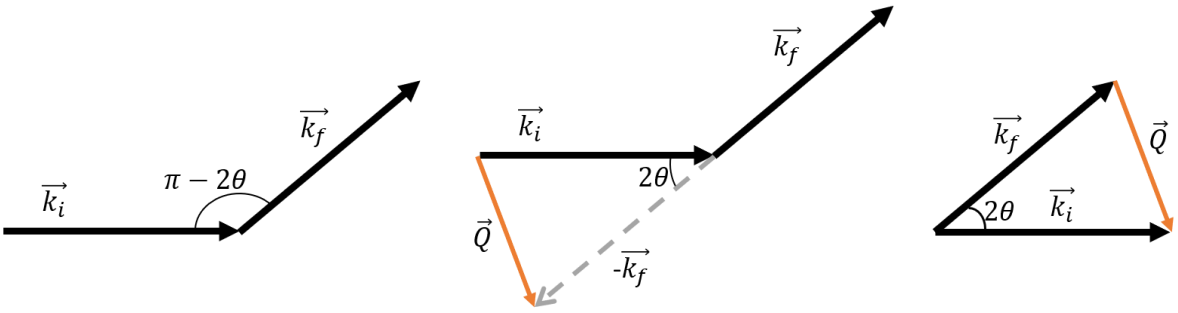

3-B An elastic scattering event | 3-C ($Q=k_i-k_f$) | 3-D ($Q=k_i-k_f$) - alternative

The magnitude of $\vec{Q}$ is related to the scattering angle θ and the neutron wavelength λ via the relationship:

$$|\vec{Q}| = Q = \frac{4\pi \sin\theta}{\lambda} \tag{3-21}$$

3.4.1 Neutron Diffraction

The wavelength of thermal[42] and cold[43] neutrons is comparable to the interatomic distance in solids so the interaction of the two can result in diffraction of the neutron wave.

In a crystal, atoms are arranged in a regular repeating pattern. Radial lines can be drawn from any atom where, in certain directions, these lines will pass through a series of atoms where the same distance separates each. This gives a series of repeating planes. Waves incident on these planes interfere coherently where the incident angle θ, neutron wavelength λ and interatomic spacing d have the following relationship:

$$n\lambda = 2d \sin\theta \tag{3-22}$$

where n is an integer.

[42] $\sim 0.025\ eV$
[43] $< 0.025\ eV$

Equation (3-22) is commonly known as Bragg's Law. It is represented graphically in figure 3-E. Varying the incident wavelength or angle results in a 'Bragg peaks' where this condition is met. From this, the interatomic spacings can be determined.

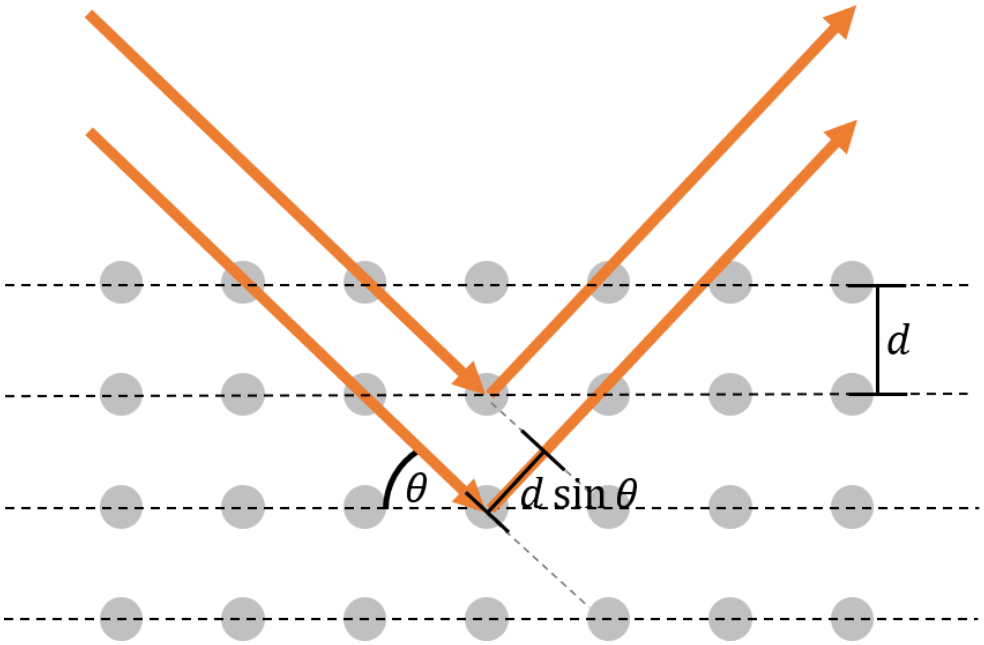

3-E Bragg condition

The planes that Bragg peaks represent are related to the length of the unit cell (a) of the crystal through cartesian co-ordinates (indexed by the Miller Indices h, k and l) that locate the next atom in each plane from any individual. This relationship can be expressed mathematically for a cubic cell as:

$$d_{hkl} = \frac{a}{\sqrt{h^2 + k^2 + l^2}} \tag{3-23}$$

The interatomic spacing d is measured in real space. Momentum transfer Q (the fundamental measurement in elastic scattering experiments) is measured in reciprocal space. Conversion between these two forms is trivial:

$$Q = \frac{2\pi}{d} \tag{3-24}$$

And, it can be seen that substituting equation (3-36) into equation (3-21) gives equation (3-22).

The intensity of Bragg peaks at specific hkl indices is determined by the structure factor of the crystal F_{hkl}. This function combines positional information for all atoms (with coordinates x, y and z) in a primitive unit cell with an atomic form factor f:

$$F_{hkl} = f \sum e^{-2\pi i(hx+ky+lz)} \tag{3-25}$$

Where f is determined by the Fermi pseudopotential that is, in turn, dependent on the coherent scattering length of the specific nucleus.

This results in sets of allowed hkl values for peaks from diffraction by different crystal structures. These are often presented as a set of selection rules for different hkl combinations.

Where the crystal basis is not monatomic, the atomic form factors and positions of each species must be considered:

$$F_{hkl} = \sum_n f_n e^{-2\pi i(hx_n+ky_n+lz_n)} \tag{3-26}$$

Equation (3-38) often results in distinct differences in the intensities of Bragg peaks from materials with multiatomic bases, with the absolute intensities of the peaks determined ultimately by the coherent scattering length of the relevant nuclei.

It should be noted that the structure factor $S(Q)$ measured by any real diffraction experiment is not simply the crystal structure factor F_{hkl}. This also contains contributions from temperature, disorder, etc.

3.4.2 Diffuse Scattering

The logic discussed in the previous section assumes that scattering occurs from a perfect crystal. In most real systems this is not likely to be the case. Disorder (vacancies, interstitials, etc.) results in a 'smearing' of Bragg peaks (reduction in intensity, increase in width). In highly disordered systems, this essentially raises the apparent noise floor that's seen in diffraction measurements.

3.5 Inelastic and Quasi-Elastic Neutron Scattering

The terms ‘inelastic’ and ‘quasielastic’ both describe neutron interactions that involve a transfer of energy ($\hbar\omega$) between the neutron and the sample. In these interactions, the direction of the scattering vector Q is determined in a similar manner to elastic scattering (see figures 3-F, 3-G and 3-H). However, the magnitude of Q is also dependent on the transfer of energy (or, more accurately, angular frequency ω) between the neutron and the sample.

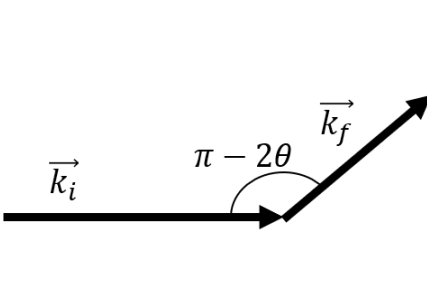

3-F An inelastic scattering event

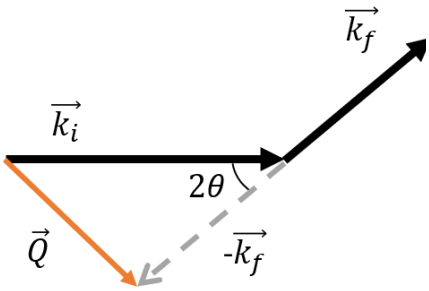

3-G Inelastic scattering vector (Q)

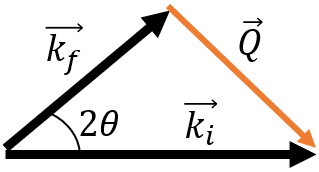

3-H Inelastic Q - alternative

Thus, where the scattering from elastic collisions is described by $S(Q)$, the scattering from inelastic collisions is described by $S(Q, \omega)$.

The term ‘inelastic scattering’ describes all non-elastic scattering. However, in neutron scattering, it is generally used to describe processes that involve the exchange of energy quanta (phonons, rotations, vibrations, etc.). Quasielastic scattering is a special case of inelastic scattering. It refers to the situation where small amounts of energy are transferred to or from the incident neutron wave by a particle in motion in a process analogous to the Doppler effect. The two techniques are usually considered to be distinct.

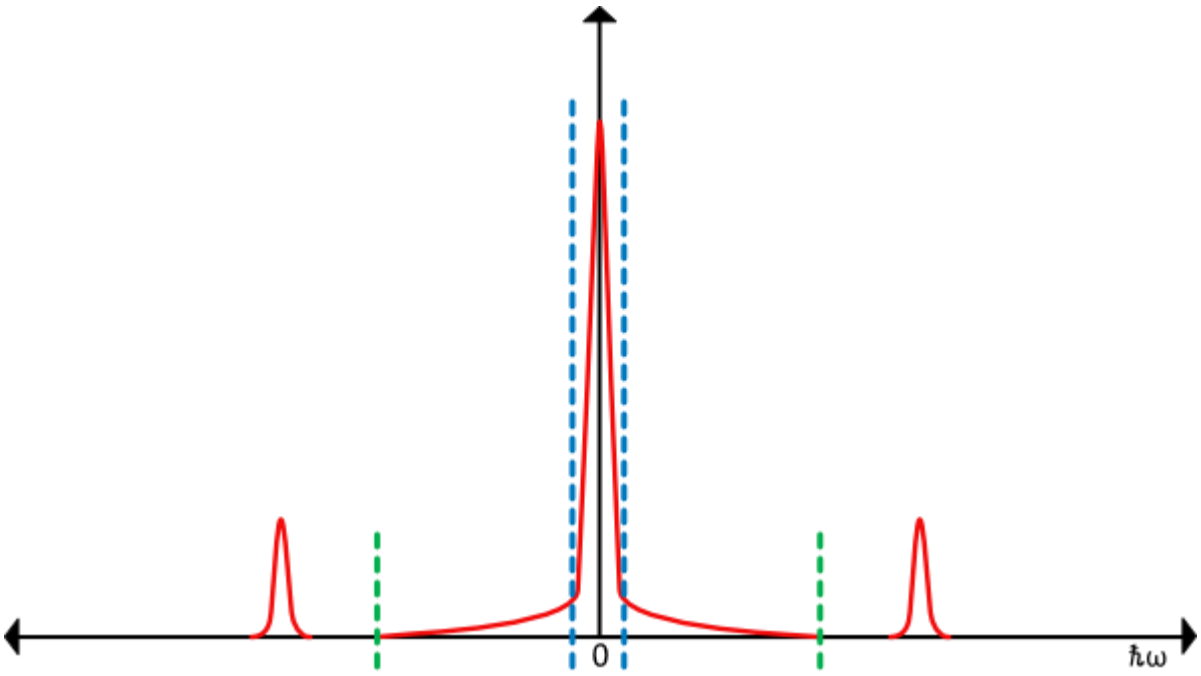

3-I Elastic, inelastic and quasielastic scattering

Figure 3-I represents some inelastic scattering data at a specific Q vector. The region between the blue dashed lines is the elastic scattering. The region inside the green dashed lines is quasielastic scattering. Everything outside the green region would be considered inelastic[44].

It could reasonably be expected that the elastic scattering from any sample should be a delta function (zero width) as it is not associated with any energy transfer. This is not actually the case in the spectra of measured data. Any real component that exists in the system is recorded as that function convoluted with the resolution function $R(Q,\omega)$.

$$S'(Q,\omega) = S(Q,\omega) \otimes R(Q,\omega) \tag{3-27}$$

For real experiments, the resolution function can be measured using a sample where no motion is expected.

Any form of motion (translation / rotation / vibration) will give rise to a characteristic component whose shape is determined by the spatial and temporal Fourier transform of underlying mechanism. In the case of translational diffusion (such as the jump diffusion

[44] All of the measurements discussed in this work are taken over the quasielastic region. As such, no further discussion of inelastic scattering is included.

expected in the Pd-H system) this is a Lorentzian with a half width half maximum (HWHM) Γ and an amplitude A:

$$S_{trans}(Q,\omega) = \frac{A}{\pi}\frac{\Gamma(Q)}{\Gamma(Q)^2 + \omega^2} \tag{3-28}$$

Various models exist that map $\Gamma(Q)$ for different translational motions. These include:

- Chudley-Elliott – Jumps on a lattice (Chudley & Elliott, 1961)[45]
- Singwi-Sjölander – Alternating oscillation and directed motion (Singwi & Sjölander, 1960)
- Hall-Ross – Restricted jump diffusion (Hall & Ross, 1981)

At low Q all of these models predict that broadening can be approximated by DQ^2 (where D is the diffusion coefficient of the motion). However, they rapidly diverge as Q increases.

Information about the geometry of motion is also found in the elastic incoherent structure factor (EISF). This is defined as the fraction of the total scattering that is elastic.

$$EISF = \frac{elastic\ intensity}{elastic\ intensity + QENS\ intensity} \tag{3-29}$$

Quasielastic measurements contain contributions from both coherent and incoherent scattering. The incoherent part of any dataset gives information about the motions of individual nuclei. The coherent part is due to collective motions.

The total scattering includes also contributions from everything else that is in the path of the beam (sample container, instrument components, etc.) and stochastic noise.

The measured scattering function $S'(Q,\omega)$, is therefore a complex composite of many components. This is discussed in more detail with respect to the measurements in this work in section 3.6.2 and the relevant experimental chapters. The method used to separate these components mathematically is described in section 3.9.4.

[45] Discussed at length with respect to the measurements in this work in section 3.6.3

3.6 Neutron Scattering from Palladium, Hydrogen and Deuterium

The neutron scattering properties of the three hydrogen isotopes are very different. Some useful known values are presented in table 3-a.

Isotope	b_{coh} (fm)	b_{inc} (fm)	σ_{coh} (Barn)	σ_{inc} (Barn)	σ_{tot} (Barn)	σ_{abs}[46] (Barn)
H	-3.7406	25.274	1.7583	80.27	82.03	0.3326
D	6.671	4.04	5.592	2.05	7.64	0.000519
T	4.792	-1.04	2.89	0.14	3.03	0
Pd	5.91	---	4.39	0.093	4.48	6.9

3-a Useful Pd, H and D neutron scattering parameters
Sourced from (NIST, 2013), original data from (Sears, 1992)

The following sections discuss these properties in relation to the Pd-H(/D/T) system and the measurements described later in this work.

3.6.1 Diffraction from Pd-H/D

Pure palladium and both alpha and beta phases in Pd-H and Pd-D all have an FCC crystal structure. They can be distinguished by changes in the lattice parameter that occur at phase boundaries.

The primitive cell of an FCC crystal is given by the atom at the origin $(0,0,0)$, and the three at the centres of the adjoining faces: $\left(0,\frac{1}{2},\frac{1}{2}\right)$, $\left(\frac{1}{2},0,\frac{1}{2}\right)$ and $\left(\frac{1}{2},\frac{1}{2},0\right)$. Inserting these values into equation (3-37) gives:

$$F_{hkl} = f\left(1 + e^{-i\pi(h+k)} + e^{-i\pi(k+l)} + e^{-i\pi(h+l)}\right)$$
$$= f(1 + (-1)^{h+k} + (-1)^{k+l} + (-1)^{h+l}) \qquad (3\text{-}30)$$

Which results in the selection rules:

$$F_{hkl} = \begin{cases} 4f, & where\ hkl\ are\ all\ odd\ or\ all\ even \\ 0, & for\ all\ other\ hkl\ values \end{cases} \qquad (3\text{-}31)$$

[46] Absorption cross section for 2200 m/s neutrons.

Diffraction of pure palladium will give Bragg peaks that follow these rules. However, the hydride and deuteride have a diatomic basis. Assuming that the H/D atoms occupy the octahedral interstitials, their position can be considered a translation from the origin by $\left(\frac{1}{2},\frac{1}{2},\frac{1}{2}\right)$. Following a similar process to that shown above but using the multi-atom basis form of F_{hkl} (equation (3-38)) gives:

$$F_{hkl} = \left(f_{Pd} + f_{H(or\ D)}^{-i\pi(h+k+l)}\right)\left(1 + e^{-i\pi(h+k)} + e^{-i\pi(k+l)} + e^{-i\pi(h+l)}\right) \tag{3-32}$$

Which results in the following selection rules:

$$F_{hkl} = \begin{cases} 4\left(f_{Pd} + f_{H(or\ D)}\right), & where\ hkl\ are\ all\ even \\ 4\left(f_{Pd} - f_{H(or\ D)}\right), & where\ hkl\ are\ all\ odd \\ 0, & for\ all\ other\ hkl\ values \end{cases} \tag{3-33}$$

Since the magnitude of the atomic form factors f_{Pd}, f_H and f_D are determined the relevant coherent scattering length (b_{coh}) it is possible to estimate the relative intensities of these peaks for both Pd-H and Pd-D (in the high concentration limit). This is summarised in table 3-b:

$b_{coh}(Pd) \pm b_{coh}(H\ or\ D)$	All even hkl	All odd hkl
Pd-H	2.1694	9.6506
Pd-D	12.581	-0.761

3-b Relative F_{hkl} for Pd-H and Pd-D

It can be seen that, palladium hydride produces intense Bragg peaks where the relevant hkl indices are all odd and shows much less intensity at peaks where these are all even. The converse situation occurs for the deuteride, but to an even greater degree.

For this work, this is simply something that has to be considered when examining diffraction plots. They have only been used as a guide as to the phase structure and are not examined analytically.

This picture is further complicated by the concentration of the interstitials in each measurement. Not only does the relative concentration of Pd to H(/D) atoms affect the

intensity of the measured Bragg peaks, but the level or disorder amongst these interstitials affects their shape.

If a high level of ordering is present in the H/D interstitials, there is a possibility of diffuse peaks occurring for hkl indices that correspond to any unique reciprocal lattice vectors associated with the superstructure formed (see section 2.2.1). As the level of order of reduces, so too will the intensity of this peak. This will also 'smear' the other Bragg peaks, causing an apparent reduction in their intensity. If the interstitials are completely disordered, the net effect will be an apparent increase in amplitude of background noise.

3.6.2 QENS from Pd-H/D

The measured QENS spectra from Pd-H and Pd-D have extremely different coherent / incoherent weighting. Hydrogen is a almost completely incoherent scatterer so the hydride sample contains almost no signal from collective motions. The coherent and incoherent cross sections of deuterium are much more evenly balanced so the signal from the deuteride sample contains large contributions from both. The implications of this for processing and fitting the data from the measurements described in this document are discussed in section 3.6.3.

3.6.3 The Chudley-Elliott Model

The Chudley-Elliott model is used in this work to map the QENS broadening (neutron energy transfer) from diffusing particles in a lattice gas. Initially intended as a way of modelling the broadening seen in neutron scattering from a liquid (Chudley & Elliott, 1961), it wasn't long before papers applying it to the palladium-hydride system (Beg & Ross, 1970; Sköld & Nelin, 1966, 1967) were published.

The model, as originally derived, describes the incoherent scattering function of a series of uncorrelated random translational jumps between nearest neighbour sites on a Bravais lattice where the jump process occurs on a much shorter timescale than the mean residence time of the sites. The solution of the relevant differential equation by Fourier transform shows that this function can be expressed as a Lorentzian with a HWHM $\Gamma(Q)$ and amplitude A:

$$S_{inc}(Q,\omega) = \frac{A}{\pi}\frac{\Gamma(Q)}{\Gamma^2(Q)+\omega^2} \tag{3-34}$$

Where $\Gamma(Q)$ for nearest neighbour jumps in any specific direction through an FCC lattice (as is the case for the system described by this work) is dependent on the mean residence time (τ) and the lattice parameter a. It has the form[47]:

$$\Gamma(Q) = \frac{1}{3\tau}\left(\sin^2\left[\frac{(Q_y + Q_z)a}{2\sqrt{2}}\right] + \sin^2\left[\frac{(Q_x + Q_z)a}{2\sqrt{2}}\right] + \sin^2\left[\frac{(Q_x + Q_y)a}{2\sqrt{2}}\right]\right) \quad (3\text{-}35)$$

Calculating the polycrystalline average (assuming that the measurement is conducted on an isotropic system) yields a function that is dependent on the length of the translational jump (l):

$$\Gamma(Q) = \frac{\hbar}{\tau}\left(1 - \frac{\sin(Ql)}{(Ql)}\right) \quad (3\text{-}36)$$

The functions above have been given in terms on energy transfer ($\Gamma(Q)$ is in units of $\hbar\omega$) as this is the natural unit of data collected with QENS.

This model is only strictly true for a lattice gas system at the limit of low concentration ($c \to 0$) and, as previously mentioned, only for the incoherent part of the scattering from any real sample. Various modified forms have been derived to suit cases outside of this. Modifications that are relevant to the measurements in this work are described in the following sections.

3.6.3.1 Modifications and Considerations for the Hydride Sample

It is common to think of QENS scattering from hydrogen (protium) as being entirely incoherent. Its incoherent cross section of 80.27 barns accounts for almost 98% of its total scattering.

The error in the fitted Lorentzian widths from QENS measurements in this work are generally of the order of a few percent. This could reasonably be expected to be larger than the error induced by failing to account for the small coherent part of the scattering from hydrogen.

[47] (Bée, 1988)

It should be noted that this error would be systematic rather than random. Therefore, it may not simply exaggerate the stochastic noise in fitted data. Features that have a significant influence over Lorentzian broadening from coherent scattering may well be visible in the fitted widths from QENS measurements on hydride samples.

Returning to the assumption of pure incoherent scattering: the actual broadening of a Lorentzian component from translational diffusion has been shown to be dependent on the average proportion of sites available for any jump. In a system where the number of potential jump sites can be reasonably approximated by the number of host lattice atoms, the ratio of occupied sites can be taken as the molar ratio of the diffusing species to host species. Therefore, the mean ratio of available sites for any occupied octahedral site in the lattice is given by $(1-c)$. Applying this correction to equation (3-36) yields:

$$\Gamma_{\mathrm{inc}}(Q,c) = (1-c)\frac{\hbar}{\tau}\left(1-\frac{\sin(Ql)}{Ql}\right) \tag{3-37}$$

It can be seen that, in the low concentration limit ($c \to 0$) this produces the result predicted by Chudley and Elliott. It is also apparent that, as concentration increases, the measured width of the Lorentzian will be reduced by the same ratio for all values of Q.

3.6.3.2 Modifications and Considerations for the Deuteride Sample

Scattering from deuterium contains considerable components from both its coherent and incoherent cross sections (Xs_{coh} and Xs_{inc}). Therefore, the assumption made for the hydrogen case (total scattering can be reasonably be approximated by treating it as purely incoherent) is not valid for measurements on deuterium. It is therefore necessary to consider the contributions from both coherent and incoherent scattering.

Ross, Kemali, and Bull (1999) shows that the coherent quasielastic scattering from a diffusing lattice gas can be described by a modified form of the Chudley-Elliott model where the measured Lorentzian is of the form:

$$S_{coh}(Q,\omega) = \frac{1}{\pi}\frac{S(Q)\Gamma'(Q)}{\left(\Gamma'(Q)\right)^2+\omega^2} \tag{3-38}$$

and the broadening predicted by the incoherent model Γ_{CE} (equation (3-36)) for any real concentration c is replaced with the modified function $\Gamma'(Q)$:

$$\Gamma'(Q) = \Gamma_{CE}(Q)\frac{c(1-c)}{S(Q)} \tag{3-39}$$

Here, $S(Q)$ is the static structure factor of the diffuse scattering from the lattice gas as given in the Mean Field Limit by Clapp and Moss (1968):

$$S(Q) = \frac{c(1-c)}{1 + \frac{c(1-c)V(Q)}{k_B T}} \tag{3-40}$$

Where $V(Q)$ is the Fourier transform of the mean field real space inter-atomic energy potential $V(r)$.

It can be seen that, in a system where the particle interaction $V(Q)$ is negligible, or in the limit of high temperature ($T \to \infty$), $S(Q)$ simply becomes $c(1-c)$. In either of these cases, substituting equation (3-40) into equations (3-38) and (3-39) gives a concentration dependence in the amplitude of the measured Lorentzian that is independent of Q:

$$S_{coh}(Q,\omega) = \frac{c(1-c)}{\pi}\frac{\Gamma'(Q)}{\left(\Gamma'(Q)\right)^2 + \omega^2} \tag{3-41}$$

and cancels the concentration dependence of the Lorentzian broadening, leaving:

$$\Gamma_{\mathrm{coh}}(Q) = \Gamma'(Q) = \Gamma_{CE}(Q) \tag{3-42}$$

Equation (3-42) shows that, in the case of a non-interacting system (or in any system that can be reasonably approximated as such), in the limit of low concentration (as assumed by the standard form of the Chudley-Elliott model), the broadening from coherent scattering is identical to that from incoherent scattering. Thus, it is possible to fit the broadening seen in the total scattering of such a system using the unmodified Chudley-Elliott model (equation (3-36)).

Returning to equation (3-39) it follows that, for any system where particle interactions cannot reasonably be neglected, measured broadening in coherent scattering has a

dependence on concentration (that is independent of Q) of the form $c(1-c)$. Broadening is further reduced around values of Q where peaks occur in the static structure factor $S(Q)$. It has been noted that this phenomenon is qualitatively similar to De Gennes narrowing (De Gennes, 1959; Sinha & Ross, 1988).

In any real QENS experiment, the total scattering function is measured. This can be expressed as the sum of the contributions from coherent and incoherent scattering weighted by the relative magnitudes of their cross sections (Xs_{coh} and Xs_{inc}):

$$S(Q,\omega) = \left(\frac{Xs_{coh}}{Xs_{coh}+Xs_{inc}}\right) S_{coh}(Q,\omega) + \left(\frac{Xs_{inc}}{Xs_{coh}+Xs_{inc}}\right) S_{inc}(Q,\omega) \tag{3-43}$$

Similarly, in this work, it has been assumed that the broadening from any individual form of translational diffusion (having a characteristic jump length l and mean residence time τ) seen in the total scattering can be approximated as a linear combination of its coherent and incoherent parts[48]:

$$\Gamma(Q) = \left(\frac{Xs_{coh}}{Xs_{coh}+Xs_{inc}}\right) \Gamma_{coh}(Q) + \left(\frac{Xs_{inc}}{Xs_{coh}+Xs_{inc}}\right) \Gamma_{inc}(Q) \tag{3-44}$$

Expanding this expression with the concentration dependent forms of $\Gamma_{coh}(Q)$ and $\Gamma_{inc}(Q)$ given in equations (3-39) and (3-37) yields:

$$\begin{aligned}\Gamma(Q) = &\left(\frac{Xs_{coh}}{Xs_{coh}+Xs_{inc}}\right) \frac{c(1-c)}{S(Q)} \frac{\hbar}{\tau}\left(1 - \frac{\sin(Ql)}{Ql}\right) \\ &+ \left(\frac{Xs_{inc}}{Xs_{coh}+Xs_{inc}}\right)(1-c)\frac{\hbar}{\tau}\left(1 - \frac{\sin(Ql)}{Ql}\right)\end{aligned} \tag{3-45}$$

Since the fractions relating to the relative contributions from the relevant cross sections can be calculated explicitly from known values, these can be reduced to constant for each case. Factorising and rearranging equation (3-45) then gives:

$$\Gamma(Q) = \left(\frac{1}{S(Q)}\ 0.7317c + 0.2683\right)\ (1-c)\frac{\hbar}{\tau}\left(1 - \frac{\sin(Ql)}{Ql}\right) \tag{3-46}$$

[48] The validity of this approximation is discussed in relation to the collected data in section 4.5.

If it is possible to consider the system to be free of contributions from the static structure factor $S(Q)$, then it is possible to fit the Lorentzian broadening using the form:

$$\Gamma(Q) = A\left(1 - \frac{\sin(Ql)}{Ql}\right) \tag{3-47}$$

where,

$$A = (0.7317c + 0.2683)(1 - c)\frac{\hbar}{\tau} \tag{3-48}$$

A further complication to this is described in work by Cook, Richter, Hempelmann, Ross, and Züchner (1991), where it is shown that a single form of translational motion with a characteristic timescale τ has independent timescales associated with its coherent (τ_{coh}) and incoherent (τ_{inc}) scattering that are related to mobility and tracer correlation factors (f_m and f_t) via Haven's ratio H_R:

$$\frac{\tau_{coh}}{\tau_{inc}} = \frac{f_t}{f_m} = H_R \tag{3-49}$$

Their work proposed a method using spin polarisation analysis for separating the coherent and incoherent scattering from deuterium dissolved in niobium to acquire direct measurements of each component[49].

The interpretation of this in a single measurement of the total scattering is problematic. Fitting an unknown number of components to measured data is a classic "ill posed problem" in mathematics. In this work, a Bayesian model selection[50] approach has been taken. This method is widely used for distinguishing whether "one or more" Lorentzian components are necessary to achieve an accurate fit to any dataset. It also provides a good guide to the widths of these components where they are sufficiently different. Even with high resolution data, it is likely that similar features will be indistinguishable and can be fitted accurately by functions that represent their arithmetic mean. Applying this logic to equation (3-46) gives:

[49] This method was not employed in this work.
[50] See section 3.9.4

$$\Gamma(Q) = \left(\frac{1}{S(Q)}\ 0.7317c + 0.2683\right)\ (1-c)\frac{\hbar}{\langle\tau\rangle_{H_R}}\left(1 - \frac{\sin(Ql)}{Ql}\right) \qquad (3\text{-}50)$$

Where $\langle\tau\rangle_{H_R}$ is the measured residence time that represents the mean of the two components weighted by Haven's ratio.

The application of this logic to the measurements in this work (as well as how it affects the analysis and outcomes in this document) is discussed in the sections about the measurements on deuterium (section 4.5).

3.7 The Multiple Scattering Problem

The chance of a single neutron in a beam interacting with any individual nucleus is vanishingly small. The scattering cross section of, even the largest, nucleus is much smaller than the distance between nuclei. This can be overcome in neutron experiments by placing a larger number of potential scatterers in the beam. In practise, this means using larger samples. However, this creates another problem. As the depth of the sample increases, so too does the potential for neutrons to be scattered by more than one nucleus before being detected. Neutrons that are scattered more than once will undergo multiple momentum transfers. This means that they will be detected at unexpected angles. It is also possible that they may undergo multiple energy transfers. Both of these issues have the potential to contribute noise to scattering experiments.

Determining the depth of sample to be used in any experiment is therefore a balancing act between maximising the number of scatterers in the beam and keeping multiple scattering to a minimum. It is generally accepted that around 90% transmission (10% scattering) is where this balance lies for QENS experiments. All of the experiments described in this work have been designed to achieve roughly[51] this figure.

3.8 Facilities and Instruments

3.8.1 Producing Neutrons

There are two common methods of producing the neutron flux that is necessary for making structural and dynamic observations within a reasonable timeframe. All of the original

[51] Hydrogen (/deuterium) concentrations for each sample are inherently variable with temperature. Efforts have been made to reduce this as far as possible. Sample depths were chosen based on an assumed mean concentration for each experiment.

experimental neutron sources were high flux fission reactors. With advances in technology came spallation sources.

3.8.1.1 Fission

The source here is straightforward: fission reactions from high mass fissile material produce numerous 'fragments'. These fragments often include isolated neutrons, unstable nuclear clusters that may emit neutrons, or even clusters that may undergo further fission.

3.8.1.2 Spallation

At spallation sources, a high Z target is bombarded with high energy protons. The nuclei momentarily absorb some of the incident particles and then undergo a rapid internal nucleon cascade process followed by a internuclear cascade that includes the emission (and subsequent absorption by neighbouring nuclei) of high energy nucleons. There then follows a de-excitation phase where numerous further neutrons are emitted (commonly referred to as *evaporation*).

3.8.1.3 Other Neutron Sources

It is worth noting that these are not the only commercial neutron production techniques. Compact sources can be created from an alpha emitter combined with a low Z element such as $AmBe$ (a mixed powder of Americium 241 and Beryllium 9). While these sources are comparatively inexpensive, they are very low flux: in the region of 10^1 neutrons for every 10^6 alpha particles (Murata & Shibata, 2002). These sources are commonly used in oil exploration.

Fusion reactors and similar fusion technologies have the potential to create vast neutron fluxes on demand. At the time of writing, this technology, in all its forms, it still in development.

3.8.2 Moderation

The neutrons produced through fission and spallation are often too energetic to be of practical use in experimental work. This can be reduced by passing through a moderator. In the moderator, neutrons undergo numerous inelastic collisions, losing energy with each one. The energy range of neutrons exiting the moderator can be tuned by selecting an appropriate medium. Common moderators found at neutron sources include liquid hydrogen and liquid methane.

3.8.3 ISIS

The ISIS neutron source at Harwell in Oxfordshire, UK is one of the world's highest flux spallation sources. The facility has thirty-five neutron instruments that receive neutrons via beamlines from two heavy metal targets (known as Target Station 1 and Target Station 2 or TS1 and TS2), as well as 6 muon instruments centred around the proton beam that feeds TS1. The instrument suite covers a wide range of neutron scattering disciplines with each being purpose designed to fill a specific niche.

Both target stations receive protons from a single accelerator system. This is a fairly complex multi-stage system. Only a brief overview will be provided here[52]

The process begins with the production of negative hydrogen ions (H^-). These are accelerated to $70\ MeV$ in a linear accelerator (linac). At the end of the linac, the H^- ions pass through a $0.25\ \mu m$ thick alumina foil that strips their two electrons. Beyond this foil lies a synchrotron that accelerates the remaining protons to $800\ MeV$. Once accelerated, groups of protons (pulses) are diverted from the ring by kicker magnets into one of two beam tubes that lead to the targets in TS1 and TS2. Four out of every five pulses are directed to TS1, with the remaining pulse being sent to TS2. This results in beam currents of around $160\ \mu A$ on TS1 and around $40\ \mu A$ TS2 with pulse frequencies of $40\ Hz$ and $10\ Hz$ respectively.

Neutrons radiating from the sources pass through appropriate moderators and then into waveguides that carry them to the instruments.

The general layout of the facility is shown in figure 3-J.

[52] A more comprehensive explanation can be found in Willis and Carlile (2013), and in documents on the STFC-ISIS website: https://www.isis.stfc.ac.uk/

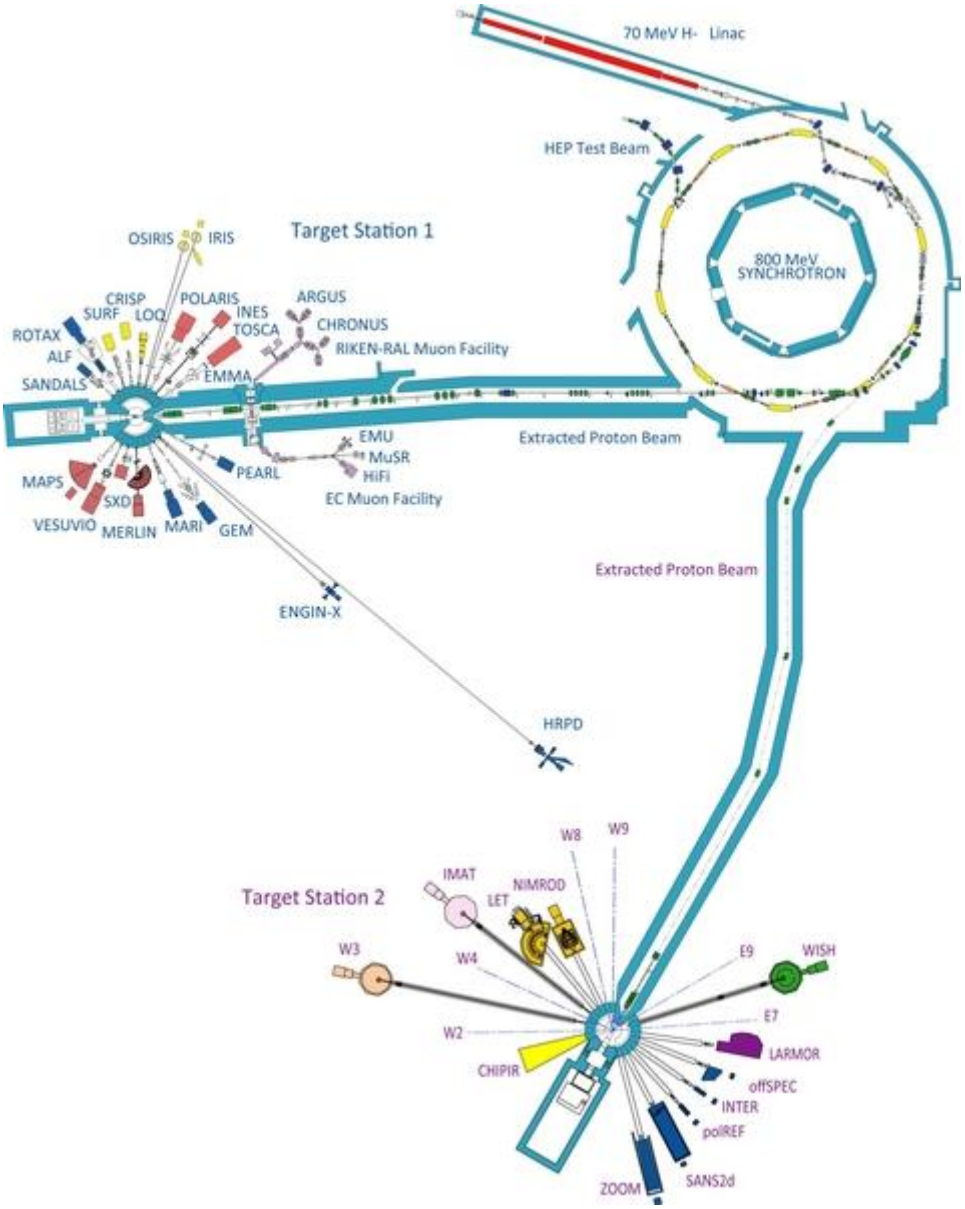

3-J ISIS beamline layout (STFC, 2013)

3.8.3.1 OSIRIS

Many of the measurements in this work were made using OSIRIS[53] at ISIS. The instrument receives neutrons from TS1 via a liquid hydrogen moderator at $25\ K$.

Osiris consists of two coupled detector banks:

The first is a backscattering diffraction bank covering a physical angle of $150° < 2\theta < 171°$. This bank consists of 962 zinc selenide detectors arranged in eight groups surrounding the

[53] https://www.isis.stfc.ac.uk/Pages/osiris.aspx

beam window. Through varying the incident energy of neutrons arriving at the sample (via a series of disc choppers), this bank has a total d-spacing range of 0.8 to 20 Å.

The second, is a spectrometer bank consisting of 42 ^3He tubes that give an angular coverage of $11° < 2\theta < 148°$. This is an indirect instrument. It has two possible configurations using either the 002 or 004 reflections of the pyrolytic graphite analyser. All of the measurements described in this work used the 002 giving a Q range of $0.18 < Q < 1.8$ Å and a resolution of 25.4 μeV. With a beam current of 150 μA at the TS1 target, neutron flux at the sample is approximately 2.7×10^7 $n\ cm^{-2}\ s^{-1}$ (Telling & Anderson, 2008)[54]. Due to the nature of indirect instruments, only a small proportion of these neutrons contribute to the count at the detectors.

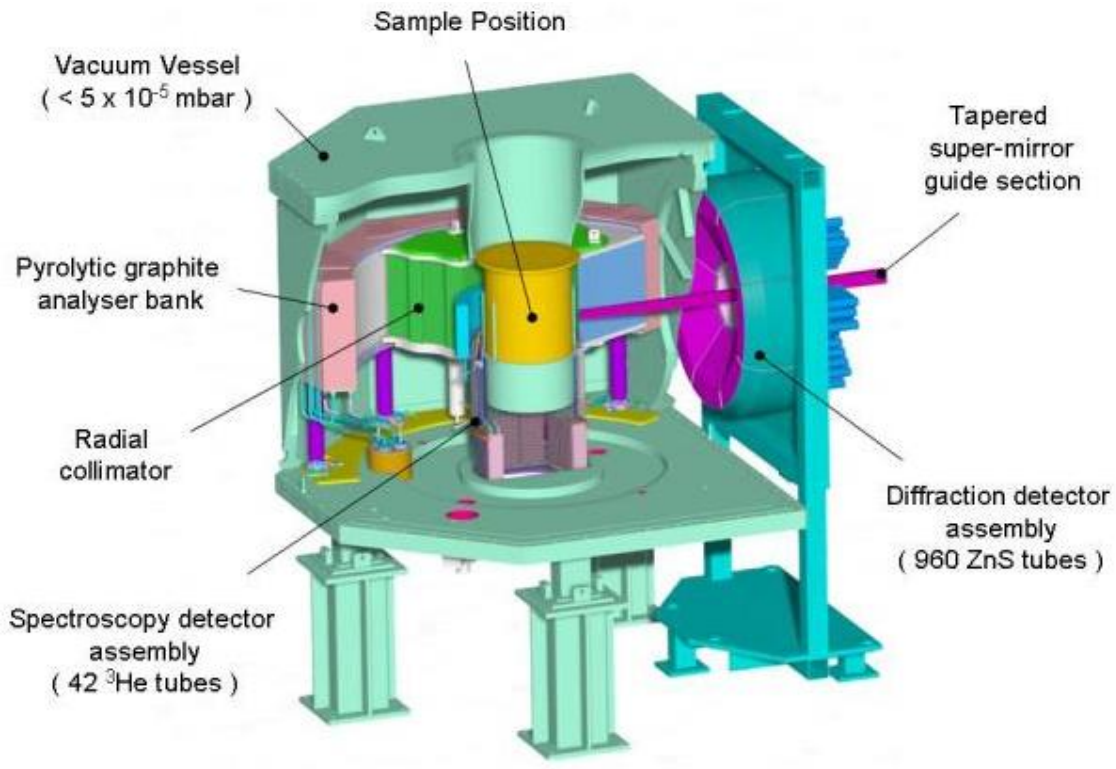

3-K Osiris schematic
(STFC, 2017a)

[54] Further details about this configuration are discussed where appropriate in the rest of this work.

Instrument control and data collection are managed via combination of a LabView[55] and OpenGENIE[56] interfaces.

3.8.4 Institut Laue Langevin

The Institut Laue Langevin[57] (ILL) in Grenoble, France, is world's highest flux continuous neutron source. At its core, is a $58.3\ MW$ enriched uranium reactor that produces $1.5 \times 10^{15}\ n\ cm^{-2}\ s^{-1}$ (measured at the moderators). The facility has a suite of around forty instruments with beamlines that provide wide range of neutron energies, from ultra-cold through to unmoderated. These instruments are arranged in three areas. A few are in the reactor hall itself. The others are split between two 'guide halls'. Neutrons are fed from the moderators in the reactor hall to the instrument in hollow guide tubes under vacuum.

3.8.4.1 IN5

IN5[58] is a direct geometry spectrometer. Its detector bank consists of 12 units of 32 ^3He tubes covering an angle of -12 to $135°$. It has a wide range of incident neutron wavelengths (1.8 to 20 Å) that are selected by altering the phase relationship between the choppers. At the settings used for the experiments described in this work, the neutron flux at the sample is approximately $6.83 \times 10^5\ n\ cm^{-1}\ s^{-1}$. While the flux at the sample is lower than that of Osiris, the direct geometry of the instrument delivers a much higher count at the detectors.

[55] http://www.ni.com/en-gb/shop/labview.html
[56] A full manual for OpenGENIE can be found at https://www.isis.stfc.ac.uk/Pages/open-genie-user-manual.pdf
[57] https://www.ill.eu/
[58] https://www.ill.eu/instruments-support/instruments-groups/instruments/in5/

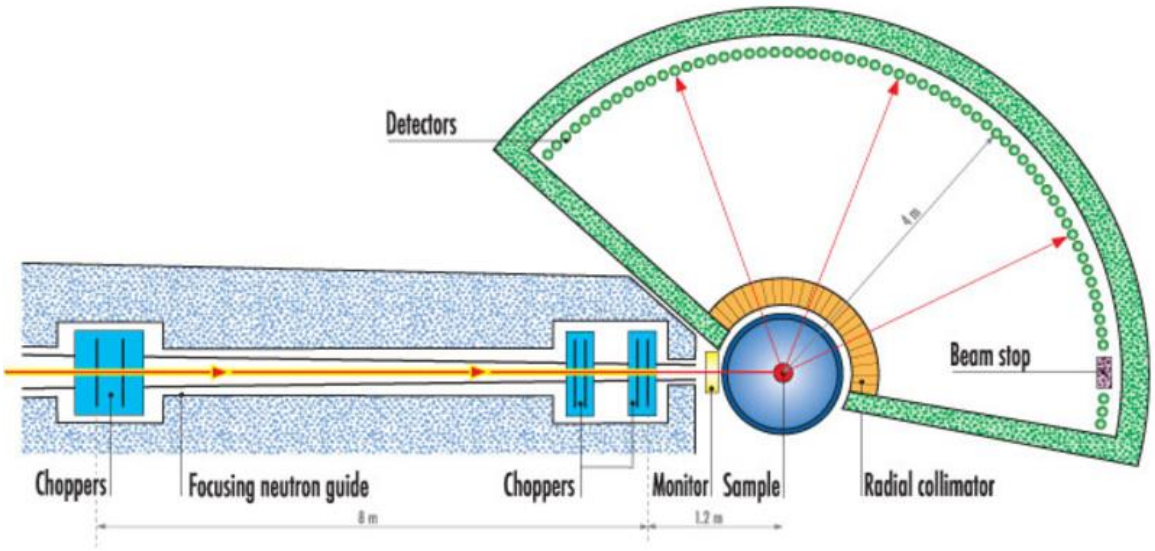

3-L IN5 schematic
(ILL.eu, 2018)

Instrument control and data collection is achieved through NOMAD[59]. This is a bespoke sequencing environment that gives point and click access to almost all monitoring and control systems for the instrument[60].

3.9 Data Collection, Reduction, and Fitting

3.9.1 Data Collection

All of the QENS measurements reported in this work were collected at steady state over considerable periods of time (ranging from an hour for some on IN5 to over twenty hours for the deuteride measurements on Osiris). Each of these measurement periods was split into shorter data collection 'runs'. This allows any periods containing bad data (due to temporary loss of temperature regulation, etc.) to be removed while maintaining the maximum possible detector count.

Diffraction measurements on Osiris have been measured as short 'snapshots' at a particular period in time. These measurements have typically been collected over a few seconds. As these were for monitoring purposes only, no attempt has been made to fully process them.

[59] Full details available at: https://www.ill.eu/instruments-support/instrument-control/software/nomad/
[60] Gas pressure control is achieved using external equipment managed via separate software.

3.9.2 MantidPlot

All of the neutron scattering data described in this work has been reduced and processed using MantidPlot[61] (Mantid, 2013). This is a suite of tools for working with neutron scattering data from a vast number of instruments at several facilities. Many of these tools can be accessed through point and click interfaces. All of them can be operated via Python scripts.

3.9.3 Data Reduction

Where appropriate, instrument specific functions have been used. However, the general process of importing and reducing QENS data is common to both instruments used in this work. After removing any bad runs[62], the following processes occur:

- Raw data are imported from each run
- Data are normalised to the beam monitor and a vanadium standard
- Any known bad detectors are removed
- Runs are merged into a single set of spectra (one spectrum per detector)
- Spectra are converted from time of flight (TOF) to $S(Q,\omega)$
- Detectors are merged (reducing the total number of spectra per set)
- Spectra are re-binned in energy (if required)
- Energy range of spectra is cropped

The parameters used in this work are discussed in the appropriate experimental chapters along with the specific considerations that led to them.

3.9.4 Quasilines

Quasilines is a Bayesian model selection algorithm specifically designed for analysing QENS data. A comprehensive description of the method employed has been published by Sivia D.S., Carlile C.J., Howells W.S., and König S. (1992). This section provides a brief overview of the method, the results derived from the algorithm, and a brief discussion on how this relates to real QENS data.

Quasilines assumes that any given set of data d is a composite of an elastic component with an amplitude A_0, a number (N) of Lorentzian components (indexed by j) with widths Γ_j and amplitudes A_j, a resolution function $r(\epsilon)$, a background $b(\epsilon)$, and stochastic noise $\sigma(\epsilon)$

[61] Full details available at: http://www.mantidproject.org/
[62] Corrupted data, loss of equilibrium conditions (temperature, pressure, …), etc.

(where ϵ is the energy transferred between the sample and the incident neutron). The relationship between these components is defined as:

$$d(\epsilon) = \left[A_0 \delta(\epsilon) + \sum_{j=1}^{N} A_j \frac{\Gamma_j}{\pi\left(\epsilon^2 + \Gamma_j^2\right)} \right] \otimes r(\epsilon) + b(\epsilon) + \sigma(\epsilon) \qquad (3\text{-}51)$$

where δ is the Dirac delta function and $\otimes$ denotes convolution.

The algorithm requires:

- A dataset consisting of a series of QENS spectra
- A resolution function (a QENS measurement of the system where no motion is present – often, a low temperature measurement where any motion is completely frozen out or below the instrumental resolution)
- Input from the user as to whether a background is present in the data (and what form it has)
- Input from the user as to whether an elastic component is present

The algorithm also allows the user to define the energy range that the fit is to be performed over (should the full range not be appropriate).

Once these details are provided, it attempts to fit a series of models (for $N = 1,2,3, \ldots$) based on equation (3-51) using a least squares method. This is a cyclical process where A_0, A_j, Γ_j, and the fit parameters of the background, are manipulated in an attempt to reduce the sum of the squares of the difference between each data point and the proposed model.

Even for $N = 1$, this is mathematically complex. Numerous sets of parameters may lead to functions that appear almost identical. It may also be possible for visibly different fits to give a similar 'quality' of fit to the data. The presence of noise in the data complicates this even further. In this sense, this is a classic "ill posed problem".

Quasilines attempts to overcome this complexity by assigning a parameter to each fitted component that describes how likely it is that it represents a real feature of the data. These are then combined with the 'quality' of the fit (determined by the least squares analysis). The algorithm attempts to minimise this value rather than simply the deviation of the model

from the fit (as is the case for standard least squares fitting). Any real dataset can usually be fitted more accurately with a larger number of components (as this may help to meet the deviations due to noise). Quasilines accounts for this by skewing the returned parameter in favour of low N.

Each returned dataset gives the calculated fit parameters along with the log of the inverse probability that has been calculated per model for each spectrum. Models that provide an accurate and likely fit will have an associated 'probability' that is close to zero.

This method is not perfect. It is often accurate in predicting whether 'one' or 'more' Lorentzian components are present in a dataset but the difference between fits with two, three, four, … Lorentzian components is usually minimal. This is not a flaw in the method, but rather, a feature of fitting such complex systems.

Further to this, where multiple Lorentzian components are present in a dataset, it can often be difficult to separate them through fitting. If they are not sufficiently different, it is very likely that a single a single component fitted by a composite of the widths and amplitudes may appear to fit the data.

It is important to be aware of these problems and to determine whether the fitted parameters represent physical features of the system or may have a more complex underlying root. These considerations are discussed alongside the appropriate theory, data, and analysis sections of this work.

4 Pd-H Vs. Pd-D Diffusion Rate as a Function of Temperature

4.1 Introduction

It has long been known that hydrogen isotopes show different, temperature dependent, rates of diffusion in palladium (see section 2.2.2). It has also been suggested that there should be an achievable temperature where the rates of diffusion of any two of these isotopes are equal (Völkl, Wollenweber, Klatt, & Alefeld, 1971) (Sicking, 1984).

In this chapter, a series of measurements made on the OSIRIS spectrometer (see section 3.8.3.1) at ISIS (see section 3.8.3) to determine the temperature at which this 'crossover point' should occur for hydrogen and deuterium are discussed.

4.1.1 Why OSIRIS

As discussed in section 3.8.3.1 (page 63), the OSIRIS instrument has two detector banks, for collecting diffraction data and QENS spectra respectively. As these measurements focus on the high concentration beta-phase, this instrument allows diffraction measurements to be taken during the loading process to determine when any regions of the alpha-phase have been eliminated and the pure beta-phase has been achieved (this is discussed further in section 4.2.5 Sample Preparation).

It is also possible to rapidly change the d-spacing range measured by the diffraction bank as well as the energy window captured by the spectrometer. This allowed the potential for taking preliminary measurements outside the predicted windows should the need arise.

4.2 Experimental Setup

4.2.1 Outline

Sets of QENS measurements were made for a series of temperatures with both hydrogen and deuterium in spherical palladium powder (section 2.4.1) at concentrations sufficient to be in the pure beta-phase; this was confirmed using neutron diffraction.

These measurements were collected in two separate allocations of instrument time. During the first, the hydride measurements described in this chapter were collected along with preliminary measurements on the deuteride sample. The deuteride measurements in this chapter were conducted under an extension proposal at a later date. No changes to the

instrument (e.g. maintenance or upgrades) occurred in the interim between the two data collection periods.

As the total scattering cross sections of the two isotopes are vastly different (see section 0) there are differences in the method for each set. These differences are detailed in the following sections.

4.2.2 Sample Cans

Standard sample cans at ISIS for experiments involving hydrogen are made from aluminium. Aluminium has a lattice constant of 4.0495 Å. This is close enough to the lattice constant of palladium hydride (4.025 Å) that the Bragg peaks of the two materials would be indistinguishable in neutron diffraction spectra at the resolution of the diffraction bank on the instrument. For this reason, two new cans were designed and commissioned in collaboration with the engineering team at the facility[63]. As these cans were designed for this experiment, it was possible to specify the depth of the sample in each case. Sample depths of $0.5\ mm$ for the hydride sample and $5\ mm$ for the deuteride sample were calculated to give around 90% transmission with a H(/D)/Pd ratio of around 0.5.

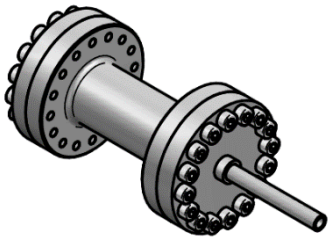

4-A OSIRIS sample can design

Both cans have an annular design (with annular gaps measuring half the appropriate calculated sample depth) with a hollow core to reduce the amount of steel in the path of the beam. They are made from 316 “stainless” steel[64] and sealed with pure gold gaskets (held in place with 16 * 316 steel screws, top and bottom). The cans have a central steel pipe (figure 4-A) in the lid to act as a shared inlet / exhaust when mounted to an appropriate ISIS ‘centre stick’. The cans were certified as safe for 200 cycles at pressures up to 110bar and temperatures up to 227°C (500K).

4.2.3 Sample Environment

OSIRIS has a bespoke Closed Circuit Refrigeration (CCR) unit (see 3.8.3.1 OSIRIS). Control of this device is achieved by passing “set point” and “PID” settings via the instrument’s

[63] Engineering designs for these sample cans can be found in Appendix A on page 28
[64] 316 steel is a chrome, nickel, molybdenum steel alloy. More information about the 316 specification can be found in appendix A.

OpenGenie interface. The CCR has built in temperature sensors that give readings in real time to the management software for the instrument.

Four resistive (ohmic) heaters were mounted to the can with copper plates, (two top and two bottom) to allow direct heating of the sample can[65]. Two platinum resistance thermometers were mounted to the can (one top, one bottom) to allow direct monitoring of the sample temperature. All six of these devices were connected to the management system for the instrument so that control and monitoring could be achieved both through the LabView interface and OpenGenie.

As the CCR surrounds the sample, it will contribute to the background seen in any measurement made on the instrument, although it has been designed to minimise this. The heaters and sensors mounted to the sample can are outside the beam window and, as such, do not contribute to any measurements.

Gas loading and evacuation was managed via a simple hand operated manifold connecting the relevant gas supply, a vacuum line (with both membrane and turbomolecular pumps), an exhaust (leading to the facility extraction system) and pressure monitoring (with separate high and low pressure gauges), to the sample. A schematic of this system is shown in figure 4-B with the two pressure gauges labelled as P_1 and P_2.

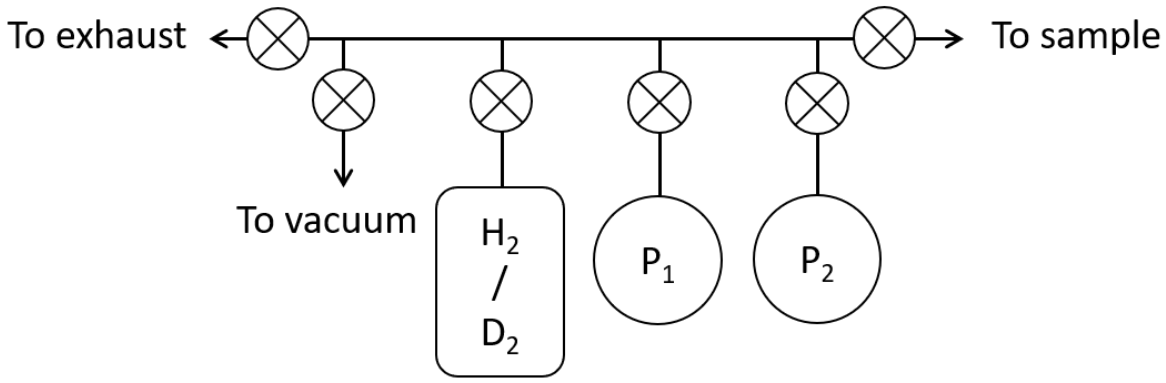

4-B Schematic of Osiris gas loading system

The manifold was connected to the sample by a long steel tube. As such, it is difficult to know that the pressure measured at that gauge head is identical to the pressure in the sample can. However, given the nature of the instrument and the equipment available at the

[65] This provides a faster response time (due to a shorter feedback system) than heating via an external furnace.

facility, it would be extremely difficult to take measurements closer to the sample position and has been assumed to be a reasonable estimate. The actual configuration of this equipment and its position relative to the sample can be seen in figure 4-C.

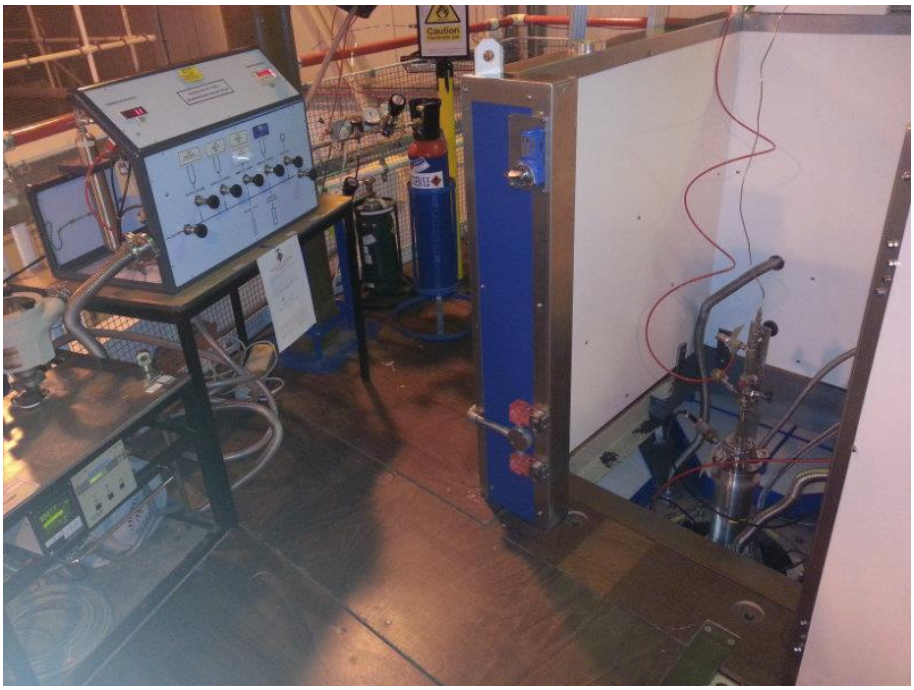

4-C Osiris gas loading equipment

4.2.4 Instrument Setup

The pyrolytic graphite analyser was set up in the 002 plane configuration to give the lowest energy transfer resolution ($25.4\mu eV$) possible on the instrument. This configuration gives a Q range of 0.18Å^{-1} to 1.8Å^{-1} at an analyser energy of $1.84meV$ (STFC, 2017b). The measurements described in this chapter were all collected with an energy transfer window of around $-1 < \hbar\omega < 2.5\ meV$.

4.2.5 Sample Preparation

Both sample cans were loaded by constructing the can without the top section (lid) and then packing the powder as tightly as possible into the annular gap using a combination of tapping and applying mechanical pressure. A small amount of glass wool was placed in the top of each can before the top section was fitted to stop any powder escaping. As this wool was placed at the very top of the can it was not in the beam window when the sample was mounted in the instrument. Figure 4-D shows photographs of the steps in this process.

Parts of can prior to loading

Both cans loaded with Pd powder

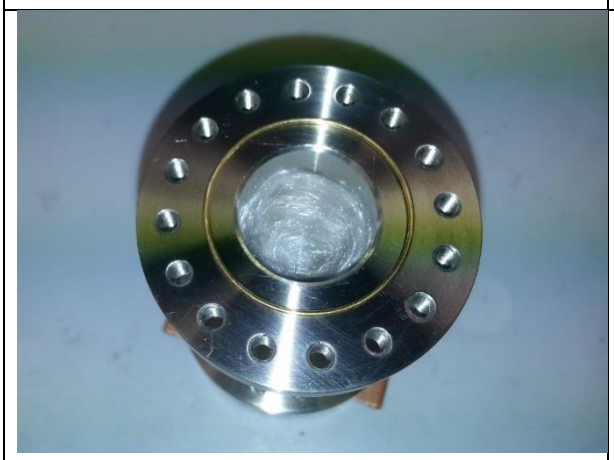

Loaded can with glass wool and gasket

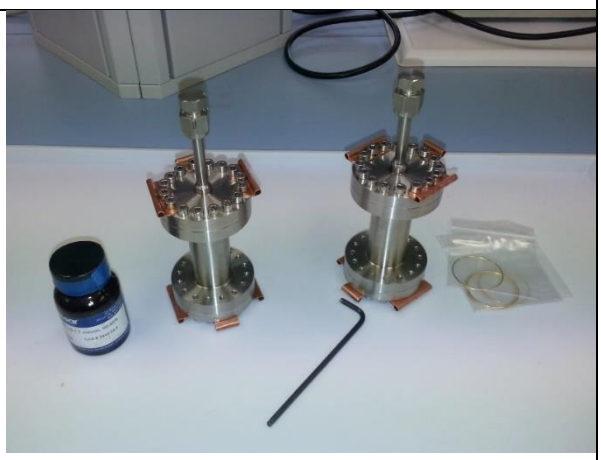

Both cans loaded and sealed with mounts for heaters and sensors

4-D Sample can construction and loading

The cans were weighed before and after loading. The mass of the sample in each was recorded as:

Annular gap (mm)	**Mass of palladium (g)**	**For use with gas species**
0.25	3.798	Hydrogen
2.5	22.101	Deuterium

4-a Mass of palladium in sample cans

Once each can had been sealed, it was attached to an appropriate gas loading centre stick and pressure / leak tested by facility engineering staff using helium. Figure 4-E shows one of the prepared sample cans mounted to the centre stick prior to be placed in the instrument.

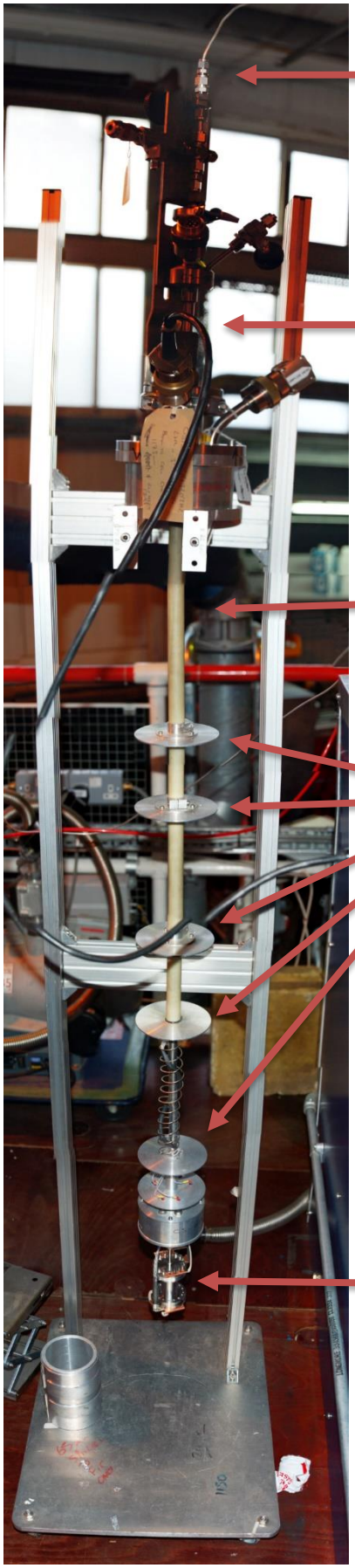

4-E Sample mounted to centre stick

4.3 Measurements

4.3.1 Pd-H

The following measurements were collected for the hydride sample:

Temperature (°C)	Temperature (K)	Pressure (Bar)	H/Pd[66]	Total Beam Current (μA)
-173.15	100	0.374		414.4604
0	273.15	0.429		713.5697
160	433.15	4	0.60591	400.0155
180	453.15	4.2	0.57599	425.6017
195	468.15	8.9	0.6105	413.6519
210	483.15	9.7	0.59256	400.042
225	498.15	10.5	0.58545	400.03

4-b Osiris Pd-H measurements

Equilibrium concentrations have not been determined for the 100 and $273\ K$ measurements. These values are not needed for the analysis in this chapter.

As mentioned in section 4.1.1, diffraction measurements were taken at each temperature, prior to QENS measurements being taken, to confirm that the sample was in the pure beta-phase and not the two phase region (as described in section 3.6.1). The plot below shows these for the Pd-H measurements.

[66] Calculated from gravimetric sorption measurements. See section 2.5.1 for general method and appendix for details of the specific measurements.

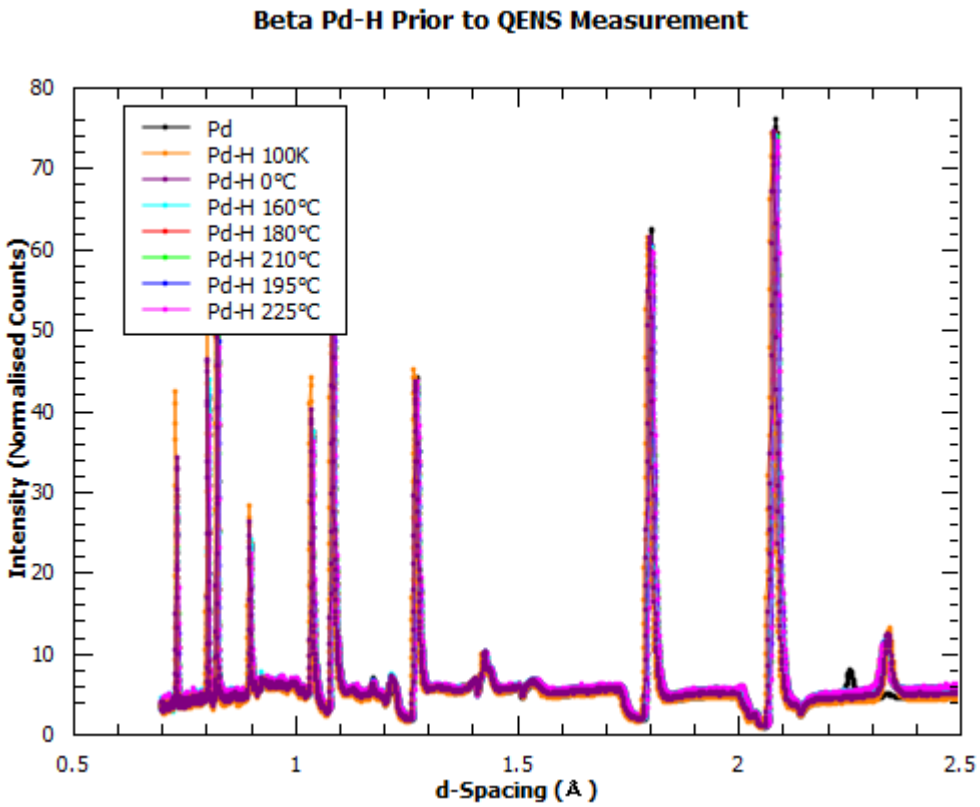

4-F Full range Pd and beta-Pd-H diffraction spectra

Much of figure 4-F is very similar across the visible range for all the Pd-H measurements. The large peaks visible throughout the spectra are from the steel can. In the bottom right hand corner, the $(1,1,1)$ Bragg peak can be seen for both the Pd and Pd-H for each temperature. Figure 4-G shows this region in more detail. In this second plot, it is clear that each Pd-H spectrum has a single peak and is therefore not in the mixed phase region.

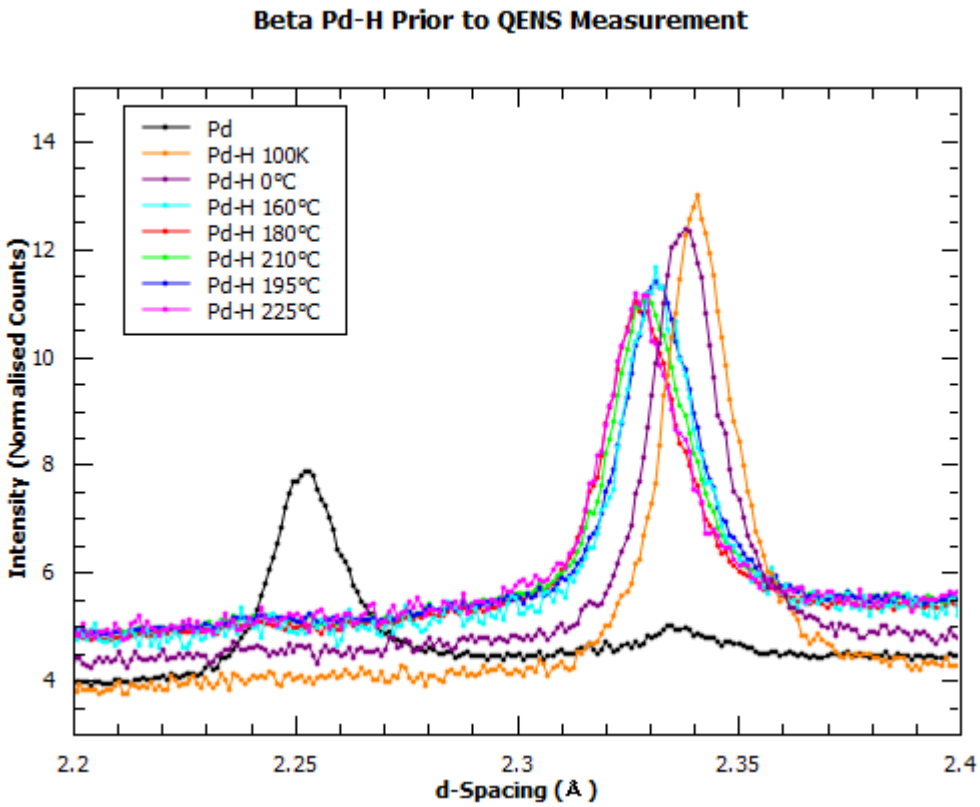

4-G Pd and beta-PdH diffraction spectra, 111 peak

The small 'bump' in the pure palladium spectrum in the beta phase region is the result of not fully desorbing the hydrogen after cleaning cycles were performed. This was a timesaving measure and has no effect on any of the measurements or calculations in this work.

4.3.2 Pd-D

The following measurements were collected for the deuteride sample:

Temperature (°C)	(K)	Pressure (Bar)	D/Pd	Total Beam Current (µA)
-173.15	100	14.2		655.0816
160	433.15	33.6	0.58	1200.0985
180	453.15	34.5	0.57	1299.1882
195	468.15	35	0.555	1200.1268
210	483.15	38	0.537	1231.8888
225	498.15	42.5	0.52	1344.9088

4-c Osiris Pd-D measurements

Again, equilibrium concentration has not been determined for the $100\ K$ measurement. This value is not needed for the analysis in this chapter.

Figure 4-H shows the region of the $(1,1,1)$ peak in the diffraction spectra captured prior to loading, and in the pure beta phase at each temperature measured. Again, it can be seen that no residual alpha phase is present.

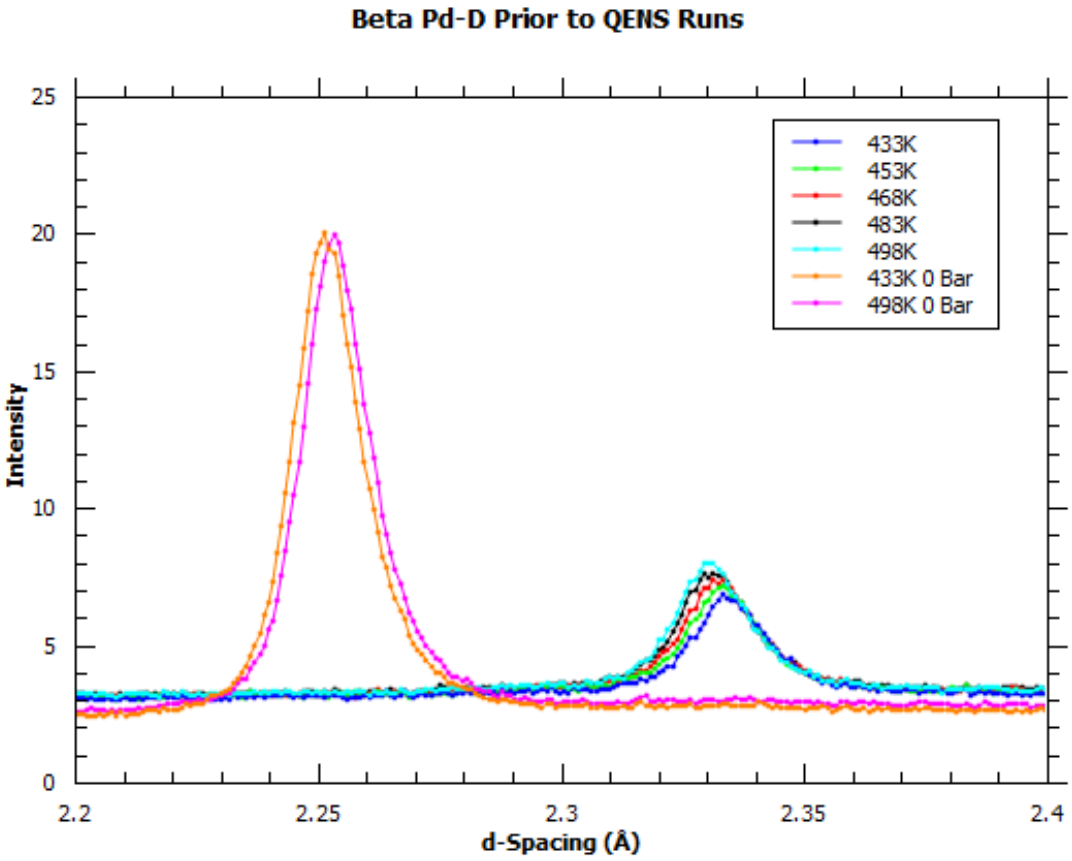

4-H Pd and beta Pd-D diffraction spectra, 111 peak

When compared with figure 4-G (the similar region for the Pd-H sample) the difference in the amount of palladium present in the beam can be seen from the relative intensities of the pure palladium peaks. The relative intensities of the loaded (beta phase) peaks are not identical but it is apparent that the sample depths chosen have resulted in broadly comparable scattering from the two samples.

4.4 Results

When looking at these datasets, it is immediately apparent that the measured data cannot be well represented using a model that assumes a single Lorentzian component. The

following sections will outline the evidence for this, and then demonstrate that the narrow component of a multiple Lorentzian model can be shown to fit the existing models for octahedral – octahedral (O-O) long range diffusion. In this chapter, chemical diffusion will be assumed to be dependent on this component. Arguments for this will be presented the following analysis. Further experimental work has been conducted to try to shed light on other motions that may be present in the system. This work is discussed in chapter 5.

4.4.1 Data Reduction

The set of measurements at each temperature were imported into MantidPlot[67]. Multiple runs with the same compositions have been merged into single sets of spectra, with the detectors grouped appropriately[68] and normalised to a vanadium 'standard' measured on the same instrument. The full recorded energy transfer range has been imported.

No further measurements have been subtracted from each dataset. It has been established that the calculated Lorentzian widths are not substantially affected by applying such corrections. As this is the parameter of interest in this work, removal of the elastic components was deemed unnecessary.

Different reduction parameters were necessary for the hydrogen and deuterium samples. These are discussed below.

4.4.1.1 Pd-H

The datasets for the hydrogen sample have been reduced to 7 grouped 'detectors'. Some points at low Q have been removed as their calculated broadening falls below the instrument resolution (see section 3.8.3.1 OSIRIS).

4.4.1.2 Pd-D

Several obvious features that reduce the Lorentzian broadening at specific Q vectors can be seen in each dataset. This is thought to be due to short range ordering (SRO) of the deuterium in the octahedral sites (see section 3.6.1). Analysis of this can be found in section 4.4.2.3 and further discussion in section 4.5.2. These datasets have been reduced to 21 groups so that the affected region can be masked leaving as many un(/less)reduced points as possible to allow a fit to be performed to the remaining widths.

[67] For more information on MantidPlot, see 3.9.2 MantidPlot
[68] For more information about detector grouping on Osiris, see section 3.8.3.1 OSIRIS

4.4.2 Analysis

4.4.2.1 Fitting Parameters

Each spectrum in this experiment has been fitted across an energy transfer range of $-0.5 < \hbar\omega < 1.5\ meV$. A linear sloping background has been assumed in each case (fitted with Quasilines which does not provide the fitted parameters of this component). As the datasets contain an elastic component, a parameter has also been fitted to account for this.

For each sample, a low temperature measurement[69], loaded with the relevant hydrogen isotope at high temperature and then cooled to $100K$, has been used as a 'resolution function'.

4.4.2.2 Evidence for Multiple Components

Each of the reduced datasets was analysed using the Bayesian 'model selection' tool Quasilines in MantidPlot (see section 3.9.2). As described in section 3.9.4, this tool attempts to fit a number of parameters to each spectrum and then assigns a 'posterior probability' (a combination of agreement with the measured data and the prior probability) to each fit. Plots showing the log of the calculated posterior probability for each model to the observed data for each dataset can be found below. Each plot shows the log of the calculated probabilities for three models containing 1, 2 or 3 Lorentzian components. Better fitting models result in the plotted parameter being closer to zero.

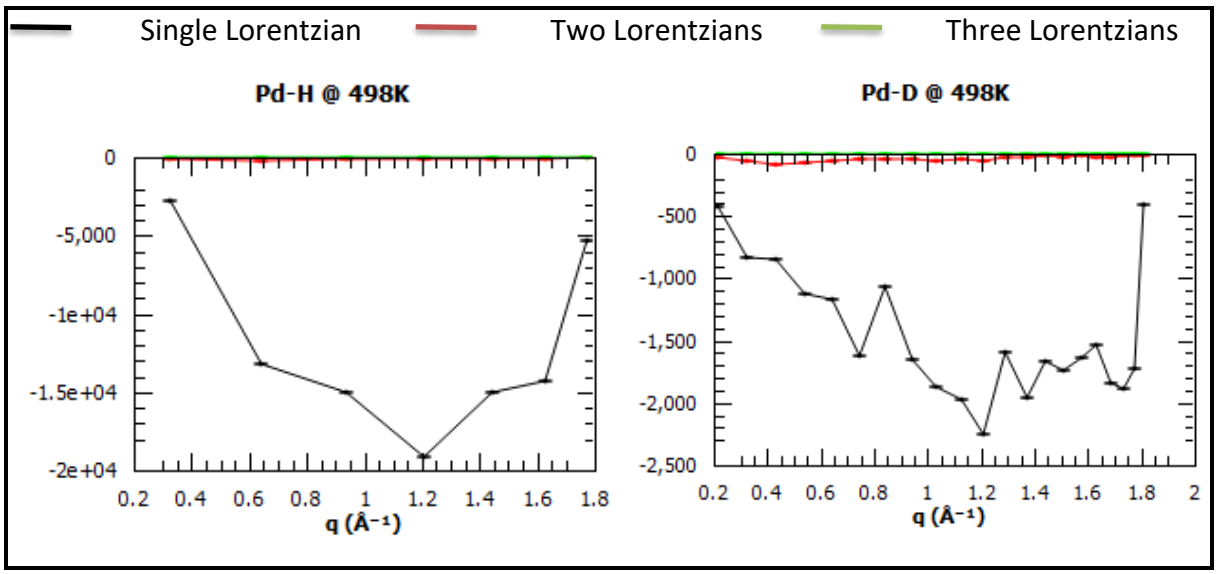

[69] Details of these measurements can be found in tables 4-b and 4-c

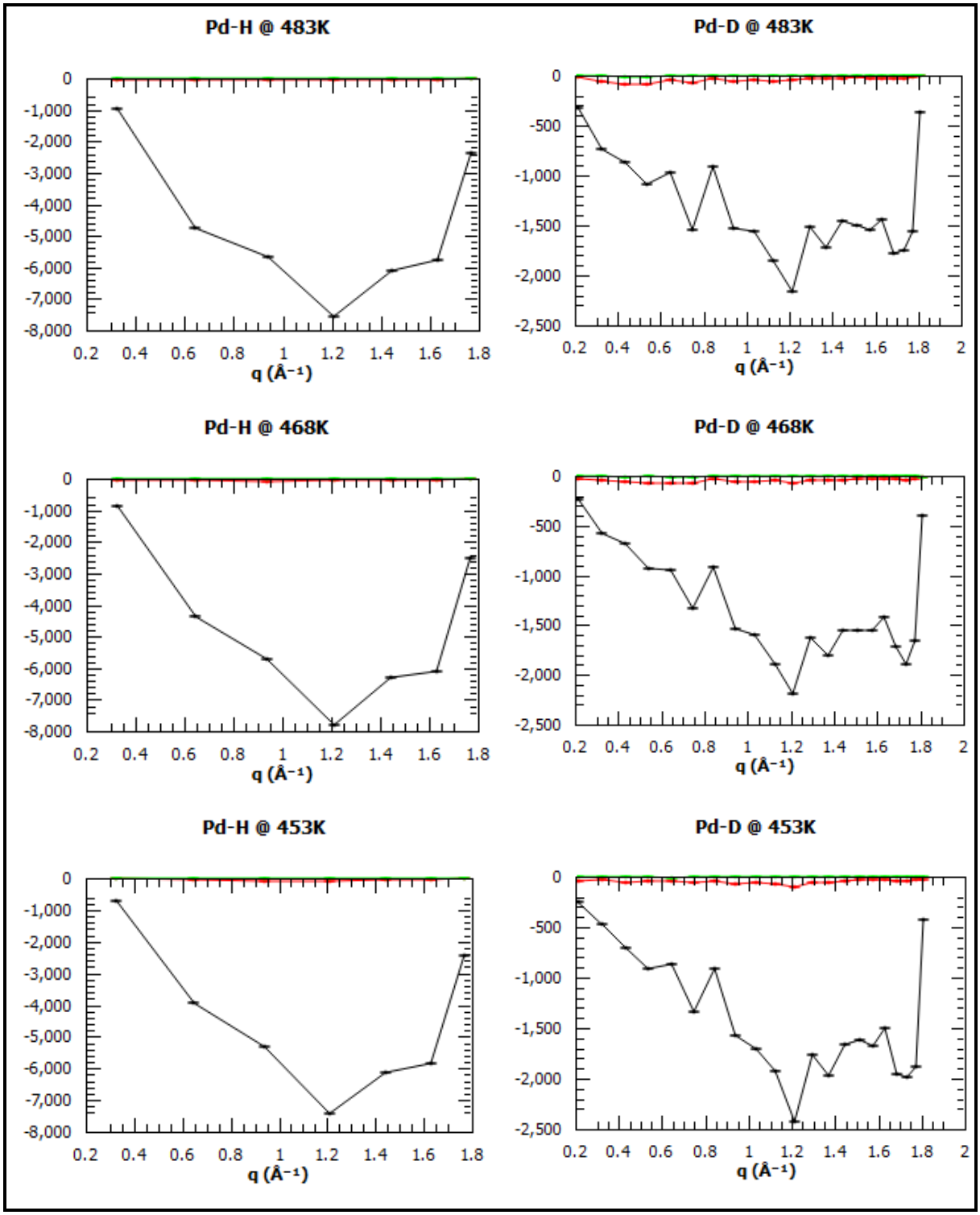
Pd-H @ 483K
Pd-D @ 483K
Pd-H @ 468K
Pd-D @ 468K
Pd-H @ 453K
Pd-D @ 453K
q (Å⁻¹)

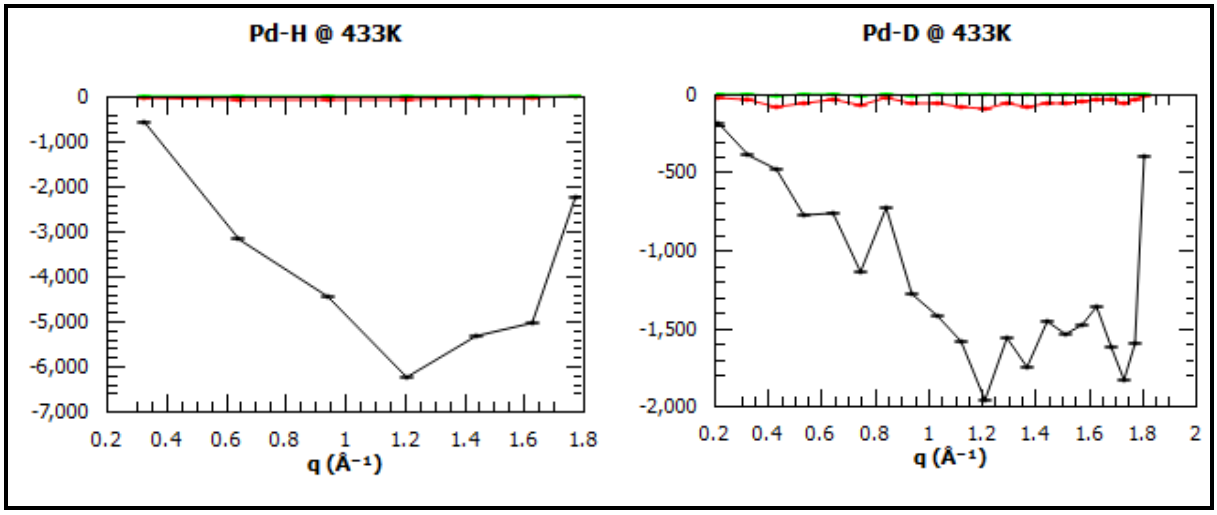

4-I Log of posterior probability plots for Osiris data

As discussed in section 3.9.4, defining the number of Lorentzian components contained in any dataset from the measured data alone, is an extremely difficult task. What can be clearly seen though, is that multiple Lorentzian components provide a superior fit to every dataset over models that assume a single Lorentzian component. There is several orders of magnitude difference in the log of calculated posterior probability between the single Lorentzian and multiple Lorentzian models.

The discrepancy that the extra Lorentzian component(s) accounts for is clearly visible in the energy transfer spectrum plot for each point. The plots below show the calculated fits for an arbitrarily chosen data point. Figure 4-J (page 86) shows the full recorded spectrum for the 6th group of 7 ($Q = 1.63\text{Å}^{-1}$) of the dataset measured for the hydride sample at 498K with two fitted curves (based on models containing 1 and 2 Lorentzian components). In the immediate region around the elastic peak, there is very good agreement between both models and the measured data. However, in the quasielastic region, the difference between the models becomes apparent. Figure 4-K is of the same data but rescaled to better show this region. In this plot, the deviation of the two models at an energy transfer of around $0.3\ meV$ is very clear. It is also clear that the fitted line for the model containing two Lorentzian components is in much closer agreement with the observed data than the single Lorentzian fit.

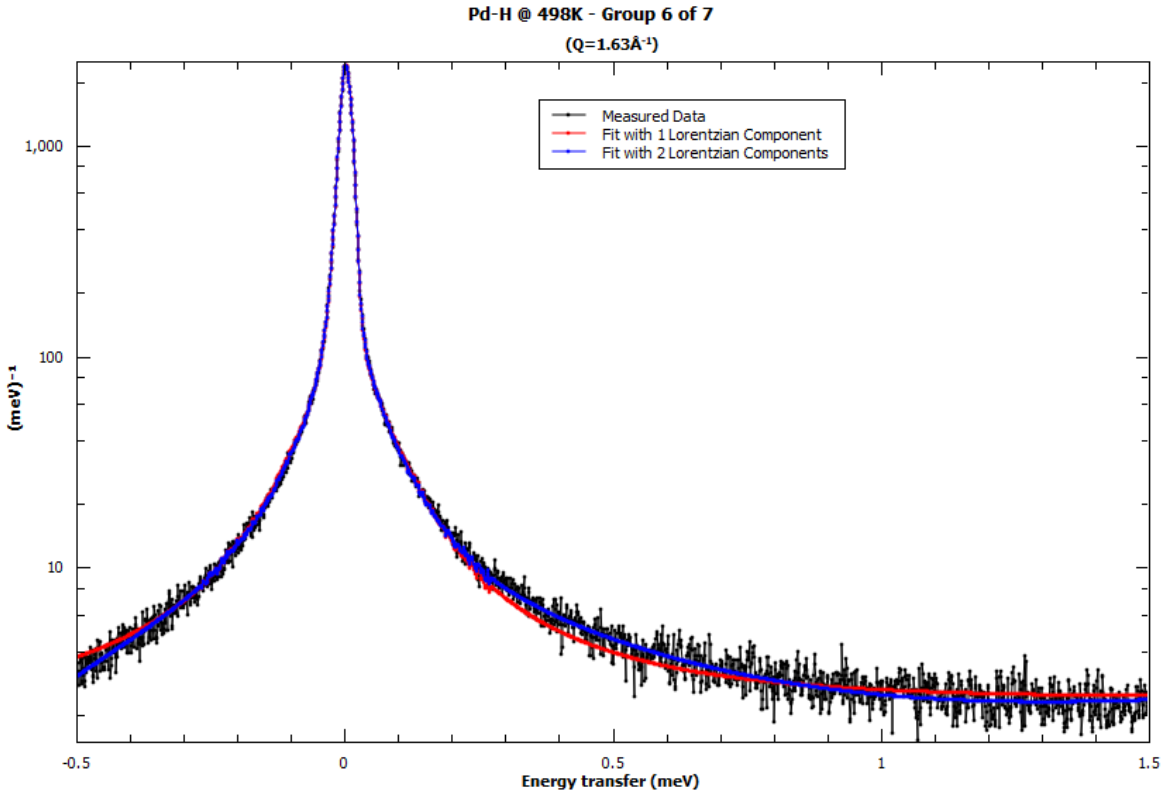

4-J Pd-H @ 498K - Fit Comparison (full)

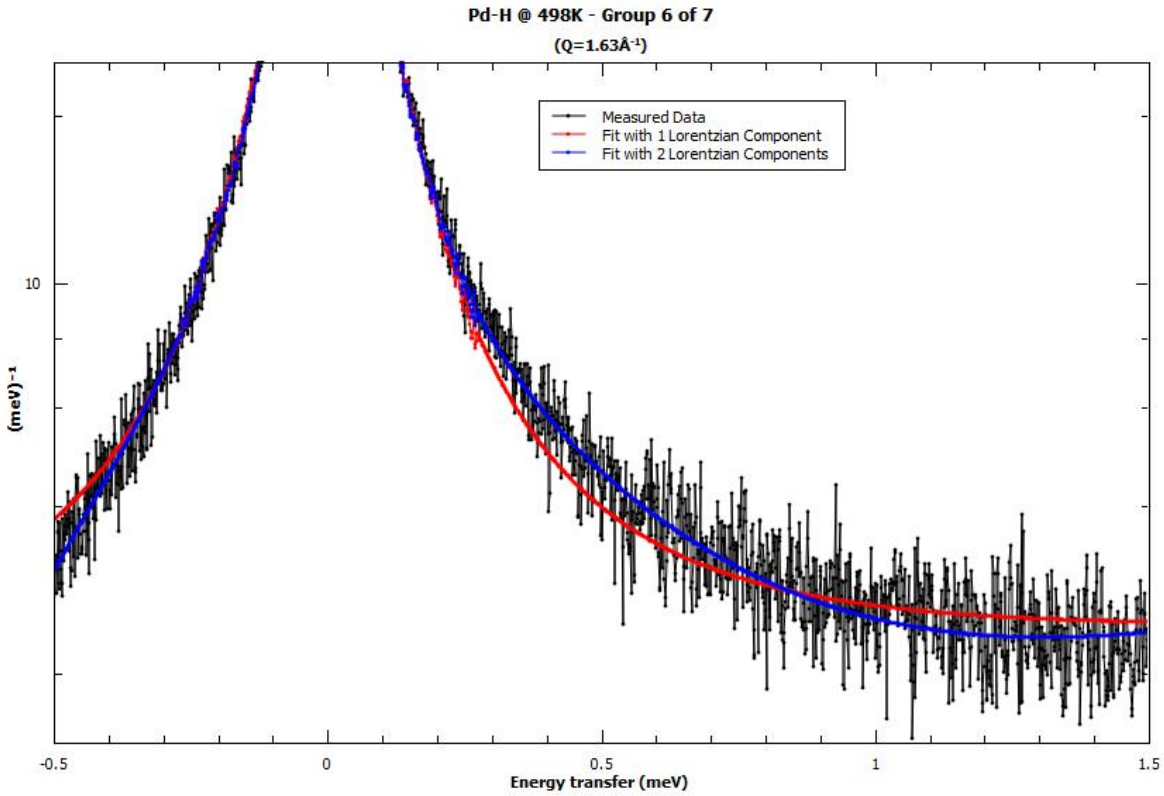

4-K Pd-H @ 498K - Fit Comparison (1 - 25 meV^{-1})

The deviation from the broadening predicted by a single component model is very similar in the datasets for the Pd-D sample:

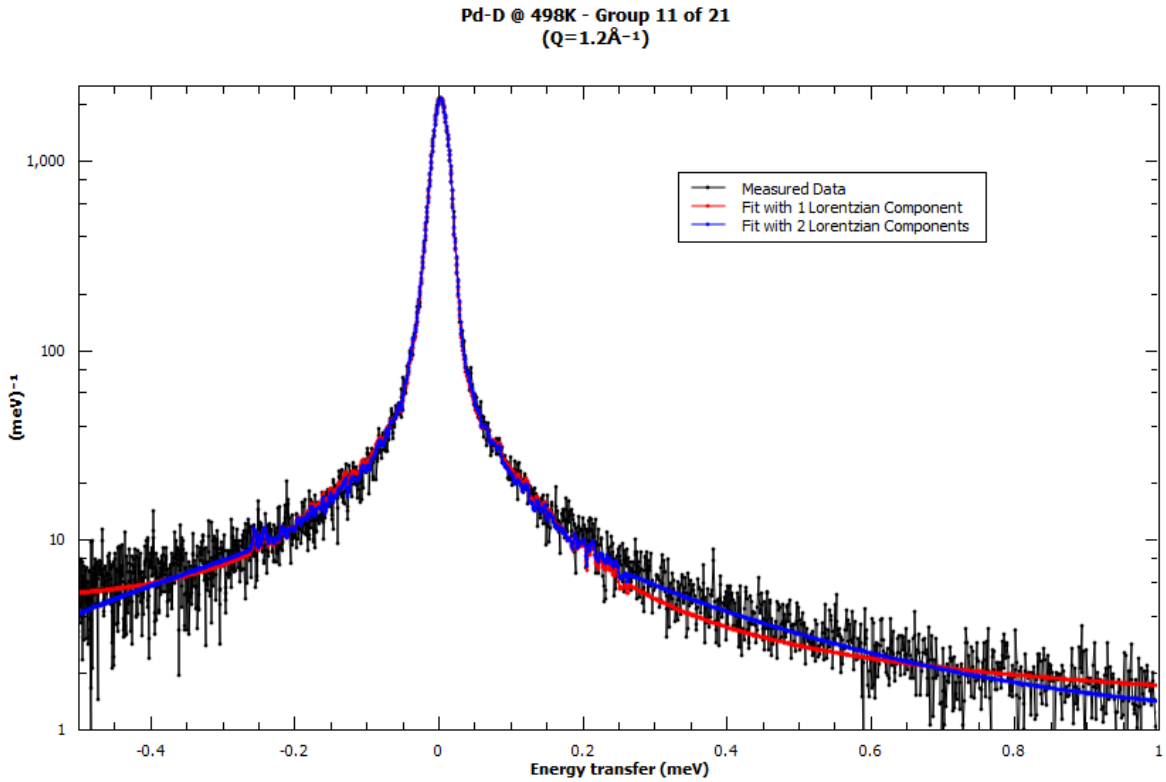

4-L Pd-D @ 498K - Fit Comparison (full)

The apparent agreement with a model requiring multiple Lorentzian components (and therefore multiple distinct motions within the sample) is reinforced when diffusion models are applied to the resulting data. This further evidence will be discussed as part of that analysis below.

4.4.2.3 Quasielatic Broadening in the Narrow Lorentzian Component

It is well established that octahedral-octahedral (O-O) site jumps occur in the palladium hydride system. Random jumps on a fixed lattice will produce a Lorentzian component in QENS spectra with Half Width Half Maximums (HWHMs) that follow a Chudley-Elliott model (see section 3.6.3). This model allows calculation of a jump length (l) and mean residence time (τ) for the diffusion seen in a set of spectra at a single temperature. The following section details Chudley-Elliott fits to the narrow Lorentzian components fitted to each dataset (each temperature) for both the hydride and deuteride samples discussed in this chapter, and the resulting calculated parameters.

Each dataset has been fitted to a model of the form:

$$\Gamma(Q) = A\left(1 - \frac{\sin(Ql)}{Ql}\right) \tag{4-1}$$

Where:

Γ	$=$	$HWHM$	(meV)
A	$=$	Proportionality constant ($\propto 1/\tau$)	(meV)
Q	$=$	$\lvert\vec{Q}\rvert$	(Å^{-1})
l	$=$	Jump length	(Å)

Fits for each dataset were calculated using a 'least squares' method in OriginPro (OriginLab, 2017) with A and l allowed to vary.

The fitted curves plotted over the appropriate data for the Pd-H measurements are reproduced below[70]:

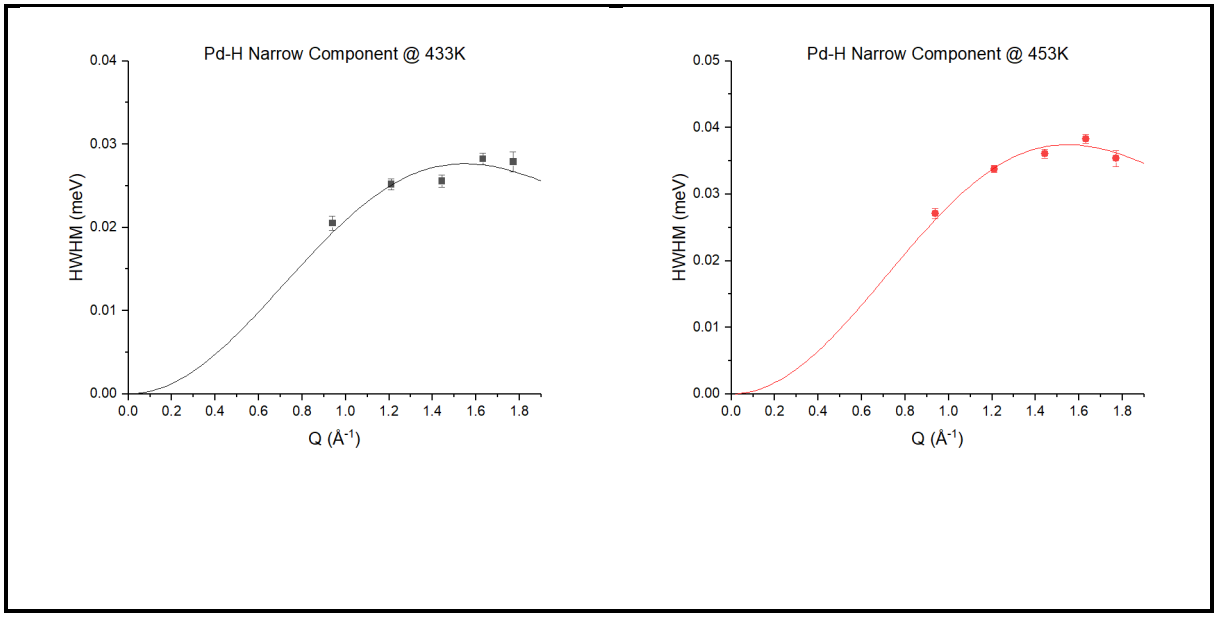

[70] Most points with a broadening of less than the instrument resolution of $25.4\ \mu eV$ have been removed. An exception to this has been made in the lowest temperature ($433K$) set where the remaining points are very close to the resolution line.

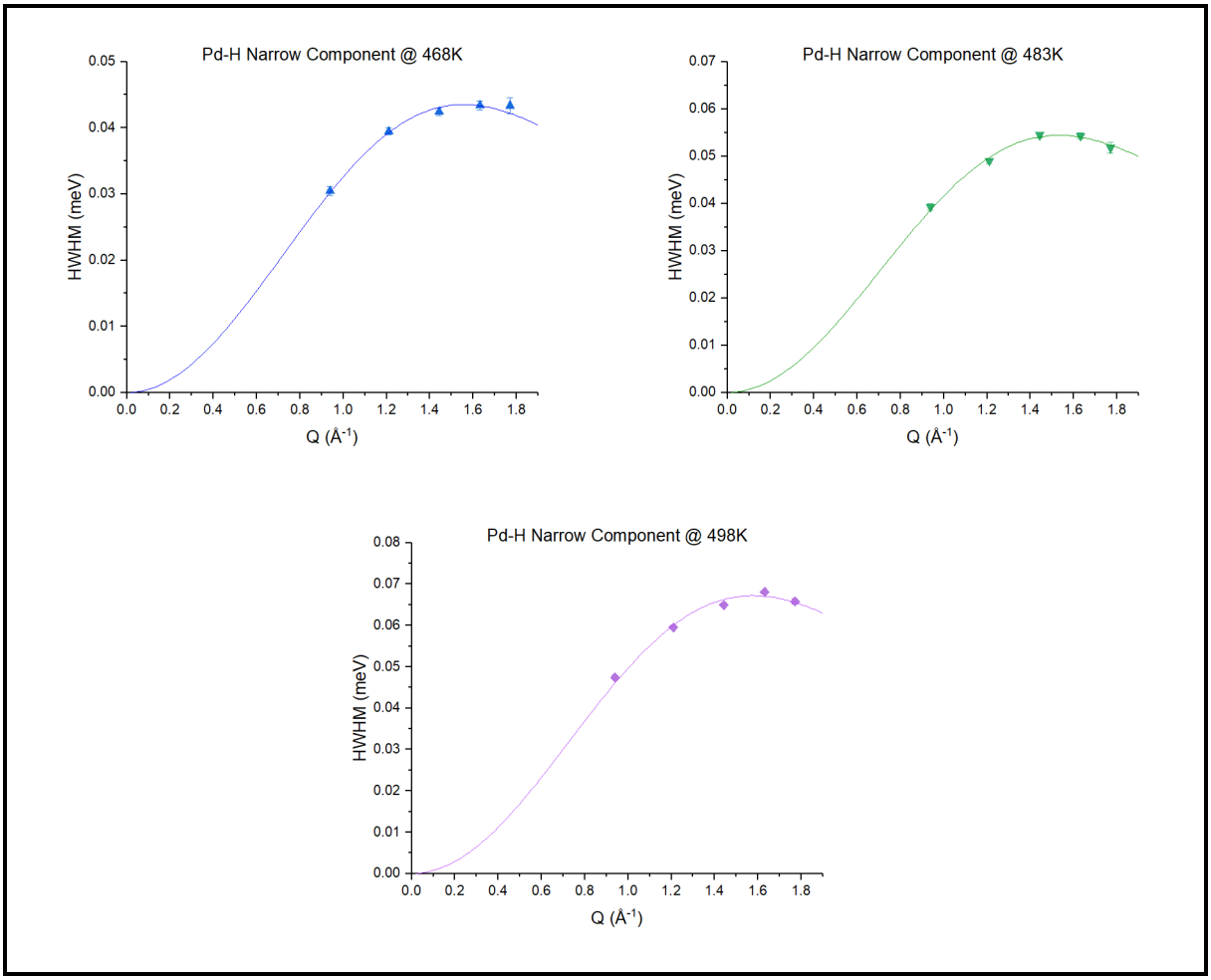

4-M Individual Pd-H Chudley-Elliott fits (Osiris)

These fitted curves are combined in a single plot, below:

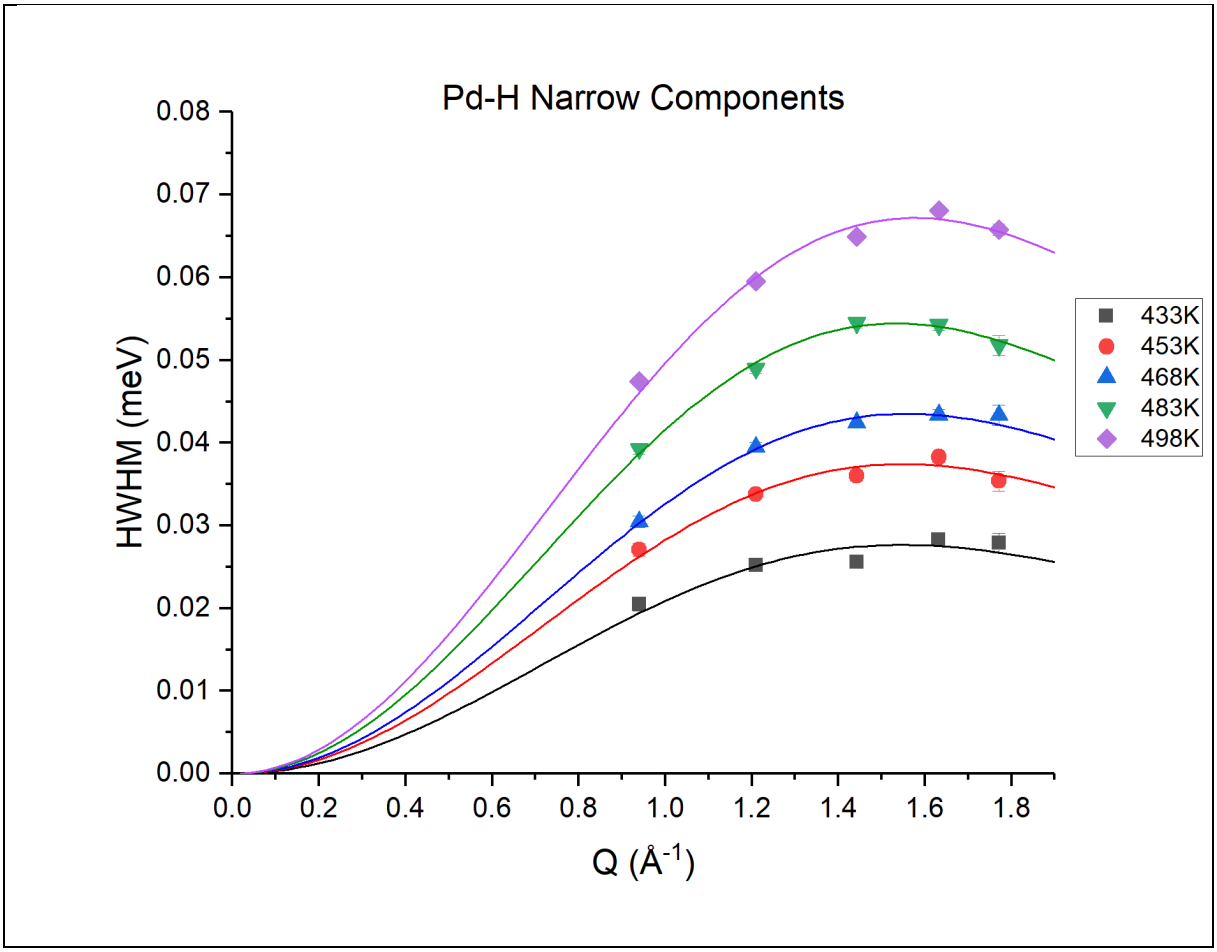

4-N All Pd-H Chudley-Elliott fits (Osiris)

Good agreement with the model can been seen in every dataset. The fitted parameters and their absolute errors (labelled Δ) for each of the curves above can be found in the table below:

Temperature (K)	A (meV)	ΔA (meV)	l (Å)	Δl (Å)
433	0.02279	7.41718E-4	2.79822	0.18091
453	0.03076	4.90377E-4	2.90294	0.07935
468	0.03575	2.83894E-4	2.88601	0.03649
483	0.04473	3.34784E-4	2.93368	0.03549
498	0.05509	8.54621E-4	2.89576	0.06698

4-d Chudley-Elliott fit parameters for Pd-H (Osiris)

The calculated jump lengths for this dataset compare well to the octahedral - octahedral jump length in β-Pd-H. These lengths are plotted in figure 4-O along with the expected O-O distance at both STP and 500K[71]. The plot shows that, while all but the highest temperature measurement appear to be slightly longer than the expected O-O jump, the predicted jump length falls within the error margin of 4 out of 5 points.

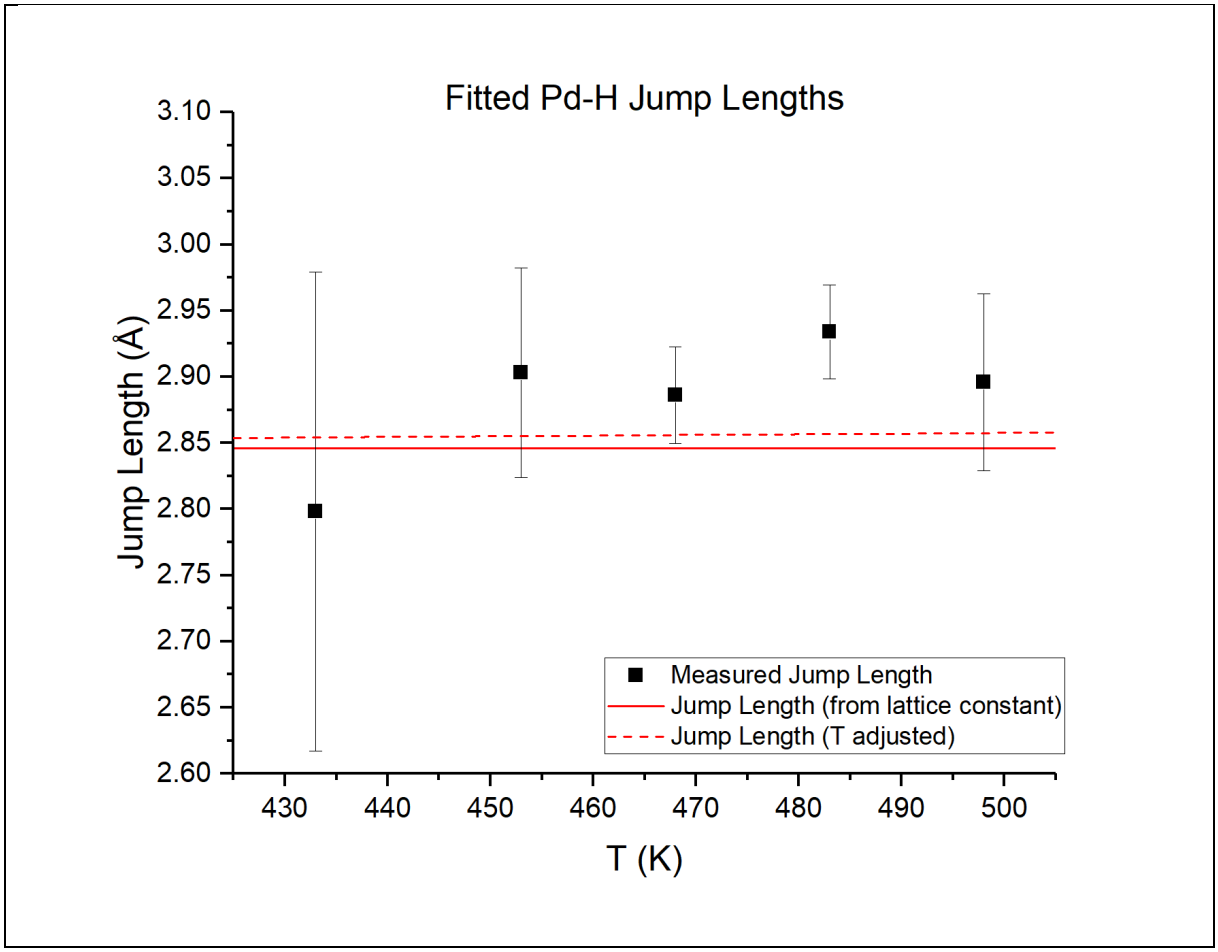

4-O Fitted Pd-H Chudley-Elliott jump lengths (Osiris)
(For detail about the predicted jump lengths, see footnote 71)

In the case of hydride measurements, it is reasonable to consider all the scattering from the hydrogen as incoherent[72]. As such, the HWHM of the measured Lorentzian broadening is reduced[73] by a factor or $(1 - c)$, where c is the ratio of filled to 'total available' octahedral

[71] The predicted jump length at high temperature is calculated from dilatometry measurements on Pd-$H_{0.7}$ (Abbenseth & Wipf, 1980), for a temperature of 500K. Lattice parameter is known to vary with both temperature and hydrogen concentration (see section 2.2.2 Isotope Dependence for more details on this phenomenon). As such, the predicted jump lengths on this plot are intended to provide a 'guide region' for O-O jumps in this system, only.

[72] The actual balance is roughly 97.5% incoherent and 2.5% coherent.

[73] see section 3.6.3.1

sites (equivalent to the atomic ratio of hydrogen to palladium in the sample). As the hydrogen concentration is unique to each measurement (table 4-b), specific corrections have been applied to each data point.

Once appropriately corrected for hydrogen concentration, the fitted proportionality constants for this Lorentzian component display Arrhenius behaviour (see section 2.3.2). This is shown in figure 4-P where it is clear that a straight line can be convincingly fitted through the corrected points.

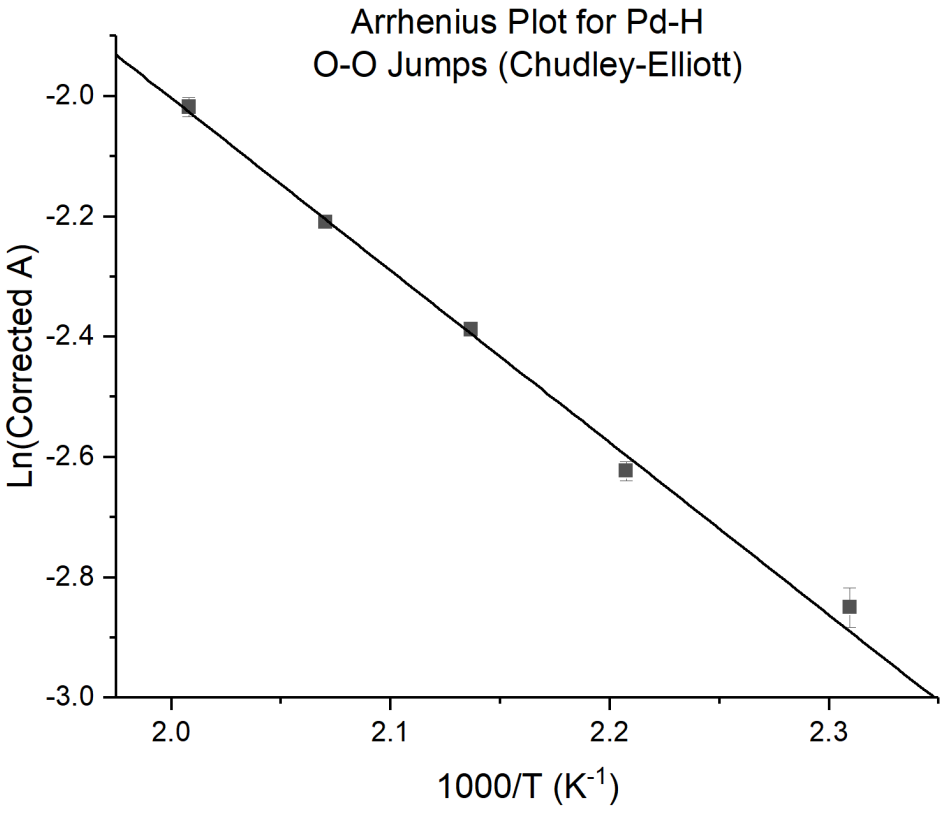

4-P Osiris Pd-H Arrhenius plot

This plot yields an activation energy[74] of $247 \pm 9\ meV$. This agrees well with previously published values ranging from 230 to $250\ meV$, measured and / or calculated using various methods[75].

[74] Method detailed in section 2.3.2

[75] Reported in numerous pieces of work including reviews by Fukai (2005), T B Flanagan and Oates (1991), and Kofu et al. (2016)

The theoretical 'jump attempt frequency at infinite temperature' (the pre-exponential factor in the Arrhenius equation) is calculated to be $(1.0 \pm 0.2) \times 10^{13}\ s^{-1}$. It is hard to directly compare this value to existing work as it is concentration dependent. It is also dependent on a projection from a small cluster of points to $1/T \to 0$. As such, when only a few temperatures are available to generate the fit, small errors in a single measurement can become vastly magnified. However, it is worth noting that this value is in perfect agreement with that reported by Kofu et al. (2016) which also attempted to isolate this component in QENS measurements on similar material at similar concentrations. (Kofu et al. also give an activation energy of $238 \pm 13\ meV$ for this component which agrees very well with this work)

The analysis for the related component in the palladium deuteride sample is slightly more complicated. Firstly, there are signals of comparable magnitude from both coherent and incoherent scattering. As such, a more complex concentration correction needs to be applied[76]. Secondly, there are visible reductions at specific Q vectors that appear to correspond to Short Range Ordering (SRO) of the deuterium within the palladium lattice. For the analysis in this section, regions in Q that are particularly affected by this second phenomenon have been removed[77]. To maximise the number of points available for fitting, these datasets have been merged to produce 21 points with each covering one third of the Q range of the points in the hydride datasets. Similar to the previous analysis, points calculated to be below the instrument resolution have also been removed from the subsequent fit.

Figure 4-Q shows an example of points that could be included or excluded from the Chudley-Elliott fitting process.

[76] Further details and derivation can be found in section 3.6.3.2
[77] Further discussion about this can be found in section 4.5.2

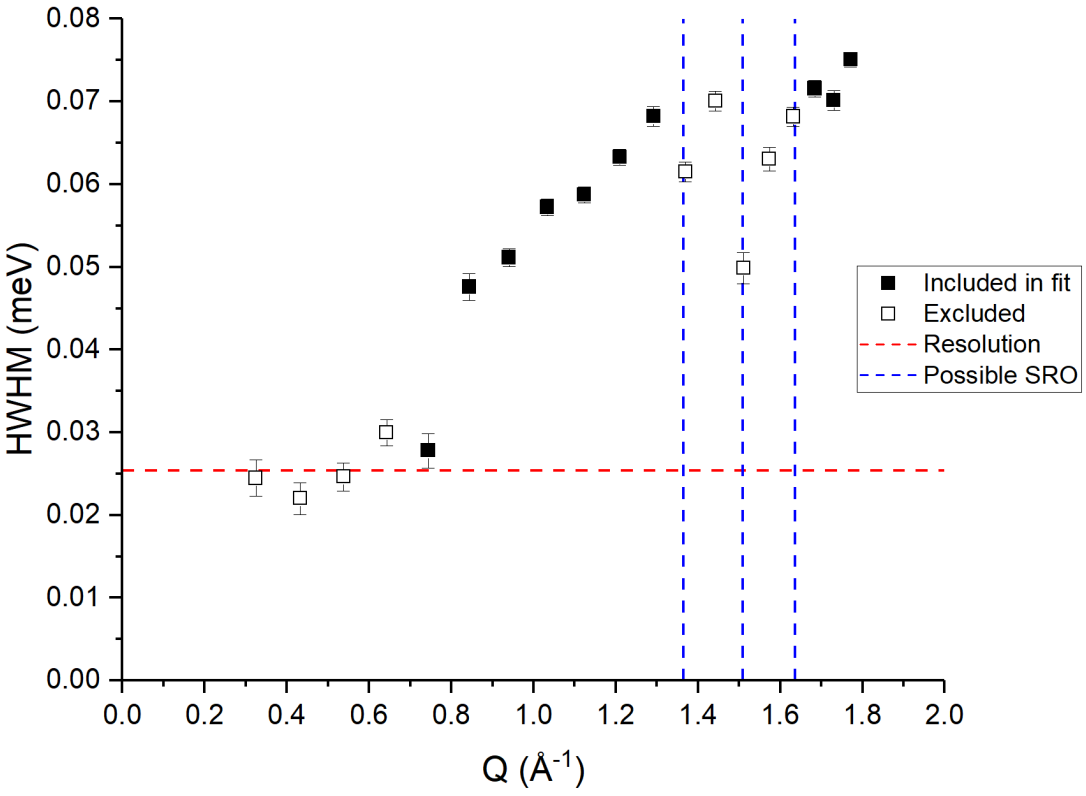

4-Q Example of points excluded from fit

In the plot above, all of the points below $Q = 0.7$ have been raised to the level of the instrument resolution. The points around the three Q values where SRO narrowing would be expected are either visibly affected or questionable. With this in mind, the Chudley-Elliott fits to width of the narrow component in the palladium deuteride sample are presented below:

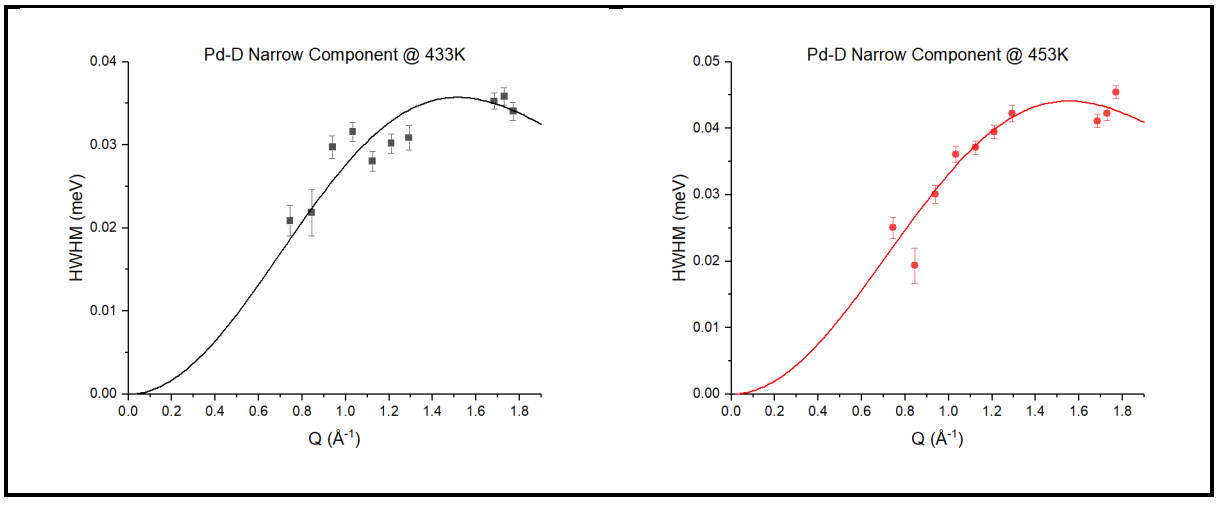

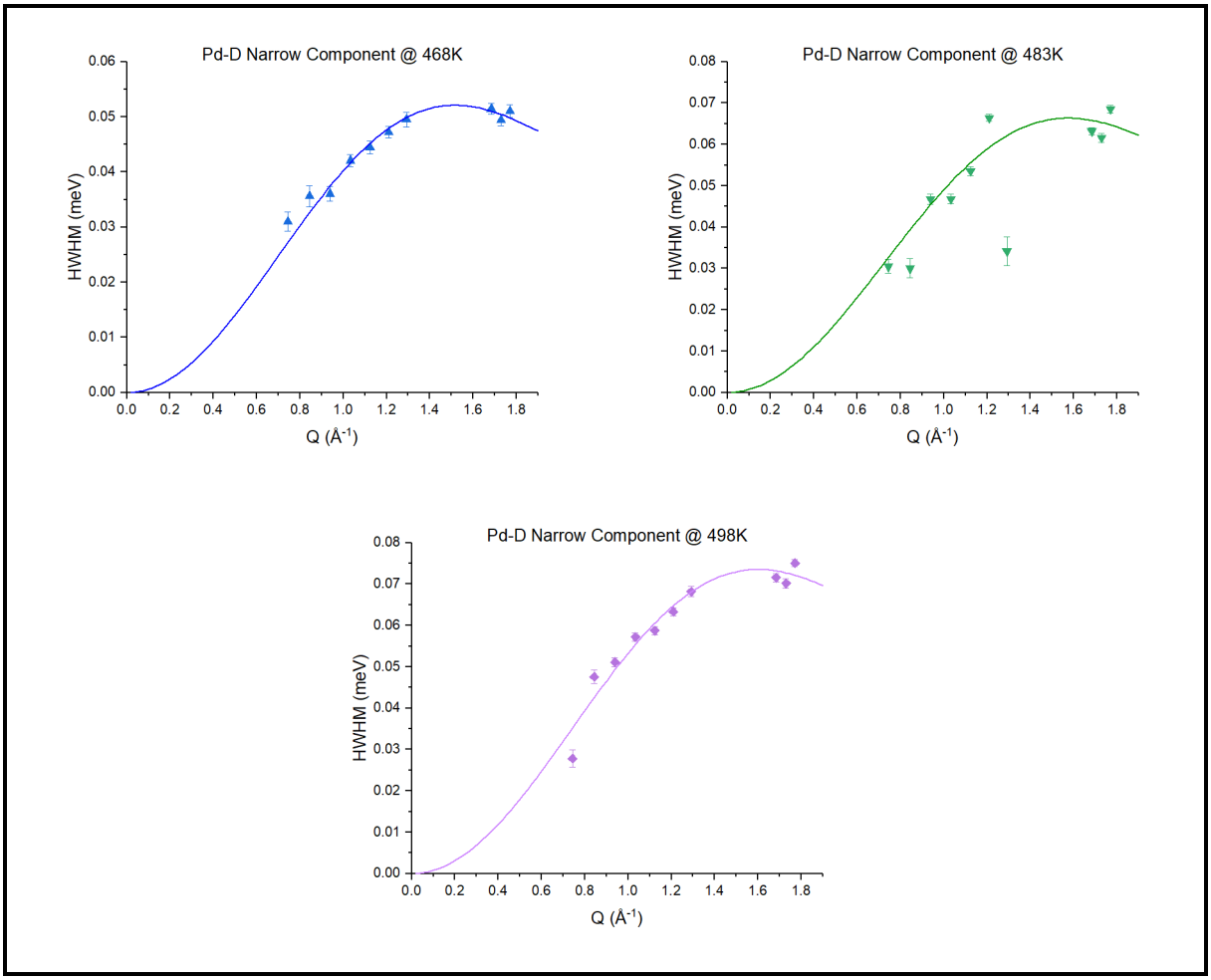

4-R Individual Pd-D Chudley-Elliott fits

The plots are combined into a single plot below:

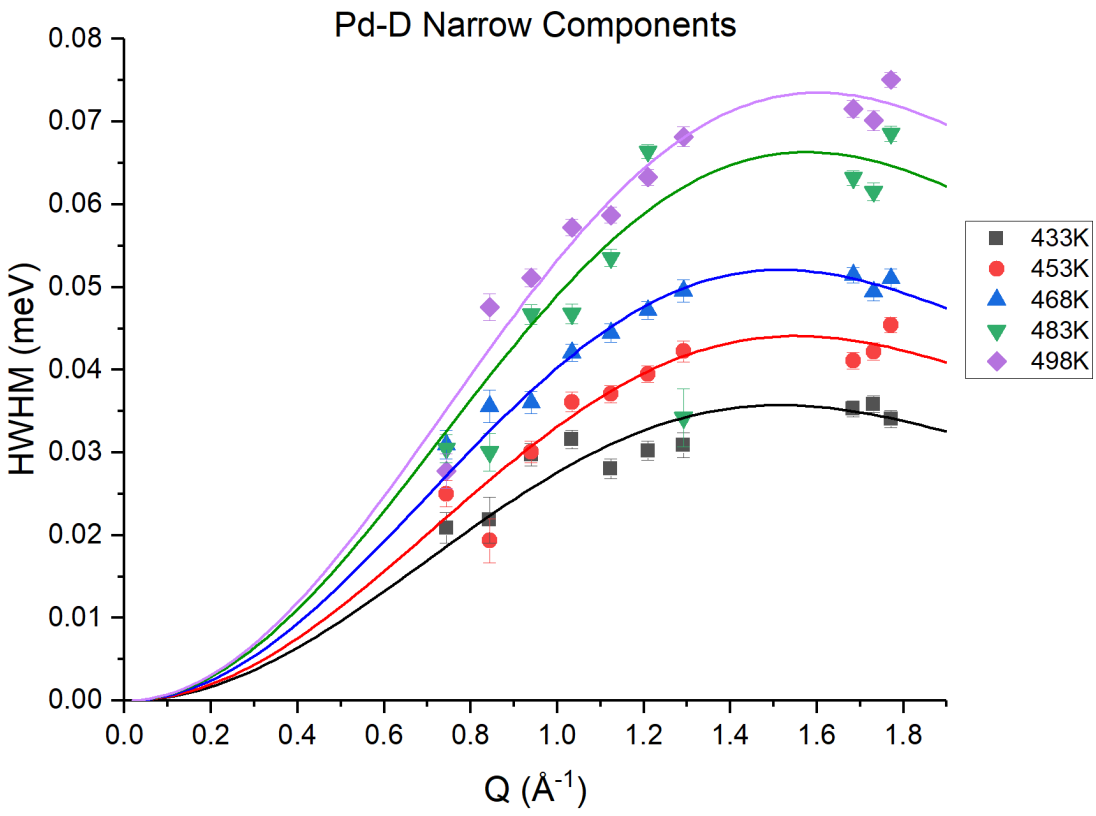

4-S All Pd-D Chudley-Elliott fits

Good agreement with the model can be seen in most of the datasets. The set at 483K is much less convincing than the others but the fitted parameters still appear to fit the general trend (albeit with larger error bars).

The fitted parameters for each of the curves above can be found in the table below:

Temperature (K)	A (meV)	ΔA (meV)	l (Å)	Δl (Å)
433	0.02935	7.72232E-4	2.9642	0.10828
453	0.03622	6.86436E-4	2.89269	0.07588
468	0.04279	4.47542E-4	2.96443	0.04191
483	0.05449	0.00184	2.8505	0.13262
498	0.06039	9.79525E-4	2.80405	0.05981

4-e Chudley-Elliott fit parameters for Pd-D

As with the fitted parameters for the hydride datasets, the jump lengths for the deuteride sets are in a suitable range to be octahedral – octahedral jumps. This can be seen in figure 4-T.

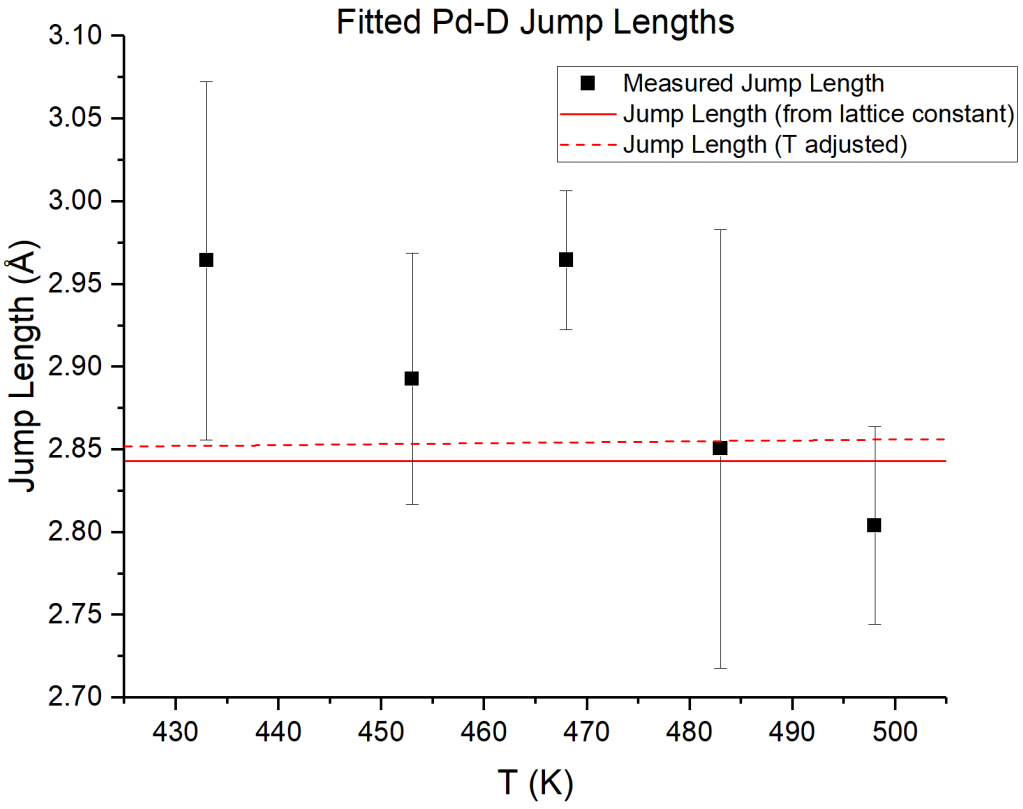

4-T Fitted Pd-D Chudley-Elliott jump lengths

As mentioned at the start of this section, the 'A' parameter in the fitted Chudley-Elliott equation (4-1) for the deuteride sample contains components from both coherent and incoherent scattering. The incoherent part has the same $(1-c)$ dependence on concentration as described for the hydride sample. It has been shown by Ross (1992) that coherent quasielastic broadening in an ordered lattice gas has a concentration dependence of $c(1-c)$. In this work, it has been assumed that the total broadening can be taken to be a linear combination of the coherent and incoherent parts, weighted by the relative magnitude of the appropriate cross sections[78]. Narrowing at Q vectors that correspond to

[78] Derivation and justifications of the exact form used can be found in section 3.6.3.2

the ordered structures described by Clapp and Moss (1968) for an FCC lattice, has been observed. As previously mentioned in this chapter, an attempt has been made to mask this phenomenon. This is discussed further in section 4.5.2.

After these corrections have been applied, the corrected points can be used to generate the following Arrhenius plot:

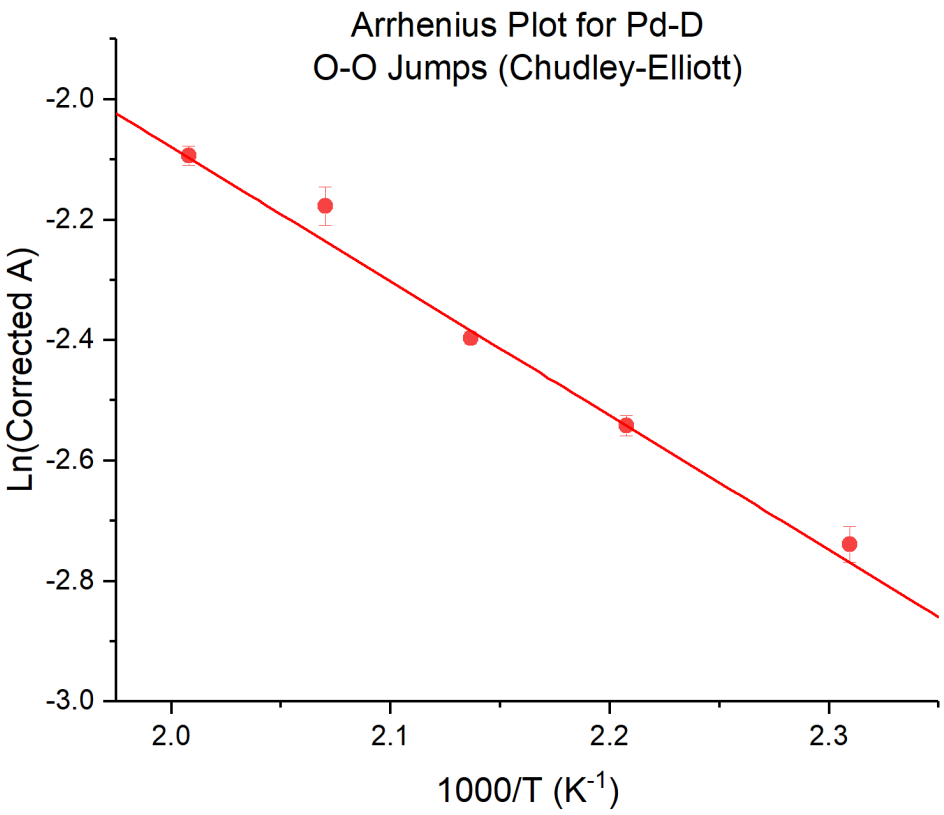

4-U Pd-D Arrhenius plot

The plot appears to show clear Arrhenius behaviour and yields an activation energy of $195 \pm 11\ meV$. The upper bound of the error on this measurement is extremely close the value reported by Völkl et al. (1971) for octahedral - octahedral jumps in palladium deuteride of $206\ meV$. The pre-exponential factor in the Arrhenius equation has been calculated to be $(4.4 \pm 1.2) \times 10^{12}\ s^{-1}$. As with the previously reported value for the hydride sample, the calculated error in this value is substantial. The reliability of this value, and exactly what it describes, is questionable. Further discussion on this subject can be found in section 4.5.1.

4.4.2.4 Pd-H / Pd-D 'Crossover Point'

Combining the two Arrhenius plots from the previous section (figures 4-P and 4-U) allows identification of a temperature where the rates of octahedral – octahedral diffusion in beta-palladium hydride and deuteride are equal. This is presented below in figure 4-V.

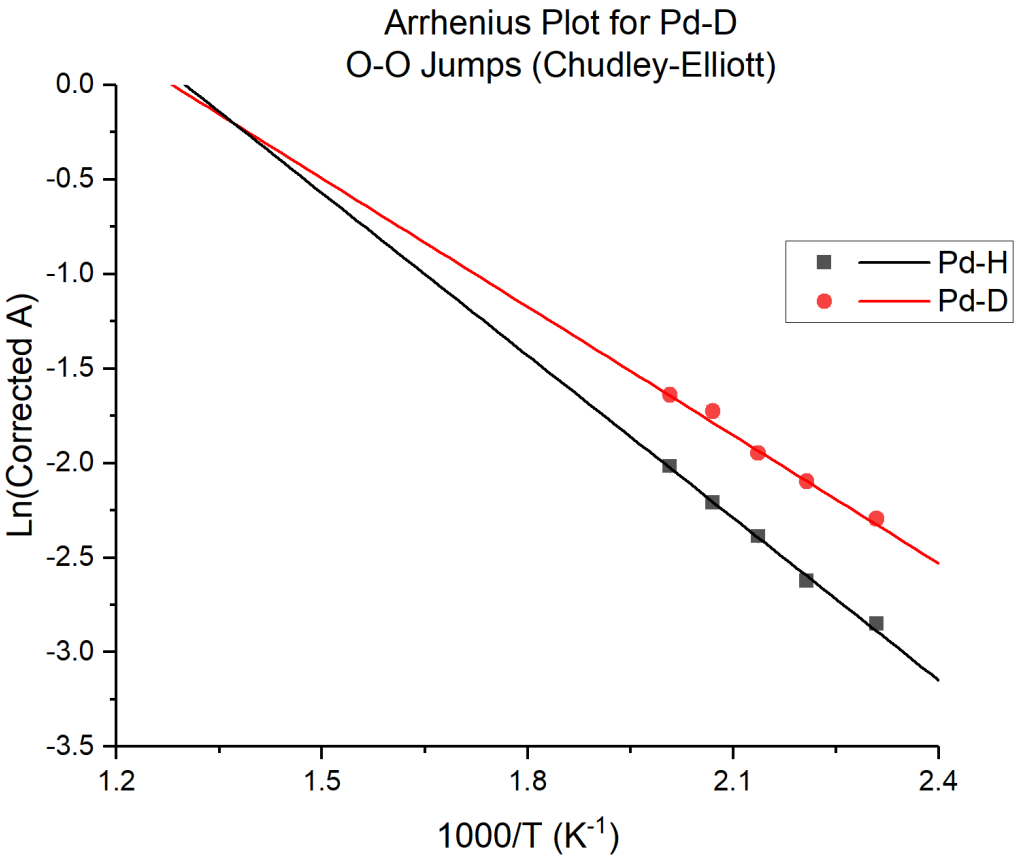

4-V Pd-H Vs Pd-D Arrhenius plot

The two lines intersect at around $729K$ $(456°C)$. However, it seems reasonable to suspect that the actual crossover point is lower than this. While the gradients of the two lines appear to lead to activation energies that agree well with previous work, there is a large error in both calculated Y intercepts. Further to this in the deuteride sample, the maximum broadening for each of the measurements coincides with an SRO peak (in $S(Q)$) of unknown form, and the time constant that determines the magnitude of the broadening is not strictly a measure of the tracer diffusion. The implications of this are discussed in section 4.5.1.

4.4.2.5 Evidence for, and Treatment of, Short Range Order (SRO)

As has previously been noted in this chapter, apparent short-range order has been noted in the QENS measurements of the deuteride. This manifests as a reduction of the quasielastic broadening around values of Q that correspond to the additional lattice vectors of the superlattice structure. Neither the sample, nor the steel sample can, have Bragg peaks in the Q range of the QENS measurements (the first expected peak occurs at $Q = 2.7$ Å^{-1}) so possible interference from this can be easily be ruled out.

Figure 4-W shows the fitted broadening of the narrow component for all of the collected measurements on the deuteride sample. The possible locations of peaks in $S(Q)$ due to ordering are marked as pairs of vertical dashed lines[79]. These lines correspond to the location of this peak as calculated from the accepted standard figure quoted as the lattice parameter for beta-phase Pd-D (4.02 Å) and an extreme value derived from this work (4.25 Å^{-1}). They are intended to show a range of possible values for any potential peak centre.

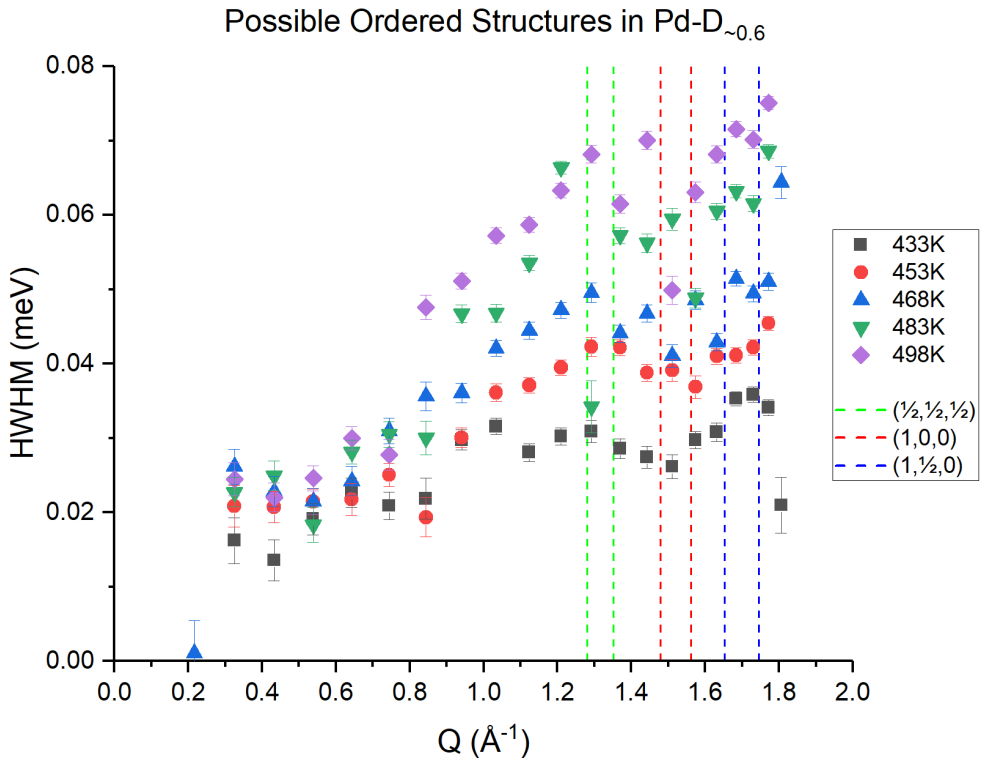

4-W Possible SRO Structures in Pd-D QENS Broadening

[79] Further detail on this subject can be found in section 4.5.2

This however, doesn't fully capture the complexity of the of necessary fit to the SRO narrowing peak centre in Q. The broadening seen in figure 4-W is assumed to be a combination of the incoherent Chudley-Elliott broadening and the modified coherent Chudley-Elliott broadening (roughly equivalent to $\Gamma_0/S(Q)$). Even taking just the coherent part, this is a positive peak that is reduced around some point other that its centre by a feature with a different centre of unknown width. Therefore, it is not realistically possible to determine the form of $S(Q)$ from these data alone.

It seems evident that $S(Q)$ contributes heavily to all three measurements below $470\ K$ but it appears that this relationship becomes more complicated in the two higher temperatures. A similar region in Q shows a negative distortion but it appears to be heavily affected by stochastic noise. As previously described in section 4.4.2.3, the region of data that is most obviously distorted, has been masked for the purpose of achieving a fit to these data. This is known to be an unsatisfactory method and is only employed so approximate Arrhenius parameters can be calculated. Further discussion on this can be found in section 4.5.2.

4.4.2.6 The Second Component

As described earlier in this chapter, none of the datasets could be satisfactorily fitted with a model containing a single Lorentzian component. The previously described 'narrow' component has been shown to agree extremely well with existing octahedral-octahedral jump diffusion models. A second wider component derived from the fit is much less simple to characterise in these data. As such a further set of measurements were planned. These are described in chapter 5. The following section presents the fitted data from this experiment and offers limited analysis where it is relevant to the discussion of the measurements that were carried out at a later date.

Across both samples and all temperatures, a Lorentzian component with a HWHM approximately an order of magnitude wider than that described in the previous section has been inferred. Figures 4-X and 4-Y show the fitted HWHM of these components for each temperature in the hydride and deuteride samples respectively.

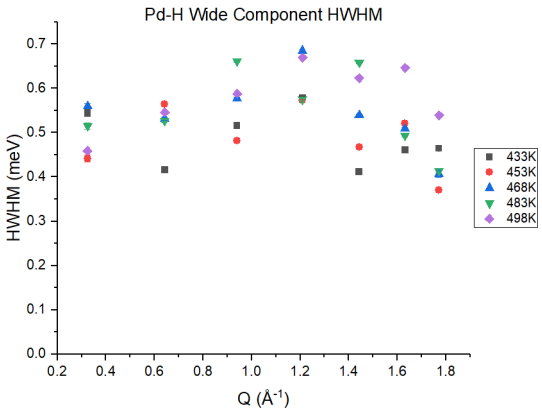

4-X Pd-H Wide Component Widths

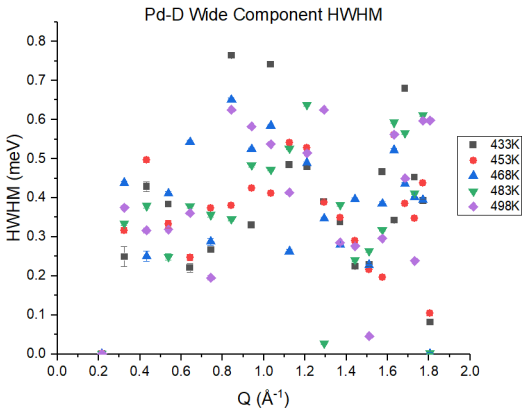

4-Y Pd-D Wide Component Widths

While the widths in each set are clustered, they do not appear to exhibit the Q dependence expected for long range translational jump diffusion. However, they appear to show some form with an apparent peak at $Q{\sim}1.2\ \text{Å}^{-1}$ (seen as an absence of points in the low HWHM region for the deuteride set). Both sets appear to be subject to considerable stochastic noise. This makes determination of temperature dependence difficult. The order of the temperatures for any single value of Q appears fairly random. In an effort to assess whether any such dependence exists, each dataset was assumed to be uniform in Q. A mean and standard deviation was calculated for each, and these values used to create Arrhenius plots. These are shown as individual plots and then combined in figure 4-Z.

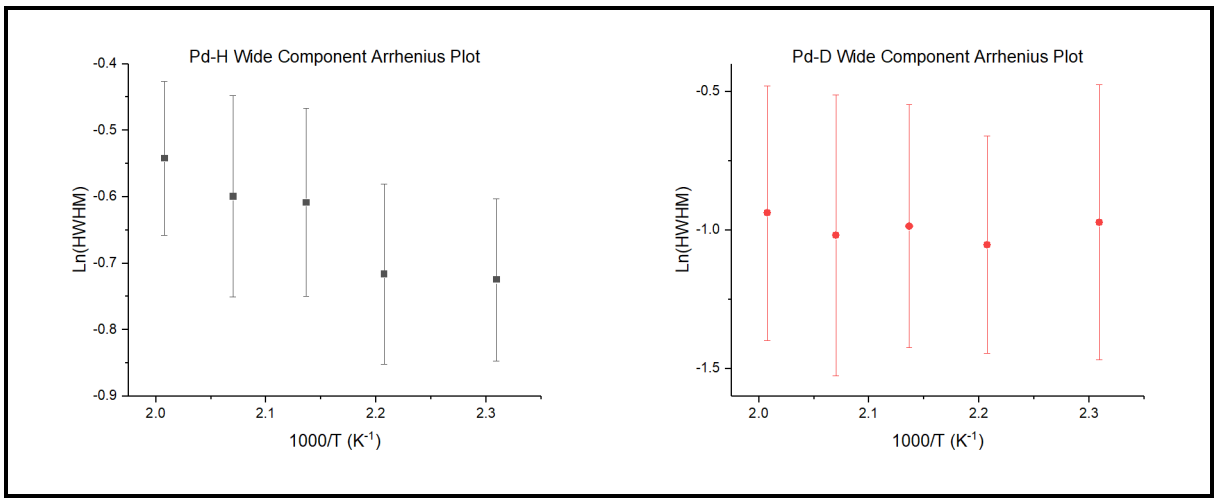

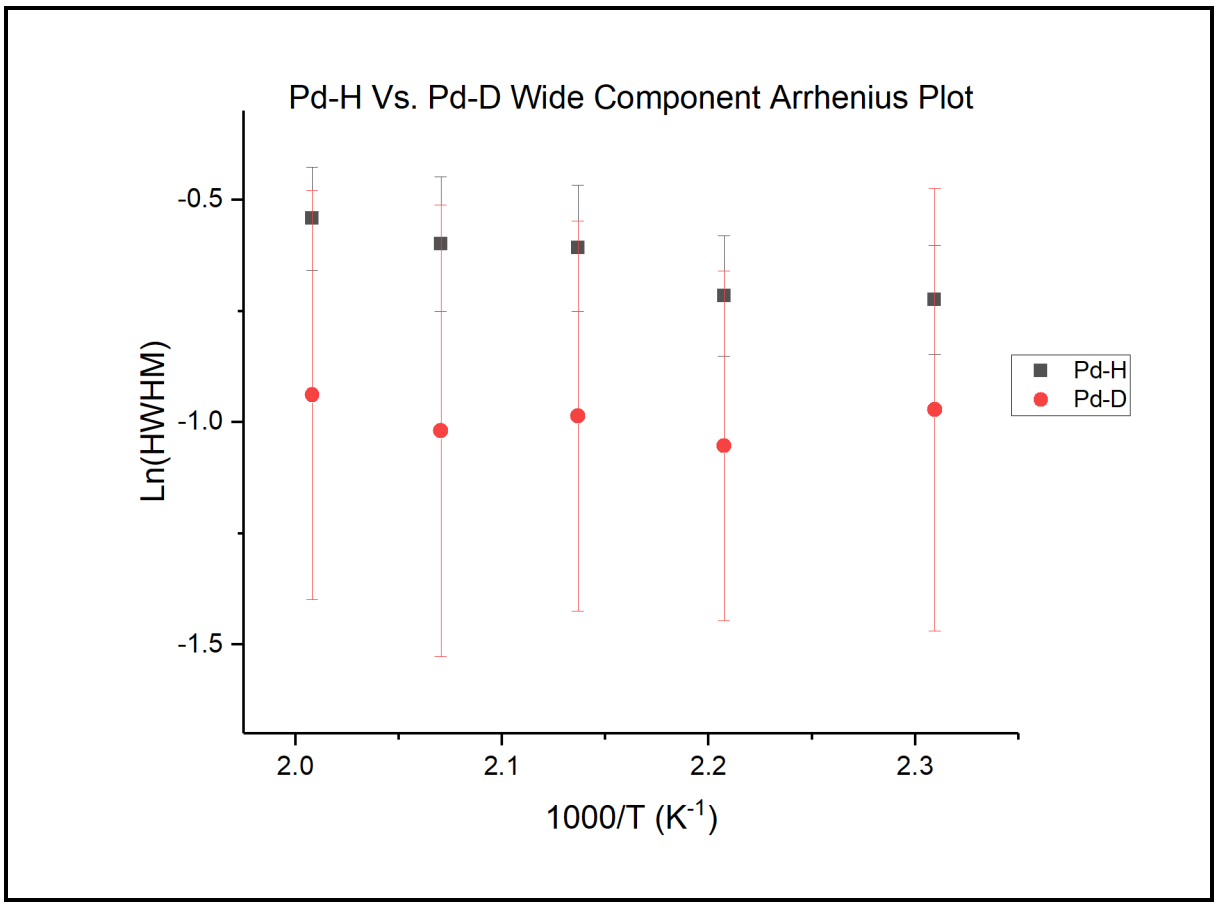

4-Z Osiris wide component Arrhenius plots

While these plots are known to be based on a flawed assumption (and contain very large errors that arise from this) there is a hint of an increase in the measured width with increasing temperature which could be expected for a process with a very low activation energy. This is more apparent in the hydride sample than the deuteride sample. With that said, it is entirely possible to plot a straight line through the error bars for each set in almost any direction.

4.5 Discussion

4.5.1 Pd-H / Pd-D 'Crossover Point'

The interpretation of the translational diffusion data from the hydride sample fits extremely well with existing data and models. The final calculated Arrhenius parameters for the narrow (slow) component are almost identical to those produced by Kofu et al. (2016) in work that also attempted to isolate this motion from a very similar set of measurements. It should be noted though that the method inherently produces a value for the intercept of the Arrhenius plot with an extremely large error. In this case, around 20% of the quoted value. Whether

this calculated error is a good indicator of the validity of the measurement is debateable. In much of the literature that describes QENS experiments it is often 'played down' or, as is the case in the work by Kofu et al. (2016), omitted entirely. This type of measurement has also regularly been shown to agree well with comparable measurements made using other techniques.

The fitted widths that have been used in the Arrhenius plot for the deuteride sample are thought to sit somewhere between the actual contributions from coherent and incoherent scattering. Without further measurements or direct knowledge of Haven's ratio for this system, it is not possible to extract a reliable mean residence time for the tracer diffusion in the system. This was not anticipated to be such a significant problem when the initial experiment was planned. It was thought that the interaction between the deuterons in the lattice would be significantly lower that was seen at the elevated temperatures used. Had this been the case, the 'negligible interaction' case described in section 3.6.3.2 would have provided a much more reasonable approximation to the system than has been achieved.

There is also a visible contribution to the total scattering from, what appears to be, short range ordering of the deuterons in the lattice. This presents itself as a reduction in broadening in the same region of Q space as the peak broadening from translational diffusion. Without explicit knowledge of the shape of $S(Q)$, it is extremely difficult accurately interpret the overall broadening from these two contributions. It is also difficult to estimate the reduction that may occur away from centre of the peak in $S(Q)$.

Early preliminary measurements on deuterium (taken when the first hydride measurements described in this work were conducted) could not be allowed to run for sufficient time for reliable statistics to be obtained. As such, the contribution from ordering could not easily be defined amongst the stochastic noise. Also, to improve the statistical quality of the data, preliminary fits were produced for datasets containing 7 detector groups (merging data from a wide Q range into each). While this did reduce the stochastic noise, it also reduced the apparent SRO narrowing. Since this appeared to agree with the belief that large contributions from SRO would not be seen, direct measurements of $S(Q)$ across the relevant Q range were not planned when the final measurements were made. Further discussion of the nature of the ordering seen, and the attempt to 'mask' it from the fitted data, can be found in section 4.5.2.

The assumptions made in the analysis of the data from the deuteride sample may lead to some ambiguity on the interpretation of the calculated crossover point. However, the calculated result falls well within the expected range.

Previous attempts to locate the crossover temperature have yielded very different results. Several sets of QENS measurements collated by Sicking (1984) predict it to be much lower. Figure 4-AA shows the original plot of the collated data from that work alongside a digitised version produced for this work[80].

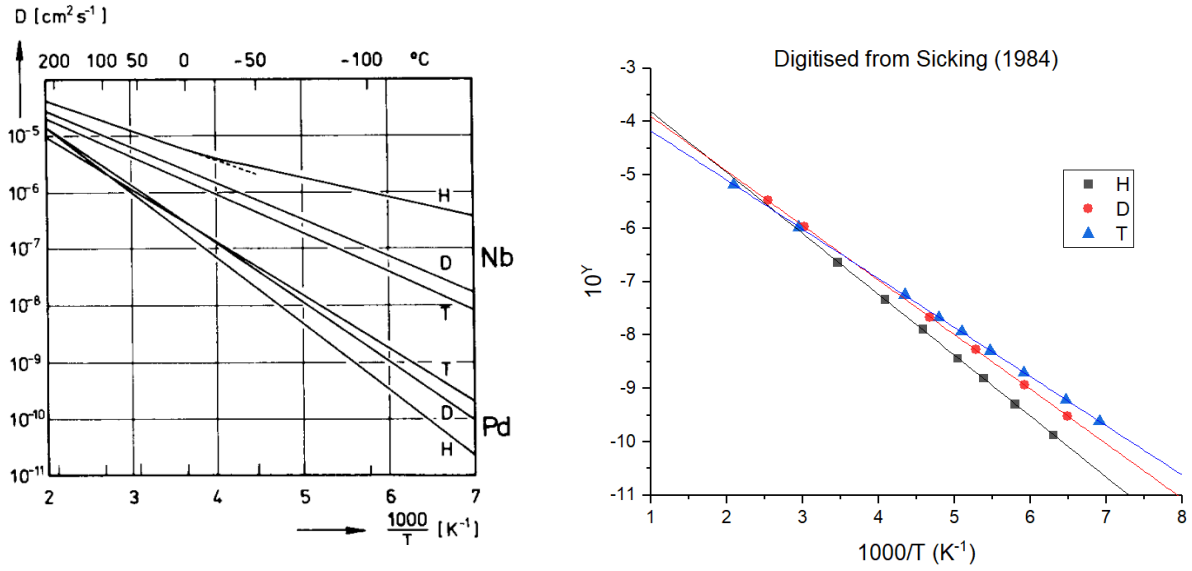

4-AA Sicking QENS Arrhenius Pd-H/D/T Plots

This plot yields a crossover temperature of around 565 K. It is difficult to know whether this result is directly comparable to the work described in this document. The exact concentrations and data reduction methods are not fully described in the work. Interestingly, an extremely similar result is produced from the data in this work if the datasets for deuterium are treated as pure incoherent scattering with neither the broadening in the hydride or deuteride datasets being assumed to be dependent on concentration.

Work by Majorowski and Baranowski (1982) to assess this phenomenon via an electrical resistance relaxation method from measurements at lower temperatures (208 to 338 K),

[80] The data points illustrated in the digitised version show the points along the lines in the original work that were used to fit the lines used to calculate the crossover point.

predicts a much higher crossover point. Figure 4-BB shows the original plot from their work is shown alongside a digitised and re-fitted plot that has been extrapolated to show the crossover point.

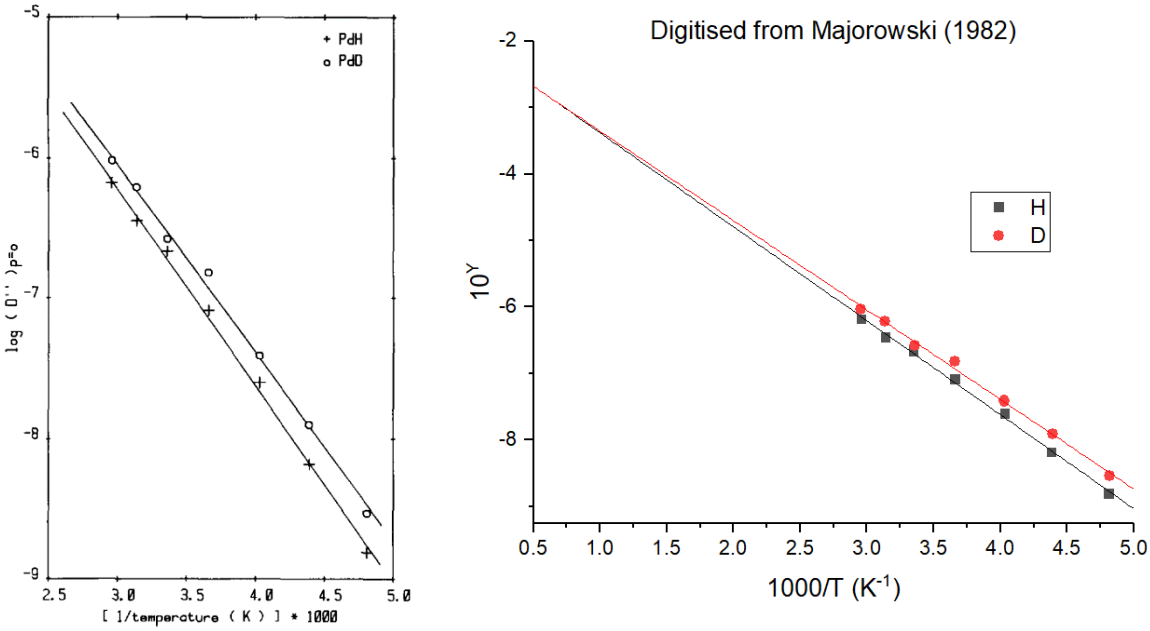

4-BB Majorowski Arrhenius Plots for Pd-H/D

The crossover point in this case has been calculated to be around 1656 K. As I am not completely familiar with the technique used, I am unable to fully critique the precise method employed. The technique gives a measure of diffusivity (that includes components outside the tracer diffusion that is directly measured by QENS) but, as their results have been presented in terms of concentration independent diffusion coefficients (and only the crossover temperature is relevant here), some comparison with the results in this work seems to be valid. It is interesting to note that, if the scattering from the deuteride sample (for the slower, narrow, component) in this work is treated as wholly coherent, a crossover point of $1602\ K$ is predicted. This treatment also yields a feasible activation energy for the deuteride of $209 \pm 12\ meV$. This is probably, simply coincidence. It is very difficult to assess how comparable the results of this work are to that of Majorowski as the techniques may not give information about the exactly the same process.

These examples have been selected as they illustrate the breadth of the values previously proposed for the beta Pd-H / Pd-D diffusion rate crossover temperature. Many other attempts using various techniques have been published. Often, these are based on

diffusivity rather than tracer diffusion or may contain contributions from other effects. Most of the work in existing literature (with any technique) has been conducted in the alpha phase and so is not directly comparable. For much of the older work, the detail that would show whether the result is truly valid, is lacking. In the absence of a full treatment of the work described by Sicking, and given the fact that this result can be reproduced from an oversimplified treatment of the measurements detailed in this work, it seems reasonable to assume that the value arrived from that data may well be unreliable.

QENS is an ideal method for measuring the desired parameter (the tracer diffusion coefficient) but previous comparable measurements on Pd-D are sparse in existing literature. The reasons for this are numerous. It requires much larger sample sizes and longer measurement times that similar measurements with hydrogen. Further, as has been shown in this work, fully analysing the total scattering from deuterium is problematic without further information. Methods to separate the coherent and incoherent components are complex. It may be possible to employ a similar technique to that described by Cook et al. (1991) to separate the tracer and mobility correlation factors via neutron spin analysis. While this is a potentially promising avenue, it has not been fully assessed for application to this system due to time constraints.

It is therefore evident that the calculated crossover point is unreliable. Exactly how unreliable is very difficult to quantify. As well as the contributions from coherent and incoherent scattering, a large contribution has been seen from short range order in the deuteride sample (further discussion of the effect of SRO on the calculated crossover point can be found in the following section). Both of these factors complicate analysis of the deuteride sample. As shown in section 4.4.2.5, it appears that the contribution from ordering may be greatly reduced at slightly higher temperatures. Unfortunately, these measurements were collected up to the operational limit of the apparatus used so further work would be needed to confirm this.

4.5.2 Short Range Order

When these measurements were planned, it was not expected that a high degree of structured ordering between the diffusing species and vacant sites would be seen at the temperatures used. Ordering has long been observed at low temperatures and is regularly shown in phase diagrams (such as figure 2-F) for the system. The phase boundary for this is

commonly given at around $50\ K$ across a very wide range of concentrations. A phase transition at this temperature has been shown in neutron scattering measurements by Anderson, Ross, and Carlile (1978a). Further work on this region (marginally above the $50\ K$ transition) by Blaschko (1984) suggests possible ordering.

The ordering taking place between the diffusing species and vacancies in the lattice is analogous to the ordering seen in binary alloys, as described by Clapp and Moss (1966). This theory predicts several potential ordered structures depending on sign and relative intensity of first and second nearest neighbour potentials (V_1 and V_2 respectively). In a binary FCC system, each of these structures give rise to a peak in $S(Q)$ centred at the (h, k, l) index of the relevant superlattice indicated in figure 4-CC.

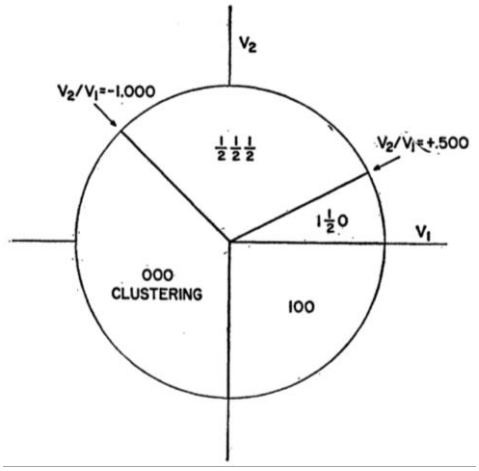

4-CC Possible peaks from SRO (FCC)
(Clapp & Moss, 1968)

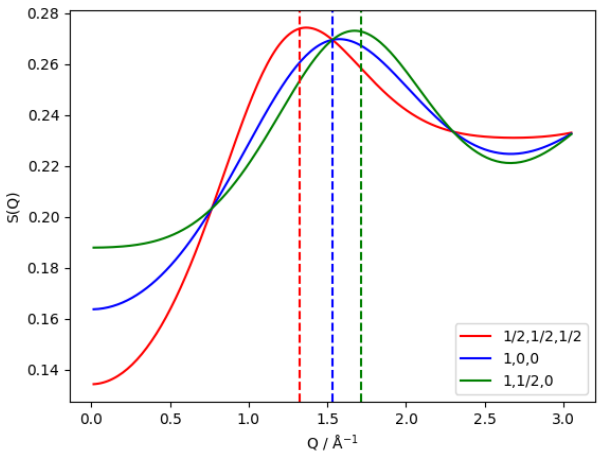

4-DD Possible forms for S(Q)

As SRO was not anticipated, nor could it be easily defined in the preliminary measurements that were made, no direct measurement of $S(Q)$ was performed. As such, little analysis as to the exact nature of the ordering seen has been possible. However, the general form of $S(Q)$ is given by equation (3-40):

$$S(Q) = \frac{c(1-c)}{1 + \frac{c(1-c)V(Q)}{k_B T}}$$

Where $V(Q)$ is the Fourier transform of the pair potential to second nearest neighbours. For any specific direction in an FCC lattice, this is given by Bull (2001) as:

$$V(Q) = 4V_1(\cos\pi h\cos\pi k + \cos\pi h\cos\pi l + \cos\pi k\cos\pi l) + 2V_2(\cos 2\pi h + \cos 2\pi k + \cos 2\pi l) \quad (4\text{-}2)$$

Figure 4-DD shows possible forms that would result from the three allowed ordered states described by Clapp & Moss for an FCC lattice[81]. The vertical dashed lines represent the value of Q associated with each of the three structures described in figure 4-CC. These have been colour coded to match the $S(Q)$ plot that corresponds to the relevant structure. The parameters chosen are arbitrary (with the exception of having the correct V2/V1 ratio for each structure) and were simply chosen for illustrative purposes. In the polycrystalline average (as employed here) the peaks in $S(Q)$ may not line up exactly with the predicted Q_{hkl} values[82].

Since the measured Lorentzian width from jump diffusion in coherent scattering is inversely proportional to $S(Q)$, the most obvious sign of ordering is an inverted peak the broadening as a function of Q. However, further reduction occurs across the entire measured range. This reduction is heavily dependent on the specific form of the superstructure. Ordering in the $\left(1,\frac{1}{2},0\right)$ plane will cause a much greater reduction in the measured width at low Q than either $\left(\frac{1}{2},\frac{1}{2},\frac{1}{2}\right)$ or $(1,0,0)$. This makes accurate determination of $S(Q)$ across the entire range of the QENS measurement vital. As the narrowing in this case is not accurately characterised, even the unmasked data for the deuteride sample cannot be considered reliable. As such, the values Arrhenius parameters calculated from these data can only be considered an approximation to the system.

As the peak in $S(Q)$ may not line up with that of Chudley-Elliott broadening, it becomes extremely difficult to accurately locate either in these measurements. The fact that the jump lengths calculated from the masked deuterium data appear to agree well with the expected jump length suggests that these peaks may be very close in Q. This appears to rule out the SRO peak being at $\left(\frac{1}{2},\frac{1}{2},\frac{1}{2}\right)$. Due to the similarity in the peaks from the other possible

[81] Plot generated from a script originally authored by Dr D.J. Bull

[82] This direct relationship between Q_{hkl} and the peak in $S(Q)$ only truly applies for measurements on a single crystal in the 111 direction

superstructures, only a tentative guess can be made between them from these measurements.

The previously mentioned work by Blaschko (1984) suggests that, just above the $50\ K$ phase transition at a concentration of around $c = 0.7$, a structure corresponding to a peak at $\left(1, \frac{1}{2}, 0\right)$ is visible in neutron scattering measurements.

Relatively recent (in terms of the published work for this system) thermal desorption spectra (TDS) taken by Rybalko, Morozov, Neklyudov, and Kulish (2001) appears to show the persistence of an ordered structure well above the temperatures previously noted across a wide range of initial concentrations. Their work suggests that, even with an initial concentration as low as 0.54, a sudden shift in concentration that is consistent with a phase transition that has no associated distortion to the host lattice can be seen at around $150\ K$. As the desorption spectra described start from a temperature above $50\ K$, it is possible that this ordered structure is not the one previously noted below this temperature. This appears to be consistent with the work of Blaschko (1984) but extends the temperature range of this phase considerably. Since TDS measures loss of concentration, it does not give a direct answer as to whether this phenomenon would persist at higher temperatures should the concentration be maintained (as is the case in this work).

Figure 4-W shows that the apparent location of the peak of $S(Q)$ appears to coincide the Q range that would correspond to $(1,0,0)$ ordering across the entire temperature range. This type of structure has not previously been reported in this system. Without direct measurements of $S(Q)$, it is difficult to rule out possible $\left(1, \frac{1}{2}, 0\right)$ ordering. This type of ordering appears in the literature for the mixed ($\alpha + \beta$) phase region below $150\ K$, but it has not previously been reported at the temperatures measured in this work (around $300\ K$ higher).

While it is not possible to draw a solid conclusion on the exact form of ordering present, the evidence for a high level of ordering at temperatures up to $470\ K$ (and possibly beyond) is conclusive. This strongly suggests that previous assumptions about the strength of the interactions between the diffusing particles may not accurately describe the system and that the 'generally accepted' phase structure model is either inaccurate or incomplete.

4.5.3 Multiple Components

The evidence for multiple components in the QENS measurements for each set appears to be conclusive. No reasonable fit can be achieved using a model with one Lorentzian component and both samples appear to show this discrepancy in a similar energy transfer region. The narrow component has been identified as octahedral-octahedral jump diffusion showing good agreement with existing models and previously published work. It has not been possible to characterise the wider component in these measurements. It appears to show some structure, being relatively uniform in Q at each temperature, with the exception of a deviation at $Q{\sim}1.2\ \text{Å}^{-1}$. This does not appear to match any two site jump diffusion model. It is possible that this component displays an Arrhenius type temperature dependence, but evidence for this is questionable.

This experiment was not designed to seek this wider Lorentzian. The useable fitting window determined by the setup parameters of the instrument is $-0.5 < \hbar\omega < 1\ meV$. This is approximately the width the HWHM of the fitted Lorentzian component. For this reason alone, parameters fitted to this component (for any specific T and Q) are likely to have errors that are much larger than those shown.

The apparent structure and possibility of temperature dependence suggest a real form of motion rather than stochastic noise or a fitting artefact. As such, this deserved further investigation. An experiment to probe the nature of this component, and its conclusions, can be found in chapter 5.

5 Multiple Diffusive Motions in Pd-H

5.1 Introduction

In the previous chapter, it was shown that models assuming a single type of motion did not agree well with the observed scattering from either sample across the entire measured temperature range. While determining the total number of Lorentzian components in any QENS measurement is a mathematically complex task, two components associated with distinct forms of motion were fitted to each dataset. The first of these motions was shown to result from translational diffusive jumps between the octahedral sites in the palladium lattice in both the hydrogen and deuterium samples. It was not possible to fully characterise the second form of motion seen but, there was convincing evidence that it gave rise to a Lorentzian with a broadening approximately an order of magnitude larger than that seen for the O-O component. This motion also appeared to display possible temperature dependence.

The experiment described in this chapter was conceived to investigate this second form of motion further. It will be shown in the analysis and conclusions that further detail about the short range ordering of the diffusing species in the lattice was also discovered.

5.2 Why IN5

The energy transfer range fitted to the data taken on Osiris was approximately equivalent to the width of the wider component that was seen. It is possible to alter the configuration of the instrument (using the 004 reflection of the pyrolytic graphite analyser) to extend this range but this results in a loss of neutron flux at the sample and a resolution limit of $99\ \mu eV$. The extra measurement time required and reduction in resolving power led to a search for other, potentially more suitable, instruments.

The increased flux available at the ILL allows for individual measurements of a similar statistical quality to those collected on Osiris, to be made in minutes. While the instrument has an almost identical quoted resolution ($\sim 99\ meV$) at the incident energy that was ultimately used, the shape of the resolution allows narrower features to be defined.

On top of this, IN5 has a comparatively high angular resolution with each detector covering around $0.4°$ (rather than $3°$ for Osiris) potentially allowing better determination of Q dependent features.

The instrument has a broad range of selectable incident energies (0.2 to $25\ meV$) and an extremely broad energy transfer window (extending to around $40\ meV$ with the settings described later in this chapter).

5.3 Experimental Setup

5.3.1 Outline

Quasielastic measurements were collected for beta palladium hydride in two samples over a similar range of temperatures to the measurements described in the previous chapter. The first sample was a fresh supply of the spherical powder that was used in the previous measurements. Powder that had not previously been loaded with hydrogen was chosen to reduce the possibility of the results being distorted by accumulated defects from repeated cycling, making the results as directly comparable to those in the previous chapter as possible. The second was a $50 \times 50\ mm$ piece of palladium foil that had been rolled to a thickness of $0.1\ mm$. Both samples were over 99.9% pure palladium of natural isotopic composition.

These two samples were chosen due to their vast difference in surface to bulk ratio in the hope that this would shed light on whether the wider component was related to rapid diffusion in the outer atomic layers of the metal or at the interface of the particles in the powder.

The foil sample was not annealed prior to the measurements being taken. The sample shows strong preferential alignment in the 111 direction as would normally be expected of a mechanically rolled FCC metal. As this is not a single crystal, the alignment is not full. As a result, the sample can neither be considered polycrystalline, nor analogous to a single crystal. There is much of qualitative interest in the results from this sample. Some quantitative analysis has been undertaken where appropriate.

This instrument does not have a simple mechanism for making broad spectrum diffraction measurements like the backscattering bank on Osiris. To ensure that each measurement was taken in the pure beta phase, the pressures at each temperature were either matched to those described in the previous chapter or higher. The compositions quoted were measured in separate gravimetric measurements that can be found in appendix C.

Instrument parameters were chosen to highlight the wide Lorentzian described in the previous chapter.

5.3.2 Sample Environment

As diffraction measurements were not of interest, a standard aluminium annular can was used for both samples. Aluminium has a much smaller total scattering cross section than the steel used in the previous experiment. This results in a dramatic reduction in the elastic scattering seen and a reduced probability of multiple scattering. The can has a very similar design to those used in the previous experiment. Gas is supplied and extracted through a pipe in the top section.

A standard ILL cryofurnace surrounded the sample position. This has a potential temperature range of 2.5 to $600\ K$. The combination of sample can and gaskets used reduced this upper limit to around $500\ K$. No further heating equipment was used. This device is controlled and monitored via NOMAD[83].

A similar physical setup is employed on IN5 to that described for Osiris. The sample can is placed on a long centre stick that carries the gas line and positions the sample in the beam window when it is placed in the instrument.

5.3.3 Instrument Setup

An incident wavelength of $4.8\ \text{Å}$ (incident energy $\sim 3.551\ meV$) was used across all of the measurements described in this chapter. This gives the maximum possible flux for the instrument and a resolution in the region of $99\ meV$ [84].

Control and monitoring of the cryofurnace, as well as the data capture windows for the instrument were controlled via NOMAD. Sequences that allowed adequate settling time were written after initial tests had been conducted.

Gas delivery and extraction was performed with a specially modified Hiden IMI. This unit controls gas flow and pressure with a range of mass flow controllers, vacuum pumps, and pressure gauges. As with the gas system for the Osiris measurements, pressure is monitored remotely rather than near the sample. The readings at the device are thought to be broadly

[83] See section 3.8.4.1

[84] As previously mentioned, this still allows features narrower this to be defined on this instrument.

representative of those at the sample. The IMI has extensive sequencing and monitoring capabilities so it was possible to see when equilibrium uptake had been achieved. Each set of recorded QENS spectra were taken after equilibrium had been reached.

5.3.4 Sample Preparation

An annular can with a gap of $1\ mm$ was provided by engineers at the facility. Two pieces of $0.4\ mm$ thick aluminium foil were cut, shaped, and positioned in the can to reduce this gap to $0.2\ mm$. While this gap is $0.05\ mm$ smaller than that used on the measurements described in the previous chapter, the vast difference in number of neutrons detected on this instrument led to a vast reduction in the time required to achieve measurements of a similar statistical quality. The aluminium foil filled the outer edge of the gap leaving a reduced gap around the core.

The powder was packed into the remaining space in the can in a similar way to that described for the measurements in the previous chapter. A combination of tapping and application of force was employed to ensure the powder was packed as densely as possible. Again, a small piece of glass wool (that would not appear in the beam window) was placed in the top of the sample can to stop any powder being removed as gas was evacuated.

The foil sample used an identical aluminium sample can. Again, two pieces of aluminium foil were placed in the can to reduce the annular gap. The foil was wrapped around the core of the can and allowed to expand to meet the aluminium. This left a small gap that would be filled with hydrogen during measurements but allowed for the free expansion of the foil(s) with heat and, more importantly for the palladium, hydrogen content.

The mass of palladium in each case was recorded as:

Sample	Mass of palladium (g)
Powder	4.33
Foil	3.01

5-a Mass of palladium in sample cans

The slightly higher mass of palladium powder in this experiment over the previous chapter is the result of a difference in the geometry of the can rather than a substantial difference in the depth of the sample.

Once sealed, the cans were mounted to an appropriate centre stick and leak tested. After this check, they were inserted into the sample position of the instrument.

Both samples were heated to the upper boundary of the available temperature range and subjected to three sorption / desorption cycles to ensure their surfaces were free of impurities before measurements were collected.

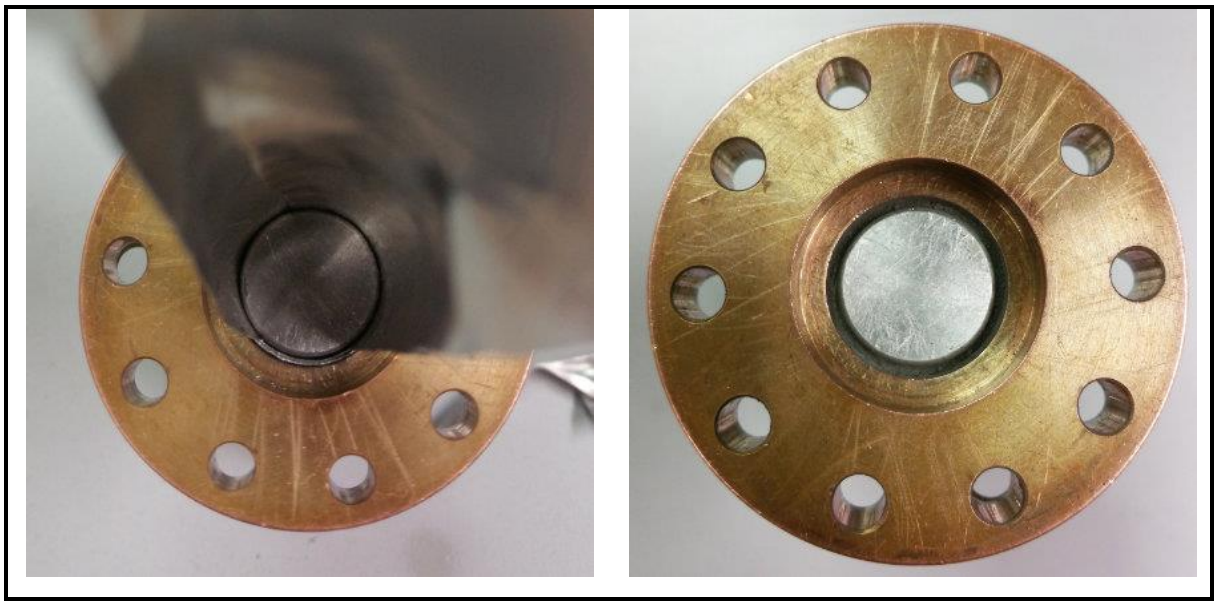

5-A IN5 spherical Pd loading

Figure 5-A shows the loading process. In the first image, the foil used to the reduce the annular gap can be seen. In this image it is being held back with a further piece of foil to allow powder to be fed to the gap near the core. The second image shows the can filled with powder. The top of the aluminium foil is obscured by a small amount of powder sitting on top of it. The third image shows the full can before the lid has been attached. This image clearly shows the steel bolts used to fasten the can together as well as the brass top section and the internal gap for the gasket (rather than the 'groove' type seen in the previous chapter). Neither the bolts, the gasket, nor the brass top section are in the beam window when the can is correctly loaded into the instrument.

5.4 Measurements

5.4.1 Powder Sample

The following measurements were taken for the powder sample[85]:

[85] These values have been rounded with reasonable accuracy. Full precision values including errors were used in calculations. These values, where relevant, can be found in the appropriate analysis sections.

Temperature (°C)	(K)	Pressure (Bar)	H/Pd[86]
27	300	0	0
225	498	0	0
-223	50	1	
-173	100	1	
-123	150	1	
-73	200	10	
-23	250	10	
27	300	10	
125	398	10	0.69
139	412	10.5	0.68
147	420	10.5	0.68
186	459	10.5	0.63
201	474	10.5	0.61
216	489	10.5	0.6
227	500	10.5	0.59

5-b IN5 powder measurements

For some of the lower temperature measurements, exact compositions have not been measured. These compositions are not necessary for the analysis in this chapter. The details and results of these measurements are included for qualitative analysis later in this chapter.

5.4.2 Foil Sample

The following measurements were taken for the foil sample[85]:

Temperature (°C)	(K)	Pressure (Bar)	H/Pd[86]
-173	100	10	
-73	200	10	

[86] Calculated from gravimetric sorption measurements. See section 2.5.1 for general method and appendix for details of the specific measurements.

27	300	10	
125	398	10	0.69
186	459	10	0.63
201	474	10	0.62
216	489	10	0.60
227	500	10.5	0.59

5-c IN5 foil measurements

As with the previous sample, compositions for the low temperature measurements have not been obtained. Knowledge of these exact compositions is not necessary for the analysis in this chapter.

5.5 Results

5.5.1 Data Reduction

Full datasets were imported directly into MantidPlot. Individual runs for each sample at each temperature were merged and detector groups created via recently created import tools[87]. This process yields the full spectrum of $S(Q,\omega)$ for each measurement. Figure 5-B shows an example of the full range of data recorded in each measurement.

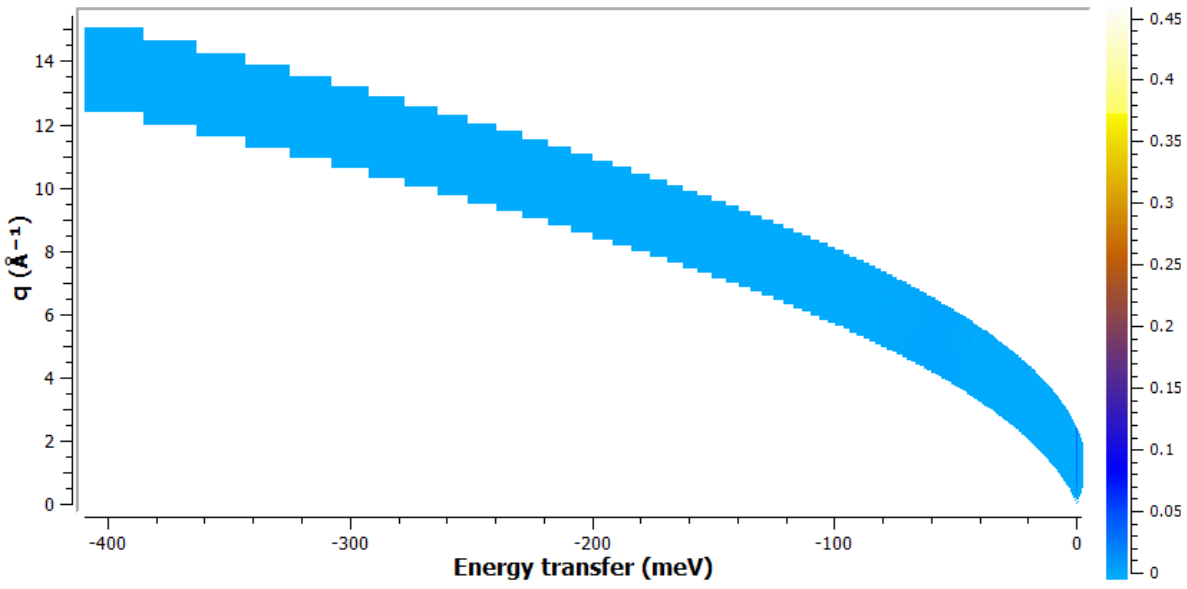

5-B IN5 powder sample @ 498K - Full S(Q,ω)

[87] Tools provided by Antti Soininen at the ILL

Most of the recorded (Q, ω) space is not relevant to this work. It has been included to demonstrate the limits in Q for QENS on this instrument at the settings used. Figure 5-C shows the same dataset cropped to highlight the available quasielastic region. The small gap in the low Q region is due to masking of the region around the beam stop. From this plot it can be seen that the available range of energy transfer varies with Q. Only a small range is available at low Q. At higher values, a greater range of negative energy transfer is available. At $Q \sim 2$ Å^{-1} the positive transfer starts to tail off, eventually intersecting the $0\ meV$ region.

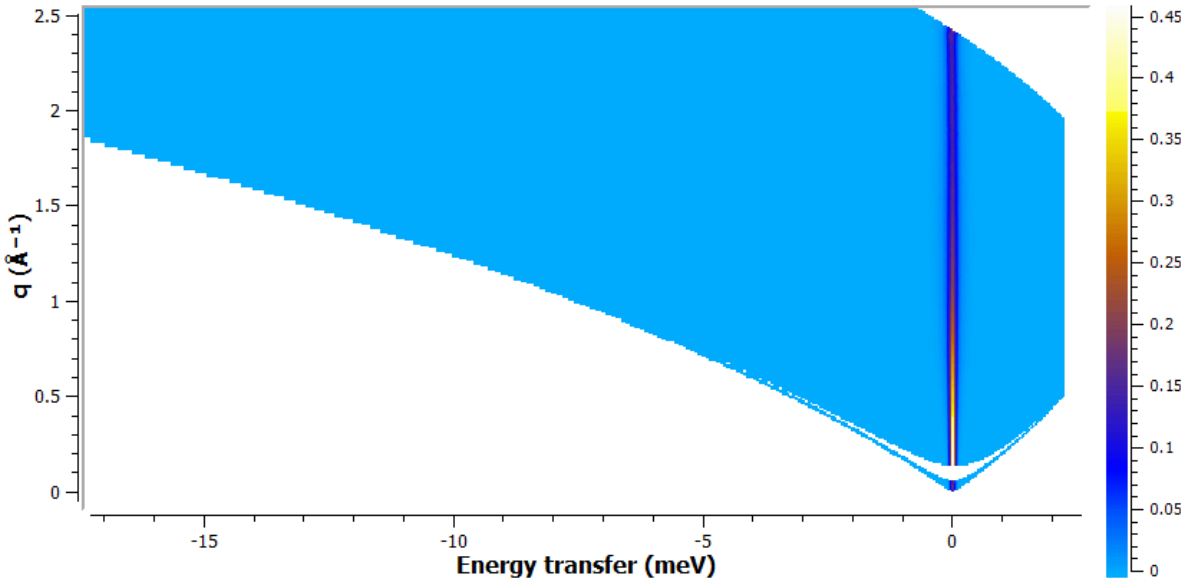

5-C IN5 powder sample @ 498K - Cropped S(Q,ω)

In the interest of creating easily comparable results for all of the measurements in this chapter, all datasets are presented over a Q and ω region that contain as much useable data as possible. The boundaries of this region have been defined as $0.7 < Q < 2.3$ Å^{-1} and $-5.5 < \hbar\omega < 1\ meV$. Figure 5-D shows an example of the data enclosed by this.

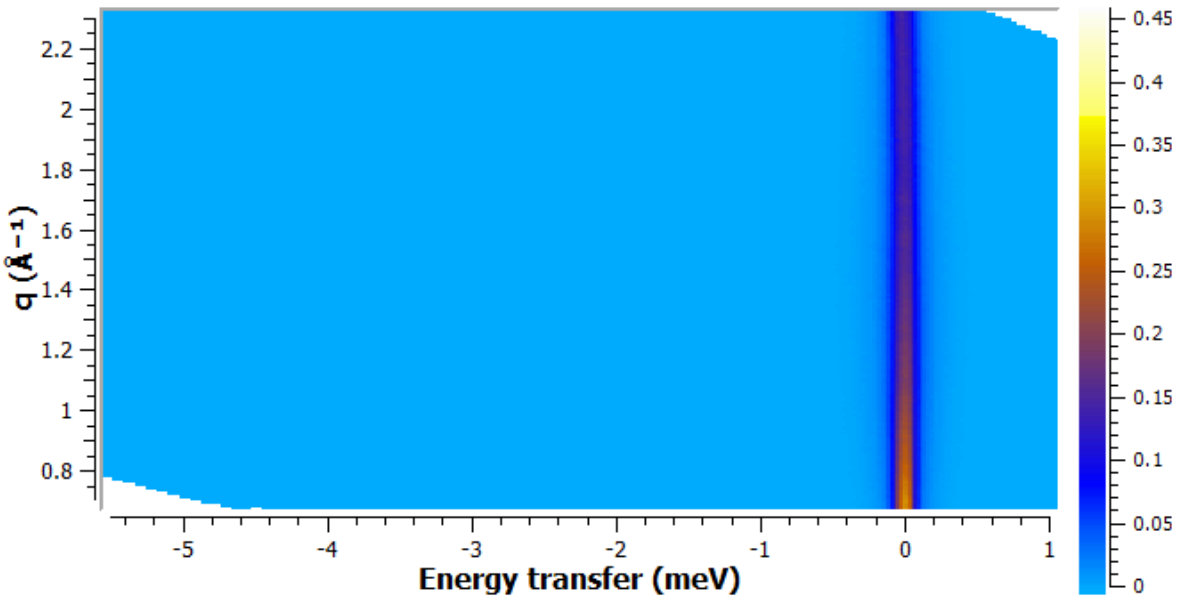

5-D IN5 powder sample @ 498K - fitting region

While information at low Q is lost, this maintains a wide energy transfer window (much wider than the Lorentzian component to be studied) with only small patches of incomplete data to be considered at the extremes of the region.

As previously mentioned, the contribution to the elastic scattering from the sample can is much lower in these measurements than those described in the previous chapter. A direct comparison between a normalised spectrum for the empty can and a normalised spectrum for the powder sample at a concentration of $c = 0.59$ is shown in figure 5-E.

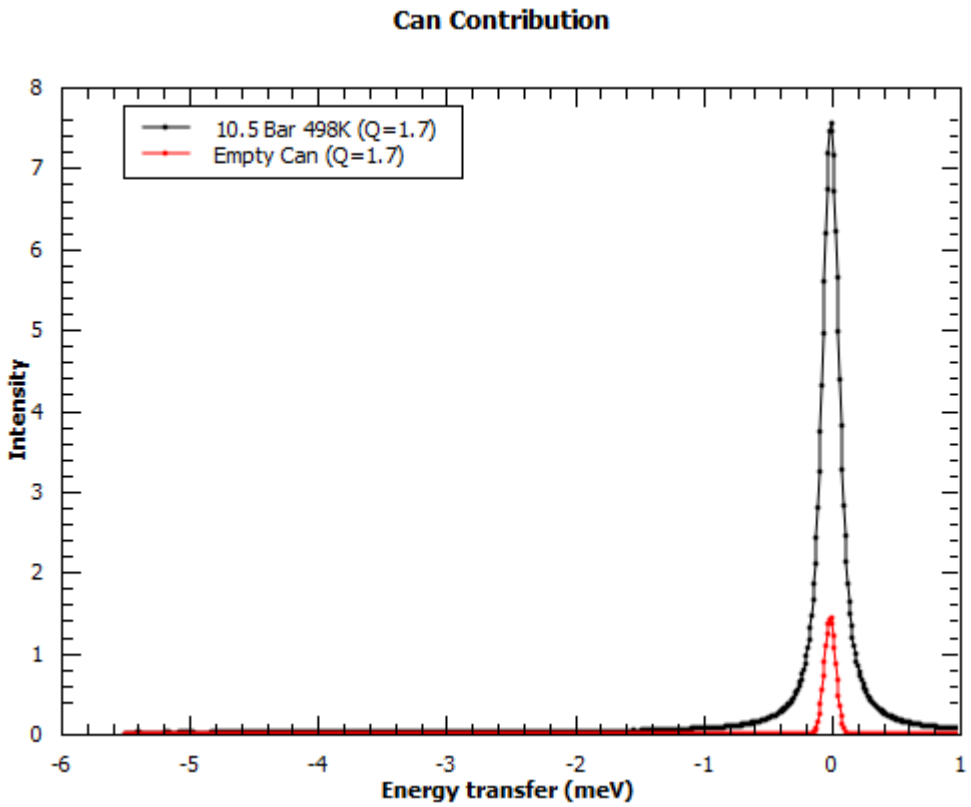

5-E IN5 sample can Vs powder sample

Preliminary trials at fitting the data with the elastic component from the can subtracted from the total scattering gave fitted Lorentzian parameters within the errors of fits performed without any such subtraction having been performed. As such, all of the fits described in this chapter have been performed on the directly imported data over the previously stated region. The small contribution from the sample can (so elastic scattering can be thought of as almost entirely resulting from the sample) has made determination of the elastic incoherent structure factor (EISF) possible.

Fitting was, again, performed using Quasilines. As the interface for this in MantidPlot was originally intended to be used with data from the indirect instruments at ISIS, a small modification had to be made to the workspaces for them to be accepted by the script. This only consisted of copying the recorded incident energy for the measurement into the parameter slot usually reserved for the analyser energy. No other alterations were necessary and, as such, this should have no effect on the fitted data.

As with the previous datasets, an elastic peak and sloping background have been fitted[88].

5.5.2 Fitted Components Overview

As with the data in the previous chapter, the need for a Lorentzian multiple component model to accurately fit the data is overwhelming. This can be seen in the probability plots for the higher temperatures in both the foil and powder samples (figures 5-F and 5-G) where, as previously described, the magnitude shown can be thought of (in simple terms) as an indication of deviation from the proposed model. The fits at lower temperatures are not shown as it becomes increasingly difficult to separate the narrow component from the elastic line width below $400\ K$.

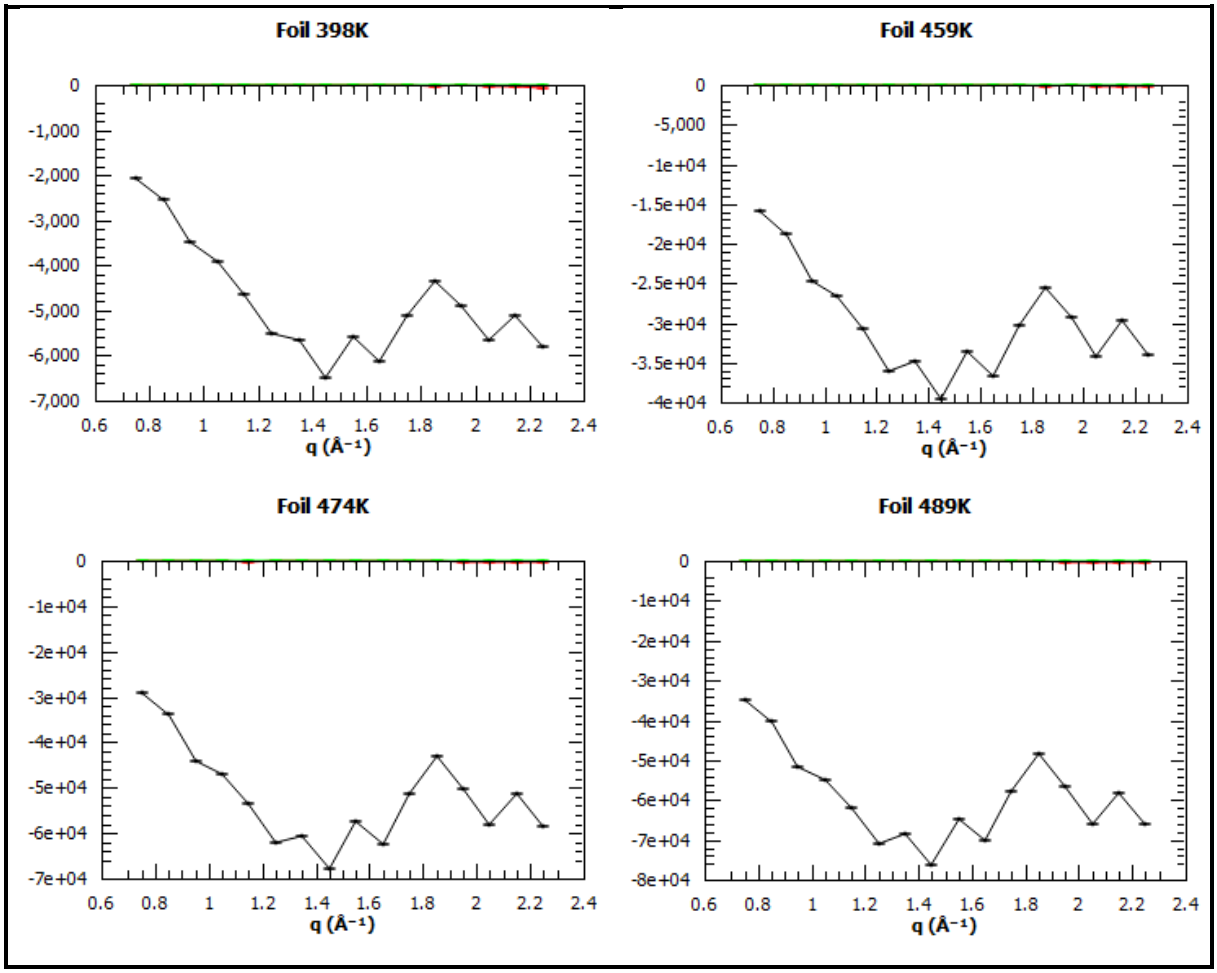

[88] Quasilines does not provide parameters for the fitted sloping background.

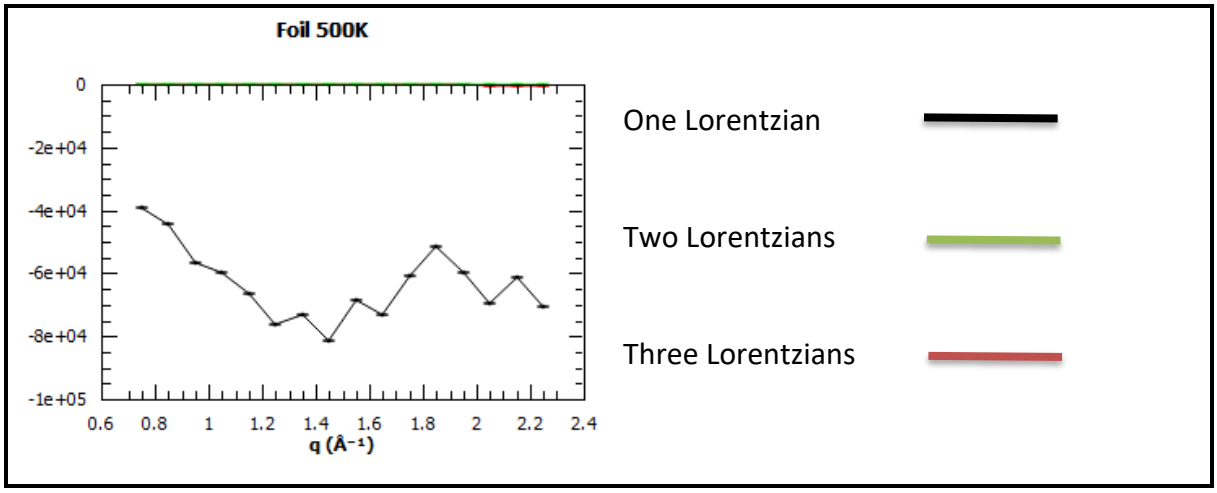

5-F IN5 foil fit probability plots

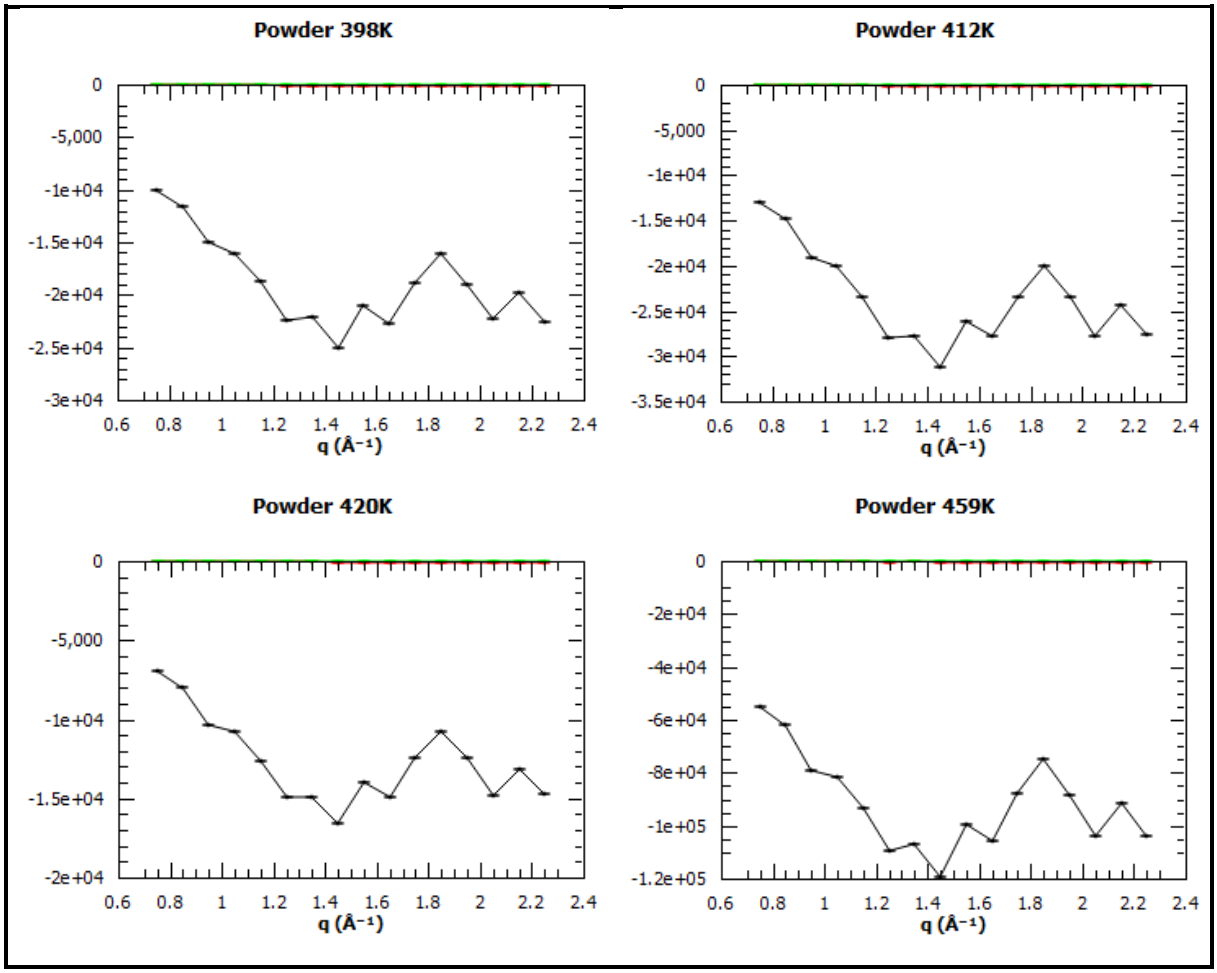

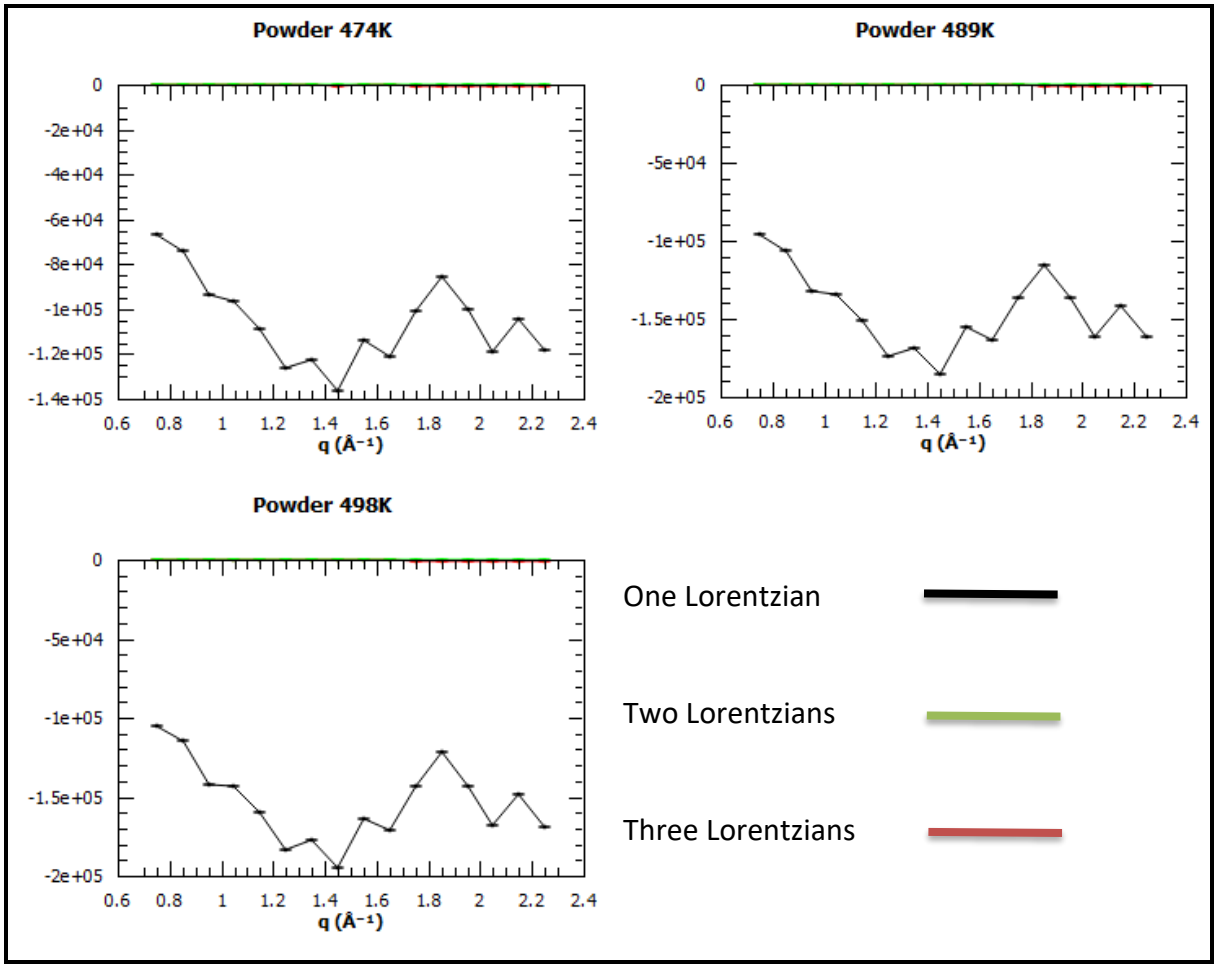

5-G IN5 powder probability plots

As with the previous experiment, the deviation from the single Lorentzian model can be seen clearly in each dataset. Figure 5-H shows an arbitrarily chosen spectrum with the fit given by the single and multiple component models. Figure 5-I shows the same data rescaled to show this deviation more clearly. In the previous experiment the fit window only extended to an energy transfer of $1.5\ meV$. In these new data, the deviation from the single Lorentzian model, and close agreement of the two Lorentzian model at higher energy transfer values, is easy to see.

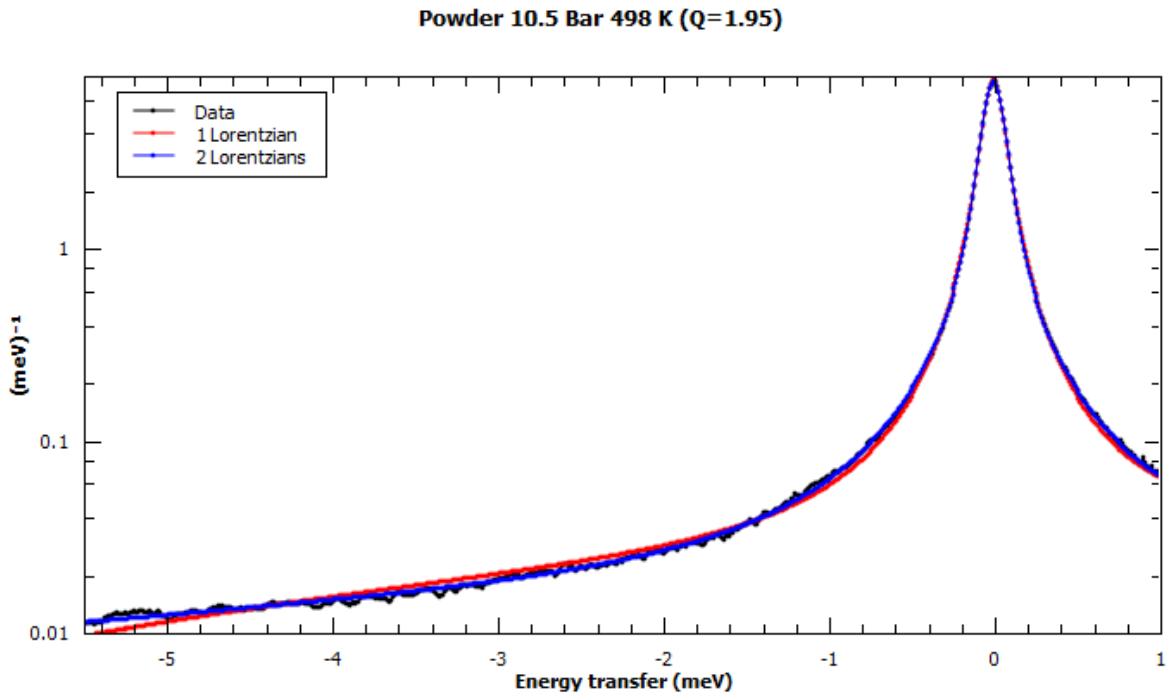

5-H Single Vs two Lorentzian fit example (full range)

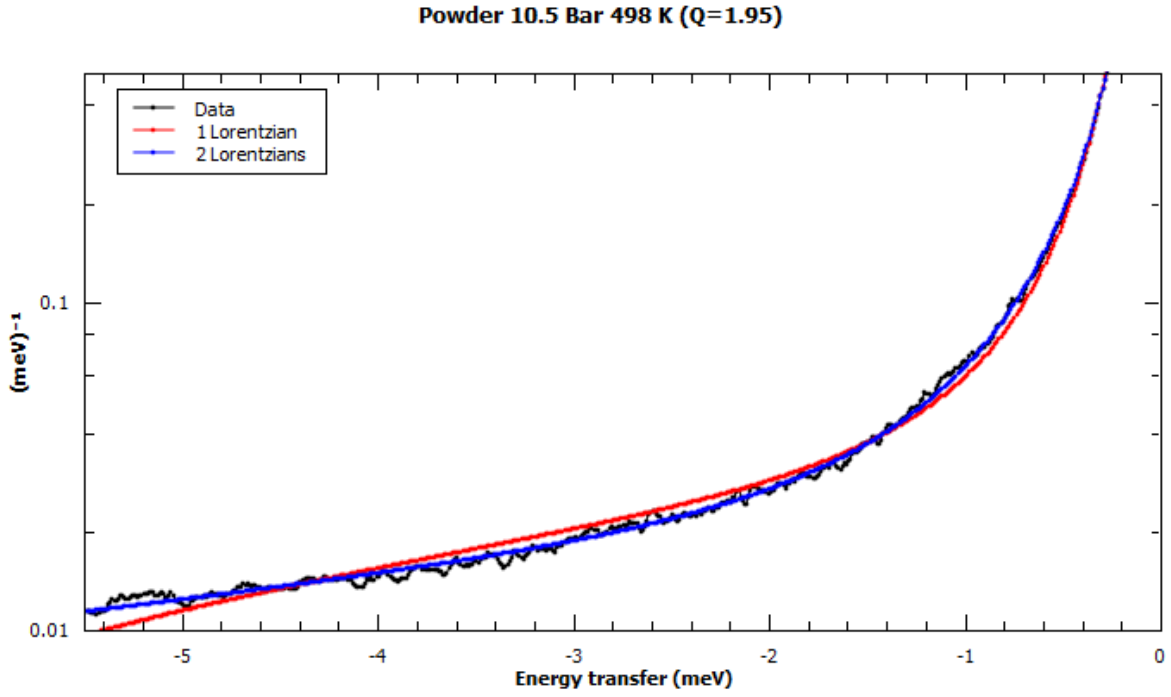

5-I Single Vs two Lorentzian fit example (cropped)

The fits to the data in this chapter give components that compare well with those described in the previous chapter for the measurements on Osiris. The narrow component can be

shown to relate to octahedral – octahedral jump diffusion. The wide component is roughly an order of magnitude wider and displays Q dependence.

As this experiment was tuned to show the wider of these components in more detail, some information about the narrow component is less clear. However, it will be shown in the following sections that this component may shed further light on the phenomenon of short range ordering as previously seen in the deuteride.

As previously mentioned, fitting the data for the measurements below $\sim 400\ K$ is tricky. The narrow component is extremely close to the elastic line at these temperatures. The remaining signal from the narrow component becomes hard to separate from the wider component. Measurements have been included for discussion in this lower temperature range, but the challenges associated with the fitting process limit their use in this analysis.

5.5.3 Narrow Component

As described in the introduction to this chapter, the two samples differ structurally. The powder sample inherently shows polycrystalline character while the foil is preferentially (though not perfectly) ordered in the 111 direction. This results in two very different sets of spectra for the narrow component. Figure 5-J shows the width of the narrow components of the measurements for both samples at $500\ K$. The powder sample displays the same polycrystalline average Chudley-Elliott broadening as seen in the previous chapter. The foil can be approximated as being fully aligned in the 111 direction.

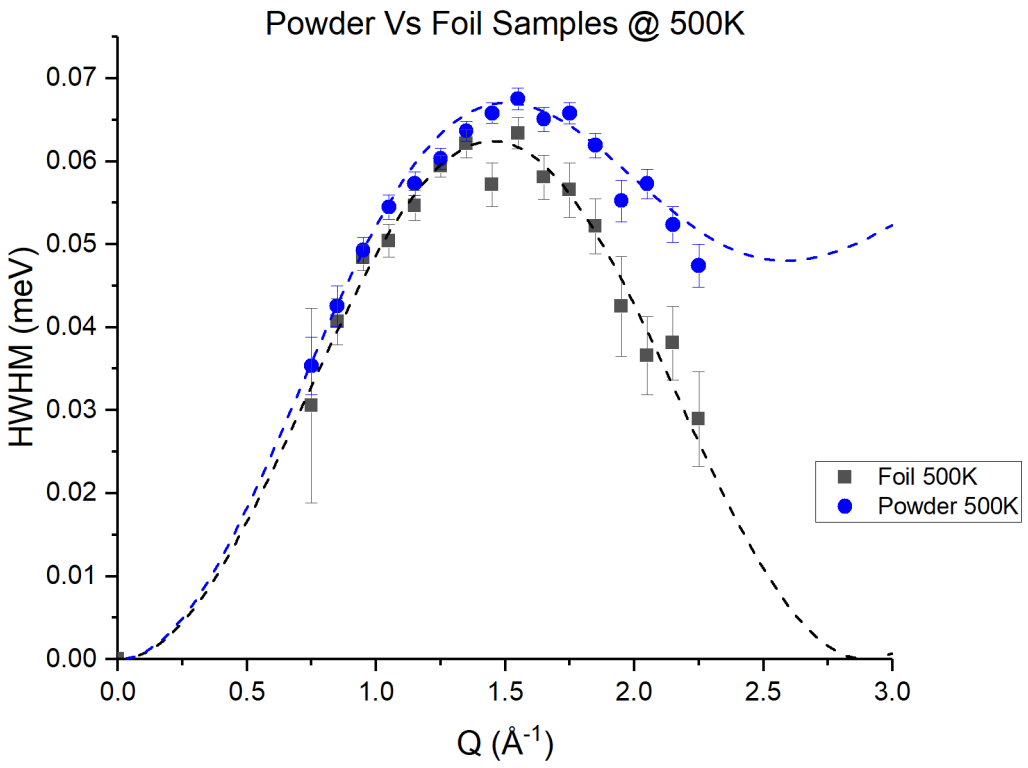

5-J Powder Vs foil narrow component widths

The specific form of the Chudley-Elliott model for the 111 plane in an FCC material is given by Bull (2001) as:

$$\Gamma_{111}(Q) = A\left(1 - \frac{1}{3}(\cos^2(\pi Q_x) + \cos^2(\pi Q_x) + \cos^2(\pi Q_x))\right) \quad (5\text{-}1)$$

Since each of the $\cos^2$ terms is identical, this reduces to:

$$\Gamma_{111}(Q) = A(1 - \cos^2(\pi Q_x)) \quad (5\text{-}2)$$

Via basic trigonometric identities, this can further be simplified to give:

$$\Gamma_{111}(Q) = A\sin^2(\pi Q_x) \quad (5\text{-}3)$$

Equation (5-3) has been used as the model to fit the narrow component of the foil measurements described in this chapter. As the material is not a perfect single crystal, the actual shape will be some combination of this single direction and the polycrystalline

average form used in the previous chapter (equation (4-1). The dashed lines in figure 5-J shows fits performed using these models to data from the respective samples.

Larger errors can be seen in the individual points for these data than was seen in comparable data in the previous chapter. This is the result of the proximity of the broadening to the elastic line and the resolution at the chosen instrument settings.

The fitted widths to the narrow component in the powder sample are summarised below.

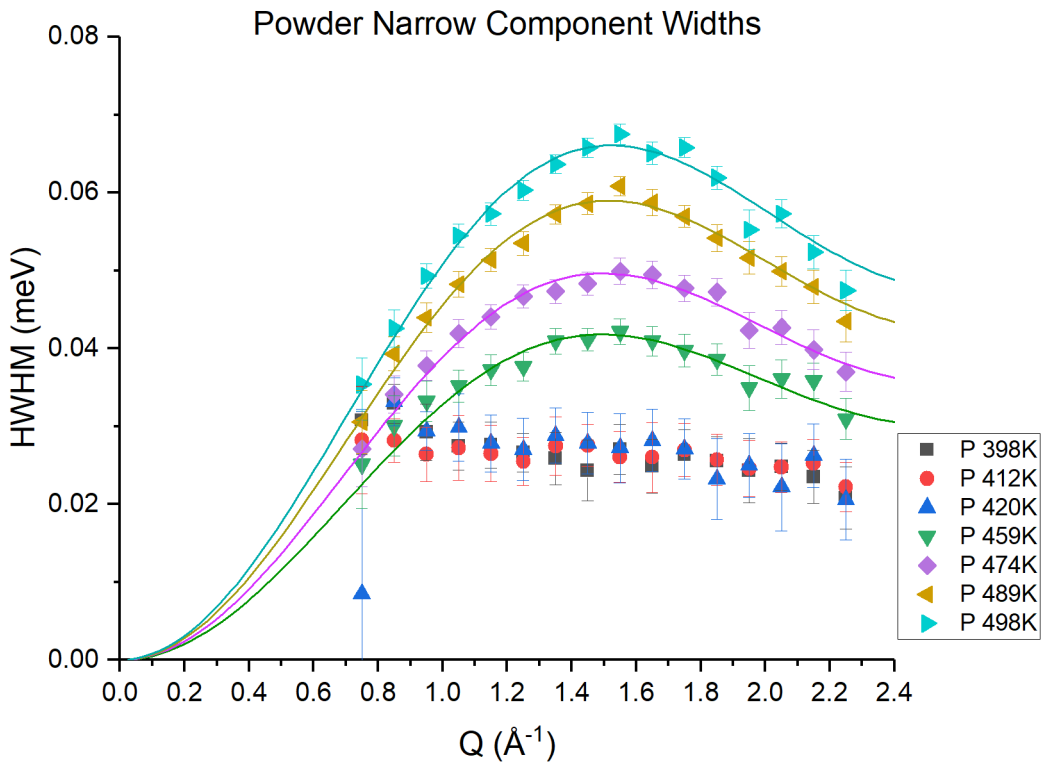

5-K IN5 Chudley-Elliott fits to powder sample narrow component

This component in the datasets below $459\ K$ dataset cannot be accurately fitted. The algorithm has failed to correctly separate it from the elastic component. It is still obvious in the probability plots (figure 5-G) that a narrow component must be fitted to the data to achieve a satisfactory fit. The general trend seen in the higher temperatures would continue should the instrument (and fitting method) allow it to be seen. This behaviour is shown in chapter 4. These data have been included in this plot for the sake of clarity and in the interest of discussion that appears later in this chapter.

The fitted parameters are shown in table 5-d to demonstrate that they broadly agree with those for the hydride sample in the previous chapter.

Temperature (K)	A (meV)	ΔA (meV)	l (Å)	Δl (Å)
459	0.03434	2.85002E-4	3.00752	0.03945
474	0.04077	2.48997E-4	3.00319	0.02733
489	0.04844	2.64488E-4	2.96707	0.02494
498	0.05427	3.45256E-4	2.95224	0.02869

5-d Chudley-Elliott fit parameters for powder sample

A similar procedure has been conducted for the widths of the narrow component in the foil sample. Figure 5-L shows fits to these data using the model given in equation (5-3).

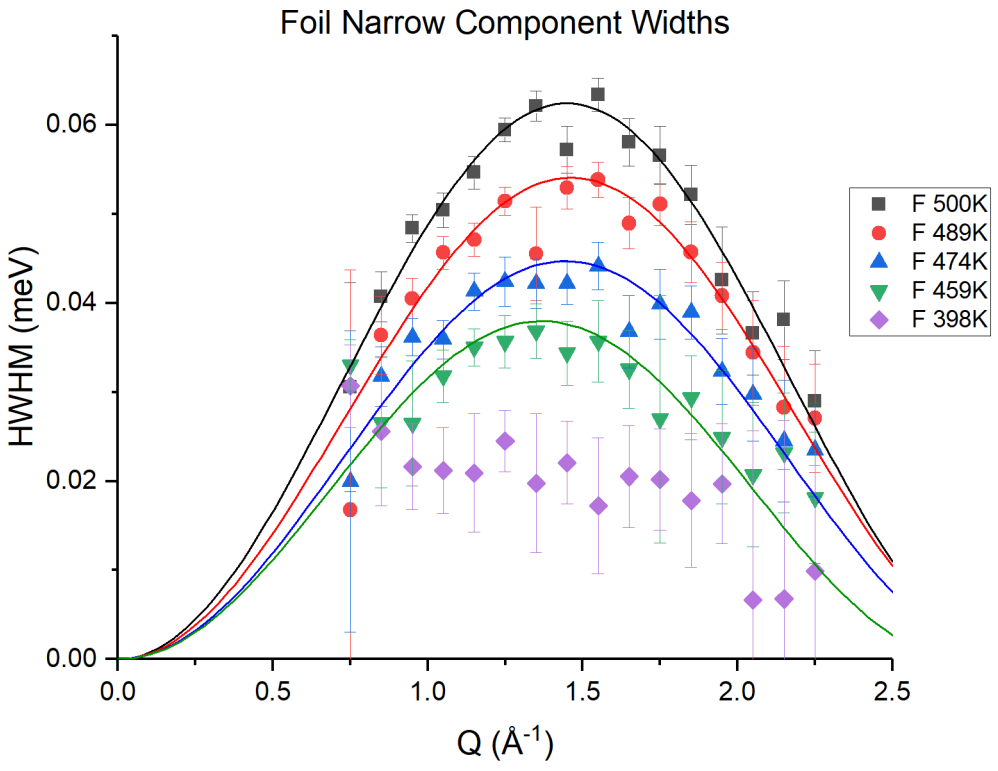

5-L Chudley-Elliott (111) fits to foil narrow components

As this model only provides a rough approximation to the system, and this component is not the focus of this experiment, no detailed analysis of the fitted parameters will be discussed

here. The magnitude of the broadening is approximately in line with that of the powder sample at each temperature. Again, below $459\ K$ the narrow Lorentzian cannot be accurately resolved and is presented for the sake of later discussion.

Of more interest here is the deviation from the fitted line (and general trend) toward the middle of each peak. Particularly in the two highest temperature measurements, a distinct reduction in the width that does not appear to be simply a statistical error can be seen. As discussed in the previous chapter, narrowing in coherent scattering due to short range order can be mapped to specific structures in the 111 direction. While the signal from this would be weak due to the comparatively small coherent scattering cross section of hydrogen, the findings in the previous chapter for deuterium suggest that it is worthy of further investigation. Discussion on this subject can be found in section 5.6.2.

5.5.4 Wide Component

The fitted widths of the second (wide) components for the powder sample display much better defined structures than was seen in the previous chapter. This is particularly true for the higher temperature measurements of the directly comparable powder sample. Plots for each of these are shown in figure 5-M.

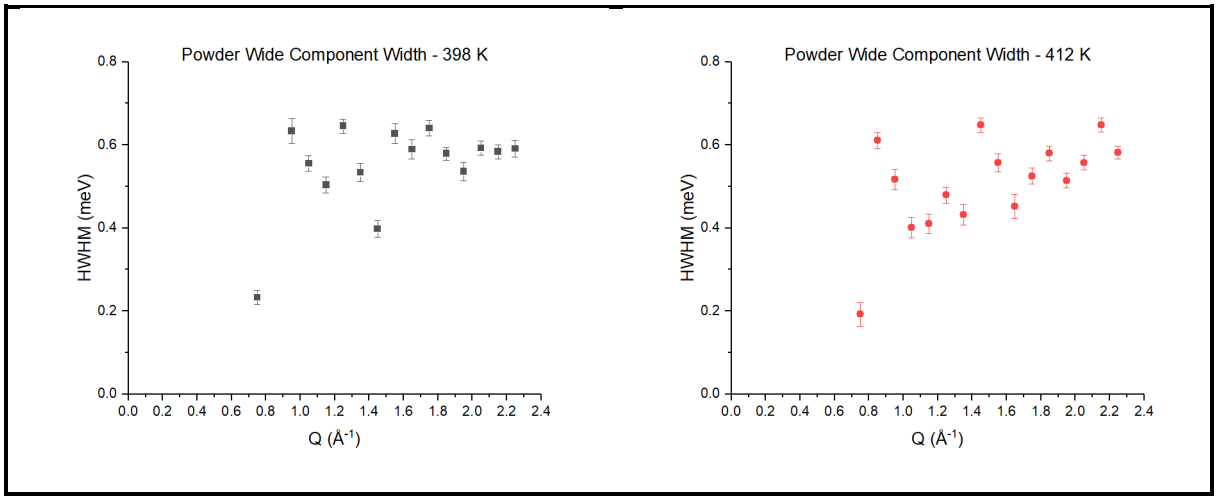

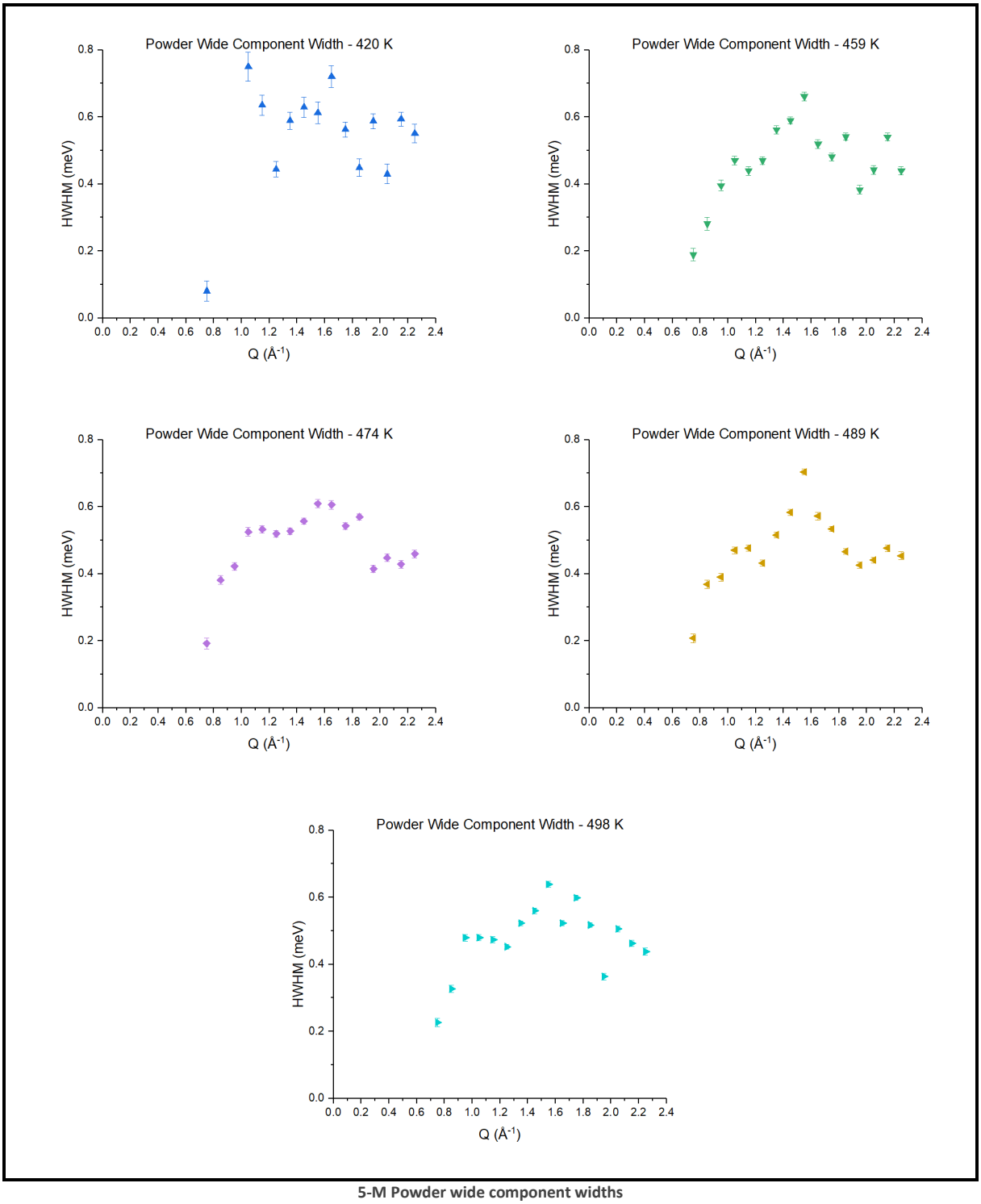

5-M Powder wide component widths

The points at low Q are thought to be unreliable. Comparison with the probability plots (figure 5-G) and the plots of the relevant narrow components (figure 5-K) suggest that the narrow component for these points is close to the elastic line and the fit not as conclusive for those at higher Q. The errors in the narrow component in this region suggest that there may be some difficulty in distinguishing the two widths. In the three lowest temperature

plots, the effect of the failure to fit the narrow component can be seen across the entire Q range. However, it should be noted that this still results in an average width that is relatively consistent with the higher temperature measurements.

The four higher temperature measurements do not immediately appear to show Arrhenius behaviour. Instead, when overlaid, their points appear to be randomly scattered around a mean for each detector group.

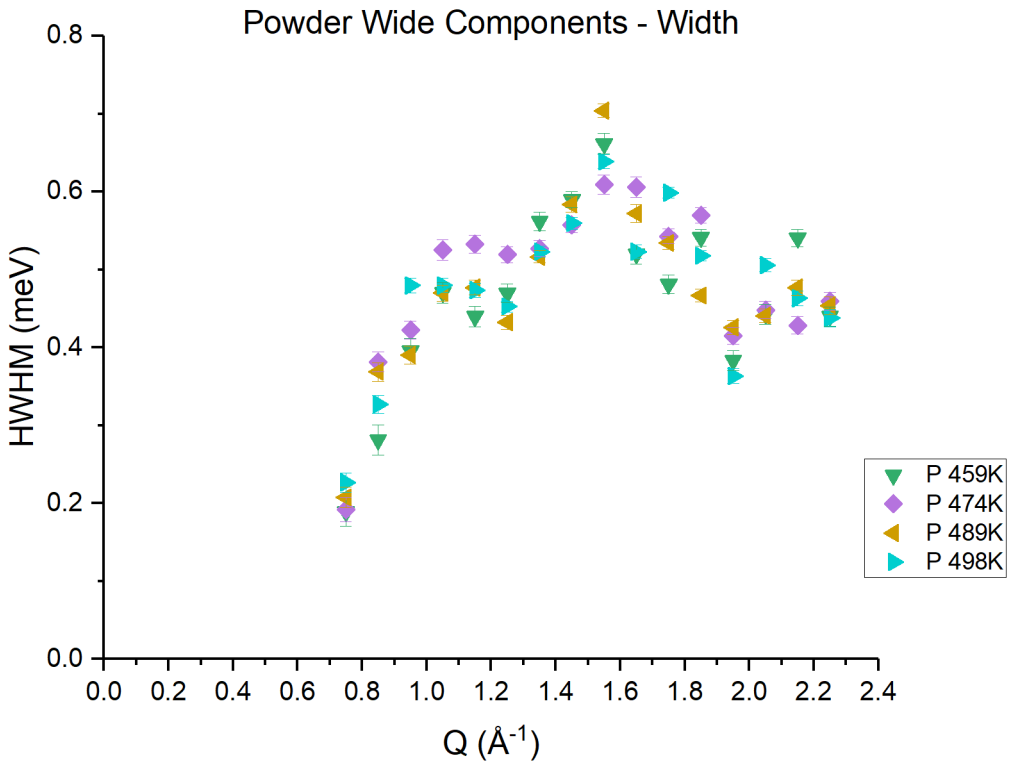

5-N Powder wide component (high temp) widths

The pattern is less clear for the foil sample. Due to the difference in the sample geometry, it was not expected that the form of these would match those of the powder sample. The widths of the wide components for the foil sample are presented in figure

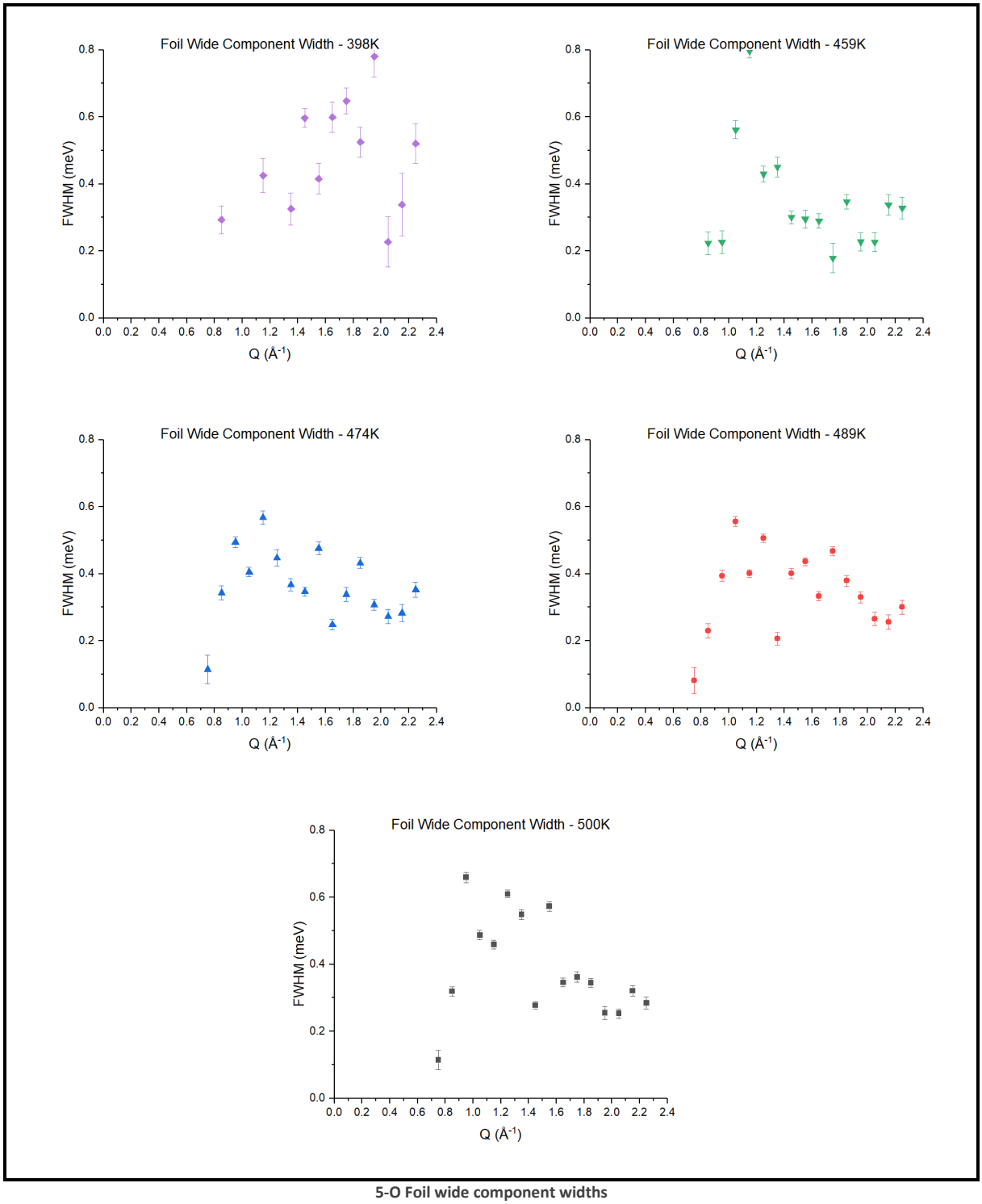

5-O Foil wide component widths

As with the previous sample, the fit at $398\ K$ varies substantially from the higher temperatures and obvious temperature dependence is not seen.

Both samples appear to show a clear pattern in the relative intensity of the wider component as a function of the total QENS scattering in both temperature and Q. This is

shown in figure 5-P(powder sample) and figure 5-Q (foil sample). The fraction in these plots is given by:

$$\frac{Amplitude\ of\ wide\ component}{Amplitude\ of\ narrow\ component + Amplitude\ of\ wide\ component} \quad (5\text{-}4)$$

This provides an approximation to the fraction of the quasielatic scattering that arrises from the wider component.

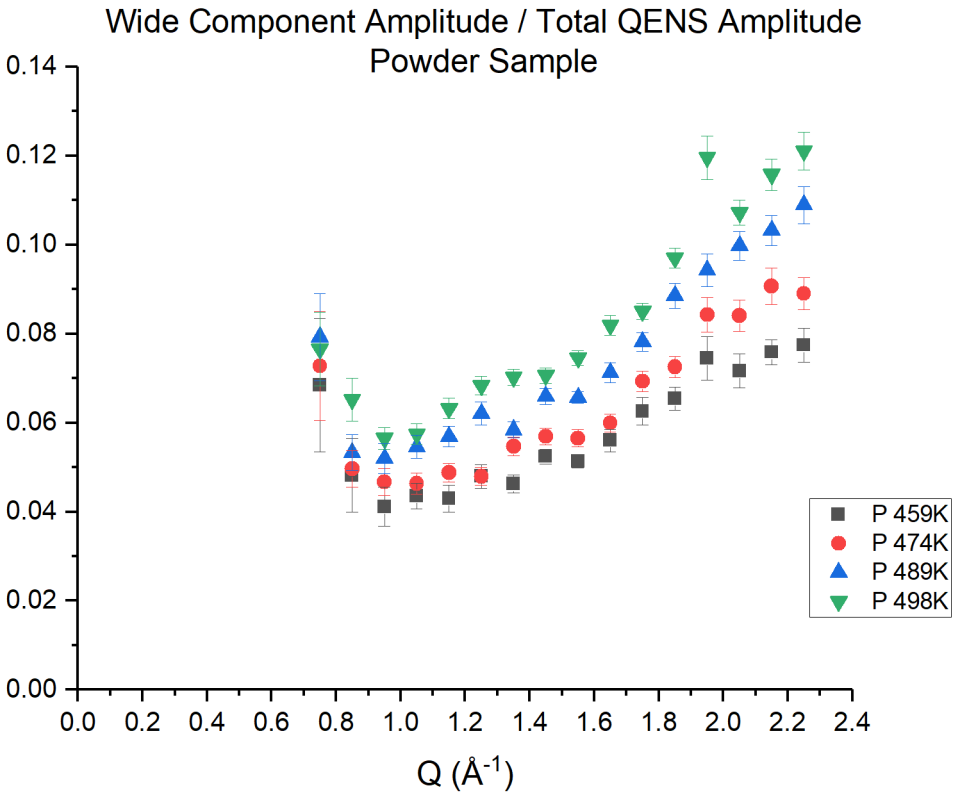

5-P Powder wide component fraction

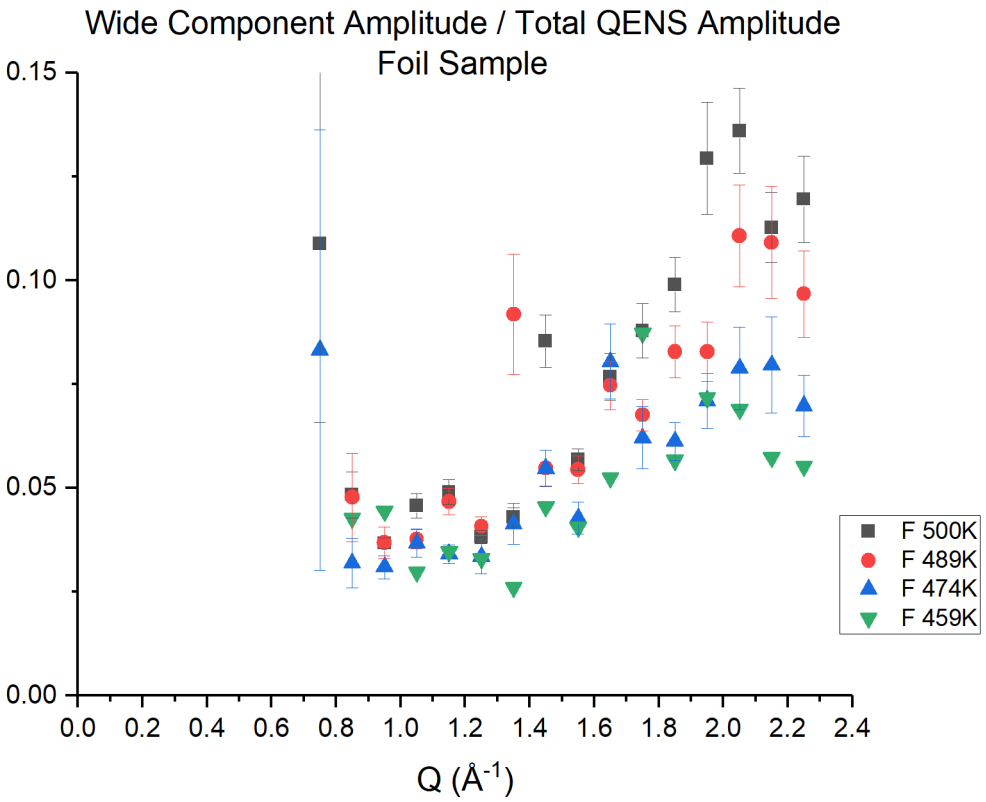

5-Q Foil wide component fraction

These two plots further show the deviation from the pattern for the fitted data below $Q \approx 1$. As with the fitted widths, the powder data appear to show very definite trends while the data for the foil sample contains a lot of stochastic noise.

It has been possible to extract the form of the elastic incoherent structure factor (EISF) for both samples (powder – figure 5-R, foil – figure 5-S). The statistical quality of the plots for each sample is broadly in line with that seen for the previously presented data (section 4.4). However, it can clearly be seen that the data for the foil sample follows the pattern seen in the powder.

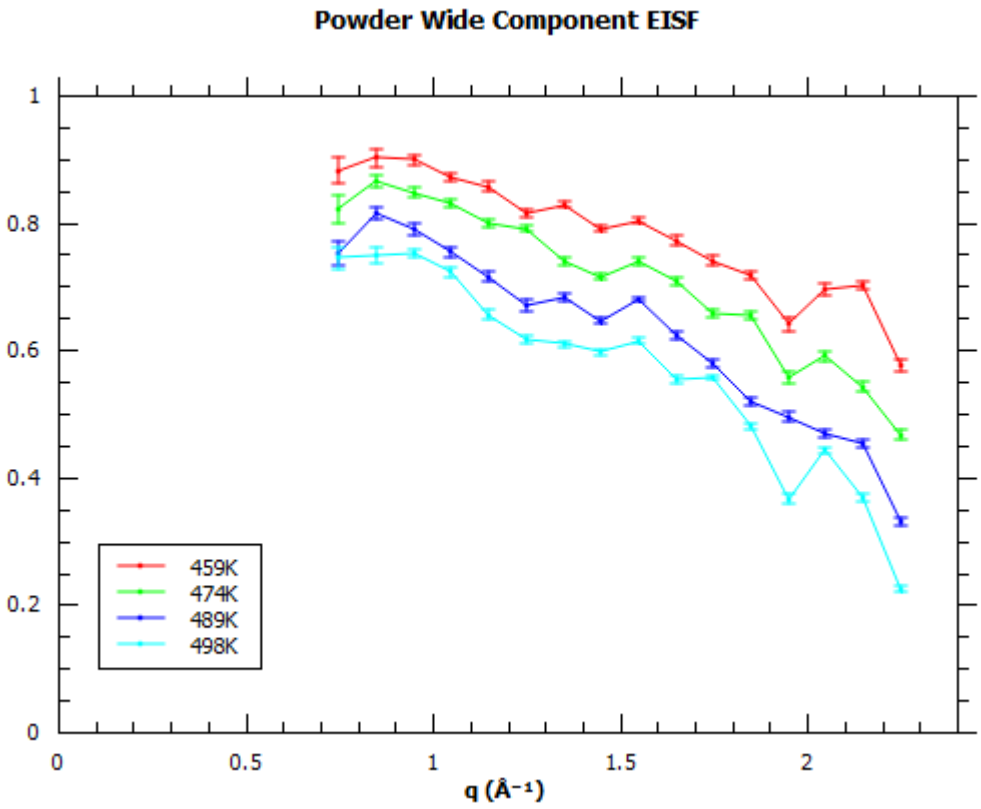

5-R Powder EISF

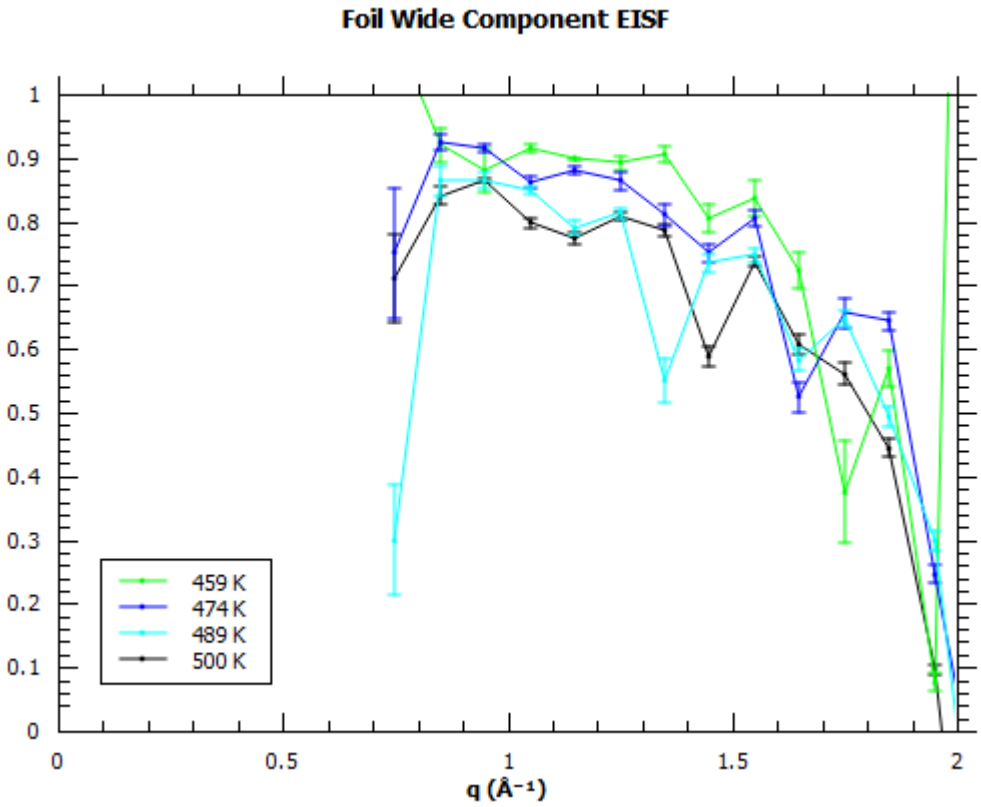

5-S Foil EISF

5.6 Discussion

5.6.1 Wide Component

This experiment was initially proposed to investigate the wide component that had been seen in the previous measurements for both the hydride and deuteride samples on Osiris. It has not been possible to fully characterise the motion that gives rise to this wide Lorentzian. The following section is a discussion on the nature of the findings and possible mechanisms that may explain this phenomenon.

There are reports in the literature of second Lorentzian components (wider than that attributed to the octahedral – octahedral long range diffusion in the bulk) being seen in QENS measurements on palladium hydride.

The measurements presented in this chapter suggest a form of motion that is distinct from both the 'pipe diffusion' described by Heuser et al. (2014) and the 'rapid diffusion near the surface' described by Kofu et al. (2016). Both of these pieces of work show broadening in different energy transfer regions that have a different $\Gamma(Q)$ form.

There is little difference in the relative intensity of the wide component at any given temperature between the two samples. This appears to rule out any effect happening at or near the surface as it seems reasonable to expect to see a greater proportion of any such scattering in the powder due to its much larger surface area. A similar converse argument can be made regarding pipe diffusion where the small particle size of the powder could be expected to lead to a much lower grain boundary density than would be seen in the foil.

No temperature dependence has been determined in the fitted widths of the higher quality data. Changes in the apparent widths seen in the lower temperature measurements can probably be put down to fitting errors due to the poor fit to the narrow component. The lower temperature measurements look very much like the data described in the previous chapter suggesting that a similar fitting error (albeit due to the lack of data at the opposite end of the energy transfer scale) may be the source of their apparent temperature dependence. However, a small but convincing temperature dependence can be seen in the relative proportion of QENS scattering from the wider component as well as the EISFs of both samples.

This appears to infer that the rate of the motion that gives rise to this Lorentzian either is not dependent on temperature or that the change in the rate with temperature is shallow enough to not be detected over the measured range. However, this motion appears to become more abundant as temperature rises. If this is a jump process, the activation energy has to be extremely low or zero. There is a possibility that the results are skewed by an unknown dependence on concentration. This seems unlikely as, for the four higher temperature measurements used in the analysis for each sample, concentrations fall into the range $0.59 < c < 0.63$. Even a heavy dependence on concentration would not be expected to effect the measured widths enough to completely obscure any the sort of temperature dependence predicted for any of the obvious jump motions in the system.

At first glance, the widths fitted to the wide component in both samples could be attributed to some sort of fast long range translational diffusion with a similar length scale to that seen in the narrow component. However, no known model predicts the exact form seen in the high temperature powder measurements. Since the form seen in these is common to all of the measurements, it cannot be dismissed as random noise distributed around one of these models.

There is some ambiguity about the quality of the fit below $Q \approx 1$. This may cast some doubt on the validity of the points that appear to suggest a drop to zero broadening at low Q. If the low Q points are discounted, the remaining data appears similar to the sort of broadening that would be expected from particles performing some sort of localised motion.

The effective quasielastic broadening from a particle performing a random walk between a number of nearest neighbour sites is uniform in Q except for a characteristic peak that with a shape determined by the number of sites involved in the motion. A summary of the possible forms for a range of different numbers of sites is shown in figure 5-T.

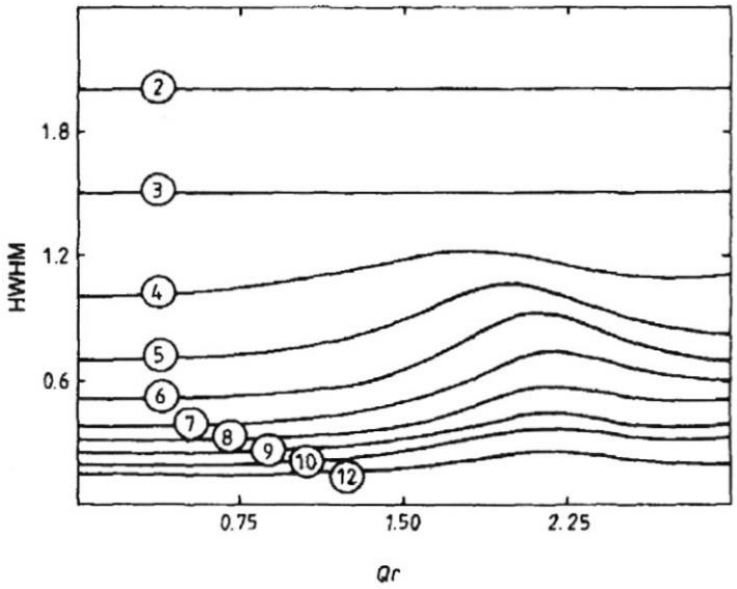

5-T QENS broadening from random walk localised motion
Bée (1988)

These models assume a random motion around a series of sites and have been shown to agree well with systems that display such localised motions. Further to this, the EISFs calculated for this component appear to show similarities in their general form (figure 5-U) and temperature dependence to those seen in previously for scattering from rapid local motions. One such case is ZrV_2H_x, where hydrogen rapidly moves around a hexagonal series of sites before making a jump to a neighbouring hexagon (figure 5-V).

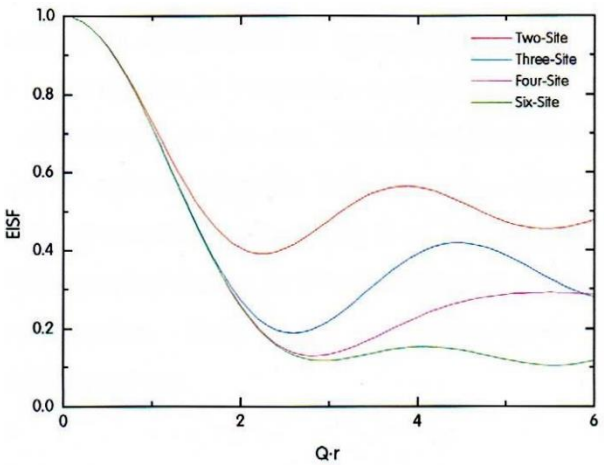

5-U EISF models for localised motion
(Bull, 2001)

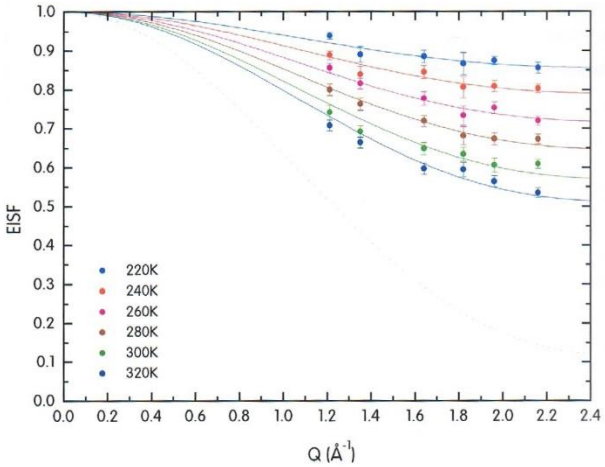

5-V ZrV_2H_x localised motion EISF change with temperature
(Bull, 2001)

Without measurements that extend to much higher values of Q, it is not possible to confirm whether the EISFs reported match any of the models given in figure 5-U. However, the

general match over the measured Q range, and the apparent similarity in the temperature dependence with the measurements shown in figure 5-V, suggest that this data could possibly describe a similar type of motion.

It is also possible that this data shows a previously unreported jump motion. Ab initio calculations performed by Totolici (2001) suggested a possible quantum state for a proton in an octahedral site where its probability density function extends into the neighbouring tetrahedral sites. Later inelastic neutron scattering studies confirmed that an excited state exists at the predicted energy (Kemali et al., 2000). At the temperatures measured, it is feasible that some of the protons may exist in this state. Thereby allowing diffusion from the tetrahedral site into a neighbouring octahedral site. The energy barrier from T-O is low enough that temperature dependence of the rate associated with this jump may not be seen. However, the relative proportion of protons in any higher energy state would be expected to increase with temperature. This could feasibly give the sort of temperature dependence seen in this data. As this would be diffusion from a state that simultaneously occupies multiple sites to a single site, the pattern seen in the broadening may not agree with the existing jump diffusion models.

Neither of these possibilities have been investigated quantitatively and, as such, are only provided here as speculation that may help to guide future work on the subject.

5.6.2 Narrow Component

Comprehensive analysis of the narrow components fitted to these data has not been undertaken in this chapter. The experiment was designed to leave these extremely close to the instrument resolution so that the wider component could be examined in more detail. In general, they appear match the fits seen in the data discussed in the previous chapter. However, there appears to be a series of minor deviations from the expected models for the broadening in the foil sample. As the rest of the fitted points appear to agree with the model, they suggest a real deviation rather than stochastic noise.

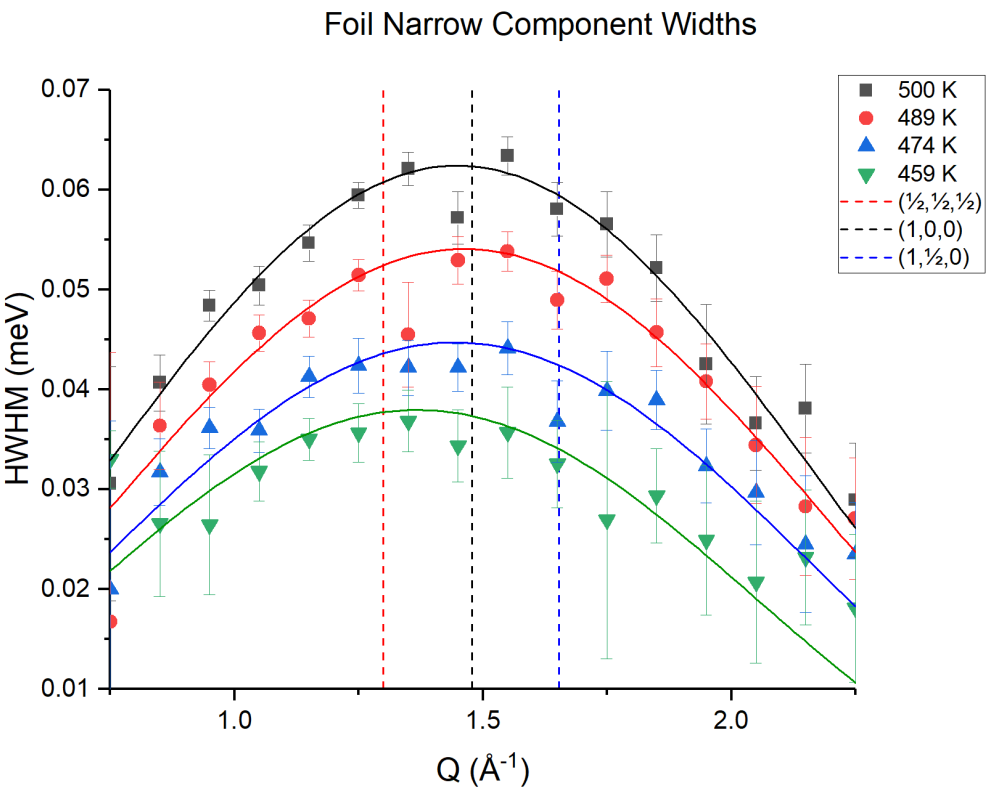

5-W Foil sample - possible SRO

It was discussed in the previous chapter that short range ordering had been seen in the deuteride sample at temperatures well above those where it has been previously reported. There are hints that this sort of behaviour has been seen in the narrow component of the foil sample. Figure 5-W shows the fitted data at the four highest temperatures (where the fit to this component is satisfactory). The three dashed lines represent the approximate location where narrowing due to short range ordering (as described by Clapp & Moss for an FCC lattice) is possible for measurements in the 111 direction, if one of the predicted superstructures is present. As the material is preferentially (and not fully) ordered in the 111 direction, these lines can only serve as a guide to the actual location of the possible peaks in $S(Q)$.

While the coherent scattering that is affected by the narrowing associated with short range order only constitutes around 2.5% of the total scattering from hydrogen, the alignment of the crystallites in the rolled foil amplifies the plane where this effect is most visible. For the points where the deviations from the model are largest, the fitted errors are also

considerable (although not large enough for the model to fit through the error bars in several of them). This suggests a slight difficulty in performing the fit and could reasonably be expected for any point where the broadening is a function of separate contributions from coherent and incoherent scattering. This phenomenon can be seen in the previous chapter where the measurements on the deuteride have consistently larger errors than the hydride for similar measurements. The level of narrowing expected for this type of structure is likely to fall within the error margins of the fitted points.

There appears to be correlation between the measured reduction in broadening and possible $(1,0,0)$ and $\left(1,\frac{1}{2},0\right)$ structures across the measured range. The latter of these structures appears to be preferential at lower temperatures with the former becoming more abundant at the top of the temperature range. The apparent deviation towards the $\left(\frac{1}{2},\frac{1}{2},\frac{1}{2}\right)$ structure in the $489\ K$ data is likely to be the result of a minor fitting error due to detector grouping.

While this is by no means conclusive, it is a strongly suggests that the ordering reported in for the deuteride, is also present in the hydride at these temperatures. It also tentatively hints at a change in the preferential ordered structure across the measured range.

6 Conclusions

6.1 Key Findings

A previously unreported form of motion has been seen QENS measurements of both beta palladium hydride and deuteride. This motion produces a Lorentzian in QENS spectra that has a width approximately ten times that of the well documented octahedral – octahedral jump diffusion. In the hydride, the width of this component has been shown to have form in Q but either no, or very little, dependence on temperature. However, this motion appears to become more abundant as temperature increases. The exact form seen does not appear to match existing models for jump diffusion. Nor does it appear to be *fully* explained as a simple localised motion. While the exact nature of this motion has not been characterised, the evidence presented here leaves little doubt that it must be a real motion in the system.

Clear evidence for short range order (amongst the deuterium residing in palladium interstitial sites) has been seen in beta palladium deuteride at far higher temperatures than has previously been reported. This phenomenon has been shown in this work for concentrations around $c = 0.55$, at temperatures between 433 and $500\ K$. Previous reports of ordering have all been below $150\ K$, and never in the pure beta phase.

Evidence has been presented for short range order in the beta phase hydride at a similar temperature and composition range as for the deuteride. The evidence for this is not as conclusive as for SRO in the deuteride. However, it is compelling enough to warrant further investigation. This evidence also appears to point towards a change in the ordered structure at around $475\ K$. Again, neither of these phenomena are previously reported.

6.2 Summary of Other Results and Discussion

After 150 years of research into the palladium – hydrogen system, there still appear to be secrets to uncover and features to characterise. This work has focussed on the high concentration, high temperature region (compared to much of the work in the literature). Existing experimental work in this region is extremely patchy. Reports of the differences in the behaviour of the three isotopes of hydrogen for this region, are rarer still.

A feasible value for the diffusion rate "crossover point" for beta palladium hydride and deuteride has been produced ($\sim 720\ K$). Therefore, the model applied to the deuteride sample appears to be reasonable. However, it is known to be an approximation (one

designed to fit to the average behaviour of a more complex system) and there are still questions that need to be answered about the underlying system.

The evidence for ordering at high temperatures calls into question some of the widely held beliefs about the system. The interparticle interactions in the lattice gas appear to be stronger than had previously been assumed (otherwise ordering would be vastly reduced at these temperatures). Further, 'ordering' in a lattice gas suggests preferential occupation of some sites over others. This potentially provides a barrier to diffusion into certain sites and suggests that, for the concentration and temperature range measured in this work, the proportion of sites available for diffusive jumps cannot simply be modelled as $(1 - c)$. It also calls into question many results where jump diffusion has been measured, but results have been presented in terms of chemical diffusion (via the $D \propto \frac{l^2}{6\tau}$ relationship).

The ordering seen also means that the phase diagram of the palladium - hydrogen system needs to be revised. It has been shown in the discussion sections earlier in this work, that existing reports of changes in ordered structures may be associated with changes in the thermal properties of the system (including the rate of lattice expansion with increasing temperature). Therefore, similar changes in these properties could occur in within, or above, the ranges covered by this work.

Nothing measured in the course this work has suggested tetrahedral occupancy on any measurable timescale. None of the motions seen correlate with jumps at this length. It is therefore thought that the tetrahedral sites can be considered more in terms of a 'pathway' than anywhere that the hydrogen can reside. The evidence presented in this work for SRO, suggests that the interaction between the interstitial hydrogen (/ deuterium / tritium) in this system is strong enough to make some neighbouring octahedral sites 'unavailable'. It therefore seems incredibly unlikely that the tetrahedral sites neighbouring an occupied octahedral could ever be occupied in any way that could be considered 'stable'.

6.3 Further work

The findings described in this work create far more questions than they answer. There is a wealth of potential further study that could help to resolve some of these.

There is one particularly obvious example that's already been discussed in this work. A direct measurement of $S(Q)$ over the Q range of the deuteride QENS measurements would have allowed a much more useful information to be extracted from the deuteride data described in this work.

It may be possibly to experimentally separate the coherent and incoherent QENS components of Pd-D using neutron polarisation analysis. Should this technique be appropriate, it would be possible to directly compare the residence time (/jump rate) of hydrogen and deuterium (potentially even tritium). It may also provide a further insight into the relationship between the tracer and bulk diffusion coefficients in the system. It could also be interesting to use this technique to investigate the hydride. This may help to determine whether the 'dips' reported here (IN5 foil experiment) stem from the small coherent contribution to the total scattering.

It would be extremely interesting to perform QENS experiments on a single crystal of palladium at similar concentrations and temperatures to those described in this work (and beyond). This may help to determine the nature of the ordered structures present. It may also help to determine the relationship between the potentials due to first and second nearest neighbours in the lattice gas.

It has been noted in this work that the neutron diffraction patterns of Pd-H and Pd-D each show distinct preference for certain Bragg peaks. It should be possible to use this phenomenon to directly assess the composition of the lattice gas where both hydrogen and deuterium are present. In a mixed isotope experiment, the measured peak intensities would be proportional to the H/D ratio in the solid. This ratio normally has to be inferred by sampling the remaining gas in the sample chamber after equilibrium has been reached. Simultaneous sorption measurements (using either the IGA-N at ISIS or the IMI system at the ILL) could help to calculate the total composition. Focus has shifted recently in the fusion community from creating 'pure isotopic gas supplies' to 'viable fuel mixes'. As such, accurate determination of this ratio as a function of temperature and the partial pressures of the isotopes could be extremely useful.

Away from neutron scattering, there are numerous measurements that would help to shed light on the phenomena reported in this document.

While there appears to be no sudden shift in the lattice parameter of Pd-H(/D) with changes to ordering, there is a suggestion that the rate of thermal expansion could change with such transitions. Therefore, it is possible that dilatometry may yield information about location of any boundaries between ordered phases.

While SRO may have little effect on the fundamental jump rate in Pd-H(/D), it could reasonably be expected to affect the diffusivity. This would be particularly true in the direction normal to the ordering plane in single crystals or other anisotropic samples. It may be possible to see changes in diffusivity via permeation or sorption. However, experiments that would probe the temperature and pressure ranges of interest are not proposed here.

It seems that there is a good case for a full revision of the sorption measurements that are used to plot the phase diagram. Modern technology allows for these to be performed by automated processes that provide much higher resolution kinetic data than has been available previously.

It would also be extremely interesting to investigate whether the properties described here for palladium can be seen in its alloys.

References

Abbenseth, R., & Wipf, H. (1980). Thermal expansion and lattice anharmonicity of Pd-H and Pd-D alloys. *Journal of Physics F: Metal Physics, 10*(3), 353.

Alvarez, L. W., & Cornog, R. (1939). Helium and Hydrogen of Mass 3. *Physical Review, 56*(6), 613-613.

Anderson, I. S., Ross, D. K., & Carlile, C. J. (1978a). The 50K transition in β-phase palladium deuteride observed by neutron scattering. *Journal of Physics C: Solid State Physics, 11*(9), L381.

Anderson, I. S., Ross, D. K., & Carlile, C. J. (1978b). *Measurements of diffusion of hydrogen in β palladium hydride by high resolution neutron scattering*. International Atomic Energy Agency (IAEA): IAEA.

Araki, H., Nakamura, M., Harada, S., Obata, T., Mikhin, N., Syvokon, V., & Kubota, M. (2004). Phase Diagram of Hydrogen in Palladium. *Journal of Low Temperature Physics, 134*(5), 1145-1151. doi:10.1023/b:Jolt.0000016734.40467.28

Baranowski, B., & Dębowska, L. (2007). Remarks on superconductivity in PdH. *Journal of Alloys and Compounds, 437*(1-2), L4-L5. doi:10.1016/j.jallcom.2006.07.082

Bée, M. (1988). *Quasi-elastic Neutron Scattering Principles and Application in Solid State Chemistry, Biology, and Materials Science*. Bristol: Adam Hilger.

Beg, M. M., & Ross, D. K. (1970). The quasielastic scattering of cold neutrons from the beta phase of palladium hydride (and hydrogen diffusion). *Journal of Physics C: Solid State Physics, 3*(12), 2487.

Benham, M. J., & Ross, D. K. (1989). Experimental Determination of Absorption-Desorption Isotherms by Computer-Controlled Gravimetric Analysis*. In *Zeitschrift für Physikalische Chemie* (Vol. 163, pp. 25).

Blaschko, O. (1984). Structural features occurring in PdDx within the 50 K anomaly region. *Journal of the Less Common Metals, 100*, 307-320. doi:https://doi.org/10.1016/0022-5088(84)90071-7

Brockhouse, B. N., & Stewart, A. T. (1955). Scattering of Neutrons by Phonons in an Aluminum Single Crystal. *Physical Review, 100*(2), 756-757.

Broom, D. P. (2011). *Hydrogen Storage Materials*. London: Springer.

Buckel, W., & Stritzker, B. (1973). Superconductivity in the palladium-silver-deuterium system. *Physics Letters A, 43*(5), 403-404. doi:http://dx.doi.org/10.1016/0375-9601(73)90393-9

Bull, D. J. (2001). *Static and Dynamic Correllation in Lattice Gas Systems: An Application to the Intermetallic Hydride ZrV2Hx.* (PhD), University of Salford, Salford.

Carlile, C. J., & Ross, D. K. (1974). An experimental verification of the Chudley-Elliot model for the diffusion of hydrogen in α-phase Pd/H. *Solid State Communications, 15*(11–12), 1923-1927. doi:http://dx.doi.org/10.1016/0038-1098(74)90118-5

Cavendish, H. (1766). Three Papers, Containing Experiments on Factitious Air, by the Hon. Henry Cavendish, F. R. S. *Philosophical Transactions of the Royal Society of London, 56*(0), 141-184. doi:10.1098/rstl.1766.0019

Chadwick, J. (1932). Possible Existence of a Neutron. *Nature, 129*(312). doi:10.1038/129312a0

Chudley, C. T., & Elliott, R. J. (1961). Neutron Scattering from a Liquid on a Jump Diffusion Model. *Proceedings of the Physical Society, 77*(2), 353.

Clapp, P. C., & Moss, P. C. (1968). Correlation functions of disordered binary alloys. II. *Physical Review, 171*(3), 754-763. doi:10.1103/PhysRev.171.754

Clapp, P. C., & Moss, S. C. (1966). Correlation functions of disordered binary alloys. *Physical Review, 142*(2), 418-427. doi:10.1103/PhysRev.142.418

Clarivate Analytics. (2017). EndNote X8. Retrieved from http://endnote.com/

Cook, J. C., Richter, D., Hempelmann, R., Ross, D. K., & Züchner, H. (1991). Quasi-elastic neutron scattering studies of collective and correlated tracer diffusion in the systems α′-NbDx and α′-NbHx. *Journal of the Less Common Metals, 172-174*, 585-594. doi:https://doi.org/10.1016/0022-5088(91)90179-8

De Gennes, P. G. (1959). Liquid dynamics and inelastic scattering of neutrons. *Physica, 25*(7), 825-839. doi:https://doi.org/10.1016/0031-8914(59)90006-0

DECC. (2013). *Energy Consumption in the UK (2013) - Overall energy consumption in the UK since 1970*. (13D/154). Retrieved from http://www.gov.uk/government/uploads/system/uploads/attachment_data/file/190618/chapter_1_overall_factsheet.pdf.

Deuterium. (2014). In *Encyclopaedia Brittanica Online* (Vol. 2014): Brittanica Online.

dotPDN LLC. (2017). Paint.net. Retrieved from https://www.getpaint.net/

Fajans, K. (1913). Radioactive transformations and the periodic system of the elements. *Berichte der Deutschen Chemischen Gesellschaft*(46), 422-439.

Flanagan, T. B. (2008). Frederick A. Lewis. *Platinum Metals Review, 52*(2), 120-122. doi:10.1595/147106708x298836

Flanagan, T. B., & Oates, W. A. (1991). The Palladium-Hydrogen System. *Annual Review of Materials Science, 21*(1), 269-304. doi:doi:10.1146/annurev.ms.21.080191.001413

Fukai, Y. (1993). *The Metal Hydrogen System*. Berlin: Springer-Verlag.

Fukai, Y. (2005). *The Metal Hydrogen System* (2nd ed.). Berlin: Springer.

Glugla, M., Antipenkov, A., Beloglazov, S., Caldwell-Nichols, C., Cristescu, I. R., Cristescu, I., . . . Tada, E. (2007). The ITER tritium systems. *Fusion Engineering and Design, 82*(5–14), 472-487. doi:http://dx.doi.org/10.1016/j.fusengdes.2007.02.025

Glugla, M., Cristescu, I. R., Cristescu, I., & Demange, D. (2006). Hydrogen isotope separation by permeation through palladium membranes. *Journal of Nuclear Materials, 355*(1-3), 47-53. doi:10.1016/j.jnucmat.2006.04.003

Glugla, M., Dörr, L., Lässer, R., Murdoch, D., & Yoshida, H. (2002). Recovery of tritium from different sources by the ITER Tokamak exhaust processing system. *Fusion Engineering and Design, 61–62*(0), 569-574. doi:http://dx.doi.org/10.1016/S0920-3796(02)00250-8

Glugla, M., Murdoch, D. K., Antipenkov, A., Beloglazov, S., Cristescu, I., Cristescu, I. R., . . . Mack, A. (2006). ITER fuel cycle R&D: Consequences for the design. *Fusion Engineering and Design, 81*(1–7), 733-744. doi:http://dx.doi.org/10.1016/j.fusengdes.2005.07.038

Graham, T. (1866). On the Absorption and Dialytic Separation of Gases by Colloid Septa. *Philosophical Transactions of the Royal Society of London, 156*, 399-439. doi:10.1098/rstl.1866.0018

Graham, T. (1869). On the Relation of Hydrogen to Palladium. *Proceedings of the Royal Society of London, 17*, 212-220.

Griffith, W. P. (2003). Bicentenary of Four Platinum Group Metals PART I: RHODIUM AND PALLADIUM - EVENTS SURROUNDING THEIR DISCOVERIES. *Platinum Metals Review, 47*(4), 175-183.

Groß, A., & Dianat, A. (2007). Hydrogen Dissociation Dynamics on Precovered Pd Surfaces: Langmuir is Still Right. *Physical Review Letters, 98*(20), 206107.

Hall, P. L., & Ross, D. K. (1981). Incoherent neutron scattering functions for random jump diffusion in bounded and infinite media. *Molecular Physics, 42*(3), 673-682. doi:10.1080/00268978100100521

Hammouda, B. (2016). Coherent and Incoherent Neutron Scattering. In: NIST. Retrieved from https://www.ncnr.nist.gov/staff/hammouda/distance_learning/chapter_9.pdf.

Hertel, P. (1974). Superconductivity in PdH, PdD and PdAgD systems. *Zeitschrift für Physik, 268*(2), 111-115. doi:10.1007/BF01669866

Heuser, B. J., Trinkle, D. R., Jalarvo, N., Serio, J., Schiavone, E. J., Mamontov, E., & Tyagi, M. (2014). Direct measurement of hydrogen dislocation pipe diffusion in deformed polycrystalline Pd using quasielastic neutron scattering. *Phys Rev Lett, 113*(2), 025504. doi:10.1103/PhysRevLett.113.025504

HMSO. (2008). *Climate Change Act 2008*. HMSO Retrieved from http://www.legislation.gov.uk/ukpga/2008/27/pdfs/ukpga_20080027_en.pdf.

Holmryd, S., Sköld, K., Pilcher, E., & Larsson, K. E. (1964). A slow neutron chopper time-of-flight spectrometer at the reactor R2 in Sweden. *Nuclear Instruments and Methods, 27*(1), 61-68. doi:http://dx.doi.org/10.1016/0029-554X(64)90137-5

IEA. (2012). *Key World Energy Statistics*. Paris: IEA Retrieved from http://www.iea.org/publications/freepublications/publication/kwes.pdf.

ILL.eu. (2018). IN5 Instrument Layout. Retrieved from https://www.ill.eu/users/instruments/instruments-list/in5/description/instrument-layout/

Janßen, S., Natter, H., Hempelmann, R., Striffler, T., Stuhr, U., Wipf, H., . . . Cook, J. C. (1997). Hydrogen diffusion in nanocrystalline PD by means of quasielastic neutron scattering. *Nanostructured Materials, 9*(1–8), 579-582. doi:http://dx.doi.org/10.1016/S0965-9773(97)00129-3

Jewell, L., & Davis, B. (2006). Review of absorption and adsorption in the hydrogen–palladium system. *Applied Catalysis A: General, 310*, 1-15. doi:10.1016/j.apcata.2006.05.012

Johansson, M., Skúlason, E., Nielsen, G., Murphy, S., Nielsen, R. M., & Chorkendorff, I. (2010). Hydrogen adsorption on palladium and palladium hydride at 1bar. *Surface Science, 604*(7-8), 718-729. doi:10.1016/j.susc.2010.01.023

Jones, D. G. (1968). *Sources of Tritium and its Behaviour upon Release to the Environment*. Oak Ridge, Tennessee: US Atomic Energy Commission / Division of Technical Information.

Joubert, J. M., & Thiébaut, S. (2009). Thermodynamic assessment of the Pd–H–D–T system. *Journal of Nuclear Materials, 395*(1–3), 79-88. doi:http://dx.doi.org/10.1016/j.jnucmat.2009.09.021

Kathawa, J., Fry, C., & Thoennessen, M. (2013). Discovery of palladium, antimony, tellurium, iodine, and xenon isotopes. *Atomic Data and Nuclear Data Tables, 99*(1), 22-52. doi:10.1016/j.adt.2012.01.004

Kemali, M., Totolici, J. E., Ross, D. K., & Morrison, I. (2000). Inelastic Neutron Scattering Measurements and Ab Initio Calculations of Hydrogen in Single-Crystal Palladium. *Physical Review Letters, 84*(7), 1531-1534.

Kharecha, P. A., & Hansen, J. E. (2013). Prevented mortality and greenhouse gas emissions from historical and projected nuclear power. *Environ Sci Technol, 47*(9), 4889-4895. doi:10.1021/es3051197

Kofu, M., Hashimoto, N., Akiba, H., Kobayashi, H., Kitagawa, H., Tyagi, M., . . . Yamamuro, O. (2016). Hydrogen diffusion in bulk and nanocrystalline palladium: A quasielastic neutron scattering study. *Physical Review B, 94*(6), 064303.

Krimmel, H., Schimmele, L., Elsasser, C., & Fahnle, M. (1994). Self-trapped hydrogen states in metals determined from quantum mechanical calculations using potentials based on ab initio data: I. Hydrogen isotopes in Pd. *Journal of Physics: Condensed Matter, 6*(38), 7679.

Lasser, R. (1984). SOLUBILITY OF PROTIUM, DEUTERIUM, AND TRITIUM IN THE ALPHA-PHASE OF PALLADIUM. *Physical Review B, 29*(8), 4765-4768. doi:10.1103/PhysRevB.29.4765

Lässer, R. (1985). Isotope dependence of phase boundaries in the PdH, PdD, and PdT systems. *Journal of Physics and Chemistry of Solids, 46*(1), 33-37. doi:http://dx.doi.org/10.1016/0022-3697(85)90192-1

Lässer, R., Bell, A., & Bainbridge, N. (1999). *The preparative gas chromatographic system of the JET active gas handling system - tritium commissioning and use during and after DTE1*. Retrieved from United Kingdom:

Lässer, R., Bell, A. C., Bainbridge, N., Brennan, D., Grieveson, B., Hemmerich, J. L., . . . Wilson, K. (1999). Operation of the JET Active Gas Handling System during and after DTE1.

Fusion Engineering and Design, 46(2–4), 307-312. doi:http://dx.doi.org/10.1016/S0920-3796(99)00023-X

Lasser, R., & Klatt, K. H. (1983). SOLUBILITY OF HYDROGEN ISOTOPES IN PALLADIUM. *Physical Review B, 28*(2), 748-758. doi:10.1103/PhysRevB.28.748

Lässer, R., & Powell, G. L. (1987). Solubility of protium, deuterium and tritium in palladium-silver alloys at low hydrogen concentrations. *Journal of the Less Common Metals, 130*(0), 387-394. doi:http://dx.doi.org/10.1016/0022-5088(87)90133-0

Lewis, F. A. (1967). *The Palladium-Hydrogen System*. London: Academic Press.

Lopez, N., Łodziana, Z., Illas, F., & Salmeron, M. (2004). When Langmuir Is Too Simple: H_{2} Dissociation on Pd(111) at High Coverage. *Physical Review Letters, 93*(14), 146103.

Maisonnier, D., Cook, I., Pierre, S., Lorenzo, B., Luigi, D. P., Luciano, G., . . . Aldo, P. (2006). DEMO and fusion power plant conceptual studies in Europe. *Fusion Engineering and Design, 81*(8–14), 1123-1130. doi:http://dx.doi.org/10.1016/j.fusengdes.2005.08.055

Majorowski, S., & Baranowski, B. (1982). Diffusion coefficients of hydrogen and deuterium in highly concentrated palladium hydride and deuteride phases. *Journal of Physics and Chemistry of Solids, 43*(12), 1119-1127. doi:http://dx.doi.org/10.1016/0022-3697(82)90140-8

Mantid. (2013). Manipulation and Analysis Toolkit for Instrument Data: Mantid Project,. Retrieved from http://www.mantidproject.org

McCracken, G., & Stott, P. (2013). *Fusion: The Energy of the Universe* (2nd ed.). Oxford: Academic Press.

McLennan, K., Gray, E., & Dobson, J. (2008). Deuterium occupation of tetrahedral sites in palladium. *Physical Review B, 78*(1). doi:10.1103/PhysRevB.78.014104

Microsoft. (2017). Office 365. Retrieved from https://www.office.com/

Mitsui, T., Rose, M. K., Fomin, E., Ogletree, D. F., & Salmeron, M. (2003). Dissociative hydrogen adsorption on palladium requires aggregates of three or more vacancies. *Nature, 422*(6933), 705-707. doi:10.1038/nature01557

Momma, K., & Izumi, F. (2011). VESTA 3 for three-dimensional visualization of crystal, volumetric and morphology data. *Journal of Applied Crystallography, 44*(6), 1272-1276. doi:doi:10.1107/S0021889811038970

References

Murata, T., & Shibata, K. (2002). Evaluation of The (α, n) Reaction Nuclear Data for Light Nuclei. *Journal of Nuclear Science and Technology, 39*(sup2), 76-79. doi:10.1080/00223131.2002.10875044

Nagel, M. C. (1982). Frederick Soddy: From alchemy to isotopes. *Journal of Chemical Education, 59*(9), 739. doi:10.1021/ed059p739

Nelin, G., & Sköld, K. (1975). Diffusion of hydrogen in the β-phase of pd-H studied by small energy transfer neutron scattering. *Journal of Physics and Chemistry of Solids, 36*(11), 1175-1182. doi:http://dx.doi.org/10.1016/0022-3697(75)90187-0

NIST. (2013). Neutron scattering lengths and cross sections. Retrieved from https://www.ncnr.nist.gov/resources/n-lengths/

NIST. (2014). Atomic Data for Palladium. *Basic Atomic Spectroscopic Data.* Retrieved from http://physics.nist.gov/PhysRefData/Handbook/Tables/palladiumtable1.htm

Nobelprize.org. (2018). The Nobel Prize in Physics 1994. Retrieved from https://www.nobelprize.org/nobel_prizes/physics/laureates/1994/

Oates, W. A., Lässer, R., Kuji, T., & Flanagan, T. B. (1986). The effect of isotopic substitution on the thermodynamic properties of palladium-hydrogen alloys. *Journal of Physics and Chemistry of Solids, 47*(4), 429-434. doi:http://dx.doi.org/10.1016/0022-3697(86)90036-3

Odom, B., Hanneke, D., D'Urso, B., & Gabrielse, G. (2006). New Measurement of the Electron Magnetic Moment Using a One-Electron Quantum Cyclotron. *Physical Review Letters, 97*(3), 030801.

Oliphant, M. L. E., Harteck, P., & Rutherford, L. (1934). Transmutation Effects Observed with Heavy Hydrogen. *Proceedings of the Royal Society A: Mathematical, Physical and Engineering Sciences, 144*(853), 692-703. doi:10.1098/rspa.1934.0077

OriginLab. (2017). OriginPro. Northampton MA. Retrieved from http://www.originlab.com/Origin

Particle Data Group, Beringer, J., Arguin, J. F., Barnett, R. M., Copic, K., Dahl, O., . . . Schaffner, P. (2012). Review of Particle Physics. *Physical Review D, 86*(1), 010001. doi:10.1103/PhysRevD.86.010001

Perricone, M. (2006). Signal to Background. *Symmetry Magazine.* 3(1). Retrieved from http://www.symmetrymagazine.org/cms/?pid=1000258

Pitt, M. P., & Gray, E. M. (2003). Tetrahedral occupancy in the Pd-D system observed by in situ neutron powder diffraction. *EPL (Europhysics Letters), 64*(3), 344.

Python Foundation. (2017). Python (Version 2.x). Retrieved from https://www.python.org/

Reynolds, E. (2015). ExcelPython. Retrieved from http://ericremoreynolds.github.io/excelpython/

Riis, T., Hagen, E. F., Vie, P. J. S., & Ulleberg, Ø. (2006). Hydrogen Production & Storage. In IAEA (Ed.). France: IAEA Publications.

Ross, D. K. (1992). The interpretation of coherent quasielastic neutron scattering experiments on lattice gases and similar systems. *Physica B: Condensed Matter, 182*(4), 318-322. doi:http://dx.doi.org/10.1016/0921-4526(92)90033-O

Ross, D. K., Kemali, M., & Bull, D. J. (1999). Coherent quasi-elastic neutron scattering from lattice gases and its relationship to fick's law of diffusion. In A. Pękalski & K. Sznajd-Weron (Eds.), *Anomalous Diffusion From Basics to Applications: Proceedings of the XIth Max Born Symposium Held at Lądek Zdrój, Poland, 20–27 May 1998* (pp. 45-60). Berlin, Heidelberg: Springer Berlin Heidelberg.

Ross, D. K., Totolici, J. E., Kemali, M., Morrison, I., Ivanov, A., Johnson, M. R., & Elsässer, C. (2001). Chapter 17 - Proton Wave Functions in Palladium Studied by Ab Initio Calculations and Inelastic Neutron Scattering Methods. In P. Maurizio & P. Rinaldo (Eds.), *Recent Advances in Hydride Chemistry* (pp. 507-530). Amsterdam: Elsevier.

RSC.Org. (2018). Periodic Table - Palladium. Retrieved from http://www.rsc.org/periodic-table/element/46/palladium

Rybalko, V. F., Morozov, A. N., Neklyudov, I. M., & Kulish, V. G. (2001). Observation of new phases in Pd–D systems. *Physics Letters A, 287*(1–2), 175-182. doi:http://dx.doi.org/10.1016/S0375-9601(01)00411-X

Schiavone, E. J., & Trinkle, D. R. (2016). Ab initiomodeling of quasielastic neutron scattering of hydrogen pipe diffusion in palladium. *Physical Review B, 94*(5). doi:10.1103/PhysRevB.94.054114

Schirber, J. E., Mintz, J. M., & Wall, W. (1984). Superconductivity of palladium tritide. *Solid State Communications, 52*(10), 837-838. doi:http://dx.doi.org/10.1016/0038-1098(84)90251-5

Sears, V. F. (1992). Neutron scattering lengths and cross sections. *Neutron News, 3*(3), 26-37. doi:10.1080/10448639208218770

Serif. (2017a). Affinity Designer (Version 1.5.x): Serif. Retrieved from https://affinity.serif.com/en-gb/designer/

Serif. (2017b). Affinity Photo. Retrieved from https://affinity.serif.com/en-gb/photo/

Sicking, G. (1984). Isotope effects in metal-hydrogen systems. *Journal of the Less Common Metals, 101*(0), 169-190. doi:http://dx.doi.org/10.1016/0022-5088(84)90093-6

Sieverts, A. (1929). The Absorbtion of Gasses by Metals. *Zeitschrift für Metallkunde, 21*, 37-46.

Sieverts, A., & Zapf, G. (1935). The solubility of deuterium and hydrogen in solid palladium. *Zeitschrift für Physikalische Chemie, A174*, 359.

Singwi, K. S., & Sjölander, A. (1960). Resonance absorption of nuclear gamma rays and the dynamics of atomic motions. *Physical Review, 120*(4), 1093-1102. doi:10.1103/PhysRev.120.1093

Sinha, S. K., & Ross, D. K. (1988). Self-consistent density response function method for dynamics of light interstitials in crystals. *Physica B+C, 149*(1), 51-56. doi:https://doi.org/10.1016/0378-4363(88)90218-5

Sivia D.S., Carlile C.J., Howells W.S., & König S. (1992). Bayesian analysis of quasielastic neutron scattering data. *Physica B: Condensed Matter, 182*(4), 341-348. doi:https://doi.org/10.1016/0921-4526(92)90036-R

Sköld, K., & Nelin, G. (1966). Neutron study of the diffusion of hydrogen in palladium. *Solid State Communications, 4*(6), 303-306. doi:http://dx.doi.org/10.1016/0038-1098(66)90458-3

Sköld, K., & Nelin, G. (1967). Diffusion of hydrogen in the α-phase of Pd-H studied by small energy transfer neutron scattering. *Journal of Physics and Chemistry of Solids, 28*(12), 2369-2380. doi:http://dx.doi.org/10.1016/0022-3697(67)90022-4

Skoskiewicz, T. (1972). Superconductivity in the palladium-hydrogen and palladium-nickel-hydrogen systems. *11*(2).

Smith, C. L. (2005). The need for fusion. *Fusion Engineering and Design, 74*(1–4), 3-8. doi:http://dx.doi.org/10.1016/j.fusengdes.2005.08.015

Soddy, F. (1913). The Radio Elements and the Periodic Law. *Chemical News*(107), 97-99.

Soddy, F. (1922). The Origins of the Conception of Isotopes. *Nobel Lecture*(1921 - Chemistry).

STFC. (2013). UK science facility praised by international review. Retrieved from http://www.stfc.ac.uk/news/uk-science-facility-praised-by-international-review/

STFC. (2017a). OSIRIS Instrument Retrieved from http://www.isis.stfc.ac.uk/images/instruments/osiris/osiris-design-6096.jpg

STFC. (2017b). OSIRIS Technical Information. Retrieved from https://www.isis.stfc.ac.uk/Pages/Osiris-technical-information.aspx

Suess, H. E., & Urey, H. C. (1956). Abundances of the Elements. *Reviews of Modern Physics, 28*(1), 53-74.

Telling, M. T. F., & Anderson, K. H. (2008). The OSIRIS User Guide In. ISIS Facility, Didcot.

Thermo Fischer Scientific. (2018a). 11515 Palladium foil, 0.1mm (0.004in) thick, 99.9% (metals basis). Retrieved from https://www.alfa.com/en/catalog/011515/

Thermo Fischer Scientific. (2018b). Alfa Aesar™ Palladium powder, spherical, APS 0.5-1.7 micron, 99.95% (metals basis) Retrieved from https://www.fishersci.co.uk/shop/products/palladium-powder-spherical-aps-0-5-1-7-micron-99-95-metals-basis/11360318

Thomson, J. J. (1913). Bakerian Lecture: Rays of Positive Electricity. *Proceedings of the Royal Society A: Mathematical, Physical and Engineering Sciences, 89*(607), 1-20. doi:10.1098/rspa.1913.0057

Totolici, J. E. (2001). *Ab Initio Simulations and Neutron Scattering Studies of Structure and Dynamics in PdH.* (PhD), University of Salford, Salford.

Trinkle, D. R., Ju, H., Heuser, B. J., & Udovic, T. J. (2011). Nanoscale hydride formation at dislocations in palladium: Ab initio theory and inelastic neutron scattering measurements. *Physical Review B, 83*(17). doi:10.1103/PhysRevB.83.174116

Tripodi, P., Di Gioacchino, D., Borelli, R., & Vinko, J. D. (2003). Possibility of high temperature superconducting phases in PdH. *Physica C: Superconductivity, 388-389*, 571-572. doi:10.1016/s0921-4534(02)02745-4

Tripodi, P., Di Gioacchino, D., & Vinko, J. D. (2004). Superconductivity in PdH: phenomenological explanation. *Physica C: Superconductivity, 408-410*, 350-352. doi:10.1016/j.physc.2004.02.099

Tripodi, P., Di Gioacchino, D., & Vinko, J. D. (2009). Answer to the remarks on superconductivity in PdH. *Journal of Alloys and Compounds, 470*(1-2), L6-L8. doi:10.1016/j.jallcom.2008.02.109

UKAEA. (2012). Home>Research>Jet. Retrieved from http://www.ccfe.ac.uk/JET.aspx

References

United Nations. (1998). *Kyoto Protocol to the United Nations Framework Convention on Climate Chance*. Kyoto: UN Retrieved from http://unfccc.int/resource/docs/convkp/kpeng.pdf.

Urey, H. C., Brickwedde, F. G., & Murphy, G. M. (1932). A Hydrogen Isotope of Mass 2. *Physical Review, 39*(1), 164-165.

Usselman, M. C. (1978). The Wollaston/Chenevix controversy over the elemental nature of palladium: A curious episode in the history of chemistry. *Annals of Science, 35*(6), 551-579. doi:10.1080/00033797800200431

Völkl, J., Wollenweber, G., Klatt, K., & Alefeld, G. (1971). Reversed Isotope Dependence for Hydrogen Diffusion in Palladium. *Z. Naturforsch. A*(26), 992-923. doi:https://doi.org/10.1515/zna-1971-0522

von Buttlar, H., & Libby, W. F. (1955). Natural distribution of cosmic-ray produced tritium. II. *Journal of Inorganic and Nuclear Chemistry, 1*(1–2), 75-91. doi:http://dx.doi.org/10.1016/0022-1902(55)80070-X

Wicke, E., Brodowsky, H., & Züchner, H. (1978). Hydrogen in palladium and palladium alloys. In G. Alefeld & J. Völkl (Eds.), *Hydrogen in Metals II* (Vol. 29, pp. 73-155): Springer Berlin Heidelberg.

Willis, B. T. M., & Carlile, C. J. (2013). *Experimental Neutron Scattering*. New York: Oxford University Press.

Wollaston, W. H. (1805). On the Discovery of Palladium; With Observations on Other Substances Found with Platina. *Philosophical Transactions of the Royal Society of London, 95*, 316-330. doi:10.1098/rstl.1805.0024

Worsham Jr, J. E., Wilkinson, M. K., & Shull, C. G. (1957). Neutron-diffraction observations on the palladium-hydrogen and palladium-deuterium systems. *Journal of Physics and Chemistry of Solids, 3*(3–4), 303-310. doi:http://dx.doi.org/10.1016/0022-3697(57)90033-1

Yussouff, M., Rao, B. K., & Jena, P. (1995). Reverse isotope effect on the superconductivity of PdH, PdD, and PdT. *Solid State Communications, 94*(7), 549-553. doi:http://dx.doi.org/10.1016/0038-1098(94)00909-0

Appendices

A. ISIS Sample Can Specification

Specification of 316 Stainless Steel

Chemical Element	% Present
Carbon (C)	0.0 - 0.03
Chromium (Cr)	16.50 - 18.50
Molybdenum (Mo)	2.00 - 2.50
Silicon (Si)	0.0 - 1.00
Phosphorous (P)	0.0 - 0.05
Sulphur (S)	0.0 - 0.03
Nickel (Ni)	10.00 - 13.00
Manganese (Mn)	0.0 - 2.00
Nitrogen (N)	0.0 - 0.11
Iron (Fe)	Balance

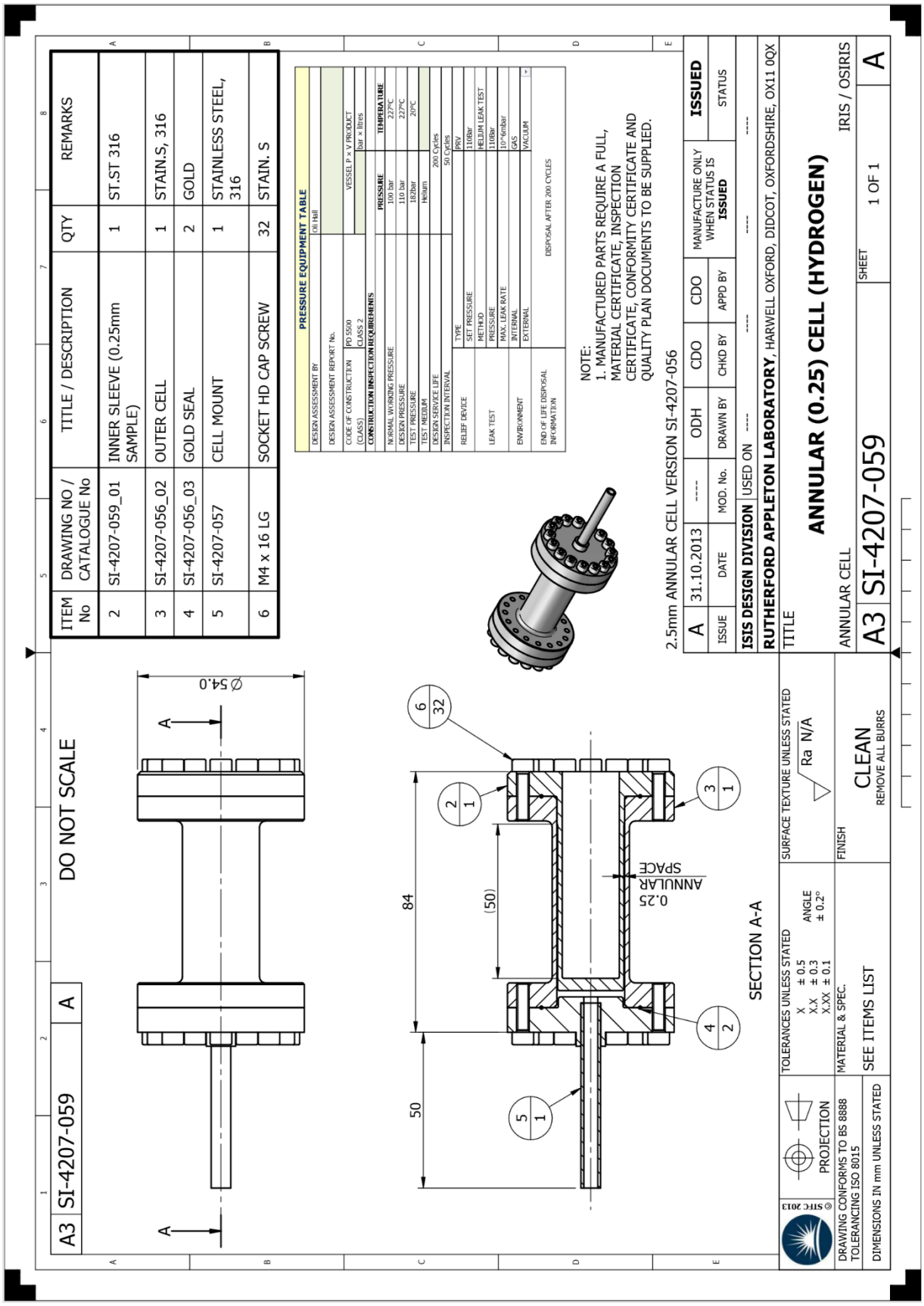
A3 SI-4207-059 A
DO NOT SCALE
ITEM No | DRAWING NO / CATALOGUE No | TITLE / DESCRIPTION | QTY | REMARKS
2 | SI-4207-059_01 | INNER SLEEVE (0.25mm SAMPLE) | 1 | ST.ST 316
3 | SI-4207-056_02 | OUTER CELL | 1 | STAIN.S, 316
4 | SI-4207-056_03 | GOLD SEAL | 2 | GOLD
5 | SI-4207-057 | CELL MOUNT | 1 | STAINLESS STEEL, 316
6 | M4 x 16 LG | SOCKET HD CAP SCREW | 32 | STAIN. S
PRESSURE EQUIPMENT TABLE
DESIGN ASSESSMENT BY: CKI Hall
DESIGN ASSESSMENT REPORT No.:
CODE OF CONSTRUCTION (CLASS): PD 5500 CLASS 2
VESSEL P x V PRODUCT: bar x litres
CONSTRUCTION INSPECTION REQUIREMENTS
NORMAL WORKING PRESSURE: PRESSURE 100 bar TEMPERATURE 22°C
DESIGN PRESSURE: 110 bar 22°C
TEST PRESSURE: 182bar 20°C
TEST MEDIUM: Helium
DESIGN SERVICE LIFE: 200 Cycles
INSPECTION INTERVAL: 50 cycles
RELIEF DEVICE: TYPE PRV; SET PRESSURE 110Bar
LEAK TEST: METHOD HELIUM LEAK TEST; PRESSURE 110Bar; MAX. LEAK RATE 10^-6mbar
ENVIRONMENT: INTERNAL GAS; EXTERNAL VACUUM
END OF LIFE DISPOSAL INFORMATION: DISPOSAL AFTER 200 CYCLES
NOTE:
1. MANUFACTURED PARTS REQUIRE A FULL, MATERIAL CERTIFICATE, INSPECTION CERTIFICATE, CONFORMITY CERTIFICATE AND QUALITY PLAN DOCUMENTS TO BE SUPPLIED.
2.5mm ANNULAR CELL VERSION SI-4207-056
A | 31.10.2013 | ---- | ODH | CDO | CDO | MANUFACTURE ONLY WHEN STATUS IS ISSUED | ISSUED
ISSUE | DATE | MOD. No. | DRAWN BY | CHKD BY | APPD BY | STATUS
ISIS DESIGN DIVISION | USED ON ---- ---- ---- ----
RUTHERFORD APPLETON LABORATORY, HARWELL OXFORD, DIDCOT, OXFORDSHIRE, OX11 0QX
TITLE
ANNULAR (0.25) CELL (HYDROGEN)
ANNULAR CELL
IRIS / OSIRIS
A3 SI-4207-059
SHEET 1 OF 1
A
SECTION A-A
84
50
(50)
0.25 ANNULAR SPACE
Ø54.0
TOLERANCES UNLESS STATED
X ± 0.5
X.X ± 0.3
X.XX ± 0.1
ANGLE ± 0.2°
SURFACE TEXTURE UNLESS STATED
Ra N/A
FINISH
CLEAN
REMOVE ALL BURRS
PROJECTION
MATERIAL & SPEC.
SEE ITEMS LIST
DRAWING CONFORMS TO BS 8888 TOLERANCING ISO 8015
DIMENSIONS IN mm UNLESS STATED
STFC 2013

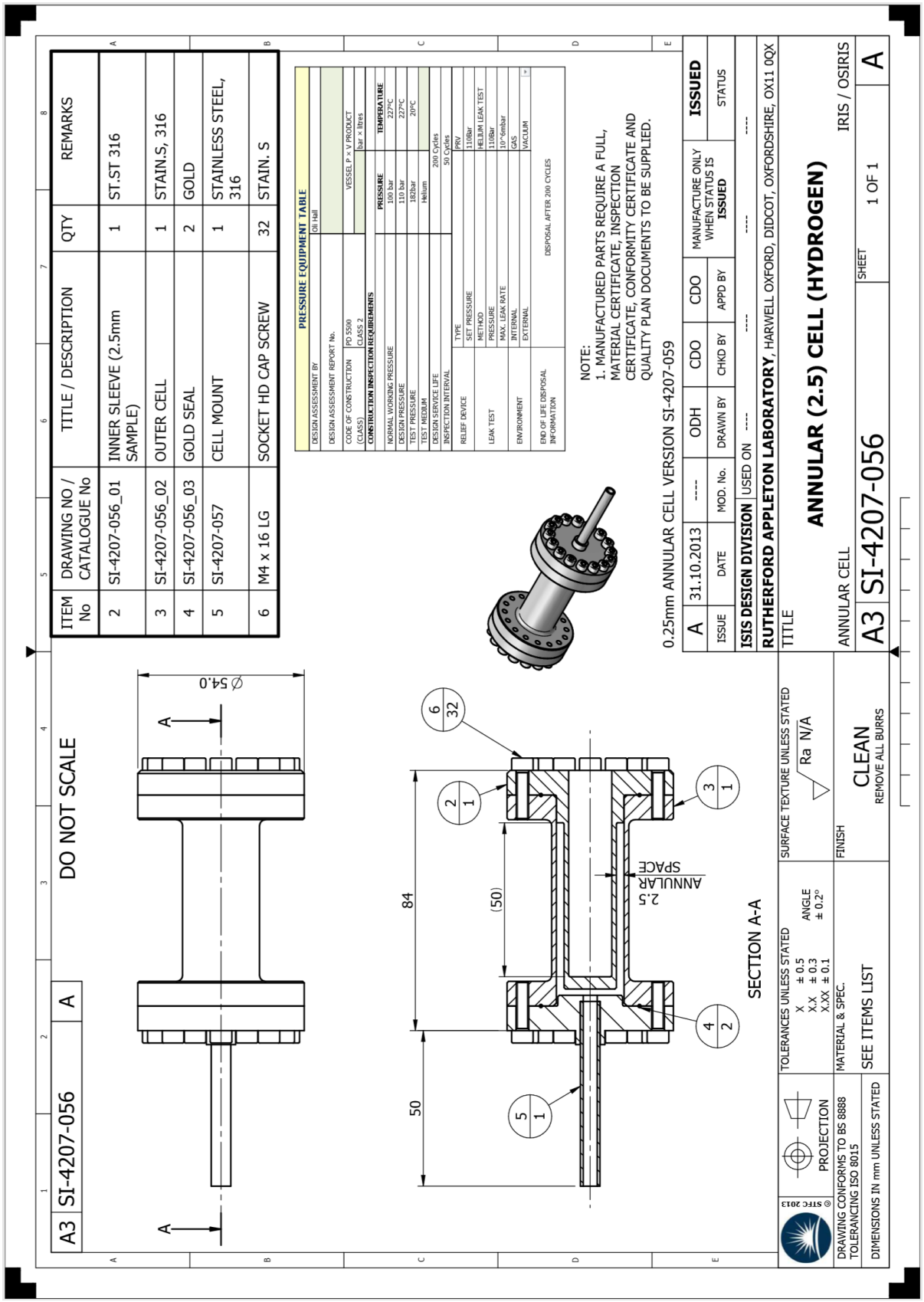
A3 SI-4207-056 A
DO NOT SCALE
ITEM No | DRAWING NO / CATALOGUE No | TITLE / DESCRIPTION | QTY | REMARKS
2 | SI-4207-056_01 | INNER SLEEVE (2.5mm SAMPLE) | 1 | ST.ST 316
3 | SI-4207-056_02 | OUTER CELL | 1 | STAIN.S, 316
4 | SI-4207-056_03 | GOLD SEAL | 2 | GOLD
5 | SI-4207-057 | CELL MOUNT | 1 | STAINLESS STEEL, 316
6 | M4 x 16 LG | SOCKET HD CAP SCREW | 32 | STAIN. S
PRESSURE EQUIPMENT TABLE
DESIGN ASSESSMENT BY: Oli Hall
DESIGN ASSESSMENT REPORT No.
CODE OF CONSTRUCTION: PD 5500 — VESSEL P × V PRODUCT
(CLASS): CLASS 2 — bar × litres
CONSTRUCTION INSPECTION REQUIREMENTS
NORMAL WORKING PRESSURE: 100 bar — 227ºC
DESIGN PRESSURE: 110 bar — 227ºC
TEST PRESSURE: 182bar — 20ºC
TEST MEDIUM: Helium
DESIGN SERVICE LIFE: 200 Cycles
INSPECTION INTERVAL: 50 Cycles
RELIEF DEVICE: TYPE PRV; SET PRESSURE 110Bar
LEAK TEST: METHOD HELIUM LEAK TEST; PRESSURE 110Bar; MAX. LEAK RATE 10^-6mbar
ENVIRONMENT: INTERNAL GAS; EXTERNAL VACUUM
END OF LIFE DISPOSAL INFORMATION: DISPOSAL AFTER 200 CYCLES
NOTE:
1. MANUFACTURED PARTS REQUIRE A FULL, MATERIAL CERTIFICATE, INSPECTION CERTIFICATE, CONFORMITY CERTIFICATE AND QUALITY PLAN DOCUMENTS TO BE SUPPLIED.
0.25mm ANNULAR CELL VERSION SI-4207-059
A | 31.10.2013 | ---- | ODH | CDO | CDO | MANUFACTURE ONLY WHEN STATUS IS ISSUED | ISSUED
ISSUE | DATE | MOD. No. | DRAWN BY | CHKD BY | APPD BY | STATUS
ISIS DESIGN DIVISION | USED ON ---- | ---- | ---- | ----
RUTHERFORD APPLETON LABORATORY, HARWELL OXFORD, DIDCOT, OXFORDSHIRE, OX11 0QX
TITLE
ANNULAR (2.5) CELL (HYDROGEN)
ANNULAR CELL
IRIS / OSIRIS
A3 SI-4207-056 SHEET 1 OF 1 A
A
54.0 Ø
SECTION A-A
84
50
(50)
2.5 ANNULAR SPACE
TOLERANCES UNLESS STATED
X ± 0.5
X.X ± 0.3
X.XX ± 0.1
ANGLE ± 0.2°
SURFACE TEXTURE UNLESS STATED
Ra N/A
FINISH
CLEAN
REMOVE ALL BURRS
PROJECTION
STFC 2013
DRAWING CONFORMS TO BS 8888 TOLERANCING ISO 8015
MATERIAL & SPEC.
SEE ITEMS LIST
DIMENSIONS IN mm UNLESS STATED

B. Error Calculation

All the errors presented in this document are calculated using standard techniques.

The error in the mean of a set of values is always given as the standard deviation.

The error in a value that has been transformed by a function is given by the following rule:

$$\Delta f(x) = \frac{df(x)}{dx}\Delta x$$

Where multiple values with errors are combined, standard techniques are employed e.g.

For:

$$(D \pm \Delta D) = (A \pm \Delta A) + (B \pm \Delta B) - (C \pm \Delta C)$$

$$\Delta D = \sqrt{(\Delta A)^2 + (\Delta B)^2 + (\Delta C)^2}$$

And, for:

$$(D \pm \Delta D) = \frac{(A \pm \Delta A)(B \pm \Delta B)}{(C \pm \Delta C)}$$

$$\Delta D = |D|\sqrt{\left(\frac{\Delta A}{A}\right)^2 + \left(\frac{\Delta B}{B}\right)^2 + \left(\frac{\Delta C}{C}\right)^2}$$

C. Pd-H Composition Measurements

The following section details the gravimetric sorption measurements used to determine the hydrogen compositions given throughout this work.

These measurements were conducted using a Hiden Isochema IGA. This unit has a pressure range of $0 < P < 20\ Bar$. The technical operating limit at the low pressure end is roughly $10^{-5}\ Bar$. The room where the unit is installed is kept at a constant $21\ °C$ with a dedicated air conditioning unit. Temperature was controlled using a Hiden Cryofurnace without a liquid nitrogen feed. This gives an operating temperature range of $21 < T < 500\ °C$.

All of the measurements detailed in this section were taken for the spherical palladium powder described in section 2.4.1.

Only a few compositions at specific temperatures and pressures were required to complete the calculations in this work. As such a slightly different method to that described in section 2.5.1 was employed.

After loading the sample and measuring the dry weight under vacuum, a series of measurements were collected at each required temperature and pressure under helium. As the helium should not be ad/absorbed by any of the components or sample, this measurement was taken as a buoyancy corrected 'dry' mass. Then the measurements were repeated with hydrogen. The difference in the relevant He and H_2 measurements was then taken to be equivalent to the mass of the absorbed hydrogen. While this method does not account for changes in the sample volume, it is as (if not more) reliable than the previously described technique.

The measurements contain substantial stochastic noise. This is thought to be due to deviations in the balance caused by turbulence. As such, each measurement was allowed to reach equilibrium and data was collected for a substantial amount of time (always over half an hour). For each of these measurements, the final calculated data points are given as the mean ± the standard deviation of the period at equilibrium.

The components of the balance and the measured mass of the sample (pre-loading, during loading, and the measured dry mass) are detailed in the table below:

Component	Weight (g)	(mg)	Material	Density (g/cm3)
Sample holder	0.3372	337.2	Quartz glass	2.203
Lower Hangdown	0.053	53	Tungsten	19.25
Upper Hangdown	0.3417	341.7	Gold	19.3
Counterweight	0.5556	555.6	Steel	7.9
Upper Hangdown	0.255	255	Gold	19.3
Lower Hangdown	0.001	1	Tungsten	19.25
Sample (balance)	0.1854	185.4	Palladium	12.023
Sample (IGA)	0.185567	185.567	Palladium	12.023
Sample (IGA dry)	0.1855	185.5	Palladium	12.023

The following measurements were collected under helium:

Temperature			Mass		Pressure	
Mean (°C)	(K)	s.d.	Mean (mg)	s.d.	Mean mBar	s.d.
128.3652	401.5152	0.029806	185.3374	0.004557	9996.223	2.309117
140.17	413.32	0.098557	185.3305	0.004458	10499.23	1.529305
147.8841	421.0341	0.097402	185.3304	0.004776	10499.28	3.529571
162.327	435.477	0.05473	185.4157	0.000531	3996.992	1.644107
181.2675	454.4175	0.038645	185.4145	0.000753	4200.735	3.287416
187.4588	460.6088	0.086108	185.3507	0.006678	9993.787	9.219358
186.7708	459.9208	0.083146	185.3451	0.007112	10496.86	10.49729
196.6203	469.7703	0.037171	185.3641	0.007892	8896.071	7.242707
201.5686	474.7186	0.061011	185.3497	0.006938	9996.346	1.44499
201.2569	474.4069	0.041019	185.3441	0.006406	10498.64	7.806693
210.2781	483.4281	0.032796	185.3594	0.006732	9687.16	18.60364
215.5357	488.6857	0.067441	185.3518	0.0068	9994.418	5.659162

214.8465	487.9965	0.068218	185.3354	0.006972	10496.1	10.05358
224.6573	497.8073	0.119961	185.341	0.008296	9991.657	15.633
224.1742	497.3242	0.086193	185.3335	0.007273	10496.76	9.86432

These measurements are summarised in the following plot:

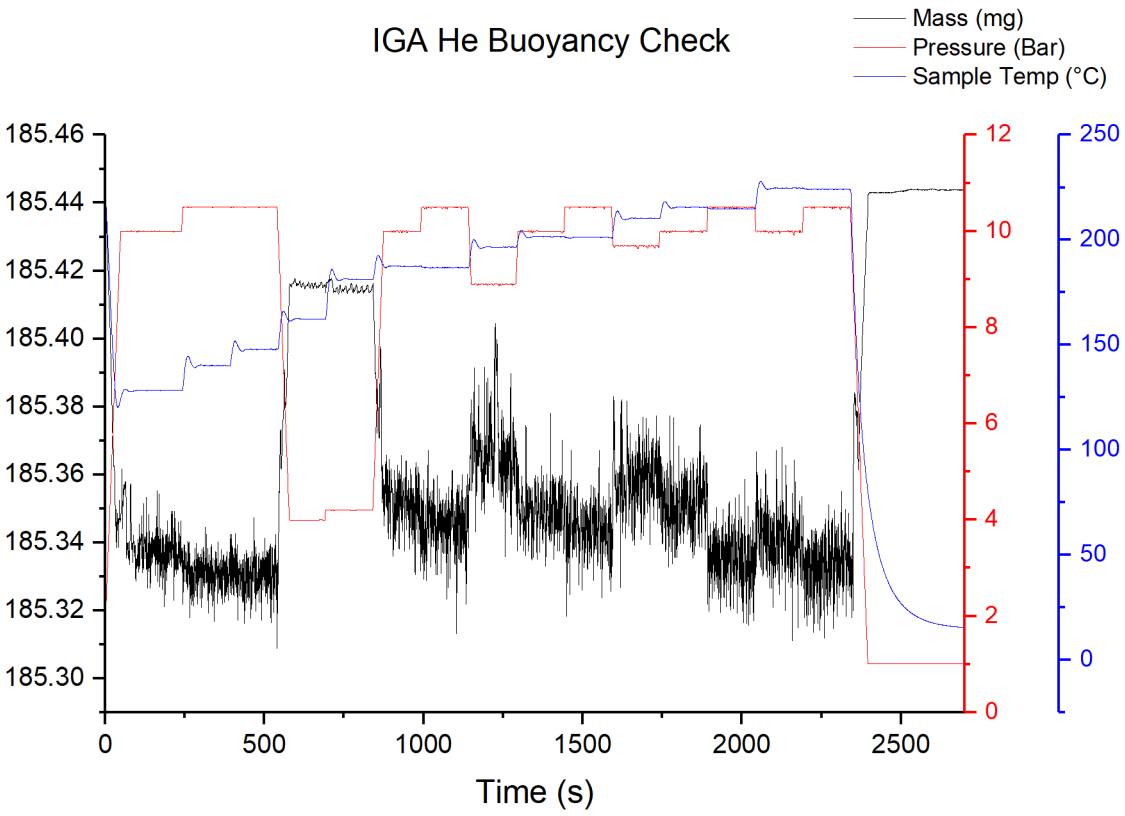

The following measurements were collected under hydrogen:

Temperature			Mass		Pressure	
Mean (°C)	Mean (K)	s.d.	Mean (mg)	s.d.	Mean mBar	s.d.
223.3886	496.5386	0.254984	186.3621	0.003548	10494.76	11.64561
212.5678	485.7178	0.536145	186.3957	0.004115	10497.01	8.891176
196.3285	469.4785	0.328352	186.4359	0.004686	10488.86	16.10802
182.5478	455.6978	0.228398	186.4627	0.003773	10496.58	8.478309
147.3217	420.4717	0.436818	186.5222	0.00441	10493.73	12.66757
139.1715	412.3215	0.214446	186.5315	0.003427	10498.01	5.744402

128.6937	401.8437	0.130992	186.5478	0.002829	9993.837	8.96365
163.9971	437.1471	0.023522	186.4802	0.000333	4000.539	2.764842
182.877	456.027	0.020503	186.4265	0.000178	4198.501	2.565756
185.7906	458.9406	0.257577	186.4565	0.0043	9989.905	15.20155
195.1742	468.3242	0.041234	186.4367	0.002315	8898.441	2.968742
200.518	473.668	0.189446	186.4229	0.003677	9992.9	10.10122
208.7175	481.8675	0.161373	186.4005	0.003307	9693.814	14.8386
224.3008	497.4508	0.191479	186.3519	0.003643	9989.282	11.99867

These measurements are summarised in the following plots:

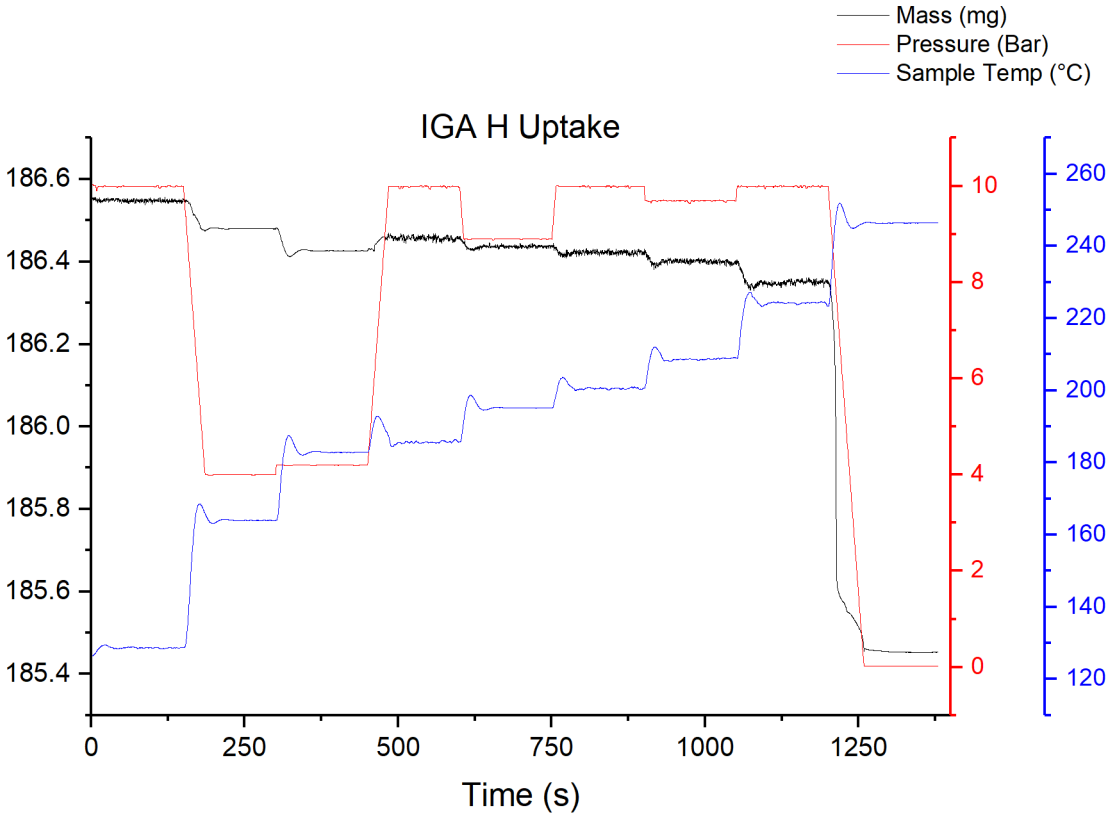

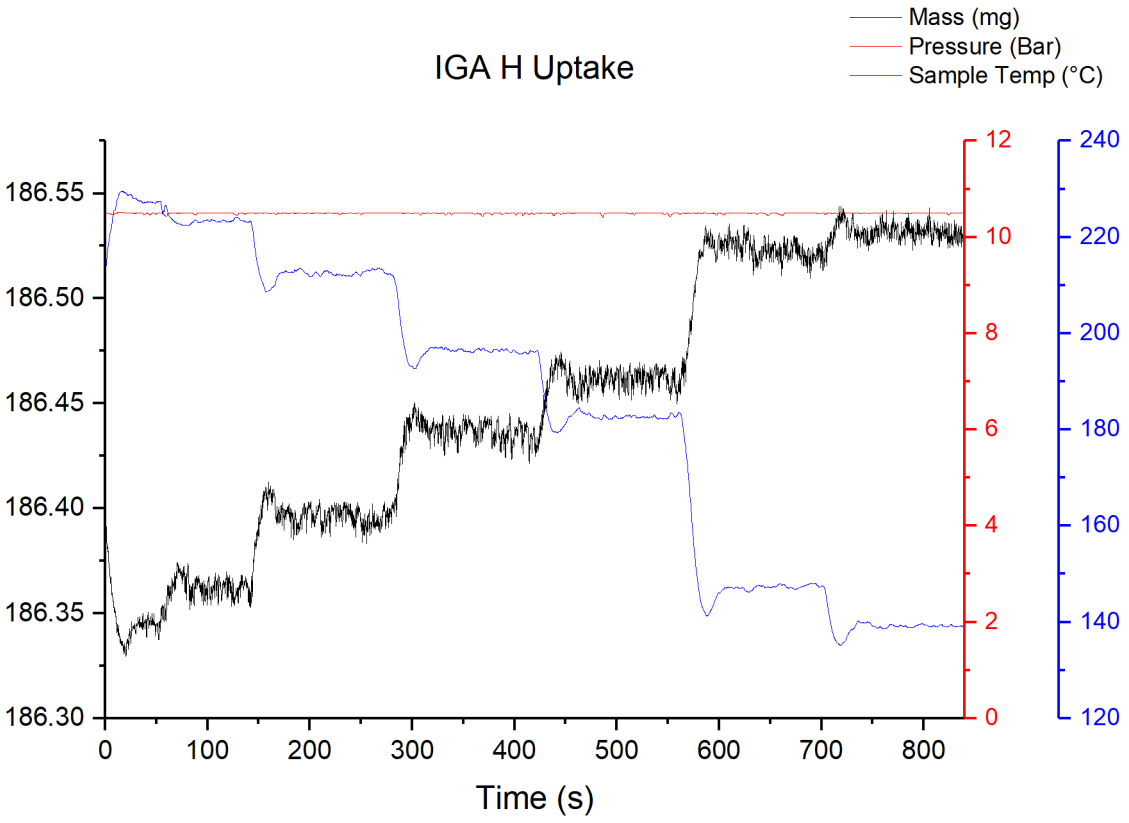

The measured mass gain (hydrogen mass) and the mass of the palladium were then converted into a molar fraction H/Pd:

Temperature			Pressure			
Mean (°C)	Mean (K)	s.d.	Mean (mg)	s.d.	H/Pd	Error
128.6937	401.8437	0.130992	9993.837	8.96365	**0.688942**	**0.004208**
139.1715	412.3215	0.214446	10498.01	5.744402	**0.683577**	**0.004491**
147.3217	420.4717	0.436818	10493.73	12.66757	**0.67837**	**0.005232**
163.9971	437.1471	0.023522	4000.539	2.764842	**0.605915**	**0.000495**
182.877	456.027	0.020503	4198.501	2.565756	**0.575987**	**0.000533**
185.7906	458.9406	0.257577	9989.905	15.20155	**0.629383**	**0.006252**
182.5478	455.6978	0.228398	10496.58	8.478309	**0.63612**	**0.006199**
195.1742	468.3242	0.041234	8898.441	2.968742	**0.610501**	**0.005812**
200.518	473.668	0.189446	9992.9	10.10122	**0.610802**	**0.006045**
196.3285	469.4785	0.328352	10488.86	16.10802	**0.621387**	**0.006316**
208.7175	481.8675	0.161373	9693.814	14.8386	**0.59256**	**0.005717**

212.5678	485.7178	0.536145	10497.01	8.891176	**0.603487**	**0.006313**
224.3008	497.4508	0.191479	9989.282	11.99867	**0.575363**	**0.006798**
223.3886	496.5386	0.254984	10494.76	11.64561	**0.585446**	**0.006162**

These values have been appropriately rounded where they are shown in the main body of this document. The precision shown here is the raw calculated values from these measurements.

It should be noted that the temperatures are not identical to those used in the neutron scattering measurements. This is due to the nature of the furnace, measurement and PID system used. However, the errors induced by these small deviations (around 1 or 2 K) are negligible.

D.Pd-D Composition Measurements

A series of isotherms were collected for palladium deuteride using a Hiden Isochema HTP1. This is an automated manometric instrument (a full description of the technique can be found in section 2.5.2). This instrument has a pressure range of $0 < P < 100\ Bar$ and a temperature range (without a cryogen supply) of $\sim 50 < T < 500\ °C$.

This instrument is not designed to measure uptake at a single temperature and pressure. Instead, full isotherms were collected for spherical powder (section 2.4.1) over the four highest temperatures used in the neutron experiments described in section 4.4.1.2. Multiple passes were performed at each temperature. These measurements are summarised in the plot below.

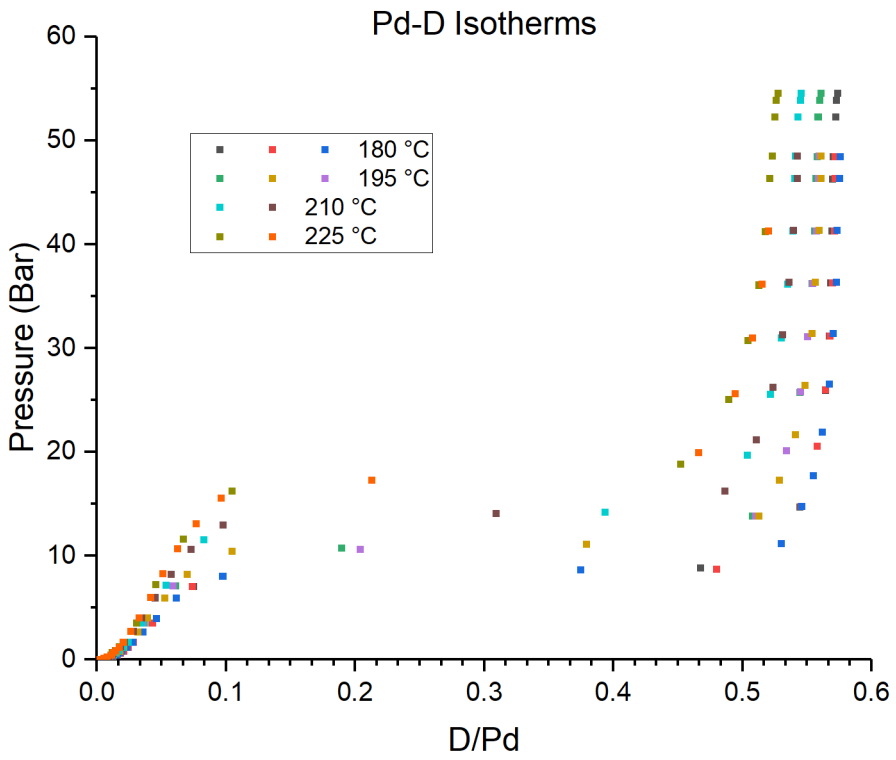

For these temperatures, the quoted concentrations in the main body of this work have been derived by linear interpolation between the means of the nearest relevant points in this plot. For the lower temperature that was not measured, concentrations have been estimated based on the data shown here.

Based on this method, the following concentrations were used in the calculations shown in chapter 4:

Temperature (°C)	K	Pressure (mBar)	D/Pd
160	433.15	33.6	**0.58**
180	453.15	34.5	**0.57**
195	468.15	35	**0.555**
210	483.15	38	**0.537**
225	498.15	42.5	**0.52**

E. Lattice Parameter (Abbenseth & Wipf, 1980)

The plot from this paper has been digitised. The values quoted in the main body of the text are extrapolated from the subsequent fit.

In this work, palladium samples were electrochemically loaded with either hydrogen or deuterium. The samples then had their surface poisoned to stop any further ab/desorption.

In the plot below-left, the original collected data are shown. The plot below-right shows the digitised points above the temperature where $\Delta l/l$ becomes linear.

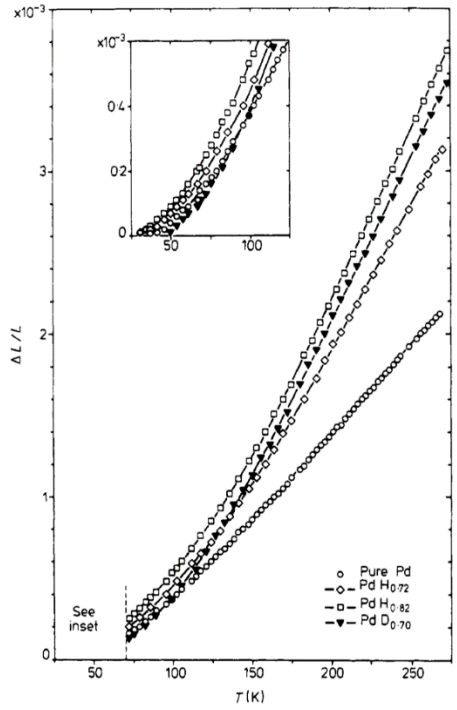

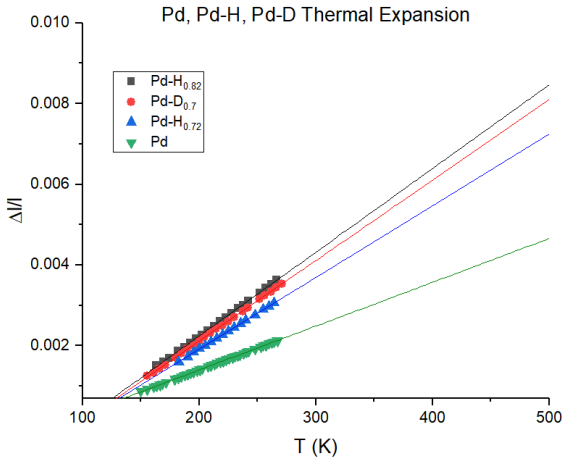

Left: Original plot from (Abbenseth & Wipf, 1980)
Top: Digitised plot (marked points used in digitisation process – trend lines fitted with Origin Pro)

The fitted lines do not converge to $\Delta l/l = 0$ for $T = 0$ as there appears to be a change in the lattice parameter – temperature relationship below around $150\ K$ and the initial measured l was taken below this point.

These fitted lines were then used to calculate lattice parameters for Pd-H and Pd-D. As the absolute measurements were not reported in the paper, the standard values quoted for Pd-H and Pd-D have been assumed to occur at STP. This assumption is not expected to accurately represent the system but provides a reasonable starting point for further calculations.

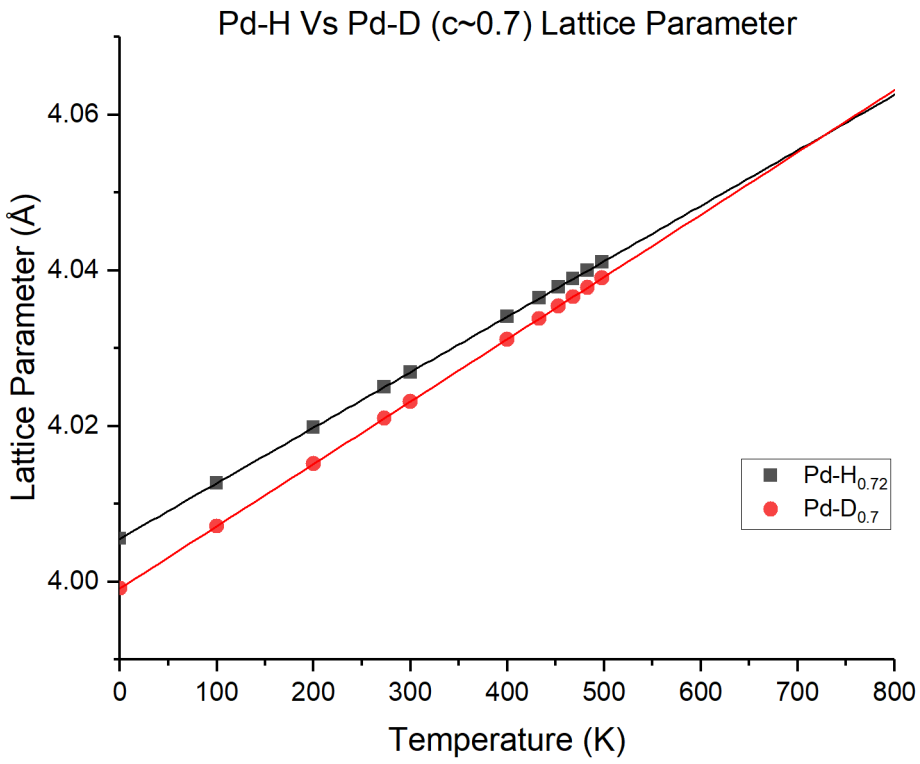

The plot above shows the extrapolated lattice parameter lines given the $l(T)$ relationships derived from the original data. The absolute lattice parameters are not expected to be accurate. However, they are close enough to the measurements made in this work that the method employed can be considered feasible.

The $l(T)$ relationship for both materials has been assumed to remain consistent at higher temperatures. There is no major structural phase boundary in this region. However, the change in this relationship at around $150\ K$ in the original data, may coincide with more subtle transition (such as a change in short range order). As this work (chapters 4 and 5) appears to suggest that ordering persists at high temperatures, it is feasible that further changes in this relationship may exist.

Setting $l(Pd-H) = l(Pd-D)$ yields a prediction that the lattice parameters should converge at around $736.1\ K$.

With the assumptions made, and the lack of precise values from the original measurements, this value is only considered a rough guide as to where the actual temperature of this convergence.

F. Software Used in This Project / Document

This document was produced using Microsoft Word 365, part of the Office 365 suite: https://www.office.com/ (Microsoft, 2017)

Referencing and bibliography in this document is managed with EndNote X8: http://endnote.com/ (Clarivate Analytics, 2017)

Many of the vector images in this document were produced using Affinity Designer by Serif: https://affinity.serif.com/en-gb/designer/ (Serif, 2017a).

The bitmap images in this document were edited with either Paint.net: https://www.getpaint.net (dotPDN LLC, 2017) or Affinity Photo by Serif: https://affinity.serif.com/en-gb/photo/ (Serif, 2017b).

Crystallographic diagrams in this document were produced using VESTA: http://jp-minerals.org/vesta/en/ (Momma & Izumi, 2011).

Many of the plots in this document were produced with OriginPro: http://www.originlab.com/Origin (OriginLab, 2017)

All of the neutron data in this body of work was, at some point, processed with MantidPlot: http://www.mantidproject.org (Mantid, 2013). Fitting of Lorentzian components used the Qlines script in Mantid which was based on Quasilines (Sivia D.S. et al., 1992). All scripts to process data were written in Python 2.x: https://www.python.org/ (Python Foundation, 2017).

Additional data processing used either Microsoft Excel 365: https://www.office.com/ (Microsoft, 2017) or OriginPro: http://www.originlab.com/Origin (OriginLab, 2017).

Python scripting of UDF's in Excel was achieved using ExcelPython: http://ericremoreynolds.github.io/excelpython/ (Reynolds, 2015)

The following additional Python libraries have been used in this work:

NumPy	http://www.numpy.org/
MatPlotLib	https://matplotlib.org/
OpenPyXl	https://openpyxl.readthedocs.io/en/stable/